

Copyright

by

Aaron Benjamin Morris

2012

**The Dissertation Committee for Aaron Benjamin Morris Certifies that
this is the approved version of the following dissertation:**

**Simulation of Rocket Plume Impingement and Dust Dispersal on the
Lunar Surface**

Committee:

David B. Goldstein, Co-Supervisor

Philip L. Varghese, Co-Supervisor

Philip Metzger

Laurence M. Trafton

Venkatramanan Raman

**Simulation of Rocket Plume Impingement and Dust Dispersal on the
Lunar Surface**

by

Aaron Benjamin Morris, B. S., M. S. E.

Dissertation

Presented to the Faculty of the Graduate School of
The University of Texas at Austin
in Partial Fulfillment
of the Requirements
for the Degree of

Doctor of Philosophy

**The University of Texas at Austin
December 2012**

Dedicated to my family.

Acknowledgements

I would first like to thank my advisors, Profs. David Goldstein and Philip Varghese for their guidance and support throughout my graduate studies. They always made themselves available and constantly gave me excellent guidance. I would also like to thank the other committee members for their contributions and proofreading of this dissertation.

This work was made possible by the efforts of past and present graduate student colleagues, namely Chris Moore, Bénédicte Stewart, Andrew Walker, Billy McDoniel, Seng Keat Yeoh, and Parvathy Prem, who all helped develop the DSMC research code. I'd also like to thank Chris Moore, Bénédicte Stewart, and Andrew Walker for teaching me the fundamentals of DSMC when I was first starting. I also want to thank Dr. Laurence Trafton for his assistance during our weekly research meetings and sharing his expertise on the lunar environment. Dr. Metzger, from the Kennedy Space Center, has been extremely helpful throughout this work. I would like to thank him for helping me understand the aspects of erosion, relevant observations during the Apollo missions, and also introducing me to other researchers working on problems associated with plume impingement.

Graduate school would not have been nearly as enjoyable without meeting and becoming friends with other students and friendly Austinites. I'd like to thank all of my friends for the great memories.

I also want to thank the Texas Advanced Computing Center (TACC) for providing the HPC resources that made these simulations possible. I also want to acknowledge NASA ARC for graciously providing me with the Navier-Stokes solver DPLR. I also thank Kelly Stephani (a former student of Profs. Goldstein and Varghese)

for showing me how to use DPLR. My graduate studies would not have been possible if not for continuous funding. Funding for the work done on my Master's thesis was provided by NASA cooperative agreement NNX08AB27A and the work in this dissertation was funded by NASA LASER grant NNX08AW08G.

Lastly, I can't thank my parents and family members enough for all the support and encouragement that they've given me over the years.

Simulation of Rocket Plume Impingement and Dust Dispersal on the Lunar Surface

Aaron Benjamin Morris, Ph.D.

The University of Texas at Austin, 2012

Supervisors: David B. Goldstein and Philip L. Varghese

When a lander approaches a dusty surface, the plume from the descent engine impinges on the ground and entrains loose regolith into a high velocity spray. This problem exhibits a wide variety of complex phenomena such as highly under-expanded plume impingement, transition from continuum to free molecular flow, erosion, coupled gas-dust motions, and granular collisions for a polydisperse distribution of aerosolized particles. The focus of this work is to identify and model the important physical phenomena and to characterize the dust motion that would result during typical lunar landings. A hybrid continuum-kinetic solver is used, but most of the complex physics are simulated using the direct simulation Monte Carlo method.

A descent engine of comparable size and thrust to the Lunar Module Descent Engine is simulated because it allows for direct comparison to Apollo observations. Steady axisymmetric impingement was first studied for different thrust engines and different hovering altitudes. The erosion profiles are obtained from empirically derived scaling relationships and calibrated to closely match the net erosion observed during the Apollo missions. Once entrained, the dust motion is strongly influenced by particle-particle collisions and the collision elasticity. The effects of two-way coupling between the dust and gas motions are also studied.

Small particles less than 1 μm in diameter are accelerated to speeds that exceed 1000 m/s. The larger particles have more inertia and are accelerated to slower speeds, approximately 350 m/s for 11 μm grains, but all particle sizes tend to obtain their maximum speed within approximately 40 m from the lander. The maximum particle speeds and erosion rates tend to increase as the lander approaches the lunar surface. The erosion rates scale linearly with engine thrust and the maximum particle speed increases for higher thrust engines.

Dust particles are able to travel very far from the lander because there is no background atmosphere on the moon to inhibit their motion. The far field deposition is obtained by using a staged calculation, where the first stages are in the near field where the flow is quasi-steady and the outer stages are unsteady. A realistic landing trajectory is approximated by a set of discrete hovering altitudes which range from 20 m to 3 m. Larger particles are accelerated to slower speeds and are deposited closer to the lander than smaller particles. Many of the gas molecules exceed lunar escape speed, but some gas molecules become trapped within the dust cloud and remain on the moon.

The high velocity particulate sprays can be damaging to nearby structures, such as a lunar outpost. One way of mitigating this damage is to use a berm or fence to shield nearby structures from the dust spray. This work attempts to predict the effectiveness of such a fence. The effects of fence height, placement, and angle as well as the model sensitivity to the fence restitution coefficient are discussed. The expected forces exerted on fences placed at various locations are computed. The pressure forces were found to be relatively small at fences placed at practical distances from the landing site. The trajectories of particles that narrowly avoid the fence were not significantly altered by the fence, suggesting that the dust motion is weakly coupled to the gas in the near vicinity of the fence.

Future landers may use multi-engine configurations that can form 3-dimensional gas and dust flows. There are multiple plume-plume and plume-surface interactions that affect the erosion rates and directionality of the dust sprays. A 4-engine configuration is simulated in this work for different hovering altitudes. The focusing of dust along certain trajectories depends on the lander hovering altitude, where at lower altitudes the dust particles focus along symmetry planes while at higher altitudes the sprays are more uniform. The surface erosion and trenching behavior for a 4-engine lander are also discussed.

Table of Contents

List of Tables	xiii
List of Figures	xiv
CHAPTER 1 . INTRODUCTION	1
Section 1.1. Motivation.....	1
Section 1.2. Objectives and Dissertation Overview.....	2
CHAPTER 2 . LITERATURE REVIEW	7
Section 2.1. Physical Overview	7
Section 2.2. Internal Nozzle and Plume Flow.....	9
2.2.1. Real Nozzles	9
2.2.2. The Lunar Module Descent Engine	11
2.2.3. Highly Under-expanded Plumes.....	13
2.2.4. Continuum Breakdown	14
Section 2.3. Plume Impingement.	16
2.3.1. Impingement on a Flat Normal Surface.....	16
2.3.2. Plume Impingement From Multiple Nozzles.....	19
Section 2.4. Dust Erosion.....	20
2.4.1. Erosion Phenomenology	20
2.4.2. Viscous Erosion	21
Section 2.5. Two-Phase Flow	26
2.5.1. Granular Flow Regimes	26
2.5.2. Rapid Granular Flows and Granular Phenomena	27
2.5.3. Granular Collisions	28
2.5.4. Drag on Spherical Particles.....	32
Section 2.6. Properties of Lunar Regolith.....	35
2.6.1. Physical Properties.....	35
2.6.2. Particle Size Distributions	36
Section 2.7. The Apollo Landings	38
2.7.2. Apollo Observations	39
CHAPTER 3 . METHOD	44
Section 3.1. Continuum Regime	44
Section 3.2. Rarefied Regime	47
3.2.1. Coupling DPLR to DSMC.....	47
Section 3.3. Two-Phase Flow	50
3.3.1. The Particle Size Distribution.....	50
3.3.2. Dust Erosion Model	53
3.3.3. Dust – Gas Coupling.....	55
3.3.4. Particle Collisions.....	66

CHAPTER 4 . THE NEAR FIELD GAS FLOW FIELD	70
Section 4.1. Internal Nozzle Flow.....	70
Section 4.2. Near Field Plume Flow	73
4.2.2. Effects of Turbulence.....	74
4.2.3. Continuum Breakdown and Hybridization	76
Section 4.3. Plume Impingement.....	80
4.3.1. Variations with Hovering Altitude	80
4.3.2. Nozzle Geometry Effects.....	82
Section 4.4. Gas Properties Near the Surface	85
4.4.1. Compressible Stagnation Point Flow and Boundary Layers	85
4.4.2. Surface Stresses and Erosion Rates	91
4.4.3. Different Thrust Engines	101
Section 4.5. Chapter Summary	102
CHAPTER 5 . NEAR FIELD DUST SPRAYS.....	105
Section 5.1. Sensitivity to Physical Models.....	105
5.1.1. The Effects of Gas-Dust Coupling	105
5.1.2. The Effects of Grain-Grain Collisions.....	119
Section 5.2. Effects of Hovering Altitude.....	127
Section 5.3. Variations in Dust Sprays with Thrust Levels	134
Section 5.4. Chapter Summary	139
CHAPTER 6 . FAR FIELD SIMULATIONS.....	142
Section 6.1. Method for Staged Simulations	142
Section 6.2. Far Field Gas Flow.....	144
Section 6.3. Unsteady Dust Sprays and Deposition.....	147
Section 6.4. Chapter Summary	153
CHAPTER 7 . INTERACTION WITH A LUNAR FENCE	155
Section 7.1. Effects of Fence Placement.....	155
7.1.1. Gas Interactions	155
7.1.2. Dust Interactions	157
Section 7.2. Fence Height	163
Section 7.3. Fence Angle	167
Section 7.4. Model Sensitivity	169
7.4.1. Fence Coefficient of Restitution	169
7.4.2. Grain-Grain Collisions.....	170
Section 7.5. Flow Unsteadiness	172
Section 7.6. Chapter Summary	175
CHAPTER 8 . FOUR ENGINE CONFIGURATION	178
Section 8.1. Computational Domain.....	178
Section 8.2. Hovering Altitude Effects	179
8.2.1. Gas Flow Field.....	179
8.2.2. Dust Motion	183

8.2.3. Erosion Rates and Trenching Behavior	191
Section 8.3. Chapter Summary	194
CHAPTER 9. CONCLUSIONS	196
Section 9.1. Summary	196
Section 9.2. Future Work	199
APPENDIX A. MOMENTUM AND ENERGY CONSERVATION FOR THE GAS-PARTICLE INTERACTION MODEL	204
BIBLIOGRAPHY	208
VITA.	214

List of Tables

Table 2.2.1. Descent engine properties for the LMDE and RL-10A-4.	11
Table 2.2.2. Composition of Nozzle-Exit Exhaust Gases for Titan Stage 2 Engine determined from JANNAF simulations (Simmons, 2000).	12
Table 2.6.1. Recommended values for physical properties of lunar soil.	36
Table 2.7.2. Angle of inclination for the various dust sprays observed during different Apollo missions.....	42
Table 3.1.1. Estimated LMDE exit plane and throat properties.	45
Table 4.1.2. Average exit plane properties for a simulated nozzle compared to those predicted for a quasi 1–D expansion of a perfect gas.	73
Table 6.1.1. Altitudes and durations simulated for an approximate landing trajectory.	144

List of Figures

Figure 2.1.1. A schematic showing the various physical phenomena that arise when modeling plume impingement on dusty surfaces.	8
Figure 2.2.1. A method of characteristics solution showing expansion and compression waves inside of a contoured nozzle. Figure adapted from (Dettleff, 1991).	10
Figure 2.4.1. View underneath the Apollo 12 Lunar Module showing that cratering does not occur and that viscous erosion is the likely dominant scouring mechanism.	21
Figure 2.4.2. Mechanisms for entrainment, adapted from (Shao, 2008). Dust emission (a) by aerodynamic lift, (b) by saltation bombardment, and (c) through disaggregation, also known as auto-abrasion.	23
Figure 2.5.1. Drag coefficient computed via Loth's equation for different particle Knudsen and Mach numbers. The dashed lines are the free molecular drag coefficients.	33
Figure 2.6.1. Particle size distributions measured for the sub 20 μm portion of lunar regolith (Greenberg, Chen, & Smith, 2007; Park, Liu, Kihm, & Taylor, 2008).	37
Figure 2.7.1. A nominal thrust profile for the Apollo lunar landings adapted from (Humphries, Hammock, Currie, Taylor, & Fisher, 1973).	39
Figure 2.7.2. Obscured view of the lunar surface as the Apollo 15 lander nears the lunar surface. The green rectangle outlines a crater. Adapted from (Immer, Lane, Metzger, & Clements, 2011).	40
Figure 3.1.1. A schematic of the DPLR computational domain and boundary conditions.	46
Figure 3.2.1. Two examples of hybrid interfaces that slice through the surface shock and show glitches. Note the offset in shock stand-off and the deflected streamlines.	49
Figure 3.3.1. Particle weight distribution for the sub 20 μm fraction of lunar regolith. Bars indicate particle diameters included in our simulations.	52
Figure 3.3.2. Spatially homogeneous test for two different sized dust grains relaxing towards the gas velocity and temperature. The gas is held fixed and is thus uncoupled to the dust. (left) 1 micron grains. (right) 50 micron grains.	59
Figure 3.3.3. Spatially homogeneous relaxation tests for dust grains with different thermal accommodation coefficients, 0.0, 0.5, and 1.0. (left) Relaxation of dust momentum. (right) Relaxation of the dust grain temperature.	60

Figure 3.3.4. The drag force computed for diffuse reflections divided by the drag force for specular reflections plotted for different temperature and speed ratios.....	61
Figure 3.3.5. Contours of Biot number for different dust particle temperatures and particle speed ratios when the gas is held at a fixed 1500 K. The dust particles were 10 μm in diameter.....	62
Figure 3.3.6. A schematic of the angles and coordinate systems used to depict gas-particle collisions.....	64
Figure 3.3.7. Momentum (left) and energy (right) fluxes for the fully coupled gas-particle interaction model. These simulations include 1 and 10 μm particles interacting with H_2O gas. Note the total momentum and energy fluxes are conserved within the noise.	66
Figure 3.3.8. Spatially homogeneous relaxation of a binary granular mixture of 1 and 10 μm particles with different initial velocities and temperatures. (left) Particles relax towards the center of mass velocity. (right) total energy for each species on the left axis and the mean particle temperature is shown on the right axis.	69
Figure 4.1.1. Contours of gas temperature (left) and pressure (right) within the engine bell.	71
Figure 4.1.2. Nozzle exit plane properties computed with DPLR for an engine bell similar to the LMDE.	72
Figure 4.2.1. Contours of temperature (left half) and pressure (right half) in the near field of the plume expansion.....	74
Figure 4.2.2. Slices through the exhaust plume 2 m downstream of the nozzle exit plane. The dashed lines are fully turbulent solutions and the solid lines are laminar solutions. Note the logarithmic x-axis.	75
Figure 4.2.3. Slices through the exhaust plume 3.5 m downstream of the nozzle exit plane. The dashed lines are fully turbulent solutions and the solid lines are laminar solutions. Note the logarithmic x-axis.	76
Figure 4.2.4. Contours of the gas mean free path (left), Bird's breakdown parameter (right), and the hybrid interface (dashed line). The hybrid interface is drawn within the barrel shock and where the breakdown parameter is small.....	77
Figure 4.2.5. Contours of gas pressure for the plume flow field for (left) DPLR solutions and (right) hybrid solutions. Line contours from the DPLR solution are superimposed on the hybrid solution to illustrate differences.....	78
Figure 4.2.6. Vibrational temperatures showing non-equilibrium for the bending mode of water computed with DPLR (left) and the hybrid solver (right). .	79

Figure 4.3.1. Contours of gas pressure and streamlines for a rocket engine hovering 20 m above the lunar surface.	80
Figure 4.3.2. Contours of gas pressure and streamlines for a rocket engine hovering 5 m above the lunar surface.	81
Figure 4.3.3. Pressure contours of the gas flow field when the lander hovers 2 m above the surface.	82
Figure 4.3.4. Contours of gas pressure comparing rocket exhaust plumes from a contoured nozzle (left) and assumed uniform exit-plane properties (right).	84
Figure 4.4.1. Boundary layer profiles at different locations in the near field when a rocket engine hovers 5 m above the surface.	86
Figure 4.4.2. Boundary layer profiles at distances further from the jet axis when a rocket engine hovers 5 m above the surface. Notice the change in scales from Figure 4.4.1.	87
Figure 4.4.3. Thermal boundary layer profiles at different locations when a rocket engine hovers 5 m above the surface.	88
Figure 4.4.4. Heat flux from the gas to an isothermal lunar surface with an assumed surface temperature of 350 K. Note the log-log scales.	89
Figure 4.4.5. Boundary layer profiles 5 m from the jet axis for different hovering altitudes.	90
Figure 4.4.6. Boundary layer profiles 20 m from the jet axis for different hovering altitudes.	90
Figure 4.4.7. Dynamic pressure profiles sampled at roughness scale heights of 2, 5, and 10 cm above the surface. The profiles are normalized to highlight differences in profile shape. The laminar shear stress, dash-dotted line, is plotted on the right axis.	91
Figure 4.4.8. Dynamic pressure distribution computed at a roughness height 5 cm above the lunar surface for rocket engines hovering at different altitudes. Note the log-log scale.	93
Figure 4.4.9. Scaled dynamic pressure distribution for different hovering altitudes compared to Roberts theory.	94
Figure 4.4.10. Location of peak dynamic pressure versus hovering altitude. DSMC results, symbols, Roberts theory, dashed line, and a proposed better fit, solid line, are shown for comparison.	95
Figure 4.4.11. Maximum value for the gas dynamic pressure scaled by the pressure at the stagnation point. The symbols are DSMC, dashed line is Roberts theory, and the solid line is the numerically determined best fit.	97

Figure 4.4.12. Erosion rates versus radial position scaled by the effective hovering altitude, h_{eff} , for altitudes ranging from 20 to 2.5 m. Note the log-log scale.	98
Figure 4.4.13. Erosion profile, square symbols, when the lander hovers 2.0 m above the surface and the surface shock structure transitions from a normal surface shock to an oblique surface shock. The erosion profile when the surface shock is normal at an altitude of 2.5 m, triangles, is drawn for comparison.	99
Figure 4.4.14. Integrated crater depth for a lander approaching the surface at 0.75 m/s.	100
Figure 4.4.15. Gas dynamic pressure sampled 5 cm for different thrust rocket engines hovering 5 m above the surface. The distributions collapse when the dynamic pressure is normalized by the thrust of the rocket engine.	101
Figure 5.1.1. Mean radial velocity contours for 2, 5, and 11 μm particles when the gas is unaffected by the presence of dust. The flow field is blanked in regions without dust. Note the change in color scale for different size particles.	106
Figure 5.1.2. Gas and dust particle speeds for different size grains along a streamline of maximum particle flux. The gas was unaffected by the dust. Note the logarithmic scale on the x-axis.	107
Figure 5.1.3. Mean radial velocity contours for the background gas. Note the gas is unaffected by the presence of dust in this computation.	108
Figure 5.1.4. Dust particle temperatures for 2, 5, and 11 μm particles when the gas is unaffected by the dust.	109
Figure 5.1.5. Dust mass loading, defined as the ratio of the total dust mass to gas mass, when the gas motion is not affected by the dust. The rocket engine is hovering at an altitude of 5 m.	110
Figure 5.1.6. Contours of the gas radial velocity when the gas is uncoupled (top) and coupled (inverted image) to the dust. The rocket engine hovers 5 m above the ground.	111
Figure 5.1.7. Contours of gas translational temperature when the gas is uncoupled (top) and coupled (bottom) to the dust. The rocket engine hovers 5 m above the ground.	112
Figure 5.1.8. Velocity (dashed lines) and thermal (solid lines) boundary layer profiles taken 40 m from the plume centerline for simulations where the gas is coupled (black) and uncoupled to the dust (red).	113
Figure 5.1.9. Rotational gas temperature when the gas is not affected (top) by the dust and fully coupled to the dust (bottom).	114

Figure 5.1.10.	Dust emission flux for a rocket engine hovering 5 m above the surface. The red line is the emission flux when the gas is unaffected by the dust and the black line is when the gas is affected.	115
Figure 5.1.11.	Dust mass loading, defined as the ratio of dust mass to gas mass, when the gas is fully coupled to the dust motion.....	115
Figure 5.1.12.	(left) Radial velocity profiles for 2 and 11 μm particles when the gas motion is coupled (circles) and uncoupled (diamonds) to the dust motion. (right) Dust spray angle of inclination probed at different heights. These profiles are sliced 50 m from the jet axis.....	116
Figure 5.1.13.	Particle mass flux for different size grains when the gas is uncoupled to the dust (left) and coupled to the dust (right). Note the logarithmic x-axis.....	118
Figure 5.1.14.	Particle radial momentum flux when the gas is uncoupled to the dust (left) and coupled to the dust (right). Note the logarithmic x-axis.....	118
Figure 5.1.15.	Granular collision rate when the gas is affected by the dust motion (bottom) and when it is unaffected by the dust (top).....	119
Figure 5.1.16.	Number density contours for 2 μm particles for simulations with different coefficients of restitution. A simulation without granular collisions is also shown for comparison. Note that the vertical axis is stretched 400% in the bottom figure.....	120
Figure 5.1.17.	Particle mass loading near the erosion regime for simulations with a coefficient of restitution of 1.0 (top) and 0.5 (bottom).....	121
Figure 5.1.18.	Gas dynamic pressure profiles at a distances 5 m (left) and 10 m (right) from the jet axis. The various lines correspond to simulations with different coefficients of restitution, ϵ . Note the logarithmic scale on the y-axis.....	122
Figure 5.1.19.	Number density contours for 2 μm particles for simulations with different coefficients of restitution. A simulation without granular collisions is also shown for comparison. Note that the vertical axis is stretched 400% in the bottom figure.....	123
Figure 5.1.20.	Particle mass (left) and momentum (right) flux profiles for simulations with different coefficients of restitution. A profile obtained from a simulation without granular collisions (solid line) is also shown for comparison. The profile is taken 40 m from the jet axis.....	124
Figure 5.1.21.	Particle radial velocity profiles for 2 μm (left) and 11 μm particles obtained from simulations with different coefficients of restitution. The data were extracted 30 m from the jet axis.....	125

Figure 5.1.22. Angle of inclination of the dust sprays versus altitude for different restitution coefficients. The dash-dot lines are reference lines which indicate the locations of peak mass flux and corresponding inclination angles.	127
Figure 5.2.1. Number density fields for 8 μm particles for rocket engines hovering at various altitudes, h	128
Figure 5.2.2. Speed profiles for 8 μm (left) and 11 μm (right) particles when the lander hovers at different altitudes. The profiles are taken 70 m from the jet axis.	129
Figure 5.2.3. Speed profiles for 800 nm (left) and 2 μm (right) particles when the lander hovers at different altitudes. The profiles are taken 70 m from the jet axis.	129
Figure 5.2.4. Collision rate for 2 μm particles when the rocket engine is hovering at 3 m (top) and 20 m (bottom).	130
Figure 5.2.5. Maximum particle speed versus hovering altitude for 5, 8, and 11 μm size particles.	131
Figure 5.2.6. Scaled particle mass flux at different radial positions from the jet axis for a rocket engine hovering 5 m (left) and 15 m (right) above the surface. Note the differences in vertical scale between the two figures.	132
Figure 5.2.7. Particle mass flux (left) and momentum flux (right) profiles for a set of hovering altitudes ranging 15 to 3 m above the surface. The profiles were taken 50 m from the plume centerline.	133
Figure 5.2.8. The angle of inclination measured at the location of peak particle mass flux for different hovering altitudes. The data are best fit by a linear function, the solid line.	134
Figure 5.3.1. Number density contours for 2 μm particles for engines 2.0 (top) and 4.0 (bottom) the nominal thrust. The lander hovers 5 m above the lunar surface.	135
Figure 5.3.2. Number density contours for 2 μm particles for an engine with a thrust of 6.54 kN. The lander hovers 5 m above the lunar surface.	135
Figure 5.3.3. Scaled number density contours for 2 μm particles for a for different thrust landers hovering 5 m above the lunar surface.	137
Figure 5.3.4. Velocity profiles for 2 μm particles taken at a distance 50 m from the jet axis. The lines correspond to engines operating at different thrust levels.	137
Figure 5.3.5. Particle mass flux profile taken 50 m from the jet axis for different thrust engines hovering 5 m above the lunar surface.	138

Figure 6.2.1. Contours of the gas mean free path within the two steady flow domains. The innermost domain interface is drawn via the white dash-dotted line. The rocket engine hovers at an altitude of 10 m.	145
Figure 6.2.2. Gas number density contours 70 s (top) and 90 s (bottom) after the lander first entrains regolith at a hovering altitude of 20 m. Note the curvature of the planet limb.	146
Figure 6.3.1. Snapshots of 800nm (right) and 8 μ m (left) particle number densities at times 30, 90, and 170s after engine shutdown. Note that the actual computational domain extends to much higher altitudes and distances from the lander.	148
Figure 6.3.2. Distributions for 2, 8, and 11 μ m particles as well as the total mass deposition density resulting from an approximate lunar landing. Note the logarithmic scale on the vertical axis.	149
Figure 6.3.3. The total mass deposited with an arc length between s and $s + \Delta s$ of the lander. The different lines correspond to different size particles and the dash-dot lines indicate maxima. Note the log scale on the vertical axis.	150
Figure 6.3.4. The distance from the lander at which peak radial-weighted deposition occurs (corresponding to data in Figure 6.3.3) for different sized particles and a linear best fit of the data.	151
Figure 6.3.5. The total particle deposition flux in the near field of the lander when the rocket engine hovers 3.0 m above the surface. Note the log-log scale.	152
Figure 7.1.1. Gas number density contours and streamlines near a 1.5 m tall fence placed 15 m from the plume axis.	156
Figure 7.1.2. Gas number density contours near a 1.5 m tall fence placed 40 m from the plume axis.	156
Figure 7.1.3. Number density contours for 8 μ m particles impinging on a 1.5 m tall fence placed 15 m from the jet axis.	157
Figure 7.1.4. Number density contours for 800 nm particles impinging on a 1.5 m tall fence placed 15 m from the jet axis.	158
Figure 7.1.5. Number density for 8 μ m particles when a 1.5 m tall fence is placed 30 m (top) and 40 m (bottom) from the jet axis.	159
Figure 7.1.6. Particle mass flux sampled 50 m from the jet axis for lunar fences placed at 15, 20, 30, and 40 m. The particle mass flux is also plotted when a fence is not used.	160
Figure 7.1.7. Shielding angle for 1.5 m tall fences placed at various locations.	161

Figure 7.1.8. Pressure distribution on a 1.5 m tall fence placed 15 m (left) and 40 m (right) from the jet axis. The separate force contributions from the dust and gas are shown as well.	162
Figure 7.1.9. (left) Mean pressure exerted on fences placed at different locations from the lander. The center of pressure is plotted on the right axis. (right) Fence pressure distributions for different fence placements.	163
Figure 7.2.1. Contours of gas density for fences placed at 15 m that are 0.75 and 2.5 m tall respectively.	164
Figure 7.2.2. Number density profiles for 8 μm particles for a 0.75 m (top) and 2.5 m (bottom) tall fence placed 15 m from the jet axis.	165
Figure 7.2.3. Simulators for 11 μm particles are colored by their speed and plotted on top of line contours of particle density.	167
Figure 7.3.1. Number density contours for 8 μm particles impacting berms angled at 30° (top) and 45° (bottom).	168
Figure 7.4.1. Color contours of 8 μm (top) and 800 nm (bottom) particle number densities for a 1.50 m tall fence with a normal restitution coefficient of 0.5. The black lines are gas density contours and the white arrows approximate dust path lines.	170
Figure 7.4.2. Number density contours for 1 μm particles impacting fences with restitution coefficients of 0.1 (top) and 0.5 (bottom). Granular collisions were not included and the line contours are gas density.	171
Figure 7.5.1. Number density contours for 1 μm grains exhibiting unsteadiness when interacting with a 1 m tall fence placed 10 m from the jet axis. Grain-grain collisions were neglected in this simulation.	173
Figure 7.5.2. Two instantaneous snapshots of gas number density taken 0.02 s apart. These profiles are unsteady and occur when the gas impinges on a 1 m tall berm placed 10 m from the lander.	174
Figure 8.1.1. Schematic showing the computational domain and symmetry planes for the 4-engine nozzle configuration.	178
Figure 8.2.1. Gas number density profiles for a multi-engine lander hovering 5 m above the surface. This is a view of the plane that bisects an engine.	179
Figure 8.2.2. Gas number density on the surface formed by the section of a cylindrical shell that passes through the center of the rocket engines. The boxes immediately below the nozzle exit planes show the location of the hybrid interface.	180

Figure 8.2.3. Radial mass flux contours for the gas along a constant radius cylindrical surface at 25 m. This surface spans a quadrant of the flow and the symmetry plane between adjacent nozzles is indicated by the white line at $s = 0$ m. The lander hovers 5 m above the surface.....	181
Figure 8.2.4. Gas number density contours on the symmetry plane between adjacent nozzles. The 4-engine lander hovers 5 m above the surface.	182
Figure 8.2.5. Gas number density profiles for a multi-engine lander hovering 10 m above the surface. This is a view of the plane that bisects an engine.	183
Figure 8.2.6. Number density contours from 8 μm particles scoured by a 4-engine lander hovering 3 m above the surface.	184
Figure 8.2.7. Bulk speed contours from 8 μm particles scoured by a 4-engine lander hovering 3 m above the surface.	185
Figure 8.2.8. Number density contours for 8 μm particles scoured by a 4-engine lander hovering 10 m above the surface.	186
Figure 8.2.9. Contours of radial velocity for 8 μm particles that are scoured by a lander hovering 10 m above the surface. Velocities slices are plotted at distance 10 and 25 m from the jet axis.	187
Figure 8.2.10. Particle mass flux along a plane of constant radius, $r = 25$ m, from the lander for hovering altitudes of 3, 5, and 10 m. Note the shift of color scale between panels.....	188
Figure 8.2.11. A top down view of particle streaks, colored by speed, overlaid on grayscale contours of particle emission flux. The lightly colored areas indicate high flux. Only particles larger than 1 μm are shown....	190
Figure 8.2.12. Mass flux for 200 nm, 2 μm , and 11 μm particles through an octant of a cylindrical surface 25 m from the jet axis. The hovering altitude of the lander is 5 m.....	191
Figure 8.2.13. Particle emission flux for a 4-engine lander hovering 3.0 m above the surface.....	192
Figure 8.2.14. Particle emission flux for a 4-engine lander hovering 5.0 m (left) and 10 m (right) above the surface.	193

CHAPTER 1. INTRODUCTION

Section 1.1. Motivation

When a rocket lands on the Moon the engine exhaust plume will strike the lunar surface and disturb and disperse dust and larger debris. Such issues were recognized early in the lunar exploration program (Choate, et al., 1969) and have been investigated over the years (Hutton, 1971). During Apollo LM landings, rocket blast sprays of dust were observed to begin at about 40 m altitude and partially obscured the landing site for the last 20 to 30 m of descent. The surface was completely obscured during some landings, requiring the terminal approach to be flown on instruments. For any pre-existing structures, or residents, such a plume of particulate ejecta represents a significant safety hazard. The scattered particles may penetrate weak surfaces, get stuck in mechanical systems, or coat solar panels, thermal radiators or optical systems. For example, during the Apollo 12 mission, astronauts recovered pieces of the Surveyor III spacecraft that was located 163 m away from the LM landing site. Surveyor was found to be covered with dust scoured by the LM rocket blast and its surfaces were found to have small pits due to blast abrasion (Immer, Metzger, Hintz, Nick, & Horan, 2011). Such debris/dust may be difficult or impossible to clear from surfaces because of electrostatic attractions and the highly adhesive properties of lunar soil. Lunar dust was considered by astronauts John Young and Gene Cernan to be among the most important obstacles to normal lunar operations (Gaier, 2005). Moreover, since the background atmosphere on the moon is negligibly thin, the range of particulate trajectories is very large. As missions to the moon resume, greater numbers of sensitive structures are going to be subject to plume ejecta hazards. Even if landing pads are established, they

will be unavailable initially and activity may extend beyond the pads. Also, an inadvertent landing off the pad may be problematic and an inclined approach flight path will pass over undeveloped surfaces. Knowledge of the high velocity dust spray will be necessary when making engineering design decisions. However, it is difficult to examine the problem experimentally because of the difficulties associated with firing a rocket engine plume into a dust bed while maintaining vacuum in a low gravity environment. The direct simulation Monte Carlo (DSMC) method (Bird, 1994) is well suited for simulating complex flows and is primarily used in this work to model various landing scenarios and the resulting dust motion.

Section 1.2. Objectives and Dissertation Overview

The main objective of this work is to model and characterize the dust sprays that arise during various lunar landing scenarios. In this work, the dust sprays are analyzed for a single engine lander hovering at different altitudes and thrust levels. Many different physical models are included and the sensitivity to model parameters is important for understanding the relevant physics. The dust particles may travel very long distances, and the particle trajectories around the moon are determined for a full landing cycle. Multi-engine configurations may also be used for future spacecraft, and the effects of plume-plume and plume-surface impingement on the scouring and transport of regolith is also studied. High velocity dust sprays are likely unavoidable and can be detrimental to sensitive structures at a nearby lunar outpost. Various mitigation techniques, such as a fence or berm, have been proposed to shield nearby structures from the dust spray. To assess the effectiveness of such techniques, the interaction between the high velocity dust spray with a protective barrier is also studied.

There are many physical phenomena that are important in this work, including: the transition from continuum to free molecular flow, erosion and gas-surface interactions, heavily mass-loaded two-phase flows, inelastic granular collisions, particle-surface interactions, and unsteady expansion of the gas and dust flow fields as they progress around the moon. The DSMC method is used in this work because of its ability to simulate complex physical processes in a rarefied environment. The specific DSMC solver used in this work is an in-house research code that uses a spherical coordinate system and has in the past been used to model planetary atmospheres. This solver has been modified to improve the resolution of the relatively small length and time scales typical for rocket plume impingement scenarios. As previously discussed, the plume flow fields span the continuum to rarefied flow regimes. The continuum solver, DPLR, (Wright, Candler, & Bose, 1998), is used to model the near field free expansion as well as the internal flow in the expansion section of the nozzle. The continuum solution is then coupled to our DSMC solver. A model for dust erosion based on the gas properties near the surface has also been developed. The two-phase flow near the surface is heavily mass loaded by dust. Consequently, we use a gas-dust interaction model such that the gas and grain motions are fully coupled (Burt & Boyd, 2004). Numerical tests are performed that verify conservation of energy and momentum for both spatially homogeneous and one dimensional two-phase flows. In certain regions of the flow, inelastic grain-grain collisions are significant and are therefore modeled. The grain-grain collision model allows for inelastic collisions with an assumed coefficient of restitution.

Although experimental data applicable to this problem are limited, we can compare our results to observations taken during the Apollo missions. Estimates for dust spray angles of inclination and particle number densities have been inferred from

analyses of the Apollo landing tapes (Immer, Lane, Metzger, & Clements, 2011). These estimates help calibrate our model and build confidence.

This dissertation contains a review of the relevant literature applicable to this problem in Chapter 2, a discussion of the methods used in Chapter 3, simulation results in Chapters 4 through 8, and conclusions and recommendations for future work in Chapter 9. The results chapters are organized as follows:

- Chapter 4 – Axisymmetric simulations without dust particles.
 - Continuum simulations of nozzle flow and near-field plume expansion;
 - Hybrid simulations of axisymmetric plume impingement for single engine landers at different hovering altitudes and thrusts;
 - Comparisons are made to classical theory and scaling relationships are discussed.
- Chapter 5 – Axisymmetric simulations with dust particles.
 - Model sensitivity analyses for the assumed inelasticity of dust particles and two-way coupling between dust and gas motions;
 - The dust sprays are characterized for landers at different hovering altitudes;
 - The effects of engine thrust on the resultant dust sprays are examined.
- Chapter 6 – Far-field simulations of dust deposition.
 - The method for simulating for a realistic landing trajectory and the unsteady dust spray evolution is discussed;
 - Gas and particle motions and deposition in the far-field (hundreds of kilometers from the landing site) are discussed.
- Chapter 7 – Interactions between the dust sprays with a lunar fence.

- Simulations of dust sprays interacting with fences of various heights, placements, and tilt angles are discussed;
- The sensitivity of the simulations to an assumed fence coefficient of restitution is analyzed;
- Recommendations for fence design are made.
- Chapter 8 – Impingement of a 4-engine lander.
 - The dust sprays are characterized for a 4-engine lander hovering at different altitudes;
 - The effects that a 4-engine lander has on surface erosion and possible trenching are discussed.

The above simulations may aid in the design of future lunar landers by predicting how the dust sprays respond as a lander approaches the lunar surface. Future landers may also be heavier in order to provide resources to support an extended mission. Such landers would require a more powerful descent engine and the effects of engine thrust on the dust sprays are examined. Some landers may use a multi-engine configuration. Multi-engine landers may produce complex 3-dimensional flows with focused jets of dust. These simulations will identify interesting phenomena that arise for a multi-engine configuration and predict the focusing behavior of the dust sprays. The high velocity dust sprays may be unavoidable without a pre-established landing platform. Even with a pre-established landing platform, certain circumstances may result in a lander performing an off-axis landing. The resulting dust sprays can be damaging to nearby structures and mitigation techniques must be used. These simulations can be used to help predict how damaging the dust sprays are and show how effective a lunar fence is at mitigating damage.

The problems associated with landing on a dusty surface will arise for missions to other celestial bodies such as asteroids, Mars, and other satellites. The problems of plume impingement on Mars are notably different than lunar missions because the Martian background atmosphere confines the expanding exhaust plume and can also inhibit the motion of dust as particles travel into the far field. Martian regolith is weathered, blown by planetary winds, and has very different physical properties than lunar regolith. The work developed in this dissertation is, however, applicable to landings on smaller bodies without a background atmosphere, such as asteroids.

CHAPTER 2.

LITERATURE REVIEW

The following literature review will briefly discuss the relevant physical phenomena associated with plume impingement on the dusty lunar surface. This work encompasses a vast variety of fluid dynamic phenomena that include: subsonic through hypersonic flow, continuum through free molecular gas dynamics, plume-plume and plume-surface interactions, two-phase flow, and granular material behavior. There is a vast literature on each of these topics, but only the relevant aspects will be discussed in this chapter. Throughout the Apollo era, scientists characterized properties of the lunar surface based on retrieved samples. The regolith properties important to this work are discussed. The Apollo missions also provide us with direct observations of plume impingement and dust entrainment. These observations provide a basis from which we can calibrate and compare our results and are discussed at the end of this chapter.

Section 2.1. Physical Overview

The flow field associated with a rocket plume impinging on lunar regolith, shown schematically in Figure 2.1.1, is complex. Within the descent engine bell, the exhaust flow is hot, chemically reacting, compressible, and largely inviscid. Just outside the nozzle, the plume expands into vacuum and the temperature, pressure and density decrease rapidly while the Mach number becomes very large. In free space, the plume would become increasingly rarefied, transitioning from continuum to free molecular flow as it expands towards vacuum. However, if the plume strikes the regolith, shock waves will form nearly parallel to the surface and turn the flow outwards. Near the stagnation point, the shock is relatively thin because the plume is most dense along the centerline. Away from the jet axis, the shock thickens and is deflected upwards. The radially

outward expanding wall-jet is a highly compressible stagnation point flow and a viscous boundary layer develops on the rough lunar surface. The resultant surface stresses may exceed the cohesive strength of the soil and can therefore lift loose regolith particles into the wall-jet boundary layer. The entrained dust is then accelerated by the expanding gas and sprayed over large areas.

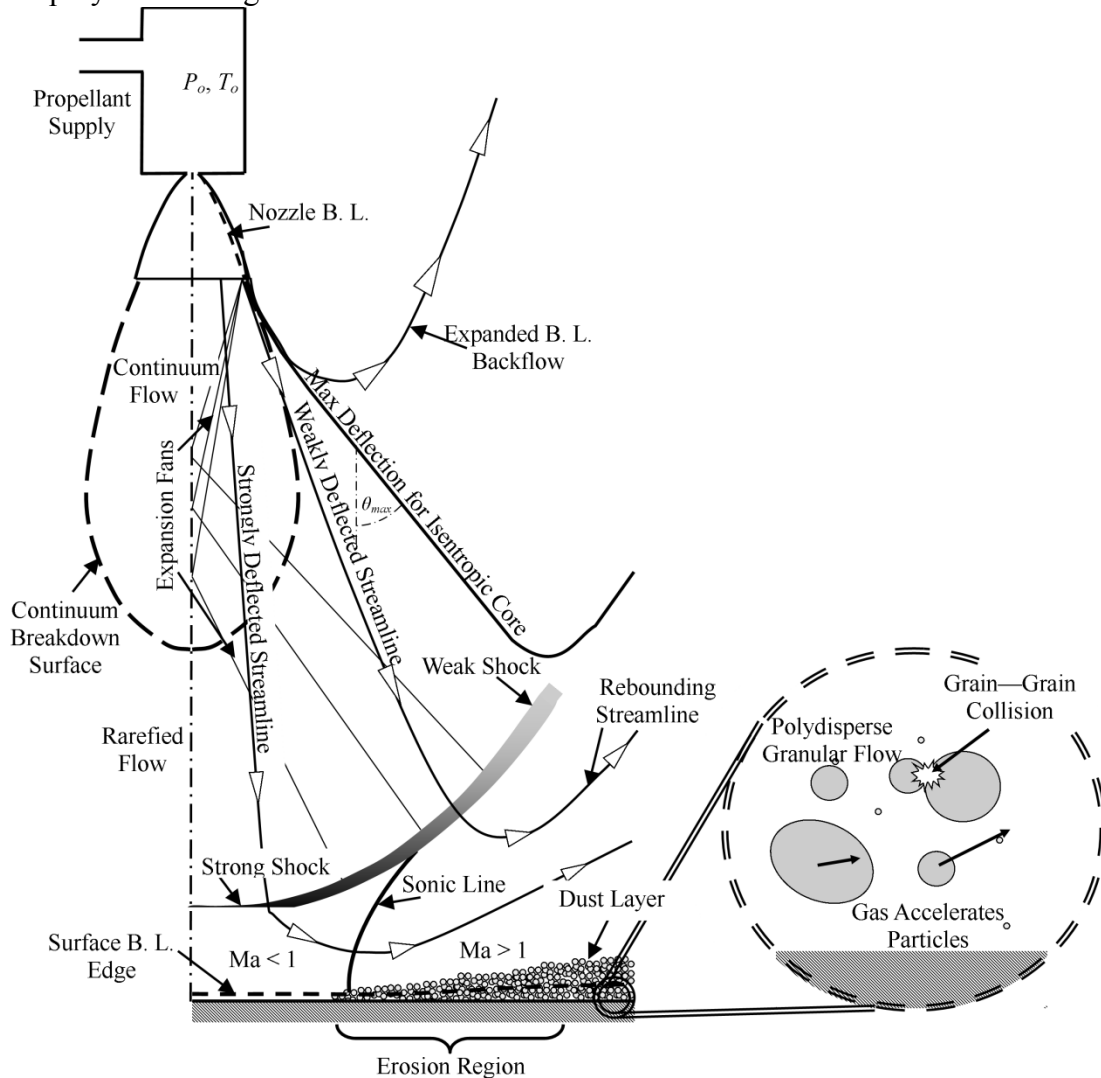


Figure 2.1.1. A schematic showing the various physical phenomena that arise when modeling plume impingement on dusty surfaces.

The dust spray consists of a polydisperse distribution of grain sizes that may collide with each other inelastically. The two-phase flow is also heavily mass loaded near the erosion area, resulting in the dust particle and gas molecule motions being strongly coupled. As this two-phase flow expands towards vacuum the gas and dust densities decrease and eventually the dust motion will decouple from that of the gas. After decoupling, the aerodynamic forces are negligible and the dust particles will travel ballistically under lunar gravity.

Section 2.2. Internal Nozzle and Plume Flow.

2.2.1. REAL NOZZLES

A basic understanding of rocket nozzles and the estimation of engine performance can be obtained by assuming quasi one-dimensional ideal flow. Such assumptions are not appropriate for plume impingement problems because real nozzles are two-dimensional and the shape of the nozzle affects its efficiency and the near-field plume flow. There are many different types of nozzle shapes, but typical high thrust engines – including the Lunar Module Descent Engine (LMDE) – have been optimized for thrust (Rao, 1958) and are bell-shaped. At first glance, one may expect only expansion to occur inside of a nozzle because the area is constantly increasing. This is not the case, as compression waves inside the nozzle can coalesce into shocks. For well designed nozzles, the strength of such shocks should be minimized. The method of characteristics (MOC) has been used to design nozzles and predict the shock structure. Although the method of characteristics does not account for viscosity or real gas effects, it is a useful tool for estimating the shock structure within a nozzle, (Dettleff, 1991). A MOC solution for a contoured nozzle geometry similar to the LMDE is shown in Figure 2.2.1. A shock forms near the nozzle throat and propagates through the nozzle.

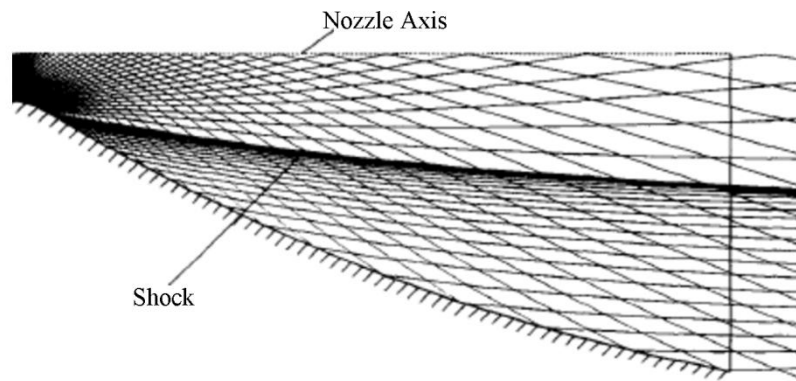


Figure 2.2.1. A method of characteristics solution showing expansion and compression waves inside of a contoured nozzle. Figure adapted from (Dettleff, 1991).

In real nozzles, the flow may also be in chemical and thermal non-equilibrium. There are many different types of engine propellants, but liquid propellants are commonly used for powered descent engines because of their high specific impulse (I_{sp}) and ability to be throttled. In such engines, liquid fuel is mixed with an oxidizer and burned in a combustion chamber. Complex chemical reactions occur, normally resulting in a variety of exhaust gas species depending on the type of fuel used. Insufficient mixing of the fuel and oxidizer and condensation within the plume can result in the formation of carbon soot for liquid hydrocarbon fuels, resulting in two phase flows. Such two-phase flow phenomena can have a large impact on the emissive properties of the plume, but are generally neglected when studying plume impingement (Simmons, 2000). Particulates of alumina are encountered in the exhaust of solid propellant rockets, and can create a conical core of two-phase flow. These effects should be considered when studying plume impingement for solid propellant engines. Two-phase flow effects are typically less significant for liquid propellant engines.

The key consequence of nozzle geometry for our interests is that the exit plane properties are spatially non-uniform. Although real nozzle effects may negligibly affect the engine thrust or efficiency, they substantially affect the near field plume flow

(Simmons, 2000). The spreading angle of the plume can also be affected because most nozzles have a small divergence angle at the nozzle lip.

2.2.2. THE LUNAR MODULE DESCENT ENGINE

In this work, we model an engine similar to that of the Lunar Module descent engine (LMDE) because it allows for comparison to the Apollo observations. The LMDE was a throttleable hypergolic engine with a maximum thrust of approximately 44.5 kN (or 10,000 lbs). The thrust was controlled by throttling the mass flow rates of propellant (Humphries, Hammock, Currie, Taylor, & Fisher, 1973). During the final 60 s before touchdown, the thrust was approximately a constant 13.3 kN (or 3,000 lbf) (Bennett, 1972). The properties of the LMDE and the RL-10A-4 are summarized in Table 2.2.1. Properties of the RL-10A-4 are given for comparison because this engine was selected for powering the heavier Altair lunar lander.

Table 2.2.1. Descent engine properties for the LMDE and RL-10A-4.

Engine	Propellant	Max Thrust	$I_{sp}(\text{vac.})$	A_e/A_t	D_e
LMDE	Aerozine-50	44.4 kN	305 s	47.5	1.62 m
RL-10A-4	LH ₂ /LOX	99.1 kN	451 s	84.0	1.53 m

The LMDE engine burned a 1:1 mixture (by volume) of Aerozine-50 (hydrazine and unsymmetrical dimethylhydrazine) and used nitrogen tetroxide as the oxidizer. The exhaust gases for this propellant are comprised of many different species and have been measured experimentally (Simoneit, Burlingame, Flory, & Smith, 1969). The Titan Stage 2 engine is included in this discussion because it used the same propellants and had a similar expansion ratio as the LMDE. The exit plane properties and chemical composition of the Titan II space-launch vehicle were determined from simulation (Simmons, 2000) using the Joint Army-Navy-NASA-Air Force (JANNAF) nozzle performance code (Nickerson, Dang, & Coats, 1985). Simoneit et al. concluded that the major exhaust products are H₂O, NH₃, CO, NO, O₂, CO₂, and NO₂. Water was the most

prevalent of these major exhaust products, followed closely by NH_3 . The molecular weights of NH_3 and H_2O are comparable and the mean molecular weight of the exhaust gas mixture is comparable to that of pure water. Simulations performed by Simmons, summarized in Table 2.2.2, also predict water to be the most prevalent exhaust product. Contrary to Simoneit et al, NH_3 was not a significant exhaust species for simulations by Simmons. The exhaust products for the LMDE and Titan Stage II are not expected to be the same though because the engines operate at different stagnation temperatures. Consequently, the effective molecular weight for the Titan Stage 2 Engine effluent is significantly higher than that predicted by Simoneit.

The most important effects of the various exhaust species on the plume structure are the effective mixture molecular mass and ratio of specific heats (Strutzenberg, Dougherty, Liever, West, & Smith, 2007). Lighter particles tend to spread more rapidly, thus increasing the plume divergence angle. In this work, H_2O is the only exhaust gas included. The nozzle flow model could be improved upon by acquiring specific data from experiments or more sophisticated simulations of the nozzle exit plane properties and the spatial distribution of species concentrations.

Table 2.2.2. Composition of Nozzle-Exit Exhaust Gases for Titan Stage 2 Engine determined from JANNAF simulations (Simmons, 2000).

Species	Mole Fraction
CO_2	0.0901
H_2O	0.4670
H_2	0.0377
N_2	0.3555
CO	0.0335
NO	0.0087
H	0.0030
OH	0.0033
$\Sigma(\text{O}_2, \text{O}, \text{N})$	0.0012

2.2.3. HIGHLY UNDER-EXPANDED PLUMES

Under-expanded rocket exhaust plumes can be characterized by two regions: an inviscid core and a viscous mantle where the plume interacts with the background atmosphere. In this work, the rocket engine exhausts into vacuum and there is a negligible background atmosphere for the plume to interact with. Studies of highly under-expanded plume flows date back to preparations for the Apollo moon landings. In vacuum, the rocket exhaust expands towards zero pressure and Mach infinity. For other under-expanded flows into an atmosphere, the flow can only expand to the ambient pressure at which point a barrel shock forms. Complete simulations of the near field including nozzle effects were computationally intractable during the Apollo era. However, reasonably accurate analytic methods were developed from physical reasoning and comparisons to experiments. These analytic approximations form the basis from which early plume impingement models were developed. Far from the nozzle exit plane, the plume flow is characterized as supersonic with nearly straight streamlines. If the streamlines are straight, the approximate form for the density is

$$\rho(r, \theta) = B \frac{1}{r^2} f(\theta), \quad 2.2-1$$

where r is the radial distance along the jet axis and θ is the polar angle measured from the jet axis (Dettleff, 1991). Various expressions for the coefficient B and polar function, $f(\theta)$, have been obtained by fitting to solutions obtained via the method of characteristics (Draper & Hill, 1966; Sibulkin & Gallaher, 1969) and comparing to experimental data (Roberts & South Jr., 1964). Roberts and South's expression for the density field for an expanding plume is

$$\frac{\rho(r, \theta)}{\rho_e} = \frac{\kappa}{2} \left(\frac{r}{r_e} \right)^{-2} \cos^2 \theta, \quad 2.2-2$$

where $\kappa \equiv \gamma(\gamma - 1)M_N^2$ is the hypersonic parameter, γ is the ratio of specific heats, ρ_e is the exit plane density, and M_n is the Mach number at the nozzle exit plane. Isentropic flow relations were used by Roberts and South in conjunction with equation 2.2-2 to obtain all other flow properties.

2.2.4. CONTINUUM BREAKDOWN

Continuum plumes that expand into vacuum will eventually undergo continuum breakdown and transition towards free molecular flow. Internal and directional temperatures are the first properties to exhibit departures from equilibrium. Breakdown occurs because collisions are no longer able to equilibrate the directional translational temperatures and internal energy modes in a sufficiently rapid manner (Bird, 1981). Consequently, a polyatomic gas may not asymptote to its maximum speed, equation 2.2-3, because energy remains trapped in internal modes.

$$u_{lim} = \sqrt{\frac{2\gamma}{\gamma - 1} RT_0}. \quad 2.2-3$$

The onset of rarefaction is commonly described by a breakdown parameter (Bird, 1981). There exist multiple breakdown parameters that describe when the continuum flow assumptions fail, but most depend on a Knudsen number based on a gradient length scale for one of the flow properties. Bird's breakdown parameter, P , for expansions is

$$P = \frac{\sqrt{\pi}}{2} \frac{u}{\sqrt{2k_b T/m}} \frac{\lambda}{\rho} |\vec{\nabla} \rho|, \quad 2.2-4$$

where T is the gas temperature, ρ is the gas density, m is the gas molecular mass, and λ is the mean free path. Other breakdown parameters have been used more generally for predicting where continuum assumptions fail (Boyd, Chen, & Candler, 1995), but Bird's breakdown parameter has often been used for supersonic expansion into vacuum.

A kinetic solver must be used once continuum breakdown occurs. DSMC is a common approach that has been used to simulate such plumes. DSMC calculations (Boyd & Stark, 1990) were compared to analytic plume models (Simons, 1972) and method of characteristics calculations (Legge & Boettcher, Modeling Control Thruster Plume Flow and Impingement, 1985). These results showed significant differences between DSMC and continuum solutions for both the plume flow and plume impingement stresses at distances beyond the free-molecular limit. In particular, the impingement pressure and shear stresses differed by approximately 20% and the plume total temperature differed by a factor of 2. DSMC plume solutions were also validated by comparing to experimental data for small cold N_2 gas nozzles exhausting into vacuum, (Boyd, Beattie, & Cappelli, 1994; Boyd, Penko, Meissner, & Dewitt, 1992). Although continuum solvers are suitable and more efficient than DSMC for simulating higher thrust nozzles, all plumes that expand into vacuum will eventually undergo continuum breakdown.

Hybridization techniques have been employed to reduce the computational cost for higher thrust engines (Lumpkin, Stuart, & LeBeau, 1996; Marichalar, Prisbell, Lumpkin, & LeBeau, 2011). In the work of Lumpkin et al., the nozzle flow and near field of the continuum expansion were computed with the Reacting and Multiphase Program (RAMP) method of characteristics solver. The continuum solution was then coupled to a DSMC solver, DAC, for simulating the far-field and plume-surface interaction. The DSMC solver was only loosely coupled and does not affect the continuum regime. Such an expanding flow lends itself well to one-way coupling because the interface normal Mach number may be kept supersonic. A similar approach is used in this work.

Section 2.3. Plume Impingement.

Plume impingement problems can be classified into two groups: the direct impingement of the isentropic core of a plume on a surface and indirect impingement from the outer mantle of the plume or backflow expansion of the nozzle boundary layer. The latter class of impingement typically applies for smaller control thrusters and impingement on spacecraft surfaces. Direct impingement is the primary concern for landing vehicles and this dissertation because of direct impingement results in surface erosion. Direct impingement can be further characterized by either free molecular impingement, characteristic of plumes striking a surface many nozzle diameters away, or continuum impingement on a closer surface. Free molecular impingement analyses are appropriate for control thrusters striking spacecraft surfaces, but the impingement considered in this work involves collisional gases.

Plume impingement on the Moon has also been simulated by (Tosh, Liever, Arslanbekov, & Habchi, 2011). In that work, plume impingement of a single species diatomic gas from a nozzle with uniform exit plane properties was simulated. A unified flow solver (UFS) that smoothly coupled a CFD solver in the near field to a Boltzmann solver in the far field was used. Their simulation data were compared to experiments and found in good agreement for the surface shock structure for a variety of background pressure ratios. Boundary layer profiles and surface stress distributions are also shown for a variety of lander altitudes. The computed surface pressures and stresses agree well with Roberts theory (Roberts, 1966), described below.

2.3.1. IMPINGEMENT ON A FLAT NORMAL SURFACE

Plume impingement phenomena have been thoroughly investigated numerically and experimentally. The earliest model, (Roberts, 1966), for plume impingement was developed in preparation for the Apollo landings. In this model, the gas properties at

the surface were computed from the normal shock recovery properties obtained from the plume flow model described by equation 2.2-2, (Roberts, 1963). The pressure at the stagnation point, P_s , depends on the nozzle Mach number, M_n , ratio of specific heats, γ , the chamber pressure, P_c , and the altitude of the nozzle exit plane, h/r_n . The stagnation pressure at the surface was calculated for the case when the nozzle is close to the surface and when it is far away. For a nearby surface, the pressure at the stagnation point is related to the chamber pressure by

$$\frac{P_s}{P_c} = (1 + \gamma M_n^2) \left(1 + \frac{\gamma - 1}{2} M_n^2 \right)^{-\frac{\gamma}{\gamma - 1}}. \quad 2.3-1$$

For a distant surface $h/r_n > \sqrt{(\kappa + 2)/2}$ the stagnation pressures decreases at higher hovering altitudes, and is

$$\frac{P_s}{P_c} = \frac{\kappa + 2}{2} \left(\frac{h}{r_n} \right)^{-2} (1 + \gamma M_n^2) \left(1 + \frac{\gamma - 1}{2} M_n^2 \right)^{-\frac{\gamma}{\gamma - 1}}, \quad 2.3-2$$

where κ is the hypersonic parameter defined in Section 2.2.3.

The pressure at the stagnation point is important because it controls the maximum shear stress and erosion rate. The dynamic pressure distribution depends on the pressure at the stagnation point and is

$$\frac{P_{dyn}}{P_s} = \left(\frac{r}{h} \right)^2 \frac{\kappa + 4}{2} \exp \left[-\frac{\kappa + 4}{2} \left(\frac{r}{h} \right)^2 \right], \quad 2.3-3$$

where r is the distance along the surface measured from the plume centerline. The dynamic pressure is zero at the stagnation point (as expected), rises towards a maximum value, and then decays further from the jet axis. The peak dynamic pressure occurs at $r_{peak}/h = \sqrt{2/(\kappa + 4)}$ and the maximum dynamic pressure is $e^{-1}P_s$. The dynamic pressure can be related to the rocket engine chamber pressure through equations 2.2-2 and 2.2-3. Two different analyses for computing the peak dynamic pressure were

performed for engines at high and low hovering altitudes. At high altitudes the peak dynamic pressure decays proportionally to h^{-2} , and approaches a constant value at low altitudes, $h/r_n < \sqrt{(k+2)/2}$. Roberts considered three different ways to compute the surface shear stress: laminar stress, turbulent stress, and using the dynamic pressure outside of the boundary layer. Roberts concluded that for a realistic lunar surface, the stress on the surface should be computed using the dynamic pressure and an assumed drag coefficient. A drag coefficient of 0.2, which corresponds to flow over a hemispherical bump, was used. He argued that the surface roughness is likely large compared to the surface boundary layer and this approach is a conservative approximation because it results in higher stresses than laminar or turbulent shear.

These analytic expressions show that the effects of chamber pressure and hovering altitude can be eliminated by appropriate scaling when the nozzle is far from the surface using equations 2.3-4 and 2.3-5.

$$\hat{P} = \frac{P}{P_c} \left(\frac{h}{D_n} \right)^2, \quad 2.3-4$$

$$\hat{\tau} = \frac{\tau}{P_c} \left(\frac{h}{D_n} \right)^2, \quad 2.3-5$$

The above scaling was applied to DSMC simulations of small control thrusters (Kannenbergh & Boyd, 1999; Hyakutake & Nishida, 2000), and they found that although the above scaling significantly collapses the data, there remains some dependency on the chamber pressure. It is suggested in (Hyakutake & Nishida, 2000), that the surface stress and pressure distributions do not collapse under the above scaling because of rarefaction effects. At lower chamber pressures, the flow within the nozzle may be rarefied, resulting in a smaller exit plane Mach number and decreased impingement pressures. Both DSMC simulations, Kannenberg and Hyakutake, agree well with

measured surface pressure and shear stress profiles (Legge, 1990), thus validating the DSMC approach for simulating rarefied impinging plumes. For large descent engines, the flow within the nozzle should be continuum and the above scaling relationships are expected to collapse the data reasonably well at high altitudes.

2.3.2. PLUME IMPINGEMENT FROM MULTIPLE NOZZLES

Future spacecraft may consider using multiple descent engines to increase the area of the lander footprint and reduce the impingement pressure. For example, the Viking spacecraft was sensitive to dust erosion and used a showerhead nozzle configuration to reduce the impingement pressure (Romine, Reisert, & Gliozzi, 1973). The Mars Science Laboratory also used a multi-engine configuration, where 8 rocket engines were used to keep a Sky Crane hovering high above the surface while the rover was lowered on cables (Steltzner, et al., 2006). Keeping the engines at a higher altitude reduced the surface stresses and the erosion. The rocket exhaust plumes on Mars are notably different than a plume exhausting into vacuum (Sengupta, et al., 2009). On Mars, the plumes are more collimated because of the barrel shocks that form as the plume interacts with the Martian background atmosphere. Consequently, the plumes from MSL were not expected to interact with each other until they struck the surface. On the Moon, the plumes are not confined by a barrel shock, and are more likely to interact with each other.

The problem of twin nozzle plumes interacting with each other is well studied, and the nature of the interaction depends on the degree of rarefaction (Koppenwallner, 1983). The interaction plane is defined as the plane between adjacent nozzles. For nearly free molecular nozzles, the exhaust gases along the impingement plane will simply pass through each other. As the gas becomes collisional, an oblique shock will form on either side of the interaction plane. In the continuum case, the plume density,

temperature, and pressure can reach peak values within the interaction region. This high pressure region between interacting plumes can consequently result in increased erosion and preferential scouring of material.

Section 2.4. Dust Erosion

2.4.1. EROSION PHENOMENOLOGY

Metzger, Smith, and Lane (2011) have identified three possible erosion mechanisms: viscous erosion, bearing capacity failure, and diffused gas eruption (Metzger, Smith, & Lane, Phenomenology of soil erosion due to rocket exhaust on the Moon and the Mauna Kea lunar test site, 2011). Viscous erosion occurs when the surface shear exceeds the cohesive strength of the soil and small dust particles begin to roll along the surface. This mechanism is commonly called ‘creep’ in the literature. The rolling dust grains can collide with neighboring particles dislodging material that is then lofted into the flow field. Bearing capacity failure occurs when the pressure exceeds the bearing capacity strength of the soil and a narrow cup is formed. The walls of the narrow cup are unstable under gravity and collapse, releasing many dust grains into the flow field while forming a wider crater. The third mechanism is diffused gas eruption, which occurs when the gas is driven into porous spaces. The gas flowing through the porous soil fluidizes the bed and can erupt at various locations, carrying entrained dust along with it. Due to the high packing density and bearing strength of lunar soil, bearing capacity failure is neglected as a dust generating mechanism. Since the lunar soil bed is tightly packed because of the absence of a background atmosphere, diffused gas eruption is unlikely to be a significant erosion mechanism. Viscous erosion is thus expected to be the dominant erosion mechanism. This argument is supported by

the Apollo landing photographs, shown in Figure 2.4.1, because the surface does not exhibit evidence of cratering.



Figure 2.4.1. View underneath the Apollo 12 Lunar Module showing that cratering does not occur and that viscous erosion is the likely dominant scouring mechanism.

In contrast, on other extra-terrestrial bodies such as Mars, diffused gas eruption and bearing capacity failure are expected to be important because of the relatively loose packing of the soil (Mehta, Sengupta, Pokora, Hall, & Renno, 2010). Erosion rates for viscous erosion tend to be slower than for the other mechanisms because, unlike viscous erosion, the soil bed becomes fluidized under bearing capacity failure and diffused gas eruption.

2.4.2. VISCOUS EROSION

Sand is eroded on Earth primarily by viscous erosion and this process has been extensively studied because of its impact on geological and climactic changes, agriculture, and negative impact on air quality. As previously stated, the onset of viscous erosion occurs when a threshold stress on the surface causes loose particles to creep. The mechanism by which loose regolith begins to creep along a surface depends on the soil properties, the stresses exerted by the gas on the surface, and the particle size (Shao, 2008). For larger particles, particle creep is determined based on the balance

between aerodynamic forces, which are proportional to D_p^2 , and gravitational forces, which are proportional to D_p^3 . For smaller particle sizes, the lift-off largely depends on the cohesive forces between particles, which are estimated to be proportional to D_p (Shao, 2008). Particles that begin to slide along the surface have not yet left the surface and are thus not yet entrained into the flow.

Three different mechanisms by which the particles can become entrained are shown schematically in Figure 2.4.2. Aerodynamic entrainment occurs when the aerodynamic lift forces exceed the gravitational forces. This typically only occurs for large sand grains or when the cohesive stress is small (Loosmore & Hunt, 2000). The dust emission rate was measured experimentally (Loosmore & Hunt, 2000) for aerodynamic entrainment, and it was found that the emission mass flux is approximately proportional to u_*^3 , where u_* is the friction velocity. Saltation bombardment occurs when a saltated particle impacts the surface with a sufficiently high energy to dislodge other particles. Lastly, some particles within a soil may aggregate under natural circumstances because of thermal cycling and cohesion. Under significant shearing, these weakly bonded aggregate particles can break apart, resulting in the emission of their constituents. This is called aggregate disintegration.

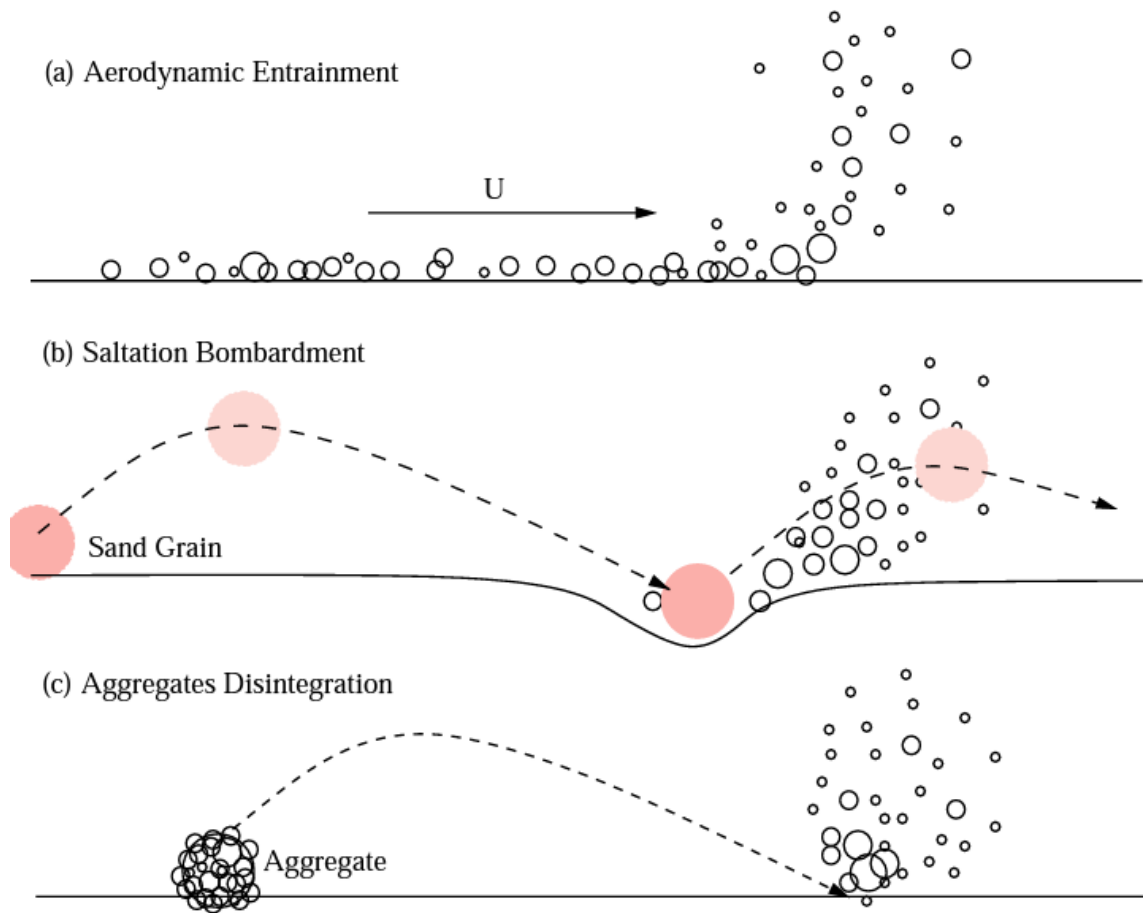


Figure 2.4.2. Mechanisms for entrainment, adapted from (Shao, 2008). Dust emission (a) by aerodynamic lift, (b) by saltation bombardment, and (c) through disaggregation, also known as auto-abrasion.

Saltation bombardment is viewed as necessary for accurate dust emission modeling for wind-blown sands because it results in higher erosion rates than aerodynamic entrainment (Shao, 2008). On the Moon, saltation may not be as significant an issue because the wall-jet expands rapidly towards vacuum. Even though saltating particles may cause dust emission far from the lander, the gas aerodynamic forces at those distances may be insufficient to entrain the lofted particles. Regardless, saltation may still have a significant impact if berms are constructed out of lunar

materials. The high velocity entrained particles can impact the berm, thus dislodging berm material. Although not included in this work, energy and volume methods for predicting the dust emission from saltation bombardment are discussed in (Shao, 2008).

Dust emission models that neglect saltation depend on the friction velocity (u_*) and its threshold value ($u_{*,t}$), as well as the soil properties. In these models, dust emission begins when the friction velocity exceeds the threshold velocity, (Bagnold, 1941). The threshold friction velocity was obtained by a force balance on individual particles, and is proportional to $D_p^{1/2}$, as recommended by Bagnold. Bagnold's prediction for the threshold velocity agrees quite well with experiments for large particles, but has large errors for small particles. An improved model, (Greeley & Iversen, 1985), agrees better with experiments and better accounts for cohesion between tiny particles. On the moon, modeling cohesion is complicated and unknown because of the highly irregular particle geometries and electrostatic forces. Roberts (Roberts, 1966) attempted to include the effects of cohesion by defining a threshold shear stress below which erosion does not occur. The threshold stress was calculated using the Mohr-Coulomb potential and is

$$\tau_c = c + P \tan \varphi, \quad 2.4-1$$

where c is the cohesive stress, P is the gas static pressure at the surface, and φ is the angle of repose of the soil. The cohesive stress was computed assuming that the attractive forces between particles are Van-der-Waals forces and vary linearly with the particle diameter and inversely as the square of the separation distance. This approximation for the cohesive stress does not take into account the jagged nature of lunar regolith and mechanical locking of particles. The erosion rate is assumed proportional to the excess shear on the surface, (Roberts, 1966), and is

$$\frac{1}{2}au\Phi = \tau - \tau_c. \quad 2.4-2$$

The product au is the estimated fraction of the free stream gas velocity to which dust particle obtain and Φ is the dust emission mass flux. Although there are more sophisticated theoretical models for modeling dust emission, (Shao, 2008), they depend on regolith properties that are in general unknown. Alternatively, we consider an empirically determined emission model rather than a more sophisticated theoretical model.

Scaling relationships for erosion rates based on the particle density and diameter, gas density and velocity, and gravity were empirically determined (Metzger, Latta III, Schuler, & Immer, 2009; Metzger, et al., 2009; Metzger P. T., et al., 2010). In these experiments, a subsonic vertical jet impinged on a bed of sand or lunar soil simulant. Low gravity experiments were performed in reduced gravity aircraft flights. Supersonic tests involving plumes from 100 lbf solid rocket engines were also performed. However, these tests are not applicable to lunar missions because the high impingement pressures resulted in erosion occurring by bearing capacity failure. The subsonic impingement tests show that the erosion rate scales with the densimetric Froude number.

$$\Phi \propto \frac{\rho_g u_g^2}{2g\rho_p D_p} \equiv Fr^2. \quad 2.4-3$$

The left hand side of equation 2.4-3 represents the particle mass flux, $\rho_g u_g^2/2$ is the dynamic pressure of the free stream gas outside of the viscous boundary layer, ρ_p is the density of an individual dust grain, g is the acceleration of gravity, and D_p is the mean diameter of dust grains. The Froude number can be interpreted as the ratio of the aerodynamic force on a particle to the gravitational force. A primary challenge when using the above model is that it does not provide the particle size distribution for airborne

particles, which may be different than the parent soil unperturbed particle size distribution. For a weakly sheared surface, where the friction velocity is close to the threshold value, the particle size distribution for airborne particles closely matches the erodible fraction of the parent particle size distribution, (Alfaro, Gaudichet, Gomes, & Maille, 1997). At higher erosion rates, the aerosolized particle size distribution becomes increasingly bimodal, because of the disintegration of aggregate particles and saltation processes liberating finer particles. In this work, the particle size distribution for the erodible fraction of grains has a degree of uncertainty because the particle size distribution varies with landing location and surface depth.

Section 2.5. Two-Phase Flow

Gaseous plume impingement and the erosion of dust particles have been reviewed thus far. The literature pertaining to the evolution of the entrained dust sprays and granular flows is discussed in this section.

2.5.1. GRANULAR FLOW REGIMES

Four different granular flow regimes have been identified (Castellanos, Valverde, Perez, Ramos, & Watson, 1999): plastic, inertial, fluidized, and entrained. The plastic regime is characterized by a tightly packed granular bed. The inertial regime is dominated by inter-particle collisions and the interstitial fluid does not affect the granular flow. In the fluidized regime, the interstitial fluid plays a significant role in the transfer of momentum between dust particles. The granular flow is still dense in this region and the mean separation between particles is of the same order as the particle diameter. A typical example of flow in this regime is the fluidized granular bed, which occurs when gas is forced through a bed of particles. If the fluid exerts a significant pressure that can overcome particle cohesion and weight, then the bed expands and becomes fluidized.

Such fluidized beds exhibit flow properties typical of liquids. In the entrainment regime, which is the primary focus of this dissertation, particles are fully suspended by the gas, the mean separation between particles is large. Particle-particle collisions are treated as brief and infrequent events and particles spend most of their time traveling through free space. Within this regime, the granular flow is typically referred to as a granular gas because of its analogies with that of a dilute gas. This is also referred to as a rapid granular flow.

2.5.2. RAPID GRANULAR FLOWS AND GRANULAR PHENOMENA

A rapid granular flow is one where grains are fluidized by sufficiently strong forcing. Grains only interact with each other by nearly instantaneous collisions. Many rapid granular flows are surrounded by an ambient fluid, with the exceptions commonly being related to astrophysical flows where the granular gas is surrounded by vacuum. If the stress due to grains exceeds the stress exerted by the fluid, the granular flow can be modeled by considering grain interactions alone (Campbell, 1990).

In this dissertation, the fluid stresses dominate near the erosion regime and are responsible for accelerating the particles into a high velocity sheet. As the gas expands, the granular flow transitions to a regime where the particle momenta exceed that of the gas and the ambient gas can be neglected. The dust particle number density also decreases as the granular gas expands and eventually becomes free molecular. At intermediate locations, between where the fluid forcing is significant and the granular gas becomes free molecular, particle collisions can be significant.

Despite the similarities between granular gases and dilute gases, there are several significant disparities between the two. Obviously, the mass and diameter of granular particles is much larger than those of gas molecules. The fundamental difference between granular and dilute gases is that granular collisions are typically inelastic.

Energy that is lost in a granular collision cannot be recovered, but internal energy of a gas molecule can be transferred to and from translational and other internal modes. Granular particles can deform upon impact or even break apart (Goldhirsch, 2003). Inelasticity can lead to interesting phenomena not observed for dilute gases, such as collapse, clustering, and microstructure formation. Such phenomena depend on how inelastic the collisions are, which is typically specified by a restitution coefficient.

Particle clustering is a defining characteristic of collisional granular flows and claimed to play a significant role in the formation of planetary rings (Spahn, Schmidt, Petzschmann, & Salo, 2000). The clustering mechanism occurs because the granular temperature cools as particles collide. The granular temperature is a macroscopic property that is analogous to the temperature for a dilute gas. Inelastic collisions decrease the granular temperature, resulting in a low pressure pocket in the near vicinity of the collision. This results in a diffusion of particles towards the low pressure region, thus increasing the collision rate. As the collision rate increases the granular temperature further decreases and a cluster is eventually formed. Clustering depends on the granular collision rate and also on the hydrodynamic forces that play a role in dissolving clusters. Clusters that form violate dilute granular gas assumptions and should be modeled with a discrete element or molecular dynamics approach.

2.5.3. GRANULAR COLLISIONS

Granular collisions are typically modeled as colliding spheres with a normal coefficient of restitution and friction coefficient (Brilliantov & Pöschel, 2004). The coefficient of restitution is a function of material properties as well as impact velocity. The simplest collision models assume a constant normal restitution coefficient, but this is shown to disagree with experiment and can also lead to inelastic collapse and unreasonably high collision rates (McNamara & Young, 1992). Inelastic collapse

occurs when particles collide with each other enough times such that their relative velocities vanish. Inelastic collapse incorrectly occurs when the restitution coefficient is held constant and independent of impact velocity. The problem of collapse is mitigated by using a restitution coefficient that becomes more elastic as the relative velocity between particles decreases. A form for the dependence of the restitution coefficient on impact velocity is

$$e(v_n) = \begin{cases} 1 - Bv_n^\alpha, & v_n < v_a \\ \varepsilon & v_n \geq v_a \end{cases} \quad 2.5-1$$

where e is the normal restitution coefficient, v_n is the normal velocity, v_a is a cutoff impact velocity, ε is a minimum restitution coefficient, and B and α are constants (Bizon, Shattuck, Swift, McCormick, & Swinney, 1998). This form for the restitution coefficient agrees well with experiments involving an oscillated bed of lead particles. Bizon et al. concluded that the precise way in which the restitution coefficient decayed did not have an impact on the granular flow structure. The cutoff velocity was defined as $v_a = \sqrt{gD}$. The selection for the cutoff velocity does not imply that material properties depend on gravity. The cutoff velocity was simply a characteristic velocity for the flow they were simulating. Collapse, however, is not expected for our simulations because the collision rates between particles are relatively low and the granular flow rapidly becomes free molecular. The above form for the restitution coefficient does not agree with all materials, but most materials tested experimentally exhibit similar trends (Schäfer, Dippel, & Wolf, 1996).

More sophisticated granular flow models also define a tangential restitution coefficient that depends on the normal impulse, normal and rotational restitution coefficients, and friction coefficient, μ (Walton, 1993). The rotational restitution coefficient is sometimes referred to as the tangential restitution coefficient (Schwager,

Becker, & Pöschel, 2008). The rotational restitution coefficient, β , relates the post-collision surface relative tangential velocity to the pre-collision value and can vary from -1 to 1 . A value of $\beta = -1$ corresponds to perfectly smooth spheres and the tangential relative velocity remains unchanged. A value of 1 corresponds to reversal of the relative tangential velocity and a value of 0 results in a total loss of tangential velocity, as in meshing gears. The rotational coefficient of restitution depends on the friction coefficient, the normal and tangential relative speeds, and if the interaction results in rolling or sliding contact. A complete description for calculating the rotational restitution coefficient and updating the particles post-collision velocities and rotation can be found in (Walton, 1993).

The previously described collision model has been applied to discrete element simulations and accurately predicts many structures observed in granular flows. DSMC has been shown to agree well with dilute granular gases and was able to reproduce the effects of particle clustering seen with MD solutions (Müller, Luding, & Herrmann, 1997; Luding, Müller, & McNamara, 1998). In that work, the collision event is simulated using a normal coefficient of restitution and the tangential velocity is assumed to be unaltered. The difference between DSMC and discrete element models is that DSMC assumes molecular chaos and that collisions do not depend on particle position within a collision cell. In denser granular flows, the collision rate is computed using an effective volume, which is the volume of the cell less the volume displaced by the particles. This simple modification results in a slightly higher collision rate for large volume fraction granular flows. In our simulations, the volume fraction of grains is expected to be negligibly small.

The effects of particle rotation were neglected in (Müller, Luding, & Herrmann, 1997), and they argue that rotation is not important because the restitution coefficient has

a larger impact on energy dissipation and flow structures than rotational effects. Subsequent work (Moon, Swift, & Swinney, 2004) suggests, however, that the role of particle friction should not be neglected even though inelasticity is the most important characteristic. The significant effect of friction is not to dissipate energy directly; rather, friction results in an increased collision rate because it reduces particle mobility. Friction also can result in translational energy being converted into rotational modes, but the rotational kinetic energy was on average 30 times less than the translational energy in the simulations discussed in (Moon, Swift, & Swinney, 2004). The ratio of rotational to translation energy depends on restitution coefficients, friction coefficients, particle moment of inertia, and the ambient gas. Unlike molecular gases, it is common for rotational energy to be in non-equilibrium with translational modes for granular gases (Brilliantov & Pöschel, 2004).

Friction can also significantly affect the scattering distribution, because the post-collision trajectories depend on the relative surface velocity when friction is included. This change in scattering behavior seems to affect the flow structures in vibrating beds. Such friction effects are seen in experiments, where clean particles and dirty particles exhibit different patterns (Umbanhowar, 1996).

The collision rates in our work tend to be insufficient to support the formation of granular structures, but the effect of particle friction on the scattering angle is significant. To improve the accuracy of our granular collision model, a more detailed description of particle scattering is required. Due to the highly irregular shape of lunar soil particles, however, the particle scattering distribution will likely have to be determined experimentally.

2.5.4. DRAG ON SPHERICAL PARTICLES

The two-phase dusty flows that would typically arise during lunar landings are locally heavily mass loaded by dust. Further, rarefaction effects are important because the mean free path for gas-gas collisions is typically long relative to the diameters of individual dust particles. Although realistic dust grains are jagged and not spherical, sphere drag approximations are commonly used. The effects of rarefaction and compressibility on the drag exerted on a sphere are reviewed in (Loth, 2008). The drag on a sphere is computed for flow regimes that are either dominated by compression, viscosity, or rarefaction. To account for rarefaction, a correction function which depends on the grain Knudsen number scales the drag coefficient computed for low Reynolds numbers,

$$C_{D,Re,Kn} = \frac{24}{Re_p} (1 + 0.15Re_p^{0.687}) f_{Kn}. \quad 2.5-2$$

$C_{D,Re,Kn}$ is the drag coefficient which includes finite Reynolds number and rarefaction effects, Re_p is the Reynolds number based on the particle diameter, f_{Kn} is the rarefaction correction function. The rarefaction correction function has been determined empirically, (Clift, Grace, & Weber, 1978), and a reasonably accurate expression is

$$f_{Kn} = \frac{1}{1 + Kn_p [2.514 + 0.8 \exp(-0.55/Kn_p)]}. \quad 2.5-3$$

Loth's equations have been used to determine the forces on lunar dust particles and the lunar dust trajectories for a fixed gas flow field (Lane, Metzger, & Immer, 2008). The Kn number based on the largest dust particles is $\mathcal{O}(1)$ near the erosion regime and rapidly increases as the gas expands. Alternatively, analytic expressions for the free molecular drag force and heat transfer rate to the dust grains from gas molecules of a certain velocity class \mathbf{c} are (Gallis, Torczynski, & Rader, 2001)

$$\mathbf{F}_\delta[\mathbf{c}] = m_g n_g \pi R_p^2 \mathbf{c} \left\{ \left(1 + \frac{4}{9} (1 - \varepsilon_p) (1 - \alpha_p) \|\mathbf{c}\| \right) + (1 - \varepsilon_p) \alpha_p \frac{\sqrt{\pi}}{3} c_p \right\} \quad 2.5-4$$

$$Q_\delta[\|\mathbf{c}\|] = \alpha_p (1 - \varepsilon_p) m_g n_g \pi R_p^2 \|\mathbf{c}\| \left\{ \frac{1}{2} \|\mathbf{c}\|^2 - c_p^2 \right\}. \quad 2.5-5$$

The velocity \mathbf{c} is the velocity of an individual gas molecule relative to the particle, ε_p is the fraction of molecules that experience specular reflections, α_p is the fraction of diffusely reflected molecules that experience isothermal diffuse reflection, m_g is gas molecule's mass, n_g is the gas number density, and c_p is the most probable thermal speed of a gas molecule based on the dust thermal temperature.

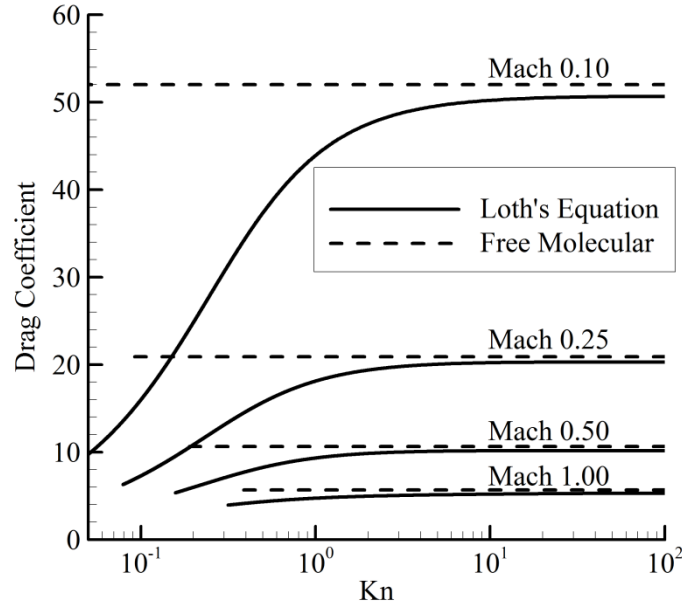


Figure 2.5.1. Drag coefficient computed via Loth's equation for different particle Knudsen and Mach numbers. The dashed lines are the free molecular drag coefficients.

Although this method is valid for any non-equilibrium distribution of gas velocities, it is important to note that this assumes the local flow about each grain is free-molecular. The drag coefficient, computed from Loth's equations, is plotted against

particle Knudsen number for a variety of subsonic Mach numbers in Figure 2.5.1. As the flow becomes increasingly rarefied, Loth's drag coefficient increases. The most drastic increases occur for low particle Mach numbers. For a Knudsen number of one, the differences between the free molecular and Loth's drag coefficient is approximately 10%. These differences decrease as the flow becomes increasingly rarefied. At a Knudsen number of 10, the differences in drag coefficient are less than 4%.

The time scale, τ_{p-g} is the amount of time required for a dust particle, initially at rest, to relax to e^{-1} of the free stream gas velocity. For a particle translating in an equilibrium gas with low speed ratios and specular reflections, this relaxation time scale is

$$\tau_{p-g} = \frac{3\pi^{1/2}m_p}{2\rho_g c_0 \pi D_p^2}, \quad 2.5-6$$

where c_0 is the most probable thermal speed of the gas. The relaxation time scale depends on the particle mass to aerodynamic cross section ratio. Since the mass scales as D_p^3 for constant density particles, the time scale therefore scales linearly with particle diameter. If diffuse reflections are considered, the expression is slightly more complicated but still depends on the particle mass to cross section ratio.

The drag coefficients, either free molecular or those from Loth, can be readily used for overlay methods (Lane, Metzger, & Immer, 2008; Morris, 2010). In overlay methods, the gas flow field is held fixed and the drag forces and heat transfer to the dust particle are computed based on the local gas properties. This approach is very useful because particle trajectories can rapidly be determined by post-processing gas simulation data. But two-phase flows can be very sensitive to the mass loading because the dust can strongly affect the gas flows, as seen experimentally in (Borée, Ishima, & Flour, 2001). In their work, particles of different mass loading were injected into a turbulent

flow over a blunt body. At higher mass loadings, the dust inhibited the development of the turbulent wake. Our early simulations also suggest that the mass loading of dust is not negligible and the presence of dust is likely to affect the gas (Morris, 2010).

A fully coupled gas-particle model that statistically conserves momentum and energy has been developed for DSMC solvers (Burt & Boyd, 2004). This model has been implemented into our DSMC solver, and a detailed description of the method and improvements is discussed in Section 3.3.3.

Section 2.6. Properties of Lunar Regolith

Lunar regolith refers to the fragmented and unconsolidated layer of pulverized rock on the surface of the moon. The regolith layer is typically only several meters thick and is formed by continuous meteorite impact and bombardment of charged particles from the sun. Many individual soil particles and rocks show evidence of this bombardment and are covered with various sized impact craters. This process is called *gardening*. The impact events can generate large amounts of heat that can melt and fuse different particles together, called *breccias*. As a result, many regolith particles are jagged and irregularly shaped. Lunar soil samples returned by the Apollo astronauts have been well analyzed and many of the important physical and geological properties of the lunar surface are summarized in (Heiken, Vaniman, & French, 1991).

2.6.1. PHYSICAL PROPERTIES

The properties relevant to this work include: the bulk density, specific gravity, porosity, and the volume coefficient (which is used to obtain the aerodynamic cross section to volume ratio). The recommended values, (Heiken, Vaniman, & French, 1991), are summarized in Table 2.6.1. The specific gravity of a soil particle is the ratio of the particle mass to the volume displaced by the particle, normalized by the density of

water. Such a measurement does not take into account the volume of enclosed voids, but for small particles this is expected to be small. The bulk density is defined as the mass of the material contained within a given volume, thus taking soil packing into account. The bulk density can be used to estimate how large a crater will be excavated by a rocket plume. The porosity is the volume of the void space between particles divided by the total volume. Although not included in this work, this parameter is useful for considering alternative erosion mechanisms that depend on the gas fluidizing the porous bed. The volume ratio is defined as the volume of a particle divided by the volume of a sphere of equivalent projected area. The projected area is the geometric area, or aerodynamic cross section, of a soil particle. Additional properties which are important for the construction of berms and to the issue of erosion are the angle of repose, or friction angle, and the particle cohesion. The friction angle is steepest angle that a granular material can sustain before it begins to slide under its own weight. The cohesion stress is the component of shear strength that is independent of other applied forces.

Table 2.6.1. Recommended values for physical properties of lunar soil.

Bulk Density	Specific Gravity	Porosity	Volume Coeff.	Friction Angle	Cohesion
1500 kg/m ³	3.1	49%	0.32	30°–50°	0.1–1 kPa

Several of these properties can change with depth and location on the moon and ranges are given where appropriate. Since most of the erosion only occurs within the top several centimeters, variations in specific gravity and the particle size distribution are neglected.

2.6.2. PARTICLE SIZE DISTRIBUTIONS

Lunar regolith consists of particles with diameters that range from approximately 10 nm to 10 mm, but particles are predominantly less than 1mm in size. Early

determinations of the particle size distributions were for particles sizes $> 20 \mu\text{m}$, and the mean particle diameters were measured between 40 and $130 \mu\text{m}$. These estimates did not include the fine and ultrafine portion of the regolith, $< 20 \mu\text{m}$, and this range accounts for approximately 20% of the soil mass. Particle size distributions for the sub $20 \mu\text{m}$ size particles have been measured and are shown in Figure 2.6.1 (Greenberg, Chen, & Smith, 2007; Park, Liu, Kihm, & Taylor, 2008).

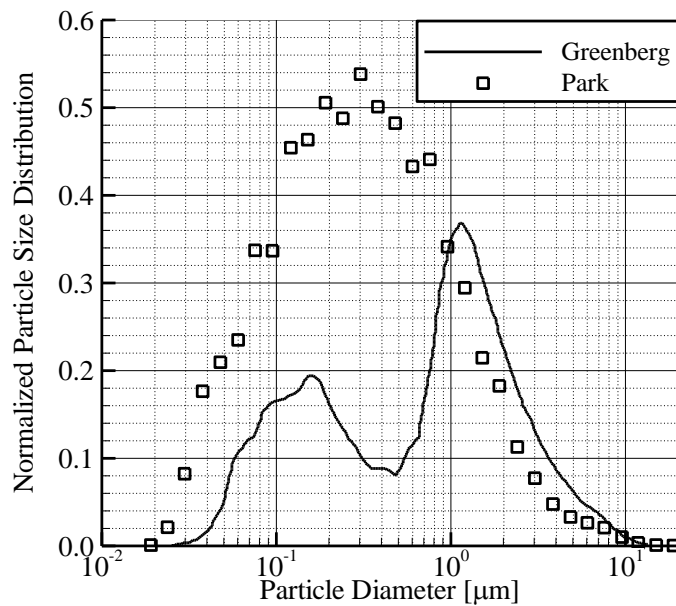


Figure 2.6.1. Particle size distributions measured for the sub $20 \mu\text{m}$ portion of lunar regolith (Greenberg, Chen, & Smith, 2007; Park, Liu, Kihm, & Taylor, 2008).

In (Park, Liu, Kihm, & Taylor, 2008), 7 mg and 10 mg lunar soil samples from the respective Apollo 11 and 17 missions were examined. The particles are first fluidized with a surfactant, in this case a polymer (N-vinylpyrrolidone) and isopropanol. The surfactant reduces the particle aggregation and separates the small grains that adhere to the larger ones. To aid in the disaggregation of particles, the solution was treated with ultrasonic vibrations. A droplet of the disaggregated solution is then placed on a

silicon wafer used with a scanning electron microscope (SEM). To prevent aggregation as the alcohol evaporates, a magnet is placed below the wafer to prevent the particles from shifting. The wafer is then imaged with a SEM and the cross sectional areas were measured and the projected area diameters determined.

In (Greenberg, Chen, & Smith, 2007), the 2.5 to 500 nm particles are measured using a Scanning Mobility Particle Sizer (SMPS) and the 500 nm to 20 μm particles are measured using an Aerodynamic Particle Sizer (APS). The SMPS method measures the diameter by virtue of the particle electrical mobilities. The electrical mobility requires knowledge of the electric charge of the dust particles. A known electric charge independent of particle composition is given to the dust grains by bipolar diffusion charging. The charged particles are then entrained into a laminar sheath gas with an applied electric field and the motion depends on the electrical mobility. An aperture is used to filter particles with a certain electrical mobility and thus particle diameter. These particles are then allowed to pass through to a detector. The APS method determines the particle diameters by measuring time of flight of particles entrained in an accelerating gas flow. The lag between the gas and particle velocities is a function of particle diameter, and the time of flight is measured by a pair of laser beams axially focused on the exit region of the acceleration nozzle.

Section 2.7. The Apollo Landings

During the six Apollo Moon landings, landing videos and photographs provide a wealth of qualitative and quantitative information about rocket plume impingement and dust dispersal. The camera that recorded the lunar landing was located inside the cabin and viewed the lunar surface from the pilot's window. The dust sprays shown in the movies tend to obscure the surface more than was actually observed by the astronauts

(Gaier, 2005). A typical thrust profile for the Apollo moon landings is shown in Figure 2.7.1. During the final approach to the lunar surface, the thrust was varied from 13.3 to 9.8 kN depending on the amount of residual fuel. The descent speed can be approximated from radio transcripts, and for most missions was approximately 0.75 m/s near touchdown.

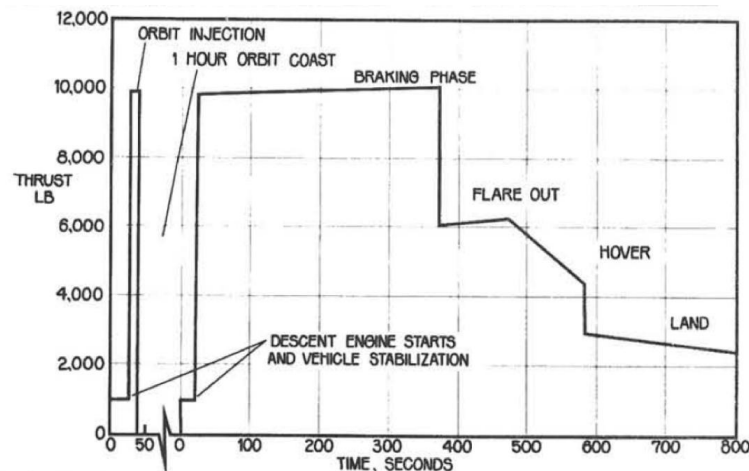


Figure 2.7.1. A nominal thrust profile for the Apollo lunar landings adapted from (Humphries, Hammock, Currie, Taylor, & Fisher, 1973).

2.7.2. APOLLO OBSERVATIONS

The Apollo astronauts' reports and debriefings are described in detail for all the lunar missions and are summarized in (Wagner, 2006). Each mission touched down at a different location on the moon and the severity of dust erosion depended on the local surface properties. For example, Apollo 11, 12, and 15 reported that dust had obscured or completely obscured the surface near touchdown. Apollo 11 astronauts mentioned that surface obscuration first became apparent at an altitude of 30 m. Dust erosion was even worse for Apollo 12 astronauts, and completely obscured the surface during the final few seconds of descent. The obscuration was bad enough for Apollo 12 that the astronauts were concerned that a landing footpad might touchdown on a large boulder.

Apollo 15 astronauts noted that the surface had become completely obscured during the final 18 m of descent, Figure 2.7.2. Lunar dust was less of a problem for Apollo 14, 16, and 17. During these missions, dust sprays were still observed but the surface was still visible throughout the entire landing. As the lunar module descended below an altitude of 18 m, surface obstacles were either completely obscured or barely visible, as shown in Figure 2.7.2.

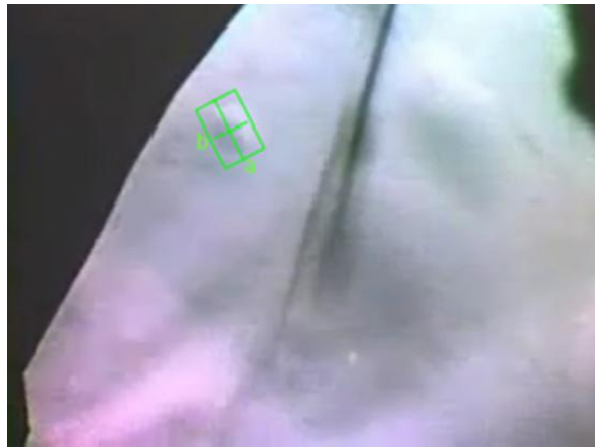


Figure 2.7.2. Obscured view of the lunar surface as the Apollo 15 lander nears the lunar surface. The green rectangle outlines a crater. Adapted from (Immer, Lane, Metzger, & Clements, 2011)

Four different stages of dust dispersal have been identified: the smooth flow stage, the streaking stage, the terrain modification stage, and the clearing stage (Metzger, Smith, & Lane, 2011). The smooth flow stage occurs at higher altitudes and indicates when erosion first occurs. The dust spray at this stage looks similar to a fog layer sitting on the surface. Although the height at which this occurs varies for different missions, the smooth flow stage begins on average at altitudes between 30–40 m. The streaking stage occurs at slightly lower altitudes when the rocket plume begins to interact with surface features, such as rocks or small craters. During this phase, streaks of eroded material are observed. These streaks can change angles and location as the vehicle

thrust and orientation change. Some rocks, with estimated diameters of 11–15 cm, were excavated and transported by the exhaust plume (Immer, Lane, Metzger, & Clements, 2011). This observation contradicts the preconceived notions that only the smallest sub-millimeter size particles would be affected by the plume (Roberts, 1966). During the terrain modification stage, large amounts of material are eroded in bulk quantities. Videos of the Apollo 12, 14, 15, and 17 missions show a sudden discharge of material immediately before touchdown. This is thought to occur because of the contact probe striking the surface. During this stage, streaks of eroded material are also observed to change direction chaotically. Metzger argues that this is evidence of the surface rapidly changing because the streaks are thought to occur because of interactions with craters or rocks. During the clearing stage, the engine shuts down and blown particles clear from the field of view. Since the background atmosphere on the moon is negligibly thin, even the smallest submicron particles fall to the ground and are not supported by buoyancy. Photographs from the surface also indicate that much of the loose material on the surface had been blown away. Astronaut Shepard reported that the maximum erosion did not occur directly under the engine, but at a distance 1 m from the engine bell. This observation matches viscous erosion theory previously discussed in Section 2.4.2.

Although the Apollo landing videos qualitatively describe the dust spray, recent work in analyzing the tapes has also provided quantitative information on the dust sprays (Immer, Lane, Metzger, & Clements, 2011). The angles of inclination of the dust sprays were determined by tracking elongation of shadows cast by the lunar module landing pads on the dust spray. The angle of inclination is measured as the angle made between the top of the dust spray and the lunar surface. Shadow elongation occurred because the shadow was cast on the partially transparent dust sheets. The shadow nearest the lunar

module was faint and cast on the top surface of the dust layer while the shadow furthest was sharp and cast on the lunar surface. Differences in the elongation in the landing pads' shadows combined with trigonometric analysis were used to predict the inclination angles of the various dust sprays, Table 2.7.1.

Table 2.7.1. Angle of inclination for the various dust sprays observed during different Apollo missions.

Apollo Mission	Inclination Angle
11	2.6°
14	2.4°
15	8.1°
16	1.4°
17	2.0°

In Apollo 15, the dust inclination angle was higher than other Apollo missions, and this is thought to have occurred because the LM landed near a crater which deflected the dust spray upwards (Immer, Lane, Metzger, & Clements, 2011).

The dust particle number densities were estimated from luminosity measurements. The dust sprays would periodically clear, allowing brightness comparisons to be made with and without the presence of dust. The ratio of brightness with and without dust, an assumed extinction coefficient, camera height, sun angle, and dust ejection angle were all used to compute the optical density and particle number density. For an average particle size of 14.5 microns, the particle number density was estimated to be between 10^8 and 10^{13} m^{-3} .

The key observations from the various Apollo missions are:

1. A large crater was not excavated during landing. This suggests that the lunar soil has high bearing capacity strength and that viscous erosion is the dominant mechanism.

2. The nature of erosion varied for different landing sites. Dust erosion was evident during all landings, but only completely obscured the surface during Apollo 11, 12, and 15 missions. The onset of erosion occurred at altitudes of 30 – 40 m on average.
3. Dust sprays travel relatively close to the surface, with the top edge of the dust layer inclined between 2° – 3° for most landings. In one landing, the inclination angle was much higher, implying that local surface topography may be important.
4. Streaks of eroded dust were observed as the vehicle approached the surface. The streaks are thought to originate along crater rims or relatively large rocks. This suggests enhanced erosion near such obstacles and that modeling surface obstacles may be important.
5. A sudden burst of material was eroded for many of the Apollo landings immediately before touchdown. This was thought to occur because of the contact probe striking the surface.

CHAPTER 3. METHOD

When near the lunar surface, the exhaust gases in the vicinity of the rocket engine are highly collisional and can be simulated using continuum models. However, as the flow expands towards vacuum, continuum assumptions break down and a kinetic model must be used. We use a hybrid approach where the near-field is solved via the Navier-Stokes solver DPLR (Wright, Candler, & Bose, 1998), and the far field is solved using DSMC. DPLR is only used to solve for the gas flow inside the rocket nozzle and in the near field of the plume expansion, while DSMC is used to simulate the two-phase flows everywhere else. Thus, most of the model development discussed herein applies to the DSMC solver.

Section 3.1. Continuum Regime

DPLR was developed at NASA Ames Research Center and is a three-dimensional Navier-Stokes CFD solver that has the ability to simulate complex flow physics, and is setup to run on massively parallel supercomputers. In this work, we model a descent engine similar to the Lunar Module descent engine (LMDE), and the engine specifications are outlined in Section 2.2.2. An advantage of the continuum solver is the ability to model complicated geometries easily, and in this work we examine the effects of using a more realistic nozzle geometry. The engine geometry was obtained by tracing the outer mold line (OML) from a scaled drawing of the LMDE (Cherne, 1967). The mean flow properties at the nozzle throat and exit plane, used for boundary conditions, are obtained by using parameters in Table 2.2.1 for the LMDE operating at a thrust of 13.34 kN. The specific impulse, I_{sp} , is essentially a measure of the rocket's fuel

efficiency. The specific impulse and rocket thrust can be used to obtain the approximate exhaust speed and propellant mass flow rate via

$$I_{sp} = \frac{F}{\dot{m}g_o} = \frac{V_e}{g_o}. \quad 3.1-1$$

In the above equation, F is the thrust, g_o is the acceleration of gravity on earth, \dot{m} is the propellant mass flow rate, and V_e is the exhaust speed. Near touchdown, the thrust of the descent engine was approximately 13.3 kN and the I_{sp} was 305 s (Humphries, Hammock, Currie, Taylor, & Fisher, 1973). To obtain the exit plane properties, the exhaust speed and propellant mass flow rate are first computed from equation 3.1-1. The exit plane Mach number is computed from nozzle area ratio assuming a calorically perfect gas, $\gamma = 1.3$, undergoing isentropic expansion. These assumptions are only used to estimate the throat and exit plane properties and DPLR readily handles real gas flows with frictional losses. The temperature is obtained from the computed exhaust speed and exit plane Mach number and the density at the exit plane is computed via mass conservation arguments. The throat properties are computed by assuming isentropic expansion and a calorically perfect gas. The results of these calculations are used to provide inflow boundary conditions and are summarized in Table 3.1.1.

Table 3.1.1. Estimated LMDE exit plane and throat properties.

	Ma	ρ [kg/m³]	P [Pa]	T [K]	V [m/s]	Re, D	T_o [K]	P_o [kPa]
Exit	5.03	1.09×10^{-3}	296	589	2,992	182,000	—	—
Throat	1.00	1.27×10^{-1}	144,630	2,458	1,214	297,000	2730	261.4

The DPLR computational domain and corresponding boundary conditions are shown schematically in Figure 3.1.1. DPLR can also be used to solve for an impinging plume by changing the bottom boundary to a wall boundary, (Morris, 2010). Using DPLR to simulate an impinging plume, however, was unstable for cases at higher hovering altitudes and when the nozzle exit plane properties are non-uniform.

Simulating an impinging plume flow field in DPLR is not necessary though, because the coupling from DPLR to DSMC is done upstream of the surface shock.

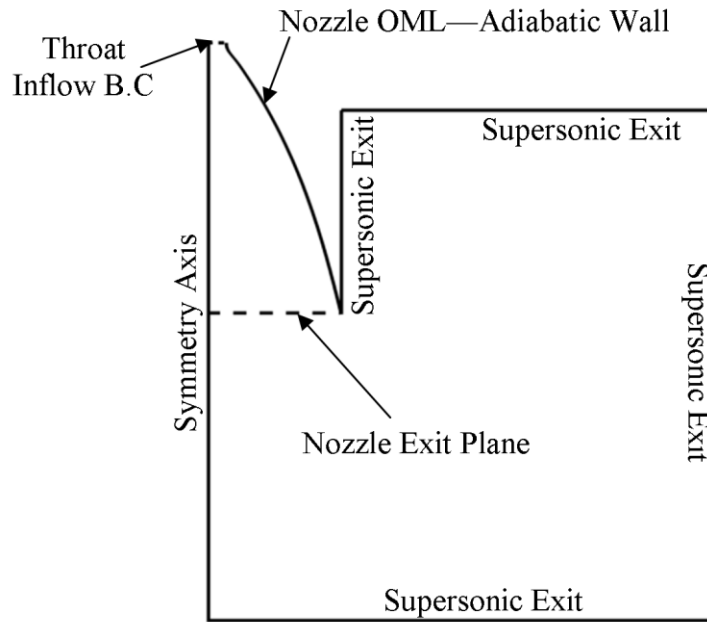


Figure 3.1.1. A schematic of the DPLR computational domain and boundary conditions.

DPLR is capable of simulating a variety of flow physics, but the conditions included in this work are:

1. Steady, 2-D axisymmetric flow;
2. Viscous compressible flow;
3. Real gas where C_p , C_v , and γ depend on temperature;
4. Transport coefficients depend on gas temperature;
5. Vibrational and rotational equilibrium;
6. Laminar flow.

The Reynolds number based on exit plane properties and nozzle diameter is approximately 206,000. This Reynolds number is moderately large, suggesting that turbulence may affect the plume structure. This is tested by using the Baldwin-Lomax

turbulent model within DPLR. Comparisons between the laminar and turbulent cases are discussed in Section 4.2.2.

Section 3.2. Rarefied Regime

The DSMC method is a kinetic solver that is commonly used to simulate non-equilibrium and rarefied flows. The erosion and transport of regolith is handled entirely within the DSMC solver. The DSMC solver used is an in-house research code that has been developed primarily for planetary science applications such as: planetary atmospheres, comet impact on the moon (Stewart B. D., Pierazzo, Goldstein, Varghese, & Trafton, 2011), volcanism on Io (McDoniel, et al., 2011; Zhang, et al., 2004), and plumes of Enceladus. Many different physical models have been implemented, and those relevant to this work include: vibrational and rotational energy, fully coupled two-phase flow, inelastic granular collisions, polydisperse distribution of grain sizes, and grain gray body radiation. To obtain solutions efficiently, the code is written for massively parallel simulations and a non-uniform load balanced processor distribution is used. In addition, an adaptive cell stretching algorithm, which is called linear segments, is used to obtain best resolution of the gas mean free path (Moore, 2011). A variable cell weighting scheme is used to improve simulator statistics along the axis. The cell weight is defined as the ratio of real molecules to simulated molecules in a given cell. In addition, the flow near the jet axis is very collisional, and collision limiting is used to reduce the computational cost (Stewart B. , Pierazzo, Goldstein, Varghese, & Trafton, 2009).

3.2.1. COUPLING DPLR TO DSMC

In this work, the DPLR solution is loosely coupled to the DSMC solver with volume reservoir cells, (Stewart B. D., Pierazzo, Goldstein, Varghese, & Trafton, 2011).

The continuum flow is first solved and reservoir, or 'ghost', cells are created along the desired interface. The reservoir cells are populated with simulators at each time step, and the molecular velocities are sampled from a Maxwellian distribution that corresponds to the macroscopic properties from the continuum solution. One could sample molecular velocities more accurately from the Chapman-Enskog distribution (Garcia & Alder, 1998; Stephani, Goldstein, & Varghese, 2012), but this is not done because the interface is typically drawn where the flow is largely inviscid and flow gradients are weak. These molecules then behave as regular DSMC molecules and can convect within the reservoir cell and possibly into the computational domain. If they move into the computational domain they are kept, but are deleted if they remain within any reservoir cell. Further, molecules that drift from the computational domain into a reservoir cell are also deleted. The size of the reservoir cell must be large enough such that the fastest moving molecules cannot convect across the entire cell within one time step.

The location of the hybrid interface is selected in a region where the flow is sufficiently continuum and the interface normal Mach number is supersonic. Bird's breakdown parameter, P in equation 3.2-1, is used to check if our interface is drawn where the flow is continuum.

$$P = \frac{\sqrt{\pi}}{2} s \frac{\gamma}{\rho} |\vec{\nabla} \rho|. \quad 3.2-1$$

The speed ratio, s , is similar to a Mach number and is defined as the flow velocity divided by the most probable thermal speed. For steady state expansions, the initial breakdown occurs when P exceeds approximately 0.02 (Bird, Molecular Gas Dynamics and the Direct Simulation of Gas Flows, 1994). The interface normal Mach number should be supersonic because the coupling is one way and the DSMC solution does not

affect the continuum regime. If the continuum and DSMC solutions closely match along the interface, it is possible to hybridize even where the flow is subsonic. This may be desirable because beneath the surface shock wave the flow is highly collisional, continuum, and computationally expensive. Although it is more efficient to use DPLR below the shock wave, interfaces that slice through the surface shock show glitches. Figure 3.2.1 shows two different hybrid interfaces when the rocket engine is at an altitude of 10 m. One interface is a cylindrical shell that extends from the ground to the nozzle exit and the other is constructed with two concentric cylindrical shells, one 3 m diameter shell near the surface and a 1 m diameter shell slightly above the surface shock wave.

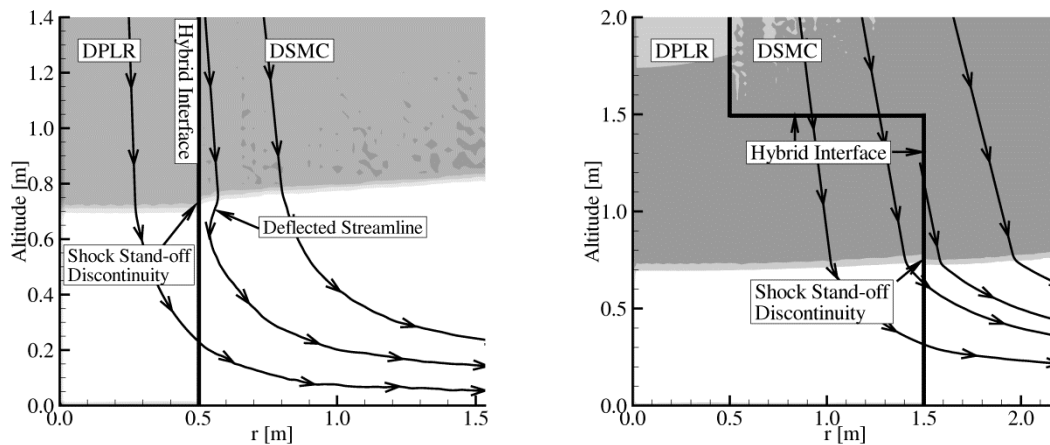


Figure 3.2.1. Two examples of hybrid interfaces that slice through the surface shock and show glitches. Note the offset in shock stand-off and the deflected streamlines.

In Figure 3.2.1 (left), DSMC streamlines near the interface non-physically deflect towards the axis of symmetry because there is a discontinuity in the shock stand-off distance between the two solvers. DPLR predicts a surface shock that rests slightly closer to the surface than the DSMC prediction. Consequently the DSMC particles immediately downstream of the shock see a low pressure boundary condition at the continuum interface and the streamlines are deflected inward. In Figure 3.2.1 (right),

the shock stand-off distance in DPLR is larger than that for DSMC and the outward pressure force does not cause streamlines to deflect inwards. The specific reason for the differences between the DSMC and DPLR solutions is unknown, but there are several plausible explanations. There may be slight mismatches in the ratio of specific heats upstream of the shock wave because internal modes are not exactly in equilibrium with translational energy. There are also slight differences in the transport properties, viscosity in particular, and these differences may alter the displacement thickness of the surface boundary layer.

Ultimately, it was decided to create the hybrid interface upstream of the surface shock wave. Although less computationally efficient, this interface placement alleviates problems with mismatches between the continuum and DSMC solutions because the interface normal Mach number is supersonic. In addition, regions of erosion and two-phase flow only occur within the DSMC solver and new model development only needs to be applied to the DSMC solver.

Section 3.3. Two-Phase Flow

In our framework, dust particles are treated as special representative molecules whose mass and diameter are many orders of magnitude greater than those of gas molecules. This section will address the relevant properties of lunar regolith, the erosion model, the dust-gas interaction model, and how particle-particle collisions are modeled.

3.3.1. THE PARTICLE SIZE DISTRIBUTION

In our work, a distribution of particle sizes is approximated by a set of dust species with discrete diameters. We also restrict ourselves to the fine and ultrafine portions of regolith, i.e. grains less than 20 μm in diameter. The particle size distribution for this

regime has been measured (Park, Liu, Kihm, & Taylor, 2008; Greenberg, Chen, & Smith, 2007), and their results are summarized in section 2.6.2. Dust particles may interact with each other through two mechanisms: inter-particle collisions and coupling through the gas in regions of significant mass loading. The best approximation to the particle size distribution depends on which regime is applicable to the problem of interest. For example, in strongly sheared dense granular flows where particle-particle collisions dominate, it may be desirable to model particle diameters that have the highest collision rates. If there is sufficiently high mass loading (and the presence of dust affects the gas), then it is important to simulate the particles that have the largest mass fractions. The latter applies to this work, and we chose to model the grains which most affect the gas. The weight distribution of particle sizes was found by assuming a constant particle density and taking the particle volume, or D_p^3 , moment of the particle size distribution shown in Figure 2.6.1. The weight distribution is then renormalized and plotted in Figure 3.3.1 along with the particle diameters that we include in our simulations.

Despite significant differences in the particle number size distributions measured by Park and Greenberg, shown previously in Figure 2.6.1, the particle weight distributions are reasonably consistent. Most of the differences between Greenberg's and Park's size distributions are for the sub 1 μm particles, but these particles have relatively little impact on the weight distribution. The 8 μm particles contain most of the mass and particles less than 1 μm contain significantly less. In this work we include dust particles with diameters of 200 nm, 800 nm, 2 μm , 5 μm , 8 μm , and 11 μm . The 200 nm and 800 nm grains are included because those diameters correspond to peaks in the bimodal particle size distribution measured by Greenberg. For these size particles, approximately 41% of the mass is comprised of the 8 μm diameter grains, 27% from 11 μm grains, 25% from the 5 μm grains, and 6% from the 2 μm grains. The 200 and 800

nm particles account for the remaining 1% of the mass. The number density of different sized particles may be vastly different, where the largest particles have a much smaller number density than the smaller ones. In order to maintain adequate statistics for all dust sizes, a species weighting scheme is implemented for the dust class of simulators. The number of real dust particles represented by each simulator varies with particle size.

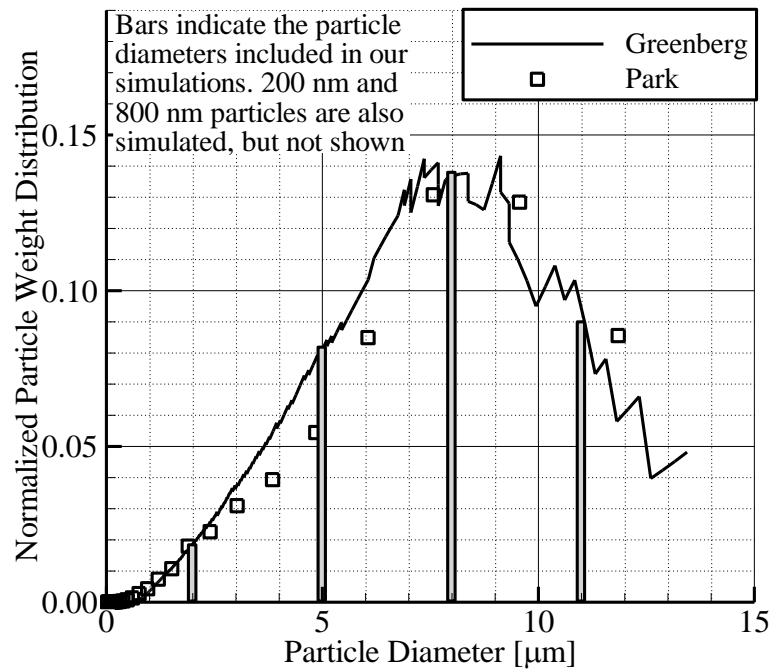


Figure 3.3.1. Particle weight distribution for the sub 20 μm fraction of lunar regolith. Bars indicate particle diameters included in our simulations.

Dust grains are treated as perfect hard spheres in our model, but realistic grains are likely to be jagged and non-spherical. An important parameter that affects the acceleration of dust particles is the ratio of the particle cross section to particle mass. Consequently, we attempt to model spheres that have the same cross section to mass ratio as realistic grains. For a hard sphere particle, the aerodynamic cross section is the mean projected area of the particle. The particle shapes have been characterized for different

lunar core tube samples. Of the many ways to describe the shape of a dust particle, the volume ratio can be used to determine the geometric cross section. The volume coefficient, α_v , is defined as

$$\alpha_v = \frac{V_p}{d_a^3}, \quad 3.3-1$$

where V_p is the volume displaced by the grain and d_a is the projected area diameter. The projected area diameter is the diameter of a sphere whose cross sectional area is the same as the projected area of the dust particle. For hard spheres, this is equivalent to the aerodynamic diameter. One can rewrite the volume coefficient in terms of the grain density, ρ_p , and an apparent density, ρ_a , as

$$\alpha_v = \frac{\pi \rho_a}{6 \rho_p}. \quad 3.3-2$$

The apparent density is the ratio of the particle mass to the volume of a sphere whose projected area is the same as the dust particle. The volume coefficient was measured for lunar dust particles larger than 60 μm in diameter, and the mean volume coefficient is approximately 0.32. We assume the small particles have a similar volume coefficient and a particle density of 3100 kg/m^3 . These parameters result in an apparent density of 1900 kg/m^3 . The apparent density and projected (or aerodynamic) diameter can be used to compute the mass of a dust particle via

$$m_p = \frac{\pi}{6} d_a^3 \rho_a. \quad 3.3-3$$

The hard sphere aerodynamic cross section is simply $\pi D_p^2/4$.

3.3.2. DUST EROSION MODEL

There are several different erosion mechanisms, outlined in Section 2.4, but viscous erosion is the dominant mechanism when landing on the moon. Viscous erosion occurs when the surface shear exceeds the cohesive strength of the soil and small dust

particles begin to roll along the surface. The rolling dust grains can collide with neighboring particles and may then be lofted into the flow field. This is a difficult phenomenon to model from first principles and would require a more detailed discrete element calculation near the lunar surface. Instead, we model this by using empirically derived scaling relationships discussed in Section 2.4.2. Plume impingement tests show that the eroded particle mass flux scales with the densimetric Froude number.

$$\Phi_e \propto \frac{\rho_g U_g^2}{2g\rho_p D_p} \equiv Fr^2. \quad 3.3-4$$

To apply the above scaling relationship to DSMC, the dynamic pressure is evaluated at a distance slightly above the boundary layer, 5 cm in this work, because the surface roughness scales are assumed to be large relative to the boundary layer scale. Near the stagnation point, the boundary layer is thin and the gas dynamic pressure is sampled outside of the boundary layer. Further from the jet axis, however, the boundary layer thickens and the dynamic pressure evaluated 5 cm above the surface is well within the viscous boundary layer. To obtain smooth erosion profiles, the dynamic pressure is spatially smoothed and temporally averaged over a short period of time. All other terms in equation 3.3-4 are constant and can be grouped into a single scaling constant. Equation 3.3-4 only provides a proportionality relationship, and a scaling constant must be used to obtain the erosion flux. The scaling constant is selected such that the simulated crater depth is comparable to what was observed throughout the Apollo missions; a shallow crater beneath the descent engine. The simulated crater depth was obtained by approximating a landing trajectory by a set of discrete hovering altitudes and then integrating the erosion mass flux to find the total eroded mass. An assumed bulk density of 1500 kg/m³ (Heiken, Vaniman, & French, 1991) was used to then determine the crater depth. This bulk density is the density of the soil bed and not of individual

particles. After calibrating the erosion profile for a simulated landing, the erosion flux is

$$\Phi_e = 0.0025 \left[\frac{\text{S}}{\text{m}} \right] \times \frac{\rho_g U_g^2}{2}. \quad 3.3-5$$

3.3.3. DUST – GAS COUPLING.

Near the erosion area, the gas mean free path is slightly larger than the largest simulated dust grains. Consequently, we are able to neglect the development of shocks and boundary layers over individual grains. In addition, there is a high mass fraction of dust near the surface indicating that a fully coupled gas-dust interaction model is necessary. Such a model (Burt & Boyd, 2004) has been implemented into this work. The momentum and energy transfer from the gas to the dust particles is first computed while keeping the background gas fixed. In the next step, momentum is transferred from the dust back to the gas via gas collisions with dust particles while keeping the background dust fixed. This approach conserves momentum and energy on average, but may be susceptible to 'random walk' effects because it is not instantaneously conservative. The method has been slightly modified to improve stability and accuracy. The detailed method, modifications, and verification tests will be discussed in this section.

The momentum and energy transfer from the gas to the dust particles is first computed. The computed drag and heat transfer to the dust particles is valid for any arbitrary non-equilibrium gas flow where the grain Kn, $\text{Kn} \equiv \lambda/D_p$, is large. The drag and energy transfer to the dust particles are computed by assuming that gas molecules that collide with a particle have some combination of diffuse and specular scattering. The expectation drag and thermal energy transfer to dust particle, p , resulting from many collisions (Burt & Boyd, 2004) with one representative gas molecule, i , are

$$\mathbf{F}_{p,i} = \frac{\pi R_p^2 N_{g,i} m_{g,i}}{V_c} \left(c_{r,i} + \frac{\tau_p}{3} \sqrt{\frac{2\pi k_b T_p}{m_{g,i}}} \right) \mathbf{u}_{r,i}, \quad 3.3-6$$

$$Q_p = \frac{\tau_p \pi R_p^2 N_g m_g}{V_c} \left(\frac{1}{2} c_{r,i}^2 + \frac{e_{rot,i}}{m_g} - \left(1 + \frac{\Lambda}{4} \right) \frac{2k_b T_p}{m_g} \right). \quad 3.3-7$$

$N_{g,i}$ is the number of real molecules represented by the gas simulator, $m_{g,i}$ is the gas molecular mass, V_c is the cell volume, $\mathbf{u}_{r,i}$ is the relative velocity, $c_{r,i}$ is the relative speed, τ_p is the thermal accommodation coefficient, and R_p is the particle radius. The original method (Burt & Boyd, 2004) computes the total force and energy transfer by summing Equations 3.3-6 and 3.3-7 over all possible interactions. The velocity of the dust particle is then updated via $\mathbf{V}_d^{k+1} = \mathbf{V}_d^k + \mathbf{F}_p^k \delta t / m_p$, where \mathbf{F}_p is the net force exerted on the dust particle p , \mathbf{V}_d is the particle velocity, m_p is the mass of the particle, δt is the time step, and k is the time step index. This accuracy of the scheme is of order δt and can be inaccurate when a large time step is used. For extreme cases where the time step is too large, the velocity of the dust particle can overshoot the gas velocity and yield oscillatory solutions. A higher order implementation has been developed to improve accuracy when a moderately large time step is used. The total force and energy transfer is obtained by summing equation 3.3-6 over all gas molecules within the collision cell.

$$\mathbf{F}_p = m_p \frac{d\mathbf{V}_p}{dt} = \sum_i^{N_g} \left[\frac{\pi R_p^2 N_{g,i} m_g}{V_c} \left(c_{r,i} + \frac{\tau_p}{3} \sqrt{\frac{2\pi k_b T_p}{m_g}} \right) \mathbf{u}_{r,i} \right] \quad 3.3-8$$

By substituting $\mathbf{u}_{r,i} = \mathbf{V}_{g,i} - \mathbf{V}_p$, equation 3.3-8 can be written as the following nonlinear differential equation,

$$m_p \frac{d\mathbf{V}_p}{dt} = \mathbf{A} - \mathbf{B}\mathbf{V}_p \quad 3.3-9$$

$$\mathbf{A} \equiv \sum_i^{N_g} \left[\frac{\pi R_p^2 N_{g,i} m_g}{V_c} \left(c_{r,i} + \frac{\tau_p}{3} \sqrt{\frac{2\pi k_b T_p}{m_g}} \right) \mathbf{v}_{g,i} \right] \quad 3.3-10$$

$$\mathbf{B} \equiv \sum_i^{N_g} \left[\frac{\pi R_p^2 N_{g,i} m_g}{V_c} \left(c_{r,i} + \frac{\tau_p}{3} \sqrt{\frac{2\pi k_b T_p}{m_g}} \right) \right]. \quad 3.3-11$$

Equation 3.3-9 is a nonlinear O.D.E because \mathbf{V}_d also appears in the relative speed, $c_{r,i}$. This differential equation can be solved if the relative speed is linearized, and the result is

$$\mathbf{v}_p^{k+1} = \frac{\mathbf{A}}{\mathbf{B}} - e^{-\mathbf{B} \frac{\delta t}{m_p}} \left(\mathbf{v}_p^k - \frac{\mathbf{A}}{\mathbf{B}} \right) \quad 3.3-12$$

Equation 3.3-12 is more accurate than the original approach because it integrates the force as the dust particle accelerates throughout the time step.

A similar procedure can be used to obtain a higher order energy transfer equation. The nonlinear O.D.E for the energy transfer equation is

$$m_p c_p \frac{dT_p}{dt} = C - D T_p \quad 3.3-13$$

$$C \equiv \sum_i^{N_g} \left[\frac{\tau_p \pi R_p^2 N_{g,i} m_g}{V_c} \left(\frac{1}{2} c_{r,i}^2 + \frac{e_{rot,i}}{m_g} \right) \right] \quad 3.3-14$$

$$D \equiv \sum_i^{N_g} \frac{\tau_p \pi R_p^2 N_{g,i} m_g}{V_c} \left(1 + \frac{\Lambda}{4} \right) \frac{2k_b}{m_g}. \quad 3.3-15$$

Equation 3.3-13 can easily be solved if the relative velocity terms are linearized, and the resulting expression for the dust particle's updated temperature is

$$T_p^{k+1} = \frac{C}{D} - e^{-D \frac{\delta t}{m_p c_p}} \left(T_p^k - \frac{C}{D} \right). \quad 3.3-16$$

A spatially homogeneous test case was simulated and the numerical results are compared to the analytic result in Figure 3.3.2. In this test case, two different sized dust

particles are initialized with a velocity and temperature of 500 m/s and 200 K. The background gas is held fixed at equilibrium, with a number density, velocity, and temperature of $1.0 \times 10^{20} \text{ m}^{-3}$, 1000 m/s, and 100 K, respectively. The analytical force and heat transfer expressions, (Gallis, Torczynski, & Rader, 2001), for a translating particle in an equilibrium gas are

$$F_p = -m_g n_g \pi R_p^2 c_o^2 \left(m_1 \left[\frac{\mathbf{u}_p}{c_o} \right] + \tau \sqrt{\frac{T_p}{T_g}} \frac{\sqrt{\pi}}{3} \right) \frac{\mathbf{u}_p}{c_o} \quad 3.3-17$$

$$Q_p = -m_g n_g \pi R_p^2 c_o^3 \tau \left(k_1 \left[\frac{\mathbf{u}_p}{c_o} \right] - \sqrt{\frac{T_p}{T_g}} k_2 \left[\frac{\mathbf{u}_p}{c_o} \right] \right), \quad 3.3-18$$

where the subsidiary functions m_1 , k_1 , and k_2 are

$$m_1[s] = \frac{(-1 + 4s^2 + 4s^4)\text{erf}[s]}{4s^3} + \frac{(1 + 2s^2)\exp[-s^2]}{2\sqrt{\pi}s^2} \quad 3.3-19$$

$$k_1[s] = \frac{(3 + 12s^2 + 4s^4)\text{erf}[s]}{8s} + \frac{(5 + 2s^2)\exp[-s^2]}{4\sqrt{\pi}} \quad 3.3-20$$

$$k_2[s] = \frac{(4 + 8s^2)\text{erf}[s]}{8s} + \frac{\exp[-s^2]}{\sqrt{\pi}}. \quad 3.3-21$$

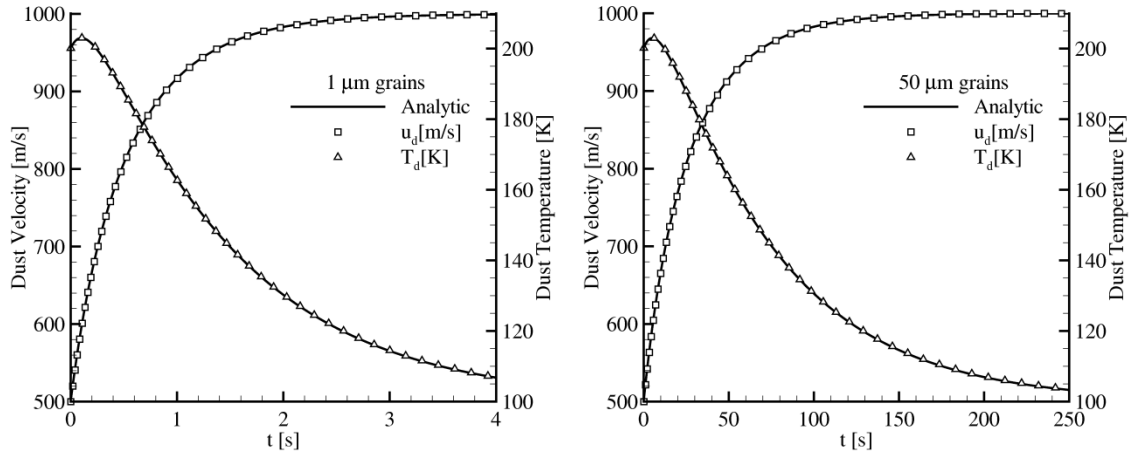


Figure 3.3.2. Spatially homogeneous test for two different sized dust grains relaxing towards the gas velocity and temperature. The gas is held fixed and is thus uncoupled to the dust. (left) 1 micron grains. (right) 50 micron grains.

Excellent agreement between the computed and analytic relaxation of the dust temperature and velocity is obtained. The initial increase in gas temperature is a gas compressibility effect that occurs when the particle Mach number is supersonic.

The computed drag and heat transfer depends on the gas-grain surface interaction, but unfortunately the details of this interaction are unknown for lunar soil particles. In this model, the thermal accommodation coefficient is the only parameter that affects the scattering. To assess how the assumed surface interaction model affects the drag and heat transfer, a series of homogeneous relaxation tests were performed for different thermal accommodation coefficients in Figure 3.3.3.

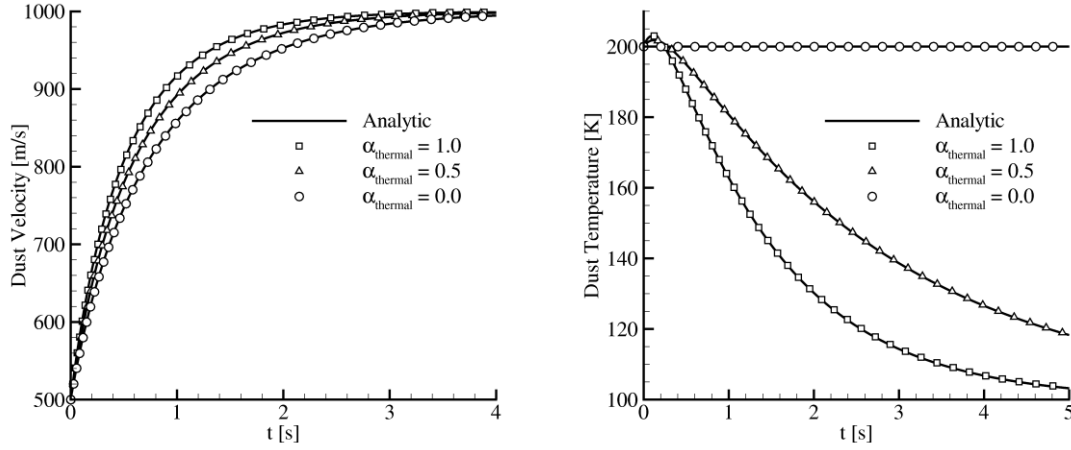


Figure 3.3.3. Spatially homogeneous relaxation tests for dust grains with different thermal accommodation coefficients, 0.0, 0.5, and 1.0. (left) Relaxation of dust momentum. (right) Relaxation of the dust grain temperature.

The momentum transfer from the gas to the dust becomes more efficient as the thermal accommodation coefficient increases, shown by the quicker relaxation times in Figure 3.3.3. This occurs because a single gas molecule that strikes a dust particle and undergoes diffuse reflection is preferentially backscattered. Consequently, more forward momentum is transferred to the dust grain. Gas molecules that undergo specular reflections scatter isotropically and consequently do not transfer momentum as efficiently. The orientation of the post-collision relative velocity vector for specular collisions is isotropic in velocity space and is mathematically justified in (Burt & Boyd, 2004). The ratio of the drag force for purely diffuse to purely specular reflections is plotted for different temperature and speed ratios.

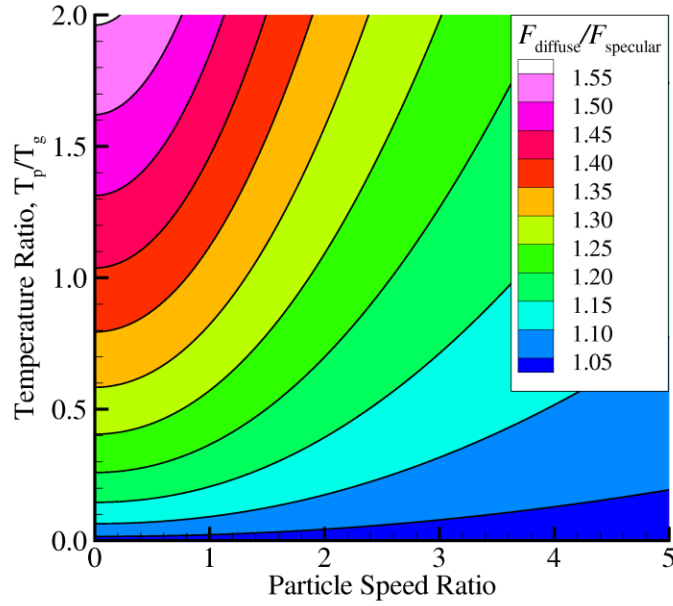


Figure 3.3.4. The drag force computed for diffuse reflections divided by the drag force for specular reflections plotted for different temperature and speed ratios.

The effect of thermal accommodation on the drag force is more apparent when the dust particle temperature exceeds the gas temperature. In all cases, however, diffuse scattering results in a higher drag force because of preferential backscattering. For temperature ratios between 0.5 and 1.0, which are typical for this work, the drag force can vary between 30–40%. In this work, the thermal accommodation coefficient is assumed to be 1.0 because the particles are jagged and rough. The temperature of the dust particle is also assumed uniform throughout the particle in this work. This assumption is only valid for small Biot numbers; $Bi \equiv hL/k$, where h is the convective heat transfer coefficient, L is the diameter of the particle, and k is the thermal conductivity of the particle. The Biot number represents the rate at which heat is transferred through the surface to how quickly it is redistributed by conduction. The

Biot number was computed for a variety of particle speed ratios and temperatures while the gas was held fixed at 1500 K, Figure 3.3.5.

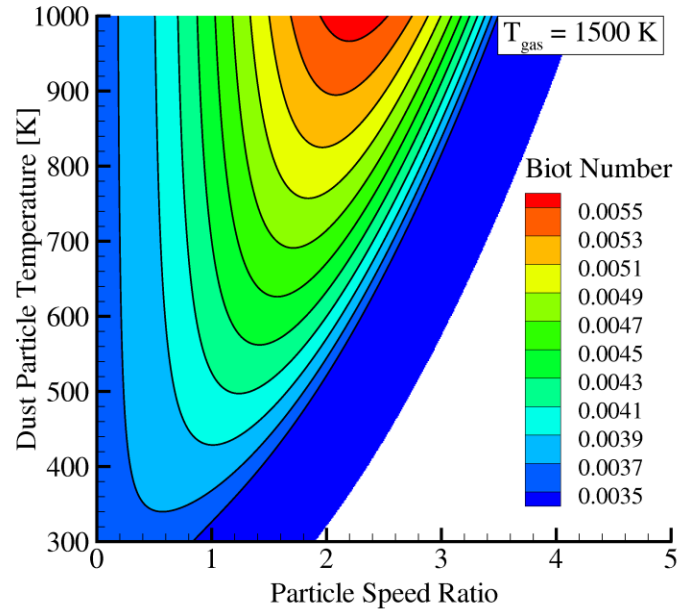


Figure 3.3.5. Contours of Biot number for different dust particle temperatures and particle speed ratios when the gas is held at a fixed 1500 K. The dust particles were 10 μm in diameter.

The Biot number is small for 10 μm particles in all cases, and therefore the isothermal particle assumption is valid for dust sizes included in this work. If particles larger than 1 mm in diameter are simulated, the uniform approximation may not be valid. Before the velocity and temperature of the dust particle are updated, an additional step to update the gas is performed to ensure momentum and energy conservation.

The gas is coupled to the dust by colliding selected gas molecules with the background dust. These collisions are handled similarly to typical gas collisions in DSMC, except only gas molecules are affected in this step. The number of candidate collisions is computed as

$$N_{cand} = \frac{\Delta t N_g N_p (q_p c_r \sigma)_{\max}}{V_c}, \quad 3.3-22$$

where q_p is the number of real particles represented by a dust simulator, c_r is the relative speed, σ is the cross section, and N_p and N_g are the number of dust and gas simulators. This form for the number of selections is slightly different than the standard NTC method, i.e. $(q_p c_r \sigma)_{\max}$ is used instead of $(c_r \sigma)_{\max}$ (Schmidt & Rutland, 2000), because dust species may have different weights. Once a candidate collision pair is chosen, it is accepted with a probability given in equation 3.3-23. If the collision is accepted, the gas molecule then undergoes a diffuse or specular reflection with a probability based on the thermal accommodation coefficient.

$$P = \frac{q_p c_r \sigma}{(q_p c_r \sigma)_{\max}}. \quad 3.3-23$$

The scattering function depends on whether the reflection is specular or diffuse. For specular reflections, the re-orientation of the post-collision relative velocity vector is isotropic in velocity space and the relative speed remains unchanged, (Burt & Boyd, 2004). For diffuse reflections, the scattering is more complicated and can be derived by considering a gas molecule colliding with a dust particle in the particle fixed frame of reference, Figure 3.3.6. It can be shown that the scattering angle, δ , for diffuse reflections is

$$\cos \delta = (\cos \theta - \sin \theta \tan \varphi \cos \varepsilon) \cos \varphi. \quad 3.3-24$$

The above angles are shown schematically in Figure 3.3.6, where θ is the angle between the pre-collision relative velocity vector and surface normal, φ is the polar angle measured between the surface normal and post-collision relative velocity vector, ε is an azimuthal angle. The scattering angle, δ , is the angle between the post- and negative

pre-collision relative velocity vectors. Values of δ less than $\pi/2$ indicate backward scattering.

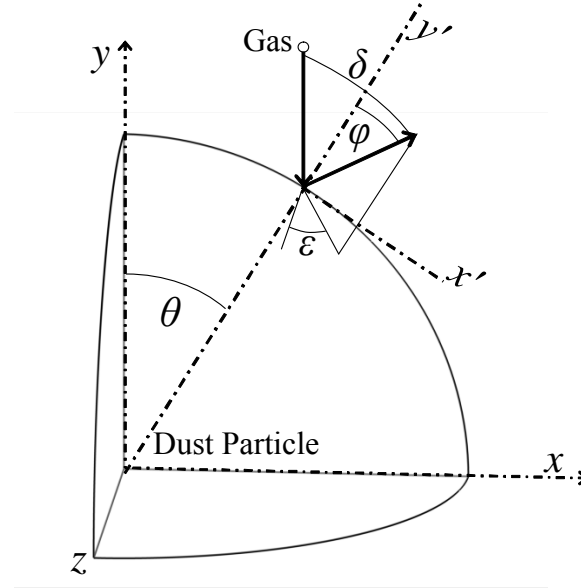


Figure 3.3.6. A schematic of the angles and coordinate systems used to depict gas-particle collisions.

Equation 3.3-24 appears different than that given in (Burt & Boyd, 2004), but is mathematically equivalent after applying a trigonometric identity. The angle of incidence, θ , is proportional to the projected area of the strip on the particle surface in the direction of the relative velocity vector. The polar angle φ is the angle that molecule leaves the surface at relative to the local surface normal. The polar angle depends on the gas-surface interaction model. A lambert surface is assumed in this work. The angle ε is assumed to be uniformly distributed. The normalized distribution functions for these angles are:

$$f(\theta)d\theta = \sin(2\theta) d\theta; \theta \in [0, \pi/2], \quad 3.3-25$$

$$f(\varphi)d\varphi = \sin(2\varphi) d\varphi; \varphi \in [0, \pi/2], \quad 3.3-26$$

$$f(\varepsilon)d\varepsilon = \frac{1}{2\pi}d\varepsilon. \quad 3.3-27$$

The distribution function for the scattering angle is

$$f(\delta)d\delta = f(\theta)f(\varphi)f(\varepsilon)d\theta d\varphi d\varepsilon. \quad 3.3-28$$

In the original work of Burt (2004), the scattering angle was sampled via acceptance rejection on a 6th order polynomial curve fit to a Monte Carlo solution for equations 3.3-28 and 3.3-24. An alternative approach that avoids acceptance rejection is now used instead. The angles θ , φ , and ε are first obtained by inverting the corresponding cumulative distribution functions, seen in equations 3.3-29–3.3-31, and δ is then directly computed from equation 3.3-24.

$$\theta = \frac{1}{2}\cos^{-1}(2R_f - 1) \quad 3.3-29$$

$$\varphi = \frac{1}{2}\cos^{-1}(2R_f - 1) \quad 3.3-30$$

$$\varepsilon = 2\pi R_f. \quad 3.3-31$$

This approach does not conserve momentum and energy instantaneously, but it is shown in Appendix A that it is conservative on average. Consequently, this scheme can be susceptible to random walk effects; especially for transient flows. To assess whether such effects are significant for this work, a simple one dimensional test case was performed.

Two-phase flow through a tube is studied where the gas and dust enter the tube with initially different velocities and different particle thermal temperatures than the gas kinetic temperature. The dust particles have an initial kinetic or granular, temperature of 0. The effects of the tube wall are neglected and the flow is assumed 1-dimensional. In this test case, 1 and 10 μm dust particles enter the computational domain with speeds of 500 and 250 m/s and thermal temperatures of 200 and 150 K respectively. The gas

enters the domain with a speed of 1000 m/s and temperature of 100 K. There were, on average, 10 gas simulators per cell and 3 simulators for each dust species and momentum and energy fluxes were determined by averaging over many samples, Figure 3.3.7.

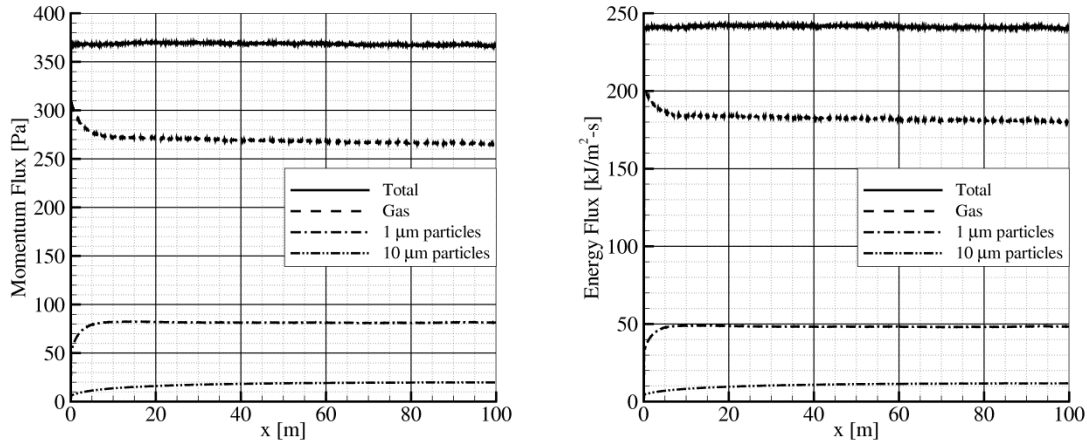


Figure 3.3.7. Momentum (left) and energy (right) fluxes for the fully coupled gas–particle interaction model. These simulations include 1 and 10 μm particles interacting with H_2O gas. Note the total momentum and energy fluxes are conserved within the noise.

These results show that for steady simulations with relatively few simulators per cell, reasonable results that conserve momentum and energy can be obtained by averaging.

3.3.4. PARTICLE COLLISIONS.

Particle-particle collisions can occur during a variety of different lunar landing scenarios. Examples include the near erosion region, where the shear stress and particle number densities are large, upstream of obstacles where incident particles can collide with the reflected ones and along symmetry planes when a multi-engine configuration is used. For the simulations presented in this dissertation, the dust particles are fluidized and collisions between particles are brief and infrequent events. For this flow regime, granular collisions can be modeled similarly to that of a dilute gas. Unlike gas

molecules, dust particles collisions are inelastic and particle kinetic energy is irreversibly transformed into thermal or deformation energy during a collision.

Simulators for different size dust particles have different weights, and the generalized NTC method is used. There are two ways to organize grain-grain collisions. One can separately consider collisions between particles of a certain size with other particles of a certain size and then perform collisions for each pairing of particle sizes. The results may then become sensitive as to the order in which grain-grain collisions are executed. The approach used in this work removes any artifacts associated with ordering and considers collisions between all dust particles in one single step. The number of candidate collisions is

$$N_{cand} = \frac{\Delta t N_p^2 (q_p c_r \sigma)_{\max}}{2V_c}, \quad 3.3-32$$

where N_p is the number of dust simulators in a cell and the factor of two is to prevent double counting. Collision partners are selected, with replacement, from a reservoir of all particles regardless of size and are accepted to collide with a probability

$$P = \frac{q_g c_r \sigma}{(q_p c_r \sigma)_{\max}}, \quad 3.3-33$$

where q_g is the greater of the two weights considered in the collision. This nomenclature is consistent with (Schmidt & Rutland, 2000) and should not be confused with the weight of a gas simulator. It is possible for a candidate collision pair to consist of a single particle colliding with itself, but such candidates are never accepted to collide because $c_r = 0$.

Particle collisions are modeled simplistically in this work, where a constant normal coefficient of restitution and friction coefficient are used. This model neglects particle rotation, hysteretic deformation, variations of the tangential and normal

coefficients of restitution, electrostatic forces, and particle cohesion. The coefficients of restitution depend on the impact speed, particle geometry, and material properties. The normal coefficient of restitution ranges from 0 to 1 and represents the fraction of the normal component of velocity retained after a collision. The tangential restitution coefficient ranges from -1 to 1 . These details have not been measured for lunar dust particles under conditions applicable to this work, and for simplicity the tangential and normal coefficient of restitution are assumed equal. This simplistic collision model is rationalized because the particle collision rates are relatively small and the dust motion is assumed to be dominated by the gas. In hindsight, particle collisions noticeably affect the dust trajectories and a more sophisticated collision model should be implemented in future work.

If a candidate pair is accepted for collision, the post-collision velocities, denoted by primes, are

$$\begin{aligned} \mathbf{u}'_1 &= \mathbf{u}_{com} + \alpha_{cor} |\mathbf{u}_1 - \mathbf{u}_{com}| \hat{\mathbf{e}} \\ \mathbf{u}'_2 &= \mathbf{u}_{com} - \alpha_{cor} |\mathbf{u}_2 - \mathbf{u}_{com}| \hat{\mathbf{e}}, \end{aligned} \tag{3.3-34}$$

where \mathbf{u}_1 and \mathbf{u}_2 are the pre-collision velocities of the participants, \mathbf{u}_{com} is the center of mass velocity, and $\hat{\mathbf{e}}$ is a unit vector uniformly distributed on a sphere. When the coefficient of restitution is less than 1 the lost kinetic energy is then added to the thermal energy of the particles. Since particles in general have different weights depending on their diameter, an additional check is performed when updating post-collision velocities. The velocity of the particle with lesser weight is always updated and the velocity of the particle with the greater weight is only updated if

$$R_f < \frac{q_l}{q_g}, \tag{3.3-35}$$

where R_f is a random number between 0 and 1, q_l is the lesser of the two weights and q_g is the greater.

A spatially homogeneous test case was performed to verify conservation of momentum and energy and the results are shown in Figure 3.3.8. Equal amounts, by mass, of 1 and 10 μm grains are initially created with velocities of 500 and -500 m/s and temperatures of 200 and 400 K, respectively. Two thousand simulators are used to represent each dust species.

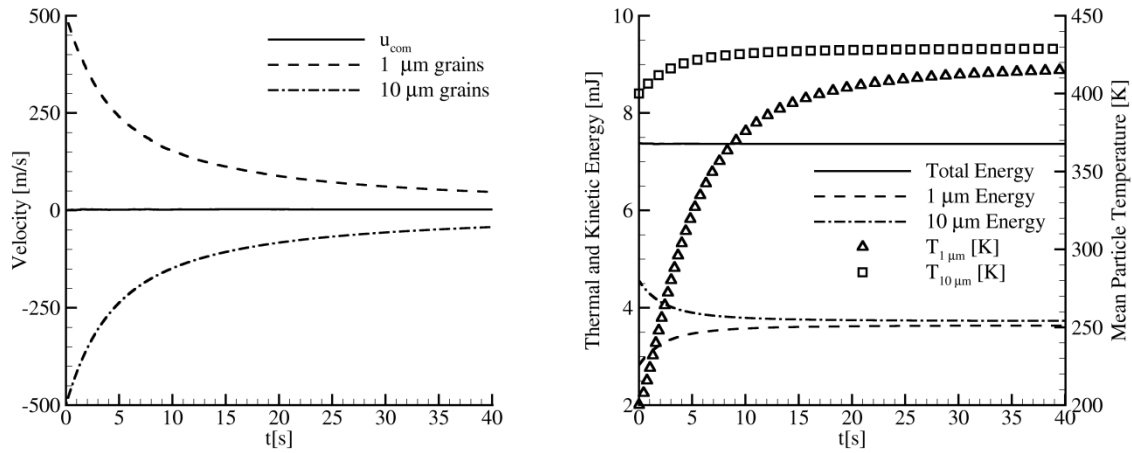


Figure 3.3.8. Spatially homogeneous relaxation of a binary granular mixture of 1 and 10 μm particles with different initial velocities and temperatures. (left) Particles relax towards the center of mass velocity. (right) total energy for each species on the left axis and the mean particle temperature is shown on the right axis.

The coefficient of restitution is 0.8 in the above simulations and particles consequently warm as they collide. The species weight reflects the number density and is 1000 times smaller for 10 μm particles than it is for 1 μm particles. Momentum and energy are therefore not precisely conserved instantaneously. Random walk effects were not significant in the homogeneous relaxation tests above and the total energy and center of mass velocity remain constant, thus validating our approach for colliding grains.

CHAPTER 4.

THE NEAR FIELD GAS FLOW FIELD

The gas flow fields (without the presence of dust) within the nozzle, expanding plume flow, and the near field impingement on the lunar surface are discussed in this chapter. The effects of nozzle geometry and assumed turbulence on the plume flow are discussed as well. These simulations are for axisymmetric configurations, where the jet axis is perpendicular to the lunar surface, and allow direct comparison to simpler plume flow and impingement models.

Section 4.1. Internal Nozzle Flow

The internal nozzle flow is simulated with the Navier-Stokes solver, DPLR. Within the engine bell, the exhaust flow is hot, chemically reacting, vibrationally active, compressible, and largely inviscid. In this work, however, chemistry is neglected and water is the only simulated exhaust gas. In real nozzles, the flow is not quasi 1-D and compression waves form inside the nozzle (Dettleff, 1991; Simmons, 2000). The shock structure inside of the nozzle depends on the geometry, and in our work a contoured or bell nozzle is simulated. The nozzle geometry was obtained by tracing the outer mold line (OML) of the engine bell in (Humphries, Hammock, Currie, Taylor, & Fisher, 1973). Contours of gas translational temperature and pressure inside the nozzle expander are shown in Figure 4.1.1.

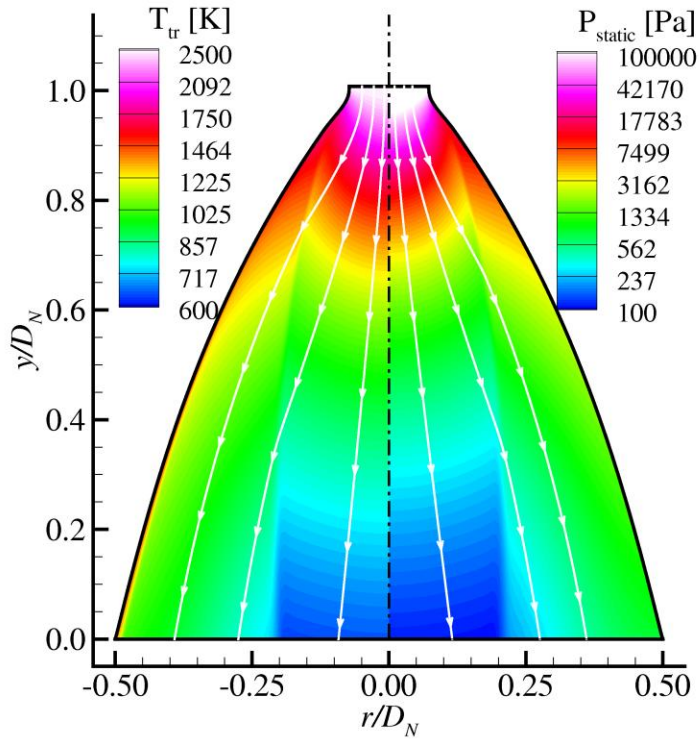


Figure 4.1.1. Contours of gas temperature (left) and pressure (right) within the engine bell.

The gas is modeled as a real gas, and it is everywhere assumed that vibrational and rotational energy are in equilibrium with translation. A compression wave forms near the nozzle throat and propagates through the nozzle. The pressure ratio across this compression wave is used to characterize the shock strength, and is approximately 1.82 at the nozzle exit plane. The shock is therefore weak and the shock normal Mach number is 1.30. The engine bell is deflected slightly outwards at the exit plane, resulting in an average outwards radial velocity of 533 m/s. The gas cools as it expands, and the coldest temperature occurs near the nozzle centerline and is approximately 645 K. The gas properties at the nozzle exit plane are non-uniform and shown in Figure 4.1.2.

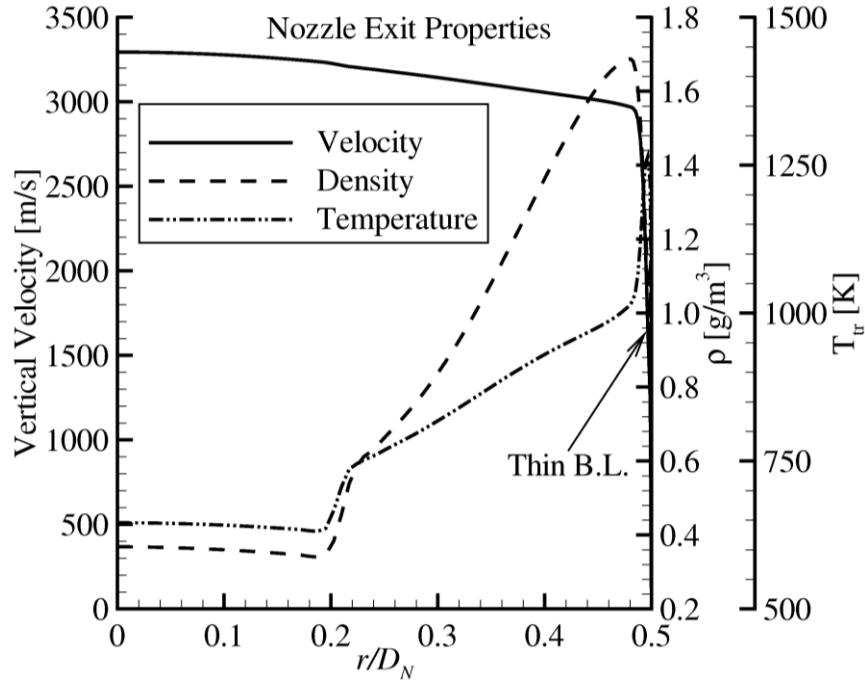


Figure 4.1.2. Nozzle exit plane properties computed with DPLR for an engine bell similar to the LMDE.

The vertical velocity is nearly constant outside of the viscous boundary layer, indicating that the nozzle is well designed. The viscous boundary layer is relatively thin and does not significantly affect the engine output. The gas is approximately 2500 K near the nozzle throat and is vibrationally active because the characteristic vibrational temperature for the bending mode of water is 2438 K. The other vibrational modes are only marginally active and have characteristic temperatures 5261 and 5404 K. As the gas expand, the gas cools and vibrational modes become less active. Consequently, the ratio of specific heats varies from 1.19 at the nozzle throat to 1.30 near the centerline at the exit plane. Such real gas effects have an impact on the exit plane properties. The actual area-weighted average exit plane properties from the simulation are compared to those predicted for a 1-D expansion of a perfect gas in Table 4.1.2.

Table 4.1.2. Average exit plane properties for a simulated nozzle compared to those predicted for a quasi 1-D expansion of a perfect gas.

	Ma	ρ [kg/m³]	P [Pa]	T [K]	V [m/s]	Thrust [N]
Perfect Gas	5.03	1.09×10^{-3}	265	589	2,992	13353 N
Simulated	4.41	1.04×10^{-3}	418	869	3,048	13070 N

Partial activation of the vibrational modes has a large effect on the gas temperature at the exit plane. The perfect gas calculations assumed a constant ratio of specific heats of 1.30 and relatively little energy is stored in vibrational modes. For real gases, some energy is stored in the vibrational modes, and this extra energy helps keep the gas warmer as it expands. Consequently, the exit plane Mach number is lower for the simulated engine than what was predicted for a perfect gas. The mean density and velocity, and therefore thrust, are relatively unaffected by real gas assumptions. The thrust of the actual LMDE is typically reported in pounds and is expected to be 3000 lbf. The thrust for the simulated engine is 2938 lbf, indicating that the simulated and actual engines are comparable.

Section 4.2. Near Field Plume Flow

The near field plume flow is computed with DPLR, and the effects of nozzle geometry and continuum breakdown are evident in Figure 4.2.1. The compression wave that originates within the nozzle reflects off the nozzle axis approximately one nozzle length downstream of the exit plane. In the far field, the streamlines are expected to be linear because pressure gradients in the radial direction are small. Within the first 3 nozzle diameters, the streamlines are deflected as they are processed by the incident and reflected shocks. Although relatively weak, these shocks can result in small irreversible losses of stagnation pressure.

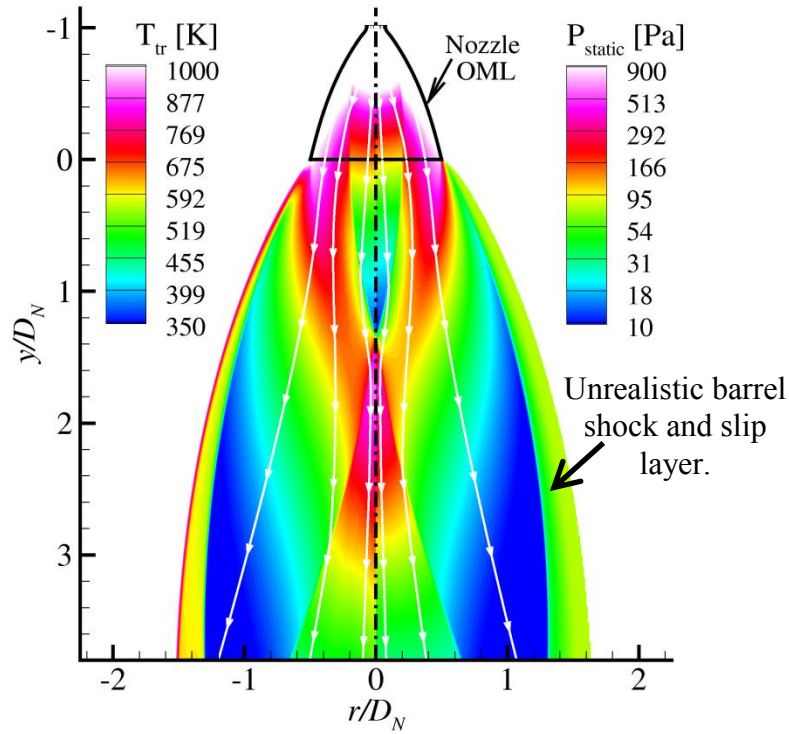


Figure 4.2.1. Contours of temperature (left half) and pressure (right half) in the near field of the plume expansion.

The background atmosphere on the moon is negligible and the exhaust gases expand to vacuum and a barrel shock should not form. The solver, DPLR, assumes a background pressure and had difficulty accommodating vacuum boundary conditions. Consequently, DPLR incorrectly predicts the formation of a barrel shock and a kinetic solver must be used.

4.2.2. EFFECTS OF TURBULENCE

The Reynolds numbers can exceed 200,000 (see Table 3.1.1) within the nozzle and the flow may transition from laminar to turbulent. To assess the effects of turbulence, a second case is run in which the nozzle flow is assumed to be fully turbulent and the Baldwin–Lomax model is used. Density and velocity profiles taken 2 m

downstream of the nozzle are compared for laminar and turbulent conditions, Figure 4.2.2.

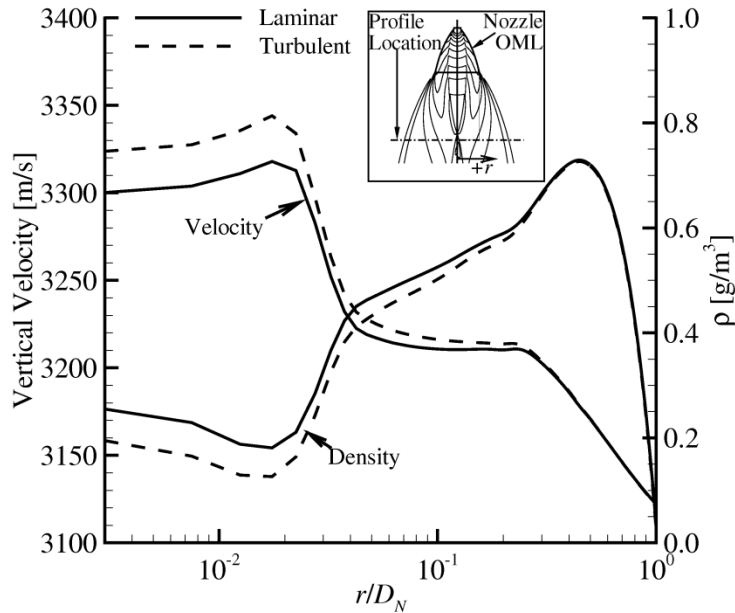


Figure 4.2.2. Slices through the exhaust plume 2 m downstream of the nozzle exit plane. The dashed lines are fully turbulent solutions and the solid lines are laminar solutions. Note the logarithmic x-axis.

The effects of turbulence within the nozzle are confined to the boundary layer. The turbulent boundary layer is slightly thicker and results in the internal nozzle shocker structure shifting slightly because of the increased displacement thickness. Downstream of the exit plane, the effects of turbulence are only observed near the axis of symmetry. Note that a logarithmic scale is used in Figure 4.2.2 to magnify the differences near the axis and that the differences between the laminar and turbulent solutions are negligible where the hybrid interface will be drawn at $r/D_N = 0.5$.

Slightly further downstream, 3.5 m from the exit plane, the differences between the turbulent and laminar solutions are negligibly small, Figure 4.2.3. Near the bottom

cap of the cylindrical hybrid interface, the turbulent and laminar solutions match. Therefore only the laminar continuum solution is coupled to the DSMC solver.

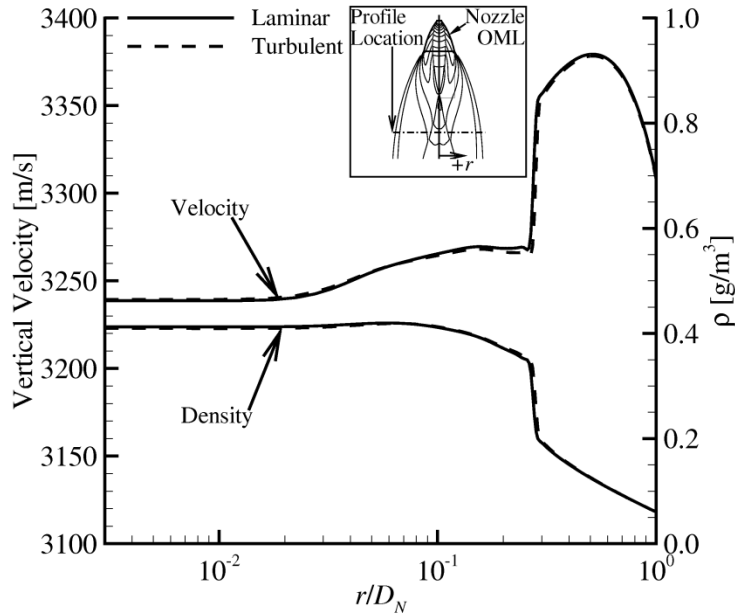


Figure 4.2.3. Slices through the exhaust plume 3.5 m downstream of the nozzle exit plane. The dashed lines are fully turbulent solutions and the solid lines are laminar solutions. Note the logarithmic x-axis.

4.2.3. CONTINUUM BREAKDOWN AND HYBRIDIZATION

The continuum solution is loosely coupled to the kinetic solver and consequently the interface must be drawn where the interface normal Mach number is supersonic and the continuum assumptions are valid. Bird's continuum breakdown parameter, P in equation 3.2-1, is used to check where the continuum assumptions begin to fail. For expansion flows, it is recommended in Bird (1994) that a continuum solver be used only for $P \leq 0.02$. The breakdown parameter, gas mean free path, and hybrid interface are shown in Figure 4.2.4. The breakdown parameter is large along the periphery of the expansion and within the nozzle compression wave, but still less than 0.01 everywhere within the barrel shock. Consequently, the hybrid interface is drawn well within the

barrel shock where the flow is not affected by the background pressure. When the engine is throttled to a lower thrust, the location of the barrel shock moves towards the axis because the plume pressure is lower. This effect is taken into account when constructing hybrid interfaces for lower thrust engines.

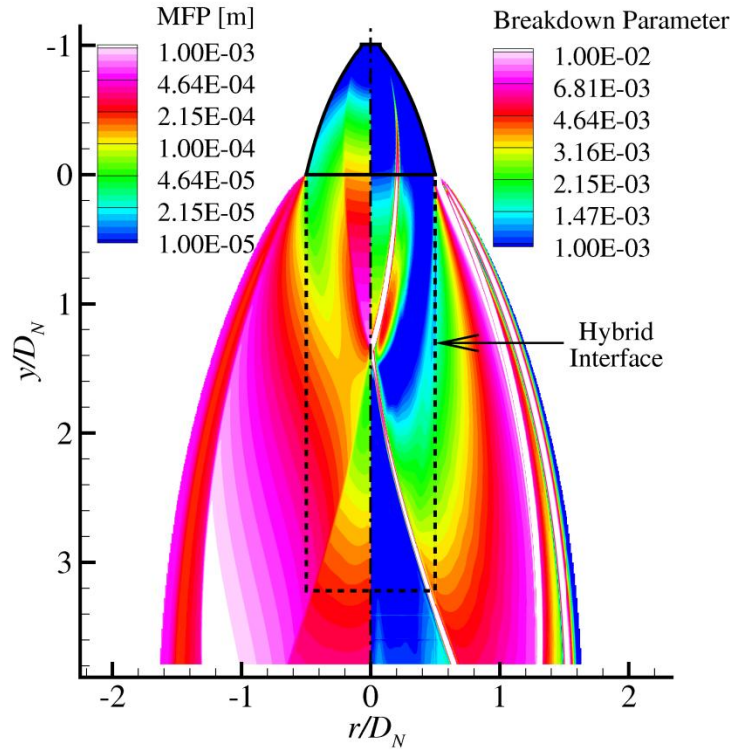


Figure 4.2.4. Contours of the gas mean free path (left), Bird's breakdown parameter (right), and the hybrid interface (dashed line). The hybrid interface is drawn within the barrel shock and where the breakdown parameter is small.

Since the continuum solver only affects the kinetic solver, it would be desirable to create a hybrid interface where the interface-normal Mach number is supersonic. The Mach number in the direction of the jet axis is supersonic everywhere in the exhaust plume. The interface normal Mach number along the length of the hybrid interface is slightly subsonic, on average equal to 0.78. Despite the interface normal Mach number

being subsonic, the hybrid and continuum solutions agree well in the overlap region. In the expanding region, the flow is largely inviscid and differences in the transport coefficients between the DSMC and continuum solvers do not significantly affect the flow. The hybrid solution to the expanding flow is compared to the DPLR solution. Excellent agreement is obtained in the continuum overlap region for the static pressure in Figure 4.2.5. Gray dashed line contours of the DPLR solution are superimposed over the hybrid solution to illustrate the subtle differences. Notice how the DSMC solution lacks the barrel shock and flow expands to the low pressure of the surrounding vacuum.

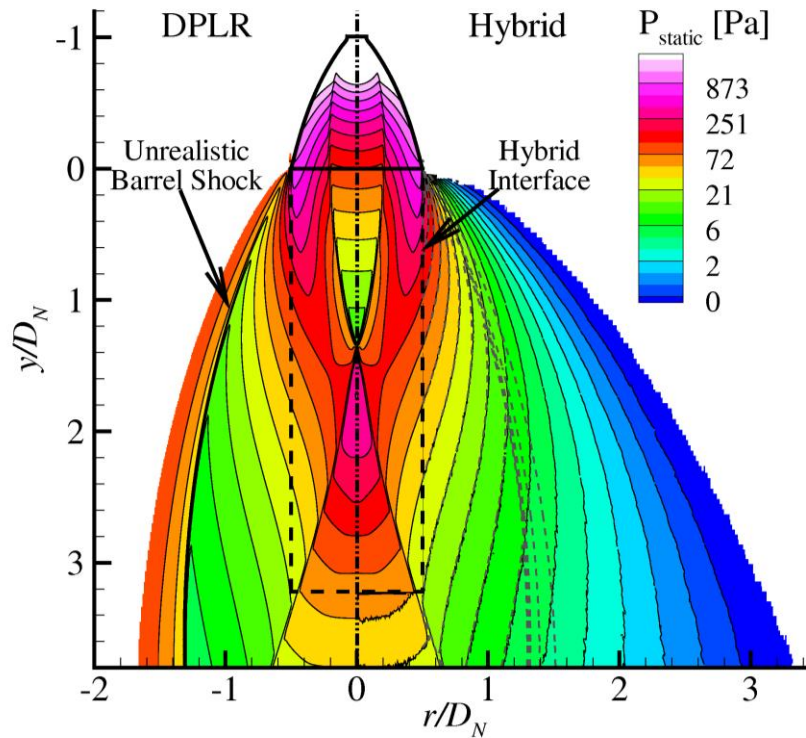


Figure 4.2.5. Contours of gas pressure for the plume flow field for (left) DPLR solutions and (right) hybrid solutions. Line contours from the DPLR solution are superimposed on the hybrid solution to illustrate differences.

Although there is excellent agreement in the density, pressure, and temperature, there are differences in the vibrational temperature, shown in Figure 4.2.6, because of vibrational non-equilibrium.

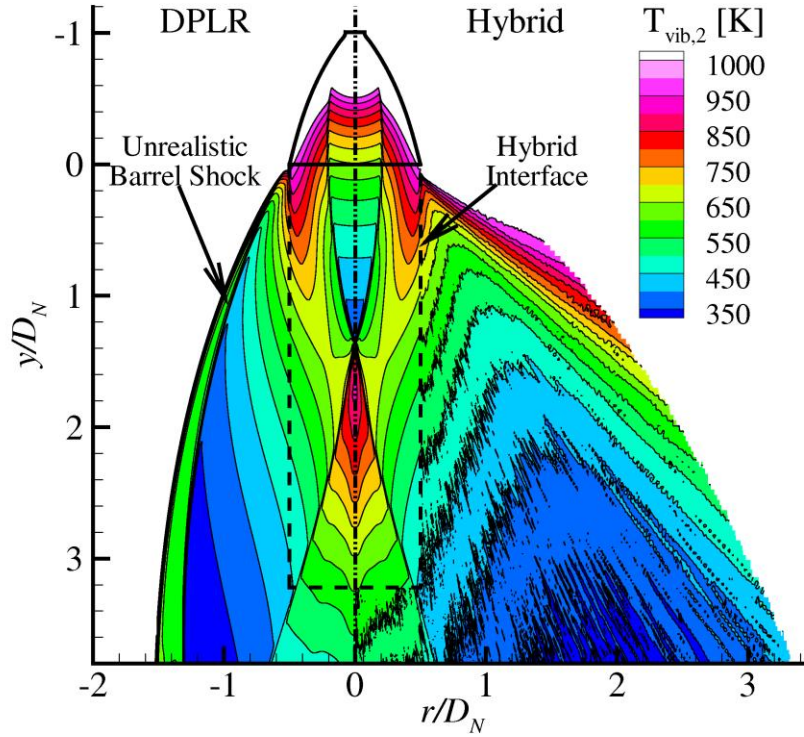


Figure 4.2.6. Vibrational temperatures showing non-equilibrium for the bending mode of water computed with DPLR (left) and the hybrid solver (right).

Vibrational energy ‘freezes out’ where the collision rates are small near the periphery of the expansion. This result also suggests that the assumption that the vibrational and translational modes are equilibrated may not be valid within the continuum regime. Although DPLR has the ability to model vibrational non-equilibrium via a two temperature model, the vibrational relaxation rates for water have gross errors. This appears to occur because the vibrational relaxation rate is computed

using the Millikan and White correlation (Wright, Candler, & Bose, 1998), which under predicts vibrational relaxation times for H_2O - H_2O collisions.

Section 4.3. Plume Impingement

4.3.1. VARIATIONS WITH HOVERING ALTITUDE

The plume structure and thus surface properties depend on the altitude of the lander. The onset of dust erosion was reported at various altitudes for the different Apollo missions, and range from 20–50 m. In this work, the altitude of the descent vehicle was varied from 20 to 2 m, or 15.2 to 1.5 nozzle diameters. The plume impingement flow field for an engine hovering at 20 m is shown in Figure 4.3.1.

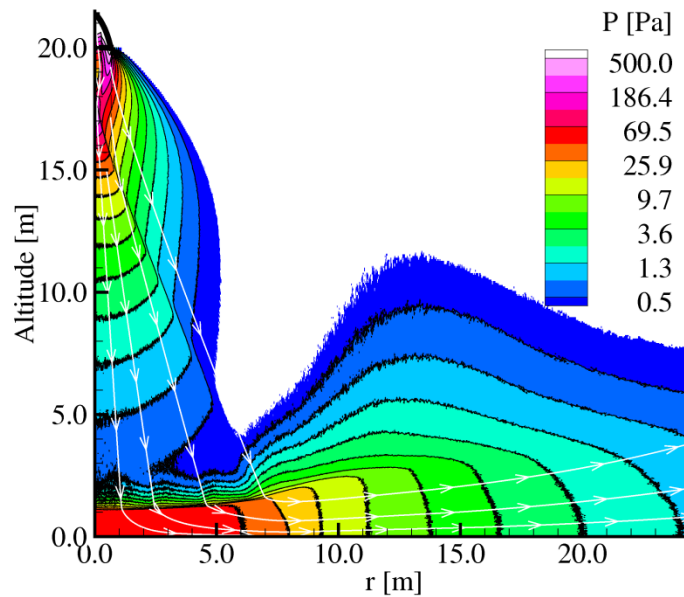


Figure 4.3.1. Contours of gas pressure and streamlines for a rocket engine hovering 20 m above the lunar surface.

To obtain smooth contours of pressure, 5,000 independent samples were averaged. The surface shock standoff distance is 1.0 m when the rocket engine hovers 20 m above the ground. The surface shock has a nearly constant standoff distance out to

where the reflected nozzle oblique shock impinges on it, approximately 6 m from the jet axis. The surface shock has a mean upstream Mach number of 9.8 and has a noticeable thickness. The waves that form at the shock front appear steady and may be an artifact of discretization when coupling the continuum to the kinetic solver.

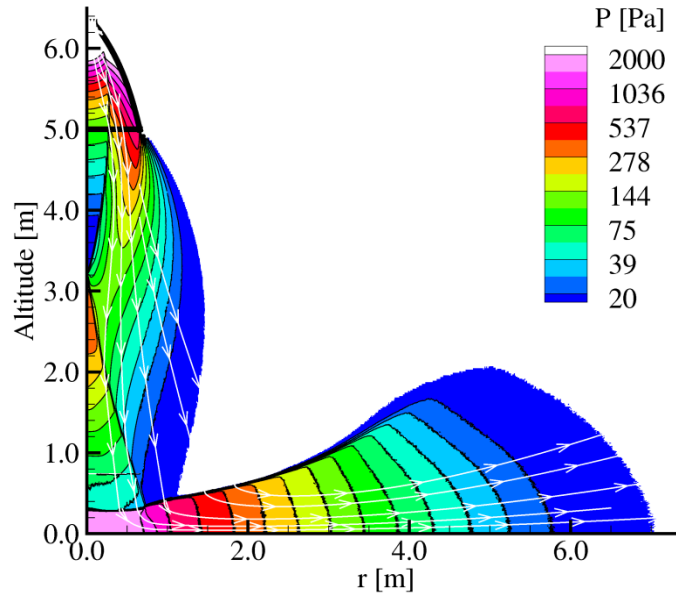


Figure 4.3.2. Contours of gas pressure and streamlines for a rocket engine hovering 5 m above the lunar surface.

As the engine descends to lower altitudes, but above 2.5 m, the flow structures remain qualitatively similar. The surface shock thickness and standoff distance decrease as the lander approaches the surface. The Mach number slightly upstream of the surface shock also decreases because the plume is not as expanded. This trend, where the shock standoff distance and Mach number concurrently decrease, is the exact opposite of what one would expect for bow shock standoff on a blunt body. This phenomenon shown in our simulations has also been experimentally observed in (Vick & Andrews, 1966). When the rocket engine hovers 5 m above the surface, Figure 4.3.2, the shock standoff

distance is 0.24 m, and the reflected oblique nozzle shock impinges upon the surface shock 0.75 m from the jet axis. This shock-shock interaction causes a slight upwards deflection in the surface shock.

4.3.2. NOZZLE GEOMETRY EFFECTS

When the lander descends to an altitude only 2 m above the surface, the flow field changes abruptly, as shown in Figure 4.3.3. The surface shock at higher altitudes is nearly parallel to the surface, but at an altitude of 2 m, the surface shock comprises both normal and oblique components. The hybrid interface is repositioned to the nozzle exit plane to avoid interacting with the complex surface shock structure.

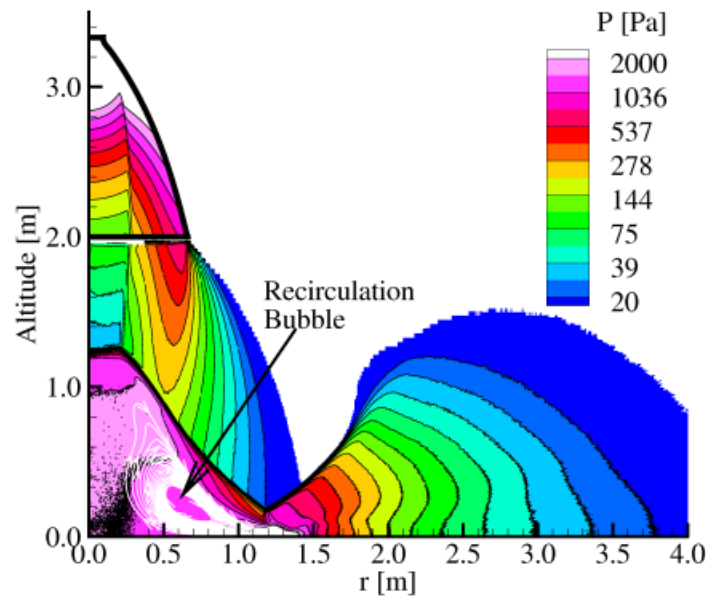


Figure 4.3.3. Pressure contours of the gas flow field when the lander hovers 2 m above the surface.

Without the presence of the surface, the nozzle compression wave would reflect across the symmetry axis 1.8 m from the nozzle exit plane. In the higher hovering altitude cases, shown previously, the shock reflection occurs well above the surface shock

and the gas pressure immediately upstream of the surface shock is highest along the jet axis. At lower altitudes, the ground prevents the shock reflection from occurring and the gas pressure just upstream of the surface shock is lowest near the jet axis. To obtain a nearly constant pressure downstream of the shock wave near the stagnation point, the near-axis gas flow needs to be processed by a strong normal shock and the higher pressure gas further off-axis must be processed by a weaker oblique shock. The interaction between the ground and the shocks that develop within a contoured nozzle are responsible for the surprising structure observed at low hovering altitudes. These features may change if different nozzle geometries are used. The recirculation bubble near the stagnation point can occur because of vorticity that is generated as the flow passes through the surface shock system. The normal and oblique shocks have different strengths and therefore create entropy gradients. From Crocco's theorem (Anderson, 2003), an adiabatic flow with gradients in entropy generates vorticity.

The large recirculation bubble that forms under the lander can significantly affect the dust dynamics, as vorticity tends to mix higher momentum fluid into the ground and increase erosion. During several of the Apollo landing videos, a large discharge of dust is observed at approximately the same time as when the contact probe touches the ground. The contact probes extended nearly 1.7 m below each footpad and the nozzle exit plane was 2.18 m above the surface at first contact. It has previously been suggested (Metzger, Smith, & Lane, 2011) that the large puff of dust occurred because the contact probe scraped across the ground. These results suggest that there may be a fluid dynamic reason instead because the flow transitions to the state with the large vortex at approximately the same altitude as when the contact probe struck the ground. Vortices can increase the erosion rate because they mix the boundary layer, driving high energy fluid containing recirculating debris into the ground (Zheng, 2009).

Nozzle geometry effects can also be seen in the plume structure, shown in Figure 4.3.4, when the lander hovers at higher altitudes. Near the exit plane, the contoured nozzle's plume has a larger spreading angle than the case with uniform exit properties. This is expected because the contoured nozzle produces a mean outward radial velocity at the exit plane.

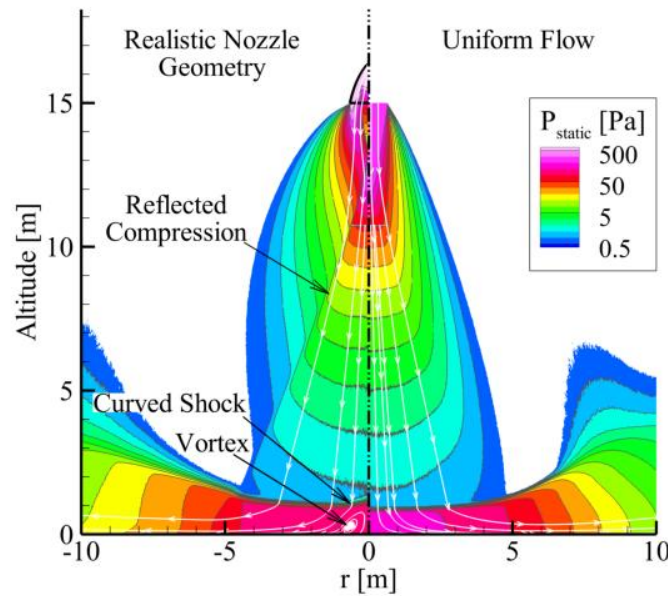


Figure 4.3.4. Contours of gas pressure comparing rocket exhaust plumes from a contoured nozzle (left) and assumed uniform exit-plane properties (right).

The core of the contoured nozzle exhaust plume, the area within the reflected compression wave, appears very similar to the uniform flow simulation. Despite these qualitative similarities, the flow beneath the surface shock is slightly different. A weak vortex forms near the stagnation point when a contoured nozzle geometry is simulated and this vortex does not appear when uniform exit-plane properties are assumed. The properties of the gas reflected off the surface also change in response to different nozzle geometries. Since the plume from a contoured nozzle is broader than that of uniform

flow, the rebounding gas sees a higher plume pressure and is pushed radially outwards. The radial pressure gradient along the surface is also reduced when a contoured nozzle is simulated. This is also expected for a broader plume.

Section 4.4. Gas Properties Near the Surface

The erosion and entrainment of dust depend on the gas flow near the lunar surface. In this section, the near-surface gas properties are evaluated without the presence of dust. These results change when dust is included because the gas is fully coupled to the dust.

4.4.1. COMPRESSIBLE STAGNATION POINT FLOW AND BOUNDARY LAYERS

We examine in detail a case of 5 m hovering. A boundary layer develops on the lunar surface as the gas is turned radially outward. Boundary layer profiles are shown at various locations along the surface in Figure 4.4.1. Near the stagnation point, the flow is subsonic and the boundary layer is approximately 5 cm thick. Further from the wall the flow transitions to supersonic and the boundary layer begins to rapidly grow. At a distance 5 m from the axis, which corresponds to $r/h=1$, the free stream gas flow is supersonic and the boundary layer is approximately 0.2 m thick. At even further distances from the jet axis, the boundary layer rapidly thickens because the top edge of the wall jet is no longer confined by the isentropic core of the exhaust plume, as shown in Figure 4.4.2.

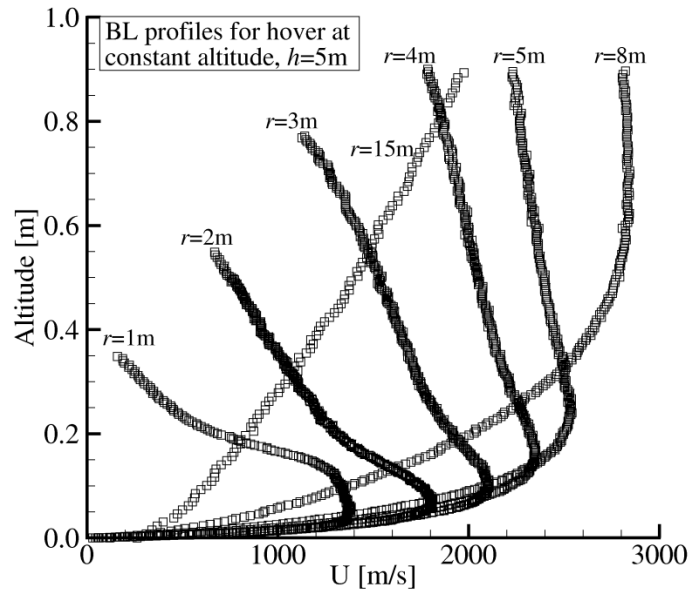


Figure 4.4.1. Boundary layer profiles at different locations in the near field when a rocket engine hovers 5 m above the surface.

Past 10 m from the jet axis, the free stream gas velocity asymptotes to a nearly constant speed of 3000 m/s. As the gas becomes increasingly rarefied the slip velocity also increases. At a distance 30 m from the jet axis, the slip velocity is approximately 600 m/s. The boundary layer also rapidly thickens and becomes nearly 6 m thick at a location 25 m from the jet axis. The thickening of the boundary layer is significant because it provides a mechanism for which dust to be entrained into the flow. If the boundary layer did not grow, the gas velocity would be nearly tangent to the surface; consequently the dust particles would not attain an appreciable vertical velocity and hence would not become fully entrained into the flow.

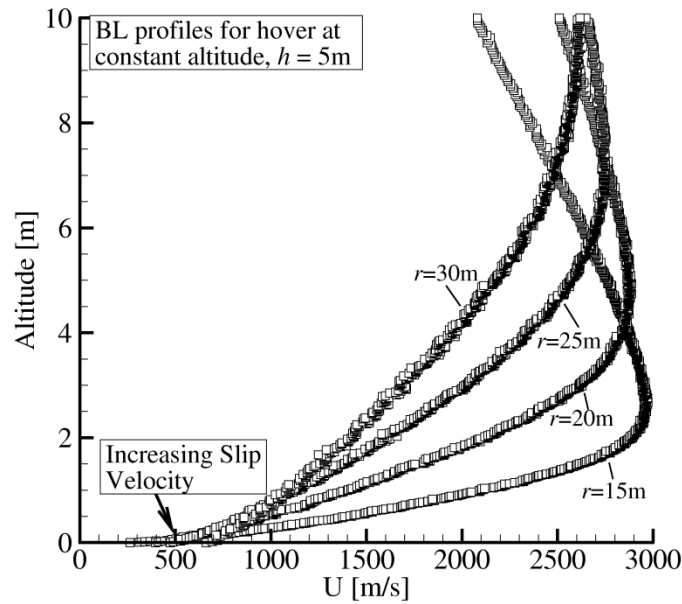


Figure 4.4.2. Boundary layer profiles at distances further from the jet axis when a rocket engine hovers 5 m above the surface. Notice the change in scales from Figure 4.4.1.

Figure 4.4.3 shows the thermal boundary layers at different distances from the jet axis when a rocket engine hovers 5 m above the ground. The free stream gas temperature is hottest near the stagnation region and is approximately 2500 K. The gas temperature then cools as the wall jet expands outwards.

The surface temperature of the moon has a large range that depends on latitude and whether it is exposed to sunlight. On the dayside, the mean surface temperature is approximately 375 K. Our simulations assume a surface temperature of 350 K. The simulations here neglect the localized surface heating caused by the rocket plume impingement. This process is complicated because as heat is transferred to the surface from the rocket exhaust, thermal energy is also removed as the loose particles are eroded, thus exposing colder layers of regolith.

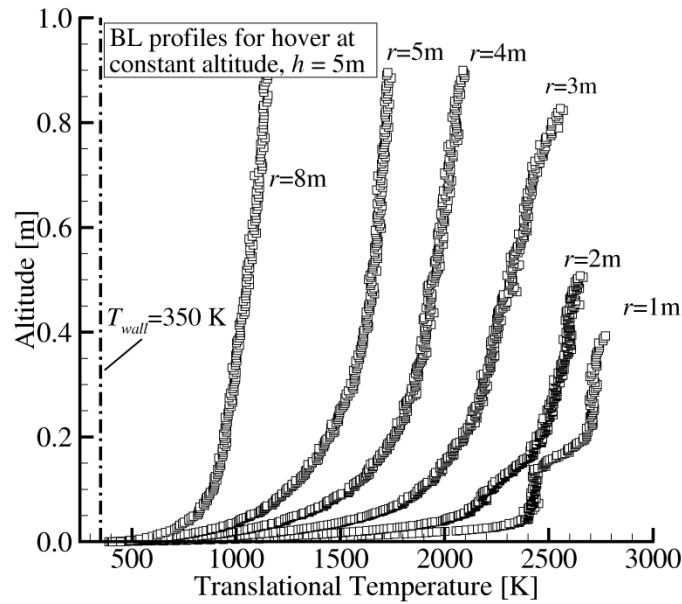


Figure 4.4.3. Thermal boundary layer profiles at different locations when a rocket engine hovers 5 m above the surface.

The heat transfer from the gas to the surface is shown in Figure 4.4.4 and was obtained by doing an energy balance on gas molecules that strike the surface with an assumed constant temperature of 350 K. The peak heat flux occurs 0.5 m from the jet axis and is approximately 400 kW/m^2 when the surface temperature is held constant at 350 K. This is a significant amount of energy that would rapidly heat the surface near the stagnation point. In reality, the heat flux would be reduced because the surface temperature will increase as the lander approaches the surface and due to erosion of the regolith. In future work, a more sophisticated thermal model that allows for the surface to warm should be used.

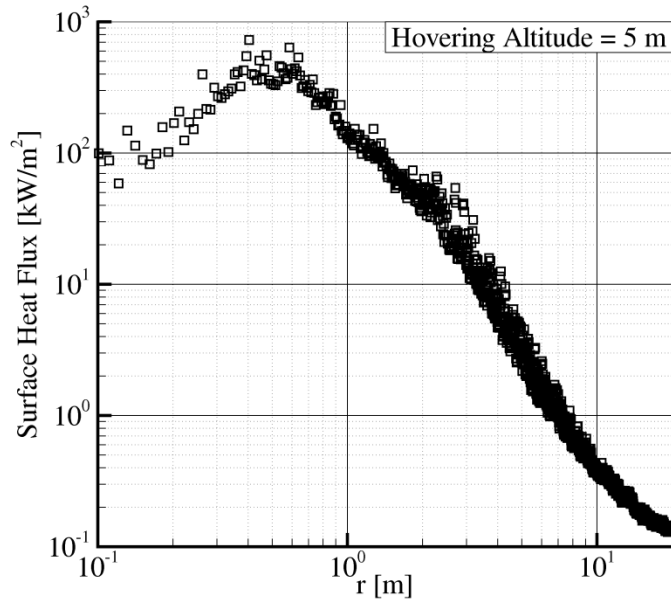


Figure 4.4.4. Heat flux from the gas to an isothermal lunar surface with an assumed surface temperature of 350 K. Note the log-log scales.

Boundary layer profiles are compared at radial distances 5 m and 20 m from the jet axis for a set of different hovering altitudes in Figure 4.4.5 and Figure 4.4.6. As the lander descends from 20 to 2.5 m, the free stream velocity 5 m from the jet axis increases from 800 to 3000 m/s. This occurs because the exhaust plume footprint is larger at higher hovering altitudes and the region of subsonic flow behind the surface shock extends further from the jet axis, see Figure 4.3.1. Despite differences in the free stream velocities, the boundary layer thickness 5 m from the axis is comparable for hovering altitudes between 2 and 20 m. This observation is also consistent with what was simulated by (Tosh, Liever, Arslanbekov, & Habchi, 2011). At distances further from the jet axis, $r \gg h$, the boundary layer profiles are similar because the wall jet appears to originate from a point source at the landing site. The simulation data are expected to

collapse for different hovering altitudes when the radial distance from the plume axis is much greater than the hovering altitude, and this is seen in Figure 4.4.6.

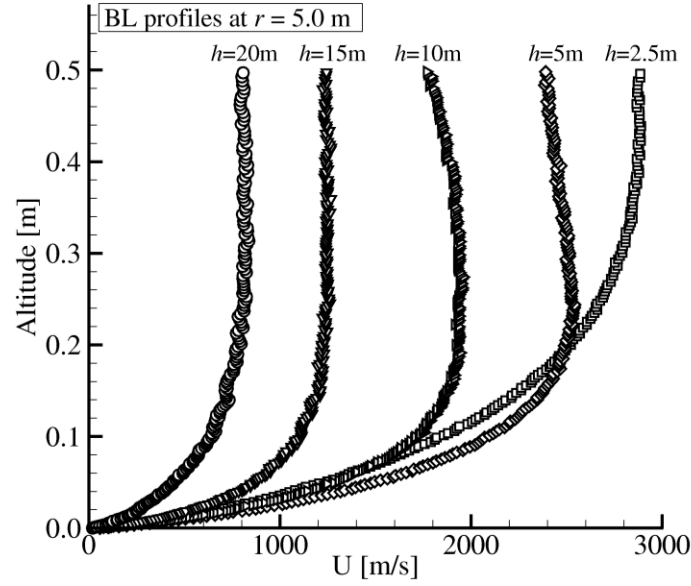


Figure 4.4.5. Boundary layer profiles 5 m from the jet axis for different hovering altitudes.

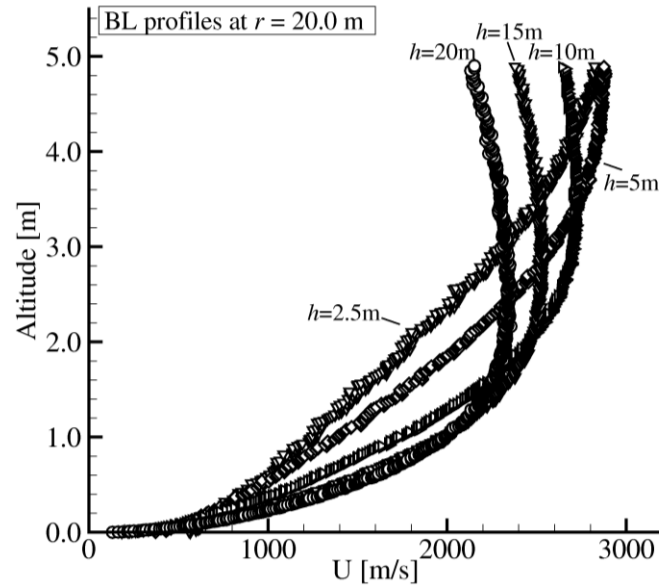


Figure 4.4.6. Boundary layer profiles 20 m from the jet axis for different hovering altitudes.

4.4.2. SURFACE STRESSES AND EROSION RATES

The surface stress is an important quantity that is useful for predicting the erosion rate. For a smooth surface, the shear stress is obtained by measuring the change in the momentum flux of the gas molecules that strike it. The actual lunar surface is quite rough, however, because of hypervelocity meteorite impacts. In (Roberts, 1966), the surface was assumed to be rough and the stress was computed from the dynamic pressure of the smooth surface and an assumed drag coefficient of 0.2. Our approach is similar, and the surface stress is computed from the dynamic pressure sampled at a chosen roughness scale height above the surface. The roughness scale height is arbitrarily chosen and can affect the shape of the erosion profile. The dynamic pressure, normalized by the peak value, was sampled 2, 5, and 10 cm above the surface and these resultant profiles are plotted in Figure 4.4.7. The surface stress distribution for laminar flow over a smooth wall is also shown for comparison on the same figure.

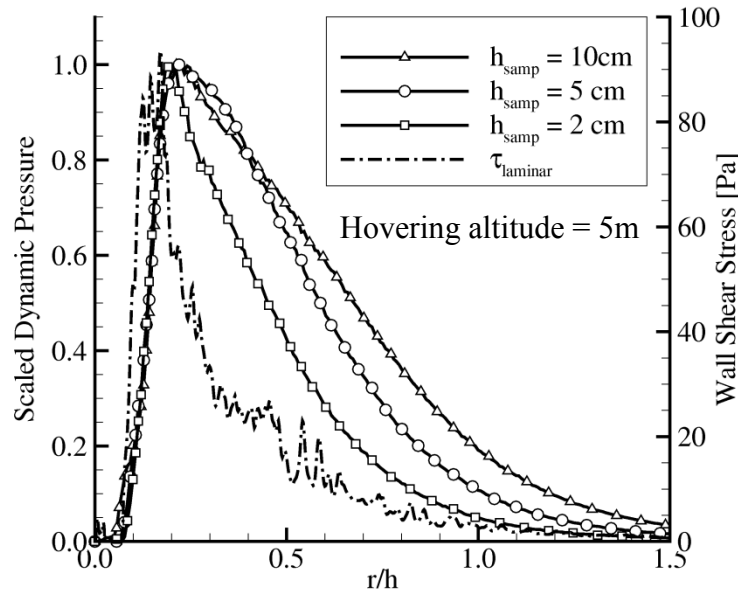


Figure 4.4.7. Dynamic pressure profiles sampled at roughness scale heights of 2, 5, and 10 cm above the surface. The profiles are normalized to highlight differences in profile shape. The laminar shear stress, dash-dotted line, is plotted on the right axis.

The height at which the dynamic pressure is sampled affects the shape of the dynamic pressure distribution outboard of the peak. When sampled closer to the ground, the dynamic pressure distribution tends to be more narrow and becomes increasingly similar to the smooth wall shear stress profile. The maximum value for the shear stress computed for laminar flow over a smooth wall is 92 Pa. The recommended value for the cohesive stress of the soil, measured from Apollo samples, exceeds the maximum value of the smooth wall shear stress and varies between 100 and 1000 Pa, (Heiken, Vaniman, & French, 1991). Erosion models (Bagnold, 1941) predict erosion to begin when the surface shear stress exceeds the cohesive stress of the soil. When hovering 5 m above the surface, the smooth wall shear stress would apparently not be sufficient to cause erosion; contradictory to what was observed during the Apollo landings.

The erosion rates used herein are computed from scaling arguments which suggest that the erosion rate scales linearly with densimetric Froude number, see Section 3.3.2. Since the soil properties and gravity are assumed constant throughout a landing, the erosion rate is therefore proportional to the gas dynamic pressure at some height. The dynamic pressure distributions, shown in Figure 4.4.8, change as the lander approaches the lunar surface.

As the lander descends to lower altitudes, the location of peak dynamic pressure shifts towards the jet axis while the peak dynamic pressure increases. The dynamic pressure distributions collapse at distances far from the jet axis, $r \gg 20$ m. This feature is consistent with the boundary layer profiles far from the jet axis, Figure 4.4.6, and occurs for reasons previously mentioned. Although the peak dynamic pressure decreases at higher altitudes, the erosion area increases because of the increased impingement footprint.

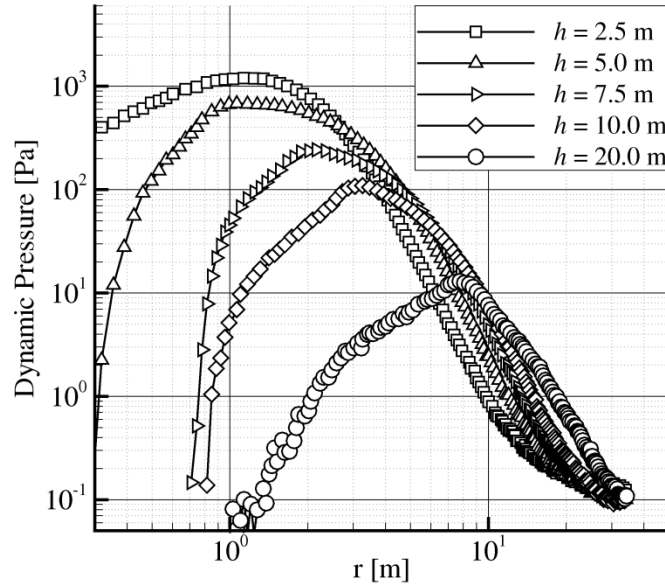


Figure 4.4.8. Dynamic pressure distribution computed at a roughness height 5 cm above the lunar surface for rocket engines hovering at different altitudes. Note the log-log scale.

Roberts developed a theory for predicting the surface stresses and derived scaling relationships that collapse the dynamic pressure profiles, see Section 2.3.1. To collapse the data, the dynamic pressure is scaled by the pressure at the stagnation point and the radial position is scaled by the nozzle hovering altitude. For the conditions of our simulated engine, Roberts theory predicts that the peak dynamic pressure is $e^{-1}P_0$ and that location of peak shear stress occurs at $r/h = 0.415$ for all hovering altitudes. These scaling relationships are applied to the data at different hovering altitudes, and the dynamic pressure distributions are compared to Roberts values in Figure 4.4.9.

The scaling relationships collapse the data reasonably well at hovering altitudes below 10 m. At higher hovering altitudes, the simulated peak dynamic pressure is significantly less than what was predicted by Roberts theory. This is expected because

at higher altitudes, the location of peak dynamic pressure occurs farther from the jet axis and the boundary layer is thicker. The peak dynamic pressure for higher hovering altitudes is thus sampled deeper within the boundary layer, resulting in lower values. Roberts theory did not take into account such effects because he neglected the formation of the boundary layer. In addition, the location of peak dynamic pressure is not constant, as Roberts theory would suggest. At lower hovering altitudes, the location of peak dynamic pressure shifts towards the symmetry axis.

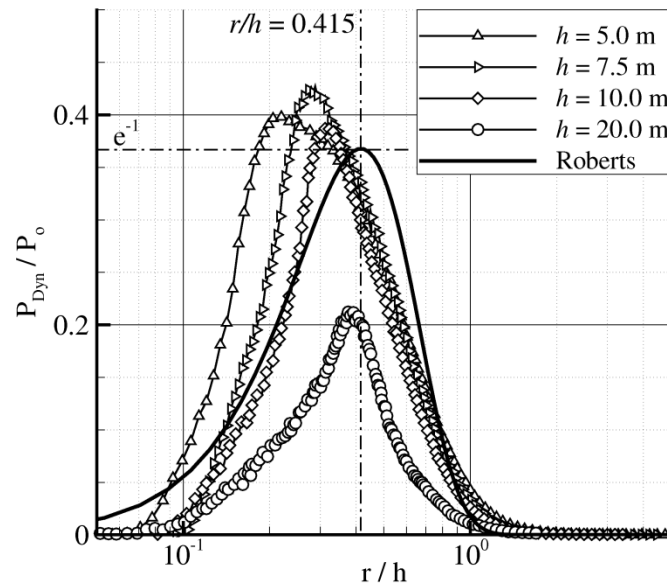


Figure 4.4.9. Scaled dynamic pressure distribution for different hovering altitudes compared to Roberts theory.

The location of peak dynamic pressure is plotted against hovering altitude normalized by the nozzle diameter in Figure 4.4.10. The location of peak dynamic pressure, and thus erosion, asymptotes towards a constant value at high altitudes that is in good agreement with Roberts theory. Significant differences are observed at lower altitudes, where the erosion rates are higher. At hovering altitudes above 2.5 nozzle

diameters, the location of peak shear stress is much closer to the axis than Roberts predicts. Roberts theory was derived from a plume flow field that originated from a point source at the nozzle exit plane. From Figure 4.3.2, the plume flow appears to originate from a point source located where the nozzle compression wave intersects the symmetry axis, approximately 1.8 m below the exit plane. Roberts also neglected the surface shock standoff distance, which is 0.24 m for a rocket hovering at an altitude of 5 m. A better fit for the data can be obtained by adding a correction term that accounts for the surface shock and near field plume structure.

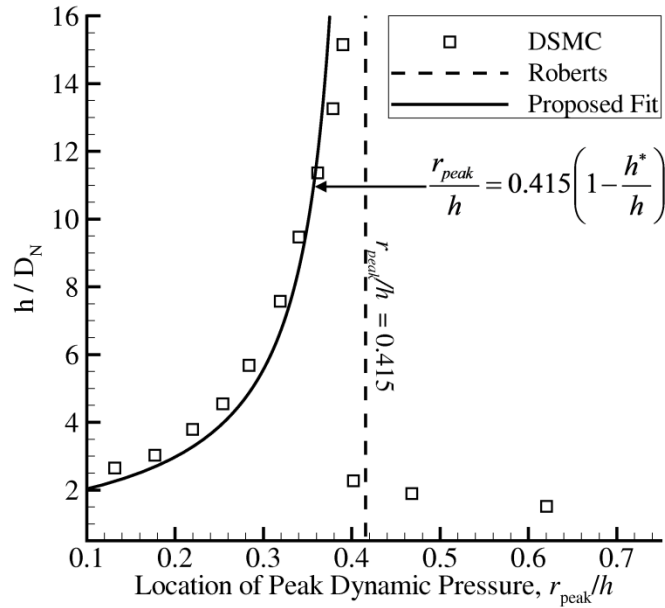


Figure 4.4.10. Location of peak dynamic pressure versus hovering altitude. DSMC results, symbols, Roberts theory, dashed line, and a proposed better fit, solid line, are shown for comparison.

Instead of scaling the radial distance from the jet axis by the hovering altitude, a better fit can be obtained by scaling by an effective hovering altitude, $h_{eff} \equiv h - h^*$, a virtual origin. The correction term, h^* , is the sum of surface shock standoff distance and the

distance from the nozzle exit plane to where the nozzle compression wave intersects the jet axis. The correction term for the simulated nozzle is 2.04 m. This scaling performs reasonably well at capturing the trends at lower hovering altitudes, and asymptotes to Roberts theory for higher hovering altitudes. Problems still remain when the engine descends within 2.5 engine diameters of the surface. A suitable scaling is not expected in this region, because the surface stresses are likely dependent on the complex nozzle flow and a relevant length scale is not obvious.

Roberts theory does a very good job at predicting the scaled peak dynamic pressure sampled 5 cm above the lunar surface, as seen in Figure 4.4.11. This is surprising because the dynamic pressure is sampled within the boundary layer, which was neglected by Roberts. Roberts identified two classes of impinging flow when computing the impingement pressure and maximum shear stress. The first class occurs when the rocket engine is near the surface and the scaled maximum dynamic pressure is constant for all lower hovering altitudes. The second occurs at higher hovering altitudes, and the maximum scaled dynamic pressure decreases as h^{-2} . The interface between these two regimes is recommended by Roberts to occur at $h/D_N = 0.219$ for the simulated nozzle conditions. Our simulations show that for higher hovering altitudes, the scaled dynamic pressure decays more rapidly than Roberts predicts, decreasing as $h^{-2.825}$. This accelerated decay of the peak dynamic pressure may occur because of the growth of the boundary layer, as discussed previously.

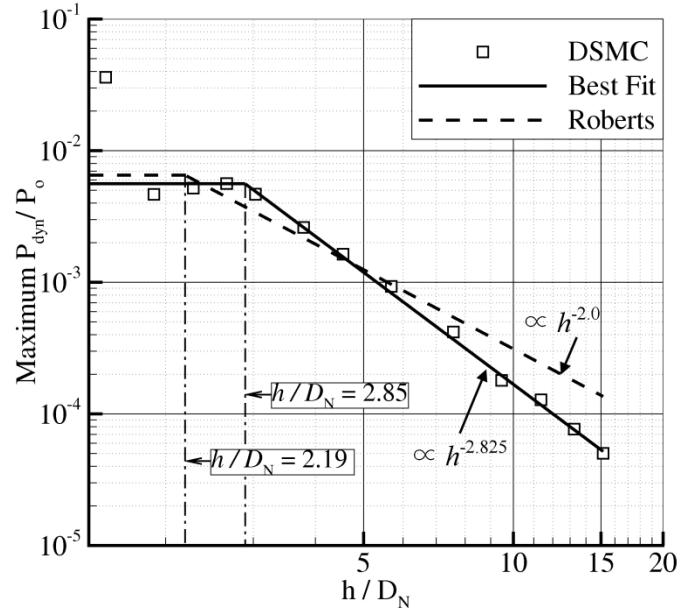


Figure 4.4.11. Maximum value for the gas dynamic pressure scaled by the pressure at the stagnation point. The symbols are DSMC, dashed line is Roberts theory, and the solid line is the numerically determined best fit.

The erosion rates, in this work, are proportional to the dynamic pressure and are shown in Figure 4.4.12 for multiple hovering altitudes. The location of peak erosion collapses for hovering altitudes above 3.75 nozzle diameters by scaling the radial position by h_{eff} . The expression that predicts the location of peak erosion is obtained by applying a correction term on Roberts theory and is

$$\frac{r_{m,max}}{h} = \sqrt{\frac{2}{\kappa + 4}} \left(1 - \frac{h^*}{h}\right), \quad 4.4-1$$

where κ is the hypersonic parameter, $\kappa = \gamma(\gamma - 1)M_N^2$. The erosion rate increases as the lander descends, as expected, but the peak erosion reaches a nearly constant maximum value of $3 \text{ kg/m}^2\text{-s}$ when the engine is within 2.75 nozzle diameters of the surface.

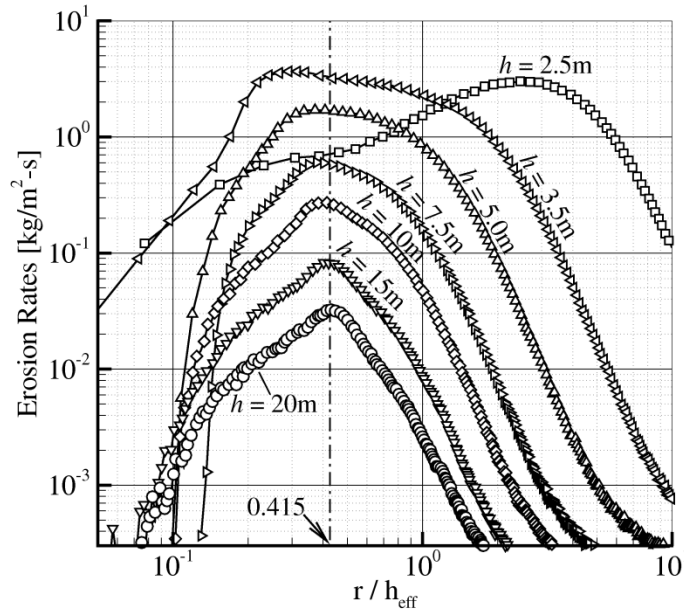


Figure 4.4.12. Erosion rates versus radial position scaled by the effective hovering altitude, h_{eff} , for altitudes ranging from 20 to 2.5 m. Note the log-log scale.

The shock structure drastically changes when the rocket engine is within 2 m of the surface, discussed in Section 4.3.2, and these changes strongly affect the erosion rates. The erosion profiles at hovering altitudes of 2.0 m, where the surface shock structure has changed, and 2.5 m are compared in Figure 4.4.13. For a hovering altitude near 2 m, the surface shock transitions to one with a normal and oblique component. The oblique shock is weaker than the typical normal surface shock that occurs at higher altitudes. Consequently, there is a lower stagnation pressure drop across the oblique shock and more energy in the gas remains available for erosion. The peak erosion rate increases by a factor of 6.8 as the hovering altitude decreases from 2.5 to 2.0 m.

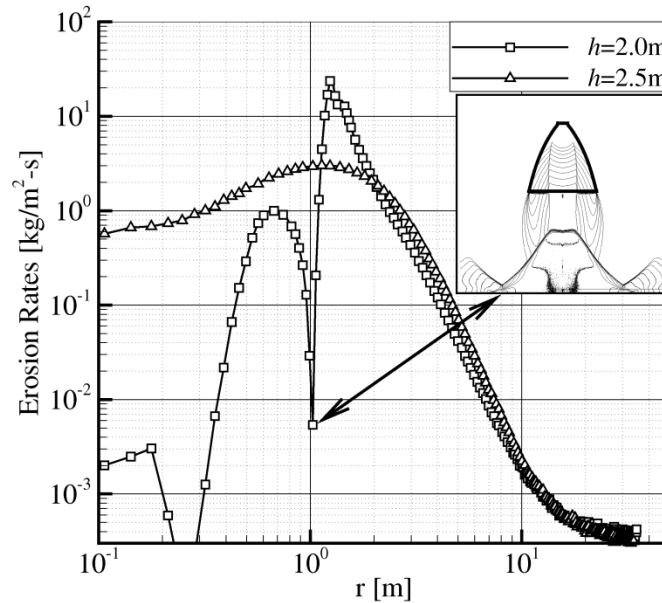


Figure 4.4.13. Erosion profile, square symbols, when the lander hovers 2.0 m above the surface and the surface shock structure transitions from a normal surface shock to an oblique surface shock. The erosion profile when the surface shock is normal at an altitude of 2.5 m, triangles, is drawn for comparison.

The erosion profile for hover at 2.0 m has two peaks. The lower peak occurs under the recirculation bubble, where the rotating fluid near the wall is traveling towards the jet axis. The larger peak occurs past the recirculation bubble where the gas begins to expand radially outward. The deficit in between the two peaks corresponds to the stagnation point where the oblique portion of the surface shock impinges on the ground. The sharp increase in erosion rate is consistent with the sudden discharge of debris that was observed immediately before the Lunar Module landed.

The dynamic pressure distribution determines the shape of the erosion profile, but in order to obtain the erosion rate a suitable scaling constant must be determined. The scaling constant was determined comparing Apollo observations to a crater depth profile computed for an approximate landing trajectory. The crater depth is computed

assuming a bulk soil density of 1500 kg/m^3 and descent rate of 0.75 m/s . The erosion rate is then scaled to give a crater depth that closely agrees with what was observed by Apollo astronauts; a crater that is approximately an inch deep. A scaling parameter was obtained, and the erosion rate is

$$\Phi_e = 0.0025 \left[\frac{\text{s}}{\text{m}} \right] \times \frac{\rho_g U_g^2}{2}. \quad 4.4-2$$

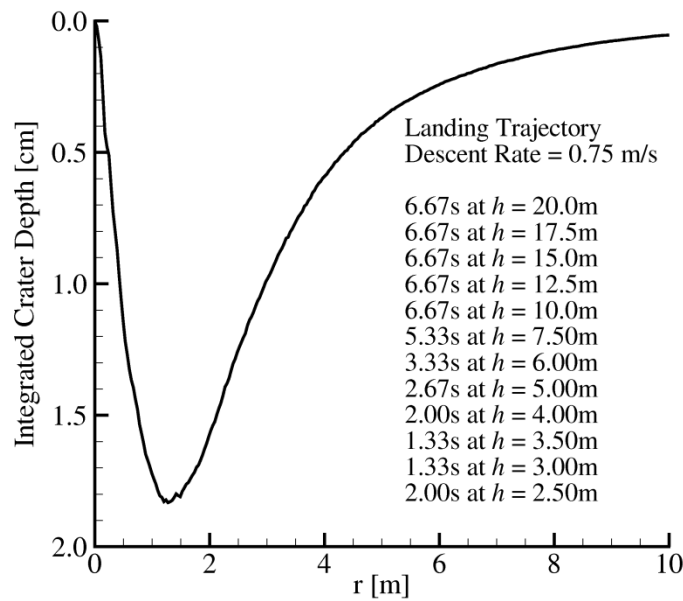


Figure 4.4.14. Integrated crater depth for a lander approaching the surface at 0.75 m/s .

The crater depth will likely change and become more shallow when dust is included because the gas motion is coupled to the dust. The integrated crater depth did not include the lowest hovering altitude at 2.0 m , where we suggest erosion will be enhanced. This altitude was not included because the crater depth does not account for redeposition. This assumption of no redeposition is not valid when dust is entrained into a strong recirculation bubble, and produced anomalous results.

4.4.3. DIFFERENT THRUST ENGINES

Many rocket engines are throttled by adjusting the mass flow rate of propellant. The impinging plume flow field in the near field depends on the gas Mach number, which does not significantly change for different thrust levels. The Reynolds and Knudsen numbers are much less significant because viscous regions are confined to the thin boundary layers and the gas is virtually continuum in the near field. When operating at very low thrust, different internal energy modes can freeze if the collision rate decreases significantly. This can cause the ratio of specific heats and Mach number to change, and can affect the plume flow field. Such non-equilibrium effects were not observed for any simulated thrust levels between 3.3 and 52.3 kN.

The dynamic pressure distributions and erosion rates for different thrust engines collapse when scaled by the engine thrust are seen in Figure 4.4.15.

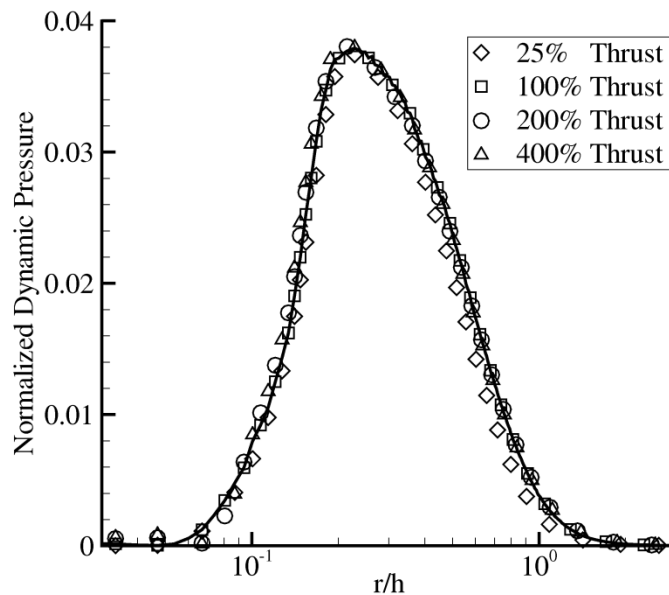


Figure 4.4.15. Gas dynamic pressure sampled 5 cm for different thrust rocket engines hovering 5 m above the surface. The distributions collapse when the dynamic pressure is normalized by the thrust of the rocket engine.

These results show that the dynamic pressure at the surface is linearly proportional to the thrust of the lander when the thrust is throttled by adjusting the mass flow rate. This is expected because the Mach number is the same in each of the different thrust cases and that is the non-dimensional number that most strongly affects the expanding plume flow. The Mach number, however, does not change because the area ratio of the nozzle is the same and the flow at the throat is sonic. Since the erosion rate is proportional to the dynamic pressure, the erosion rate of material is also expected to be linearly proportional to the engine thrust. Roberts theory also predicts that the surface stresses are linearly proportional to the engine thrust.

Section 4.5. Chapter Summary

The internal nozzle flow, near field of the expansion, and impingement on the surface, without the presence of dust, were studied in this chapter. A contoured nozzle geometry, similar to the OML of the Lunar Module Descent Engine, was simulated. A weak shock, characteristic of contoured nozzles, formed within the nozzle expander and a very thin boundary layer developed within the nozzle that did not affect the exit plane flow significantly. The nozzle shock is significant and results in highly non-uniform exit plane density and temperature profiles. This has a significant impact on the plume flow and impingement fields. Within the nozzle, the lowest pressure regions are found near the centerline, where the flow is not processed by the nozzle compression wave. The nozzle shock passes through the exit plane and is turned inward, eventually intersecting the nozzle centerline 1.8 m downstream of the exit plane.

The hybridization between the continuum and kinetic solvers was also discussed. Bird's breakdown parameter was used to ensure that the hybrid interface was constructed where the flow is continuum. After validating the coupling, impinging plume flows on

a normal surface were simulated for a set of hovering altitudes. At altitudes above 2.5 m, a surface normal shock forms as the gas impinges on the surface. The reflected nozzle compression wave can intersect the surface shock, creating subtle distortions. At altitudes lower than 2.0 m, the surface shock structure changes drastically. Vorticity is produced as the gas is processed by the complex surface shock system, and results in a strong recirculation bubble. These results suggest that the recirculation bubble amplifies the erosion and entrainment of dust and offers an explanation of why a sudden burst of dust was observed immediately before touchdown during the Apollo landings.

The surface stresses and erosion rates are also computed for various hovering altitudes. Roberts derived theoretical expressions that predict peak surface stress and the location at which it occurs. Roberts used theoretical reasoning and comparisons to experiment to develop a set of scaling relationships that collapse the data for different hovering altitudes and engine thrust. To collapse the distributions for different hovering altitudes, Roberts scaled the dynamic pressure by the pressure at the stagnation point and the radial position is scaled by the distance from the nozzle exit plane to the ground. Roberts analyses were derived from a simple point source plume flow model that neglected boundary layer and real nozzle effects. These scaling relationships were nonetheless applied to our DSMC simulations and we found that although Roberts theory performs well at high altitudes, there are significant deviations for altitudes below 10 nozzle diameters. Significant improvement can be made to Roberts theory by applying a correction term that takes into account real nozzle effects. Instead of scaling the radial position by the distance from the ground to the nozzle exit plane, better agreement can be found by scaling the radial position by the distance from the top of the surface shock to where the internal nozzle compression wave intersects the jet axis. Roberts also predicted that the peak surface stress decays proportionally to h^{-2} , but our simulations

show that this decay may be too slow if boundary layer effects are important. In this work, the dynamic pressure is sampled at a roughness scale height, which is typically within the boundary layer. At higher hovering altitudes, the boundary layers are thicker at the location of peak erosion. Consequently, the sampled dynamic pressures are less at higher altitudes than what would be predicted if boundary layer effects were neglected. Our DSMC simulations show that the maximum shear stress decays in radius quicker than Roberts theory at higher hovering altitudes, and decreases proportionally to $h^{-2.825}$. The peak shear stress is also shown to agree well with Roberts prediction and is proportional to the thrust of the engine.

CHAPTER 5.

NEAR FIELD DUST SPRAYS

This chapter characterizes the dust sprays that arise during plume impingement on a flat surface. There are several different parameters that are significant to this work, including the particle mass loading and the coefficient of restitution between colliding grains. This chapter first discusses the impact that mass loading and granular collisions have on the resultant flow fields. Next, the effects that lander thrust and altitude have on the dust spray are presented. For each of these cases, the dust flow fields can be treated as quasi-steady because the lander descent is slow compared to the time for dust to convect across the domain.

Section 5.1. Sensitivity to Physical Models

Additional physical models for various processes have been implemented as our simulations matured. This section addresses how the physical models affect the simulation results. The two major additions include fully coupled dust-gas motions and granular collisions.

5.1.1. THE EFFECTS OF GAS-DUST COUPLING

In our early work (Morris, 2010), we assumed that the background gas was unaffected by the dust and particle trajectories were computed using an overlay method. For realistic erosion rates, it was determined that the mass fraction of grains was not negligible and that a fully coupled gas-dust interaction model should be used. To assess the effect of mass loading, we simulate one scenario where the gas is unaffected by the dust and one fully coupled simulation. The uncoupled simulation is discussed first.

In this simulation, a rocket engine hovers 5 m above the surface. A set of 6 discrete grain sizes, 200 nm, 800 nm, 2 μm , 5 μm , and 8 μm , and 11 μm diameter

particles are simulated simultaneously. Particles can interact with each other through inelastic granular collisions with an assumed restitution coefficient of 0.8. The mean radial velocity for different size particles is shown in Figure 5.1.1.

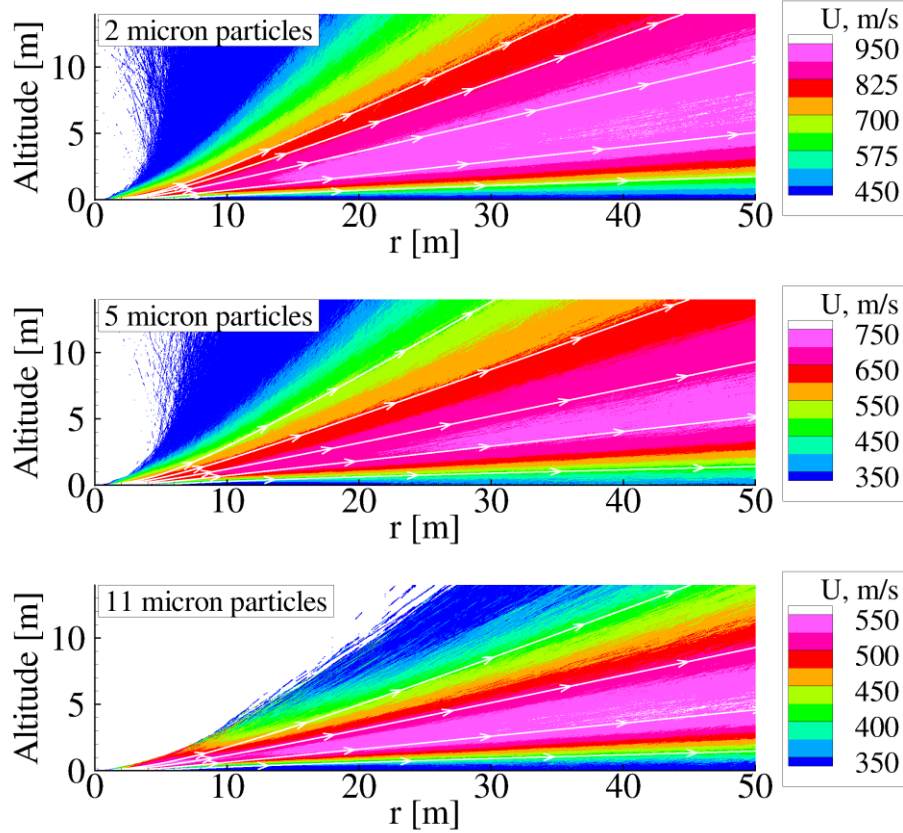


Figure 5.1.1. Mean radial velocity contours for 2, 5, and 11 μm particles when the gas is unaffected by the presence of dust. The flow field is blanked in regions without dust. Note the change in color scale for different size particles.

The smaller particles quickly respond to the gas and are accelerated to higher velocities. The peak speed for the 2 μm particles is 1000 m/s while the peak speed for 11 μm particles is only 575 m/s. The smallest, 200 nm, particles accelerate to speeds of nearly 2000 m/s. The differences in particle velocity result in the particles separating by size as they travel into the far field. This process is analogous to size separation of alumina pellets in the plume of solid-propellant rockets (Simmons, 2000). A key

parameter that determines the maximum speed of the particles is the ratio of the aerodynamic cross section to particle mass.

Streamlines are also drawn in Figure 5.1.1. The radial velocity does not change significantly along each streamline beyond distances approximately 20 m away from the plume centerline. This indicates that the dust decouples from the gas relatively quickly because the particle acceleration is small. This decoupling occurs very rapidly because the drag force is proportional to the gas density, which decays approximately proportional to r^{-2} . The specific location where the dust particles decouple from the gas is illustrated in Figure 5.1.2.

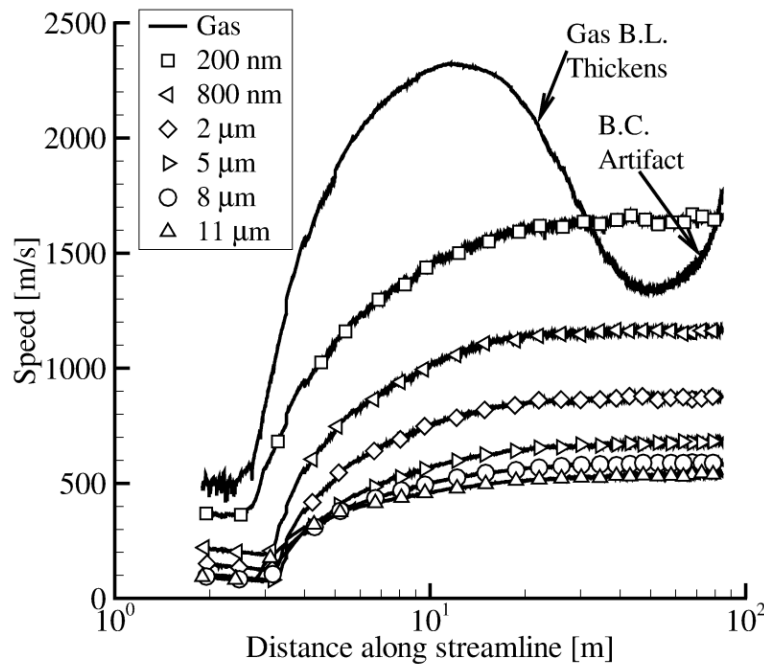


Figure 5.1.2. Gas and dust particle speeds for different size grains along a streamline of maximum particle flux. The gas was unaffected by the dust. Note the logarithmic scale on the x-axis.

The height of maximum particle mass flux is 3.56 m above the surface, at a distance 50 m from the jet axis. A streamline that intersects this location is created and data for all dust and gas species are extracted along that streamline in Figure 5.1.2. Numerical artifacts are present along the first couple meters of the streamline as dust particles creep along the surface. This is done for a simulation where the gas is unaffected by the dust and another where the gas is fully coupled. As previously discussed, the smaller particles accelerate to a higher velocity than the heavier ones. All particles tend to stop accelerating near the same location, approximately 25 m from the jet axis. The gas boundary layer rapidly thickens, and eventually causes the gas velocity along this particle streamline to decrease approximately 12 m from the plume jet axis, see Figure 4.4.2 for a reference to unperturbed viscous boundary layers.

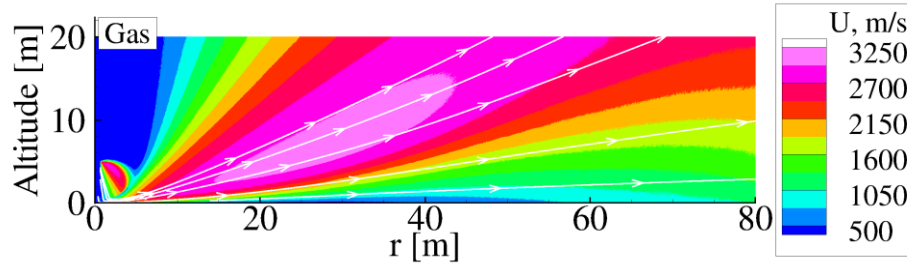


Figure 5.1.3. Mean radial velocity contours for the background gas. Note the gas is unaffected by the presence of dust in this computation.

The gas velocity increases near the right boundary. Contours of gas velocity also show this effect near the right wall in Figure 5.1.3. This occurs because the flow within the boundary layer is either subsonic or moderately supersonic, but the DSMC right wall boundary condition is appropriate only for hypersonic outflow. A better boundary condition would account for molecules entering the domain from the right wall, but this is not implemented and remains a challenge for DSMC solvers. The boundary

is assumed to not affect the dust motion because the dust is nearly decoupled from the gas where the boundary effects are noticeable.

All reflections for gas molecules colliding with dust particles are diffuse with thermal accommodation in this work. The dust particles can then be heated/cooled directly by the gas or, to a lesser extent, by inelastic granular collisions. Mean particle temperatures are plotted for various size grains, Figure 5.1.4.

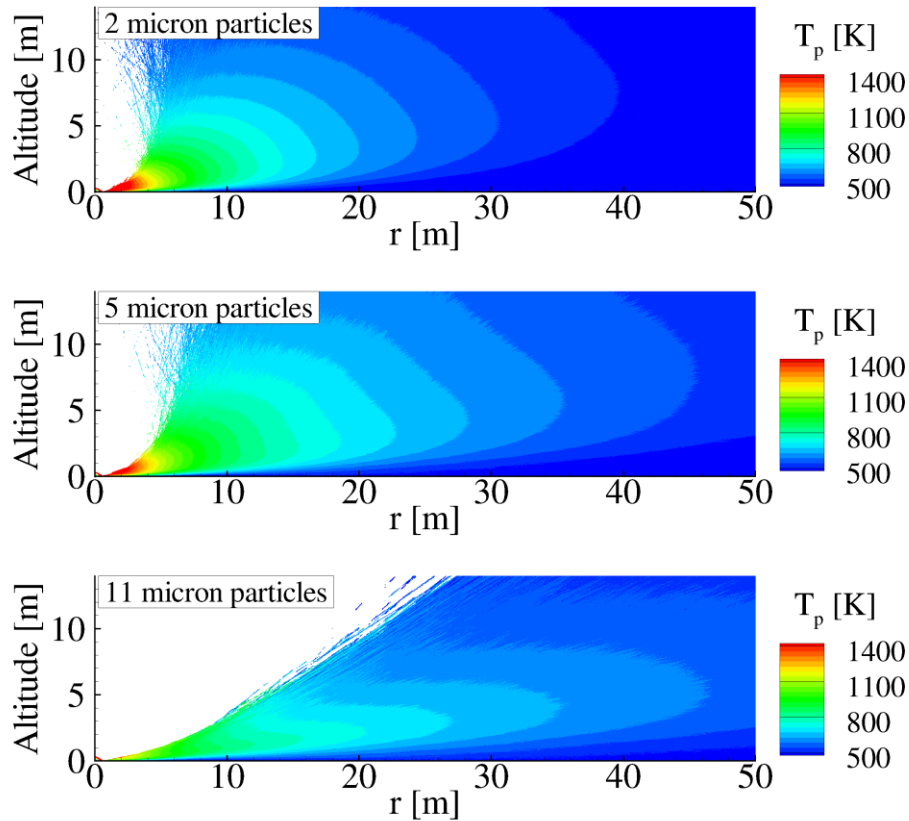


Figure 5.1.4. Dust particle temperatures for 2, 5, and 11 μm particles when the gas is unaffected by the dust.

The particles leave the surface at the local surface temperature, 350 K. The particles are rapidly heated by the hot exhaust gas near the stagnation point. The smaller particles have a quicker thermal response and reach a temperature of nearly

1400 K. The larger particles reach a maximum temperature near 1150 K. The hot grains radiate away energy as they expand outwards. The radiation model assumes that all the radiated energy is lost to space and not reabsorbed by the gas or neighboring particles. This model fails to capture phase change effects because the melting point of basaltic silica or lunar regolith is approximately 1050 K (Heiken, Vaniman, & French, 1991). Phase change energies may be important to include because sintering or melting will affect granular collisions and can also affect the aerodynamic cross sections.

The simulations previously discussed did not account for the effect that the dust has on the gas motion. The mass fraction is commonly used to identify when the coupling from the particles to the gas is significant. The mass fraction, or loading, is defined as the mass of all dust particles divided by the mass of gas molecules, Figure 5.1.5.

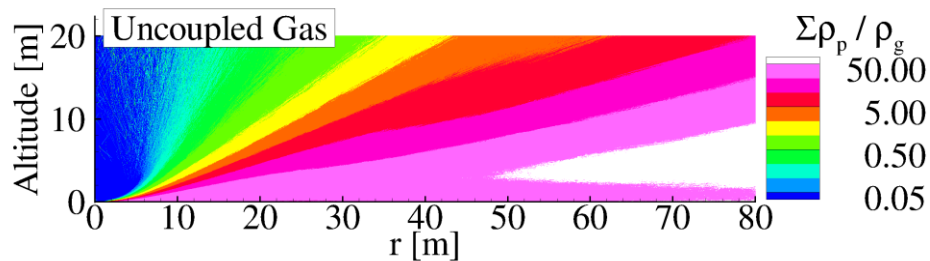


Figure 5.1.5. Dust mass loading, defined as the ratio of the total dust mass to gas mass, when the gas motion is not affected by the dust. The rocket engine is hovering at an altitude of 5 m.

The highest mass loading occurs in the lower layers of the dust spray, and there is approximately 45 times as much dust mass as gas. This means that 98% of the total mass is comprised of dust near the erosion region. The mass loading decreases at higher altitudes because relatively few particles are scattered upwards via granular collisions. At greater distances from the axis, where the dust is relatively decoupled from the gas,

the dust mass fraction increases. This occurs because the gas molecules are light and can expand more readily away from the surface than the heavy dust particles.

In the next set of simulations, the gas is fully coupled to the dust and the results are compared to the uncoupled simulations. First, the effects of coupling on the gas flow field are examined. The gas radial velocity, defined as the velocity tangent to the surface, is contoured in Figure 5.1.6.

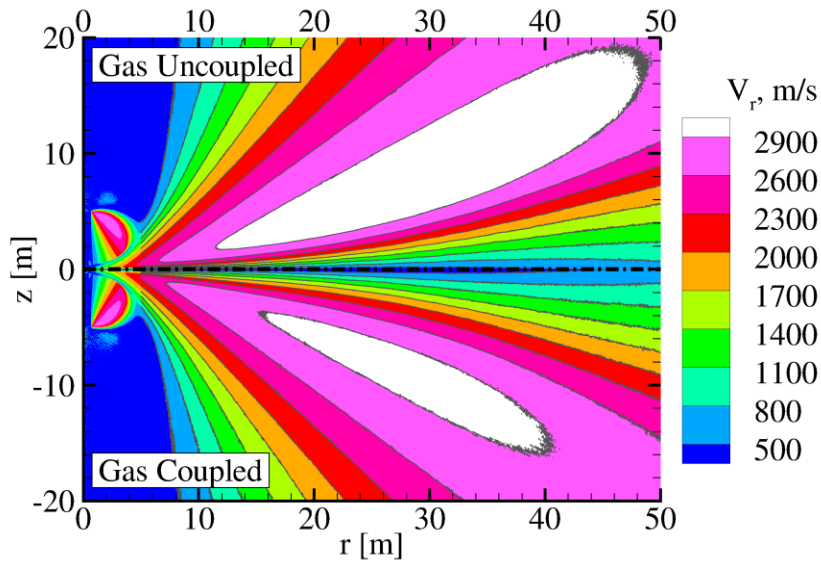


Figure 5.1.6. Contours of the gas radial velocity when the gas is uncoupled (top) and coupled (inverted image) to the dust. The rocket engine hovers 5 m above the ground.

The inclusion of dust coupling inhibits the gas motion near the surface, thus delaying the gas expansion. This is seen in Figure 5.1.6 where the radial velocity for the uncoupled gas tends to be faster than the coupled gas. If the mass loading were to increase further, the differences in velocity would be more apparent. The effect of coupling has a larger impact on the gas temperature than the velocity as shown in Figure 5.1.7. The dust leaves the surface at the local surface temperature of 350 K. The gas therefore loses energy as it heats the particles. The rate of cooling is further accelerated

because the dust particles irrecoverably radiate energy to space. This acts as a sink mechanism for removing energy from the gas.

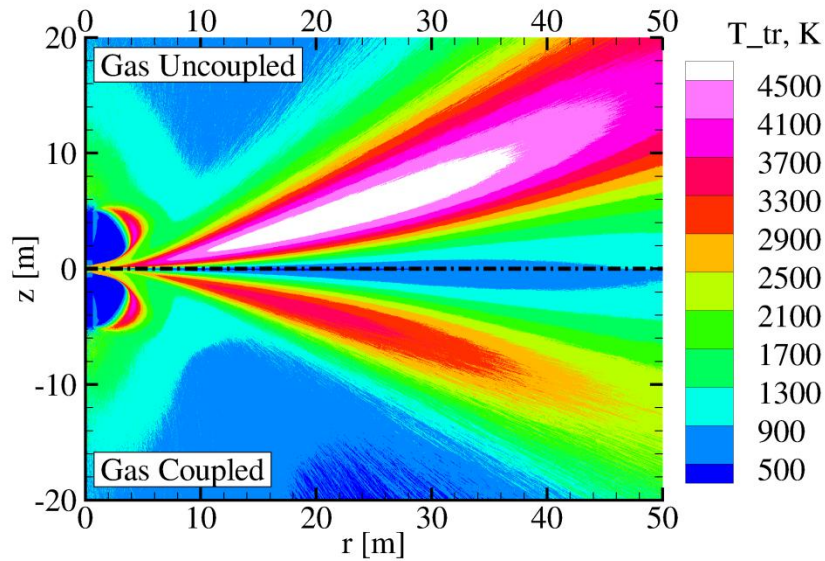


Figure 5.1.7. Contours of gas translational temperature when the gas is uncoupled (top) and coupled (bottom) to the dust. The rocket engine hovers 5 m above the ground.

Gas velocity and thermal boundary layer profiles are plotted at a location 40 m from the jet axis in Figure 5.1.8. The dust acts as a resistive stress on the gas, and causes the boundary layer to thicken. This action is similar to how an adverse pressure gradient thickens a boundary layer. The temperature is more significantly reduced by interactions with the dust than momentum. The peak temperature is 4400 K when the gas is uncoupled and 2800 K when coupled. The gas temperature may be misleading because the gas, at this distance, is less collisional and very non-equilibrium. There is a large relative velocity between the high velocity expanding wall jet and the low speed molecules that reflect off the wall. This increased relative velocity results in a higher kinetic temperature near the surface.

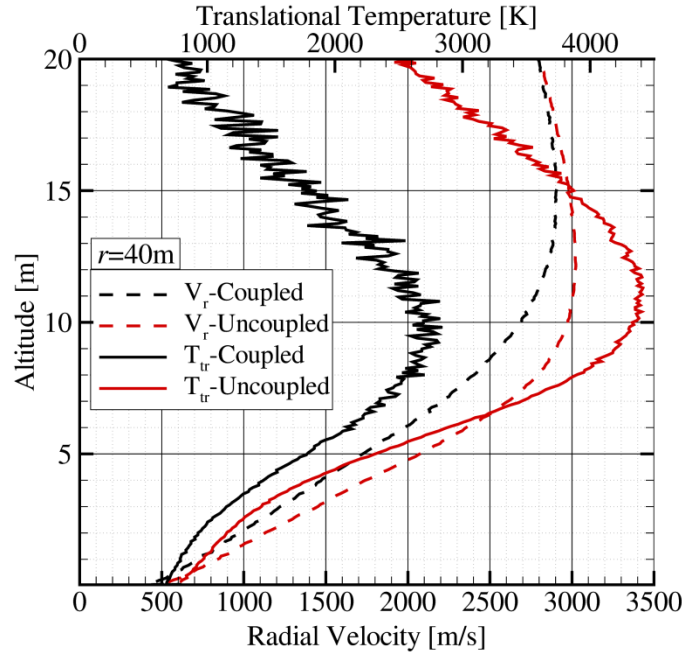


Figure 5.1.8. Velocity (dashed lines) and thermal (solid lines) boundary layer profiles taken 40 m from the plume centerline for simulations where the gas is coupled (black) and uncoupled to the dust (red).

The rotational temperature of the gas is out of equilibrium with the translational temperature in Figure 5.1.9. The rotational temperature is significantly less than the translation temperature, because the particles that reflect off the surface are in rotational equilibrium with the surface temperature, 350 K. The gas is not collisional enough to equilibrate the rotational energy, resulting in higher translation energies than an equilibrium gas. The rotational temperature tends to be higher when the gas is unaffected by the dust because the dust does not act as a sink for removing energy from the flow. The rotational temperature is less dependent on the gas-dust coupling than the translational temperature. Although gas-dust collisions significantly affect the gas translational temperature, that translational energy is not distributed into rotational modes because of rarefaction effects.

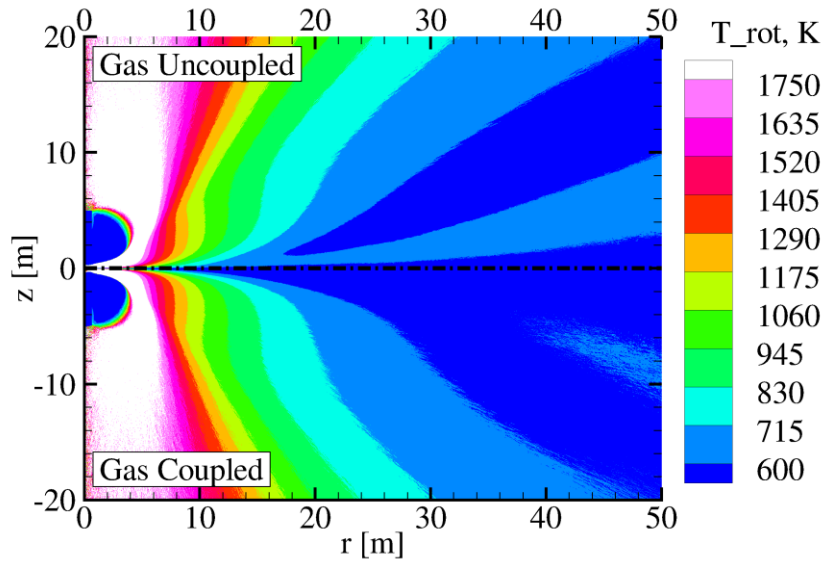


Figure 5.1.9. Rotational gas temperature when the gas is not affected (top) by the dust and fully coupled to the dust (bottom).

The slowing of gas near the surface results in a loss of dynamic pressure and thus a decreased erosion rate. The erosion rates, with and without coupling to the gas, are plotted in Figure 5.1.10. The peak erosion rate decreases by approximately 15% and the profile narrows significantly when the gas is affected by the dust. The erosion profile narrows because momentum is sapped from the gas as dust becomes entrained, resulting in reduced dust emission downstream. Despite the decrease in net erosion, the dust mass loading remains significant, and there is approximately 25 times as much dust as gas near the erosion regime, contoured in Figure 5.1.11.

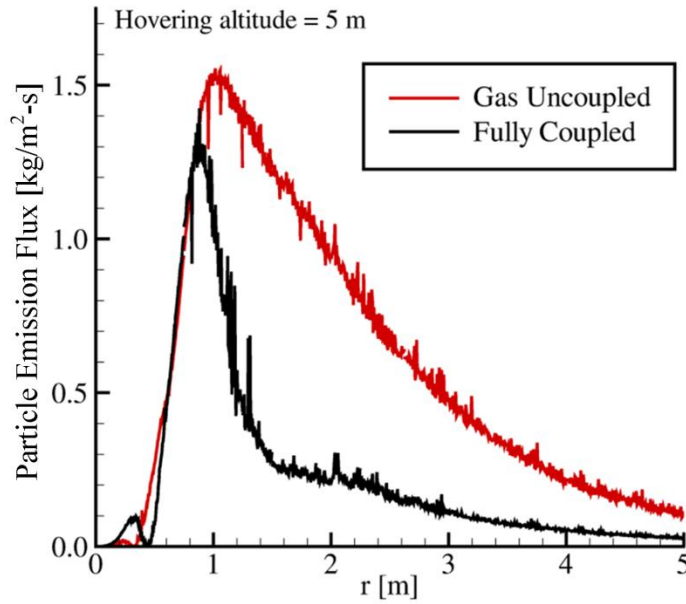


Figure 5.1.10. Dust emission flux for a rocket engine hovering 5 m above the surface. The red line is the emission flux when the gas is unaffected by the dust and the black line is when the gas is affected.

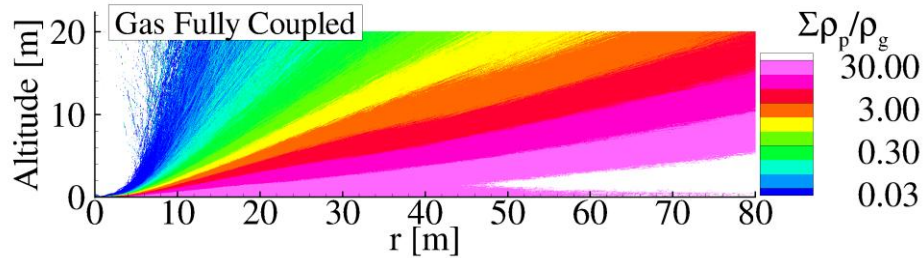


Figure 5.1.11. Dust mass loading, defined as the ratio of dust mass to gas mass, when the gas is fully coupled to the dust motion.

The gas velocity and temperature decrease and the boundary layers thicken slightly when their motions are inhibited by the presence of dust. Consequently, the dust particles are accelerated to lower velocities. Figure 5.1.12 (left) compares dust velocity profiles for 2 and 11 μm particles for simulations where the gas is and is not affected by the dust motion. Other dust sizes follow similar trends. The profiles were

sliced 50 m from the jet axis, far downstream of where the dust asymptotes to its terminal velocity. The maximum radial velocity of the 2 μm particles is reduced from 945 m/s when the gas is uncoupled to 740 m/s when coupled. Likewise, the maximum radial velocity of the 11 μm particles is reduced from 545 m/s when the gas is uncoupled to 370 m/s when coupled.

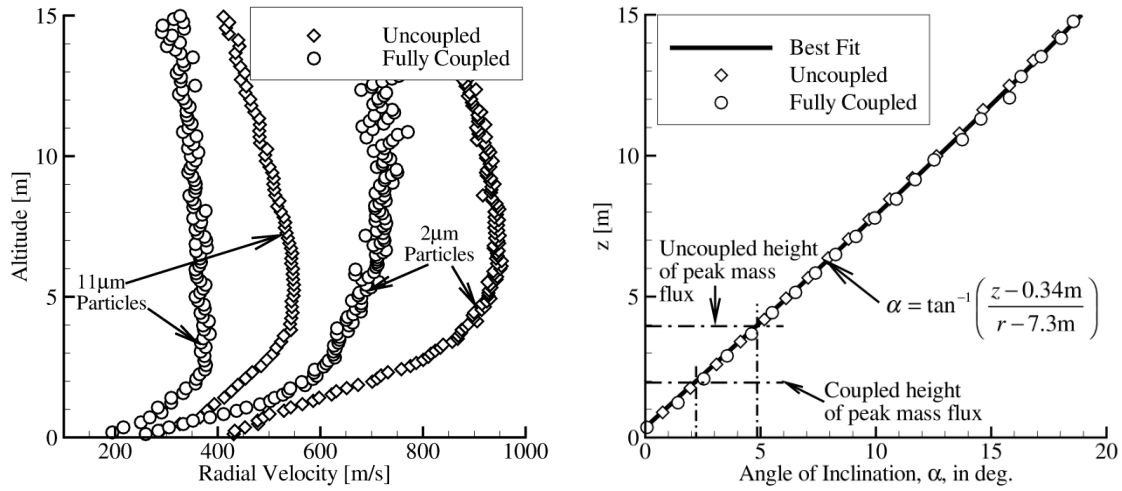


Figure 5.1.12. (left) Radial velocity profiles for 2 and 11 μm particles when the gas motion is coupled (circles) and uncoupled (diamonds) to the dust motion. (right) Dust spray angle of inclination probed at different heights. These profiles are sliced 50 m from the jet axis.

The angle of inclination of the particulates, $\alpha \equiv \tan^{-1}(V_z/V_r)$, is plotted in Figure 5.1.12 (right) when the gas is and is not affected by the dust. The gas coupling has little effect on the dust spray inclination angle profile. This profile is well approximated as a radial source of particulates originating at a height 0.34 m above the surface and location 7.3 m from the plume centerline. Although the angle of inclination profiles are similar, the dust spray shape is significantly affected by the gas coupling because the location of peak particle mass flux changes. The angle of inclination

measured at the location of peak particle mass flux is 4.85° and 2.2° when the gas is uncoupled and coupled to the dust, respectively.

The radial particle mass flux is plotted for all particle sizes larger than $2\text{ }\mu\text{m}$ in Figure 5.1.13. The particle mass flux is reduced when the gas is fully coupled, which is expected because of the decrease in emission rate. Of all simulated particle sizes, the $8\text{ }\mu\text{m}$ particles have the highest particle mass flux. This reflects the assumed particle size distribution of aerosolized particles in this work, see Section 3.3.1. Approximately 41% of the mass is contained in the $8\text{ }\mu\text{m}$ diameter grains, 27% in $11\text{ }\mu\text{m}$ grains, 25% in the $5\text{ }\mu\text{m}$ grains, and 6% in the $2\text{ }\mu\text{m}$ grains. The 200 and 800 nm particles account for the remaining 1% of the mass and are not shown. The peak particle mass flux is $4.5\text{ g/m}^2\text{-s}$ when the gas is uncoupled and $1.8\text{ g/m}^2\text{-s}$ when the gas is affected by the dust. If the dust accumulates on a surface with a bulk density of 1500 kg/m^3 (the same as the unperturbed lunar surface), the maximum accumulation rate is $1.2\text{ }\mu\text{m/s}$ when coupled and $3\text{ }\mu\text{m/s}$ when uncoupled. The $11\text{ }\mu\text{m}$ particle flux also decreases more rapidly with increasing altitude than the other particle sizes. This occurs because the larger grains have more inertia and are less susceptible to scattering via granular collisions. This effect is more apparent in the uncoupled simulation, suggesting higher overall collision rates.

The particle radial momentum flux is plotted in Figure 5.1.14 for different particle sizes. The profile is extracted 50 m from the jet axis, beyond where the dust particles reach their terminal velocity. The peak momentum flux at this location is approximately 3.1 Pa when the gas is affected by the dust and 0.9 Pa when unaffected. The dust particle streamlines are nearly linear, and the particle mass and momentum flux decrease proportional to r^{-2} .

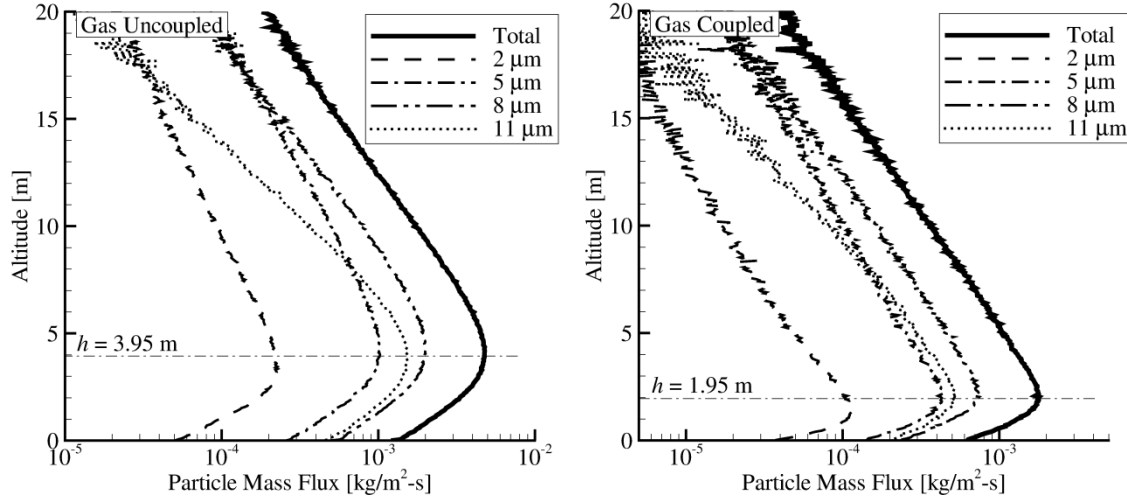


Figure 5.1.13. Particle mass flux for different size grains when the gas is uncoupled to the dust (left) and coupled to the dust (right). Note the logarithmic x-axis.

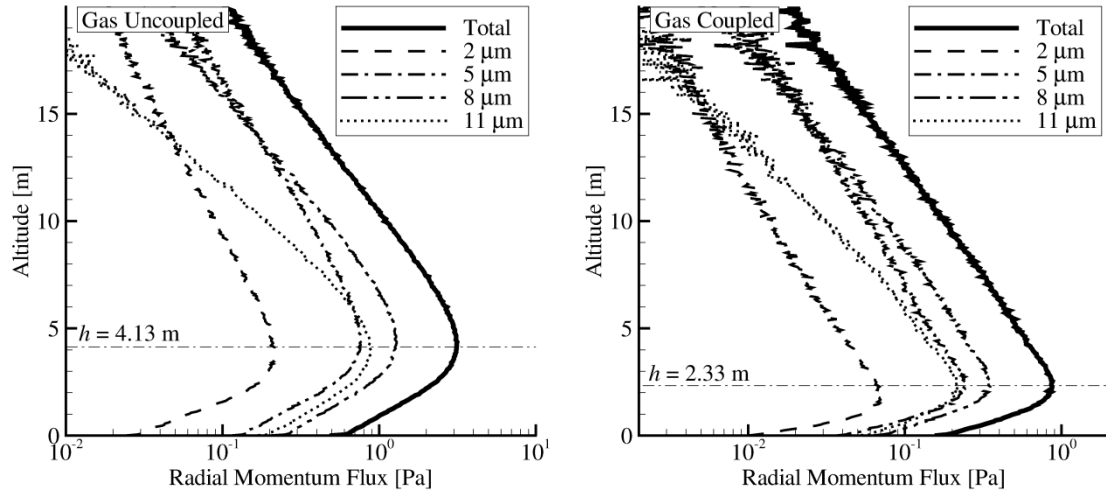


Figure 5.1.14. Particle radial momentum flux when the gas is uncoupled to the dust (left) and coupled to the dust (right). Note the logarithmic x-axis.

The gas boundary layer tends to thicken as a response to the dust layer. Although one might expect dust to behave similarly, the dust layer actually becomes thinner. The height of maximum particle mass flux decreases from 3.95 to 1.95 m when

the gas is affected by the dust. Similarly, the height of maximum momentum flux decreases from 4.13 to 2.33 m. The dust layer thins because of the coupling between different physical models. When coupled, the aerosolized dust saps momentum from the gas, resulting in lower erosion rates. The dust layer is less sheared and has a lower number density, resulting in lower granular collision rates when the gas is coupled to the dust motion. A decreased number of granular collisions limits diffusion of the dust layer, causing it to thin when the gas is affected by the dust.

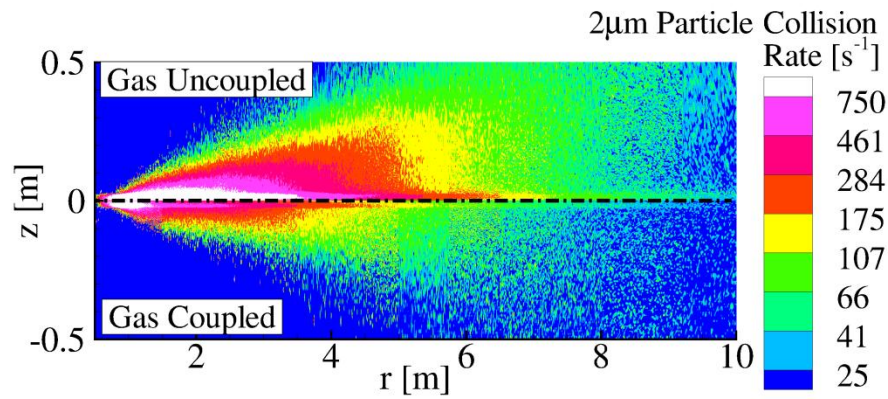


Figure 5.1.15. Granular collision rate when the gas is affected by the dust motion (bottom) and when it is unaffected by the dust (top).

The granular collision frequency for 2 μm particles is plotted in Figure 5.1.15 for simulations when the gas is affected by the dust and when the gas is unaffected. The grain-grain collision rate is higher when the gas is unaffected by the dust because of higher erosion rates and increased shearing of the dust layer. In the next section, the effects of granular collisions and the sensitivity to model parameters are discussed.

5.1.2. THE EFFECTS OF GRAIN-GRAIN COLLISIONS

Granular collisions are inelastic and are modeled via a constant coefficient of restitution. The normal and tangential coefficients of restitution are assumed equal and the scattering is consequently isotropic. Despite the large uncertainty in the scattering

distribution, the assumed coefficient of restitution has significant impact on the computed dust flow fields.

The number density of $2\text{ }\mu\text{m}$ particles is contoured in Figure 5.1.16 for different granular coefficients of restitution, ϵ , and when granular collisions are not modelled.

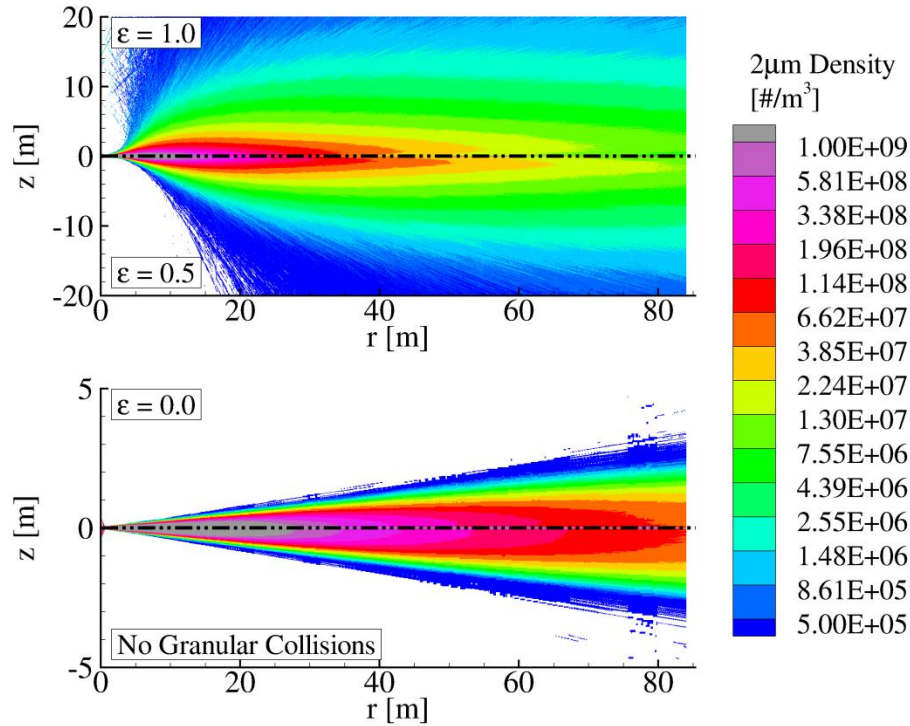


Figure 5.1.16. Number density contours for $2\text{ }\mu\text{m}$ particles for simulations with different coefficients of restitution. A simulation without granular collisions is also shown for comparison. Note that the vertical axis is stretched 400% in the bottom figure.

Granular collisions with moderately large coefficients of restitution tend to diffuse the dust sheet via scattering. The dust layer is significantly broader for simulations with restitution coefficients of 0.5 and 1.0 compared to the simulation without granular collisions. Note that the vertical scale is stretched by 400% for simulations with a 0.0 restitution coefficient and when granular collisions are neglected. For completely

inelastic granular collisions, the dust layer is negligibly broadened. More elastic granular collisions result in broader dust sheets because such collisions can efficiently transfer radial momentum into vertical momentum. This occurs because the relative velocity vector can be rotated into any direction because the scattering is assumed isotropic. If the collision is completely inelastic, the post-collision relative velocity vanishes, and the two colliding particles travel parallel to each other at the center of mass velocity. Consequently, radial momentum is not transferred into the vertical direction and the dust spray looks qualitatively similar to a simulation without granular collisions.

The collision broadening also results in lower particle number densities for more elastic collisions. This affects the mass loading and consequently the gas flow field. The mass loading is contoured for simulations with 1.0 and 0.5 coefficients of restitution in Figure 5.1.17.

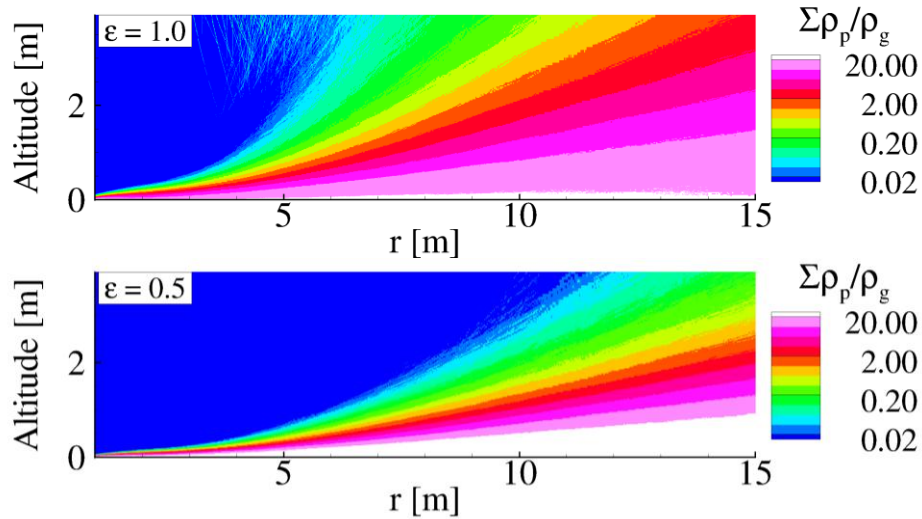


Figure 5.1.17. Particle mass loading near the erosion regime for simulations with a coefficient of restitution of 1.0 (top) and 0.5 (bottom).

The mass loading is higher near the surface for a restitution coefficient of 0.5 than it is for elastic granular collisions. Further from the surface, the mass loading is higher

for more elastic collisions because of increased scattering. The mass loading can affect the gas flow field which can in turn affect the drag force to the dust particles. Changes in gas properties influence the dust most significantly near the erosion regime where drag forces are the highest. In Figure 5.1.18 the gas dynamic pressure is plotted versus altitude at locations 5 and 10 m from the jet axis for simulations with different coefficients of restitution.

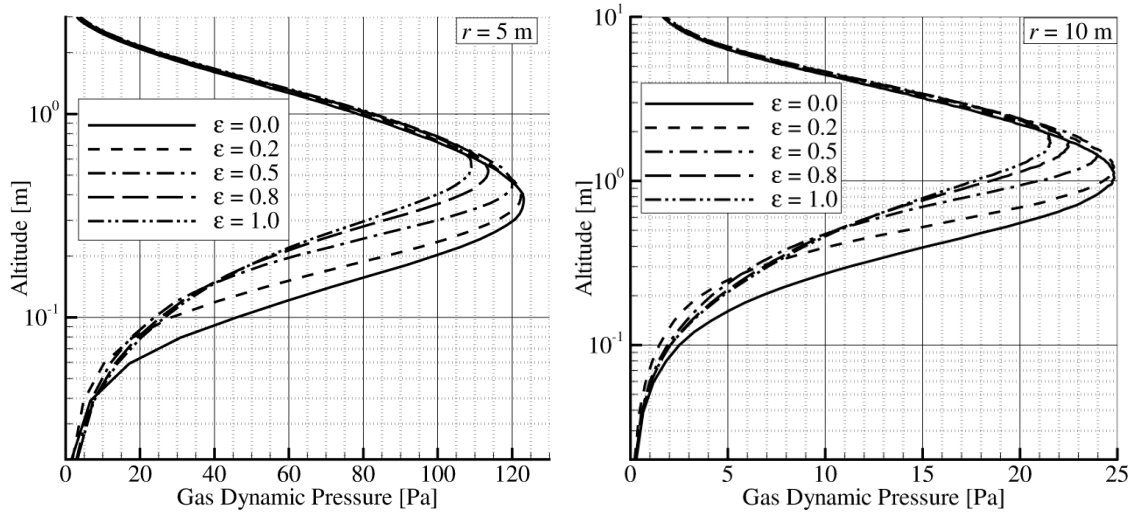


Figure 5.1.18. Gas dynamic pressure profiles at a distances 5 m (left) and 10 m (right) from the jet axis. The various lines correspond to simulations with different coefficients of restitution, ϵ . Note the logarithmic scale on the y-axis.

The effect of granular collisions on the gas dynamic pressure is confined to regions near the wall. More elastic granular collisions tend to reduce the gas dynamic pressure. The ratio of peak dynamic pressure for elastic collisions to completely inelastic collisions is 0.89 at $r = 5$ m and 0.86 at $r = 10$ m. The granular restitution coefficient affects the gas and also affects particle speeds. Velocities of the $2 \mu\text{m}$ particles are contoured in Figure 5.1.19 for different restitution coefficients.

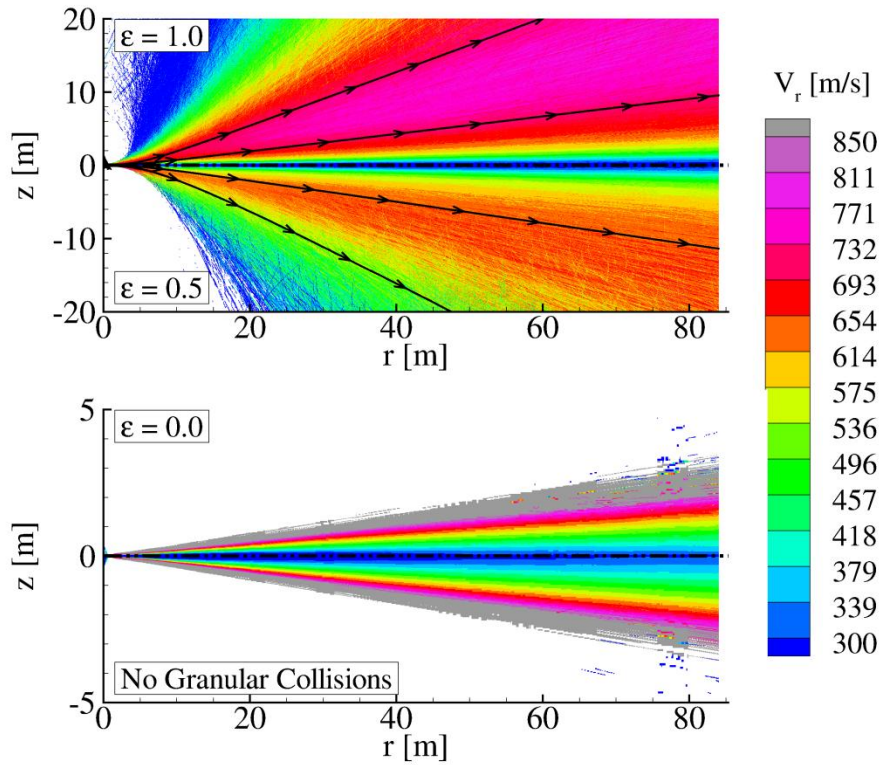


Figure 5.1.19. Number density contours for 2 μm particles for simulations with different coefficients of restitution. A simulation without granular collisions is also shown for comparison. Note that the vertical axis is stretched 400% in the bottom figure.

Particles that collide elastically attain a higher velocity, 750 m/s, than the particles that collide with a restitution coefficient of 0.5, which asymptote near 650 m/s. This occurs because more elastic collisions broaden the dust layer, deflecting some particles outside the viscous boundary layer and into the high velocity free stream gas. The gas dynamic pressure decreases for more elastic collisions because more of the gas momentum is transferred to the dust particles as was shown on Figure 5.1.18. For completely inelastic collisions, a mantle of high velocity particles which exceed 800 m/s surrounds a slower moving core. Relatively few particles reside within the high speed mantle though.

The particle mass and momentum flux profiles extracted 40 m from the jet axis are shown in Figure 5.1.20.

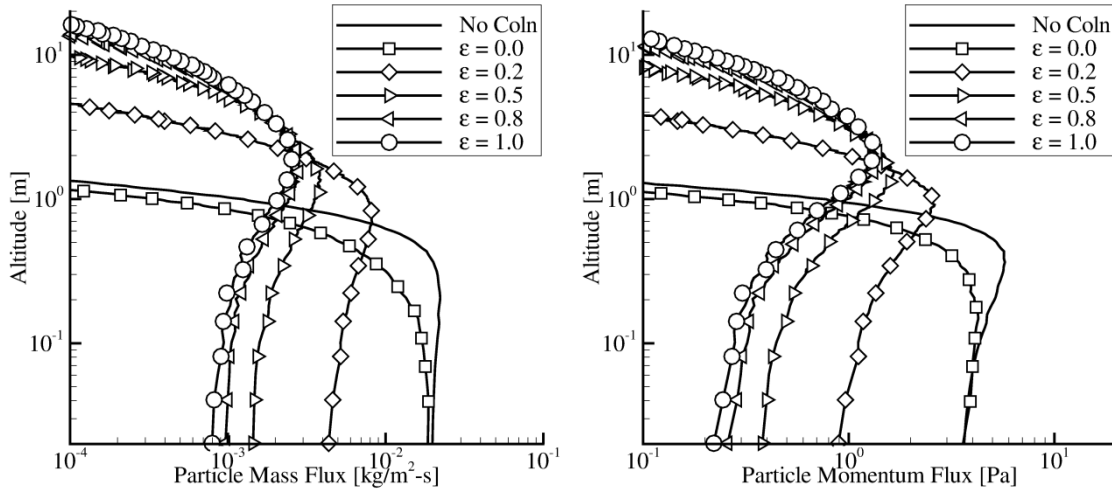


Figure 5.1.20. Particle mass (left) and momentum (right) flux profiles for simulations with different coefficients of restitution. A profile obtained from a simulation without granular collisions (solid line) is also shown for comparison. The profile is taken 40 m from the jet axis.

The mass and momentum flux are very sensitive to the coefficient of restitution between colliding grains. The dust sheet broadens for more elastic collisions, resulting in decreased peak values for the mass and momentum flux. These simulations bracket the complete range of restitution coefficients. The peak particle flux is nearly 8 times larger for completely inelastic granular collisions compared to elastic collisions. The peak particle flux is reduced by a factor of 1.5 when a restitution coefficient of 0.5 is used compared to elastic collisions. The peak particle flux for a restitution coefficient of 0.8 is only 7.6% larger than the peak flux for elastic collisions. If all particles were assumed to strike and adhere to a surface 40 m from the jet axis, the peak accumulation rate on the surface depends on the restitution coefficient of colliding grains and could

vary from 14.2 to 1.8 $\mu\text{m/s}$. The particle flux and accumulation rates decrease proportionally to r^{-2} and will be discussed later in this chapter. The rate calculated above assumes that the particles that stick to the surface have the same packing density as unperturbed regolith. The simulations without granular collisions and completely inelastic collisions are similar. Completely inelastic collisions result in slightly lower particle mass and momentum fluxes. These simulations are similar because completely inelastic collisions do not cause particles to scatter, and scattering is the main mechanism by which granular collisions affect the flow.

The mean particle velocities for 2 and 11 μm particles are plotted for different restitution coefficients in Figure 5.1.21.

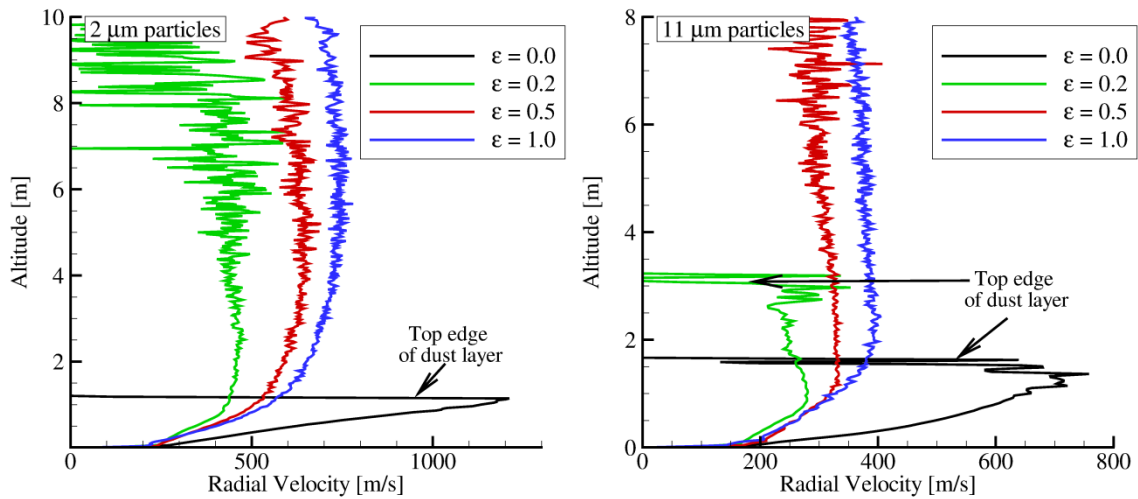


Figure 5.1.21. Particle radial velocity profiles for 2 μm (left) and 11 μm particles obtained from simulations with different coefficients of restitution. The data were extracted 30 m from the jet axis.

The particle velocities increase as the coefficient of restitution increases from 0.2 to 1.0. The noise in the calculation increases at higher altitudes because fewer particles are scattered that high. The maximum radial velocity of the 2 μm particles is 460 m/s

when the coefficient of restitution is 0.2. The maximum radial velocity of the 2 μm particles is larger for elastic collisions, and is 730 m/s. The maximum radial velocity of the 11 μm particles is 275 m/s when the coefficient of restitution is 0.2 and is 390 m/s for elastic collisions. The particle velocities for completely inelastic collisions are significantly higher and are 1200 and 720 m/s for the 2 and 11 μm particles, respectively. These velocities are higher than those shown in Figure 5.1.12 where the restitution coefficient is 0.8 and the gas is unaffected by the dust. Gas coupling effects are not sufficient to account for the differences in velocities. The high speeds occur because particles are not scattered and radial momentum is not redirected upwards.

The coefficient of restitution also affects the inclination angle, $\alpha \equiv \tan^{-1} V_z/V_r$, of the dust sprays. The inclination angle is plotted versus altitude 30 m from the jet axis for simulations with different coefficients of restitution in Figure 5.1.22. The inclination angle profiles depend weakly on the coefficient of restitution. This occurs because the virtual origin of the dust spray changes position slightly depending on the scattering. For higher restitution coefficients, the virtual origin is located at slightly higher altitudes. This is shown in Figure 5.1.22 because the height at which the inclination angle is 0.0 increases as restitution coefficient increases. The heights of peak particle flux are also shown for the different restitution coefficient simulations. The angle of inclination of the dust spray at the location of peak mass flux increases as collisions become more elastic. The bracketed range of inclination angles varies from 1.56 to 3.12° for restitution coefficients varying from 0.2 to 1.0.

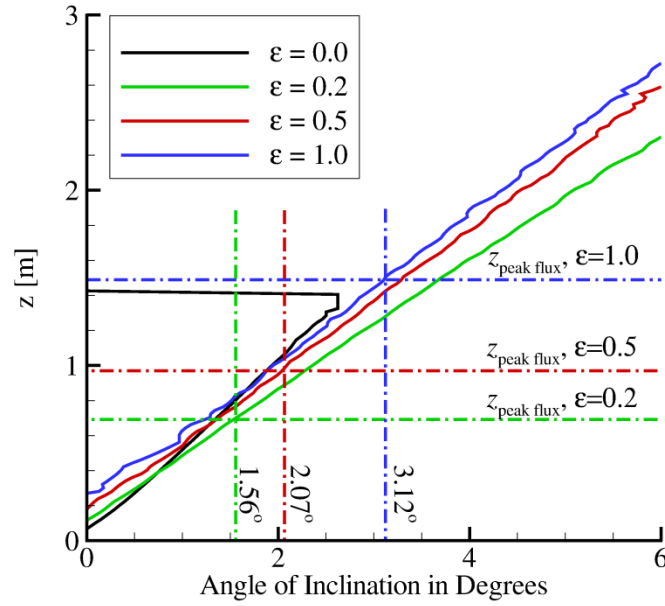


Figure 5.1.22. Angle of inclination of the dust sprays versus altitude for different restitution coefficients. The dash-dot lines are reference lines which indicate the locations of peak mass flux and corresponding inclination angles.

Section 5.2. Effects of Hovering Altitude

As a lander approaches the lunar surface, the impinging plume flow fields and dust sprays change. The $8\text{ }\mu\text{m}$ particle number density fields are contoured in Figure 5.2.1 for a rocket engine hovering at different altitudes. At higher altitudes, the erosion rate decreases approximately as h^{-2} and the location of peak erosion occurs further from the jet axis. The dust sprays reflect this and tend to originate further from the axis at higher hovering altitudes. The number densities are comparable in each of these simulations despite the rapid decrease of erosion rate with altitude. Both the erosion rate and drag on the aerosolized particles are proportional to the gas dynamic pressure. At higher altitudes, the emission rate decreases and the particle velocity decreases. Consequently, the number density remains relatively constant.

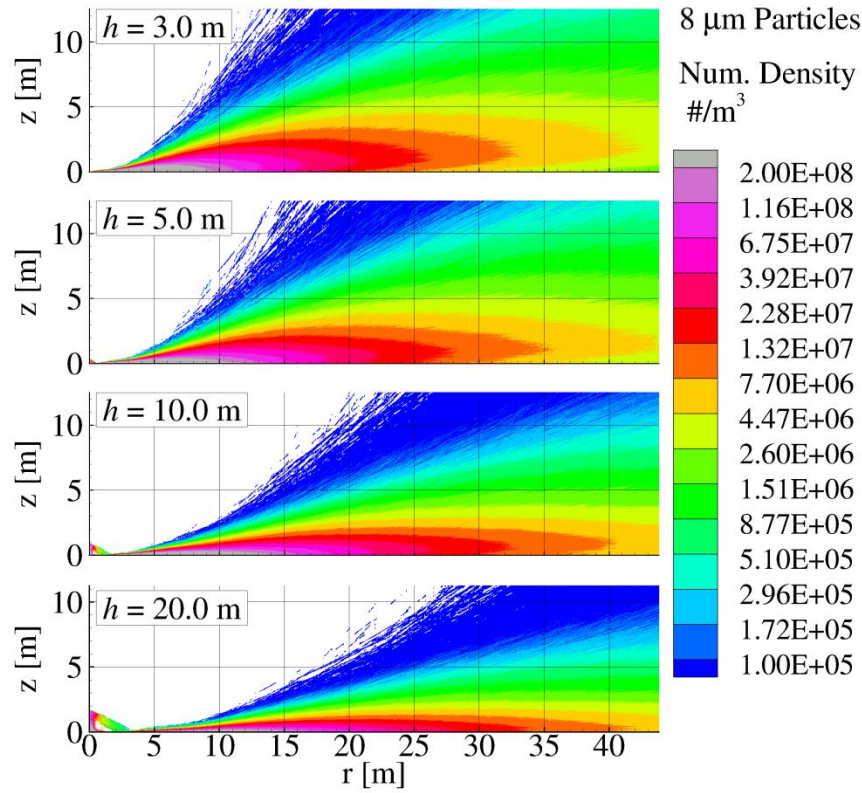


Figure 5.2.1. Number density fields for 8 μm particles for rocket engines hovering at various altitudes, h .

At lower altitudes, the gas exerts a stronger shear stress on the dust layer resulting in an increased collision rate. A higher collision rate increases the scattering of the dust layer, resulting in more highly deflected particles.

Particle speed profiles are shown for a set of different hovering altitudes for 8 and 11 μm particles in Figure 5.2.2. The velocity profiles were taken 70 m from the jet axis. Both the 8 and 11 μm particles are accelerated to higher speeds at lower hovering altitudes. The speed profiles for the larger particles diverge immediately above the surface for different hovering altitudes. The velocity gradient near the surface increases at lower hovering altitudes, reflecting the increased drag force on the particles.

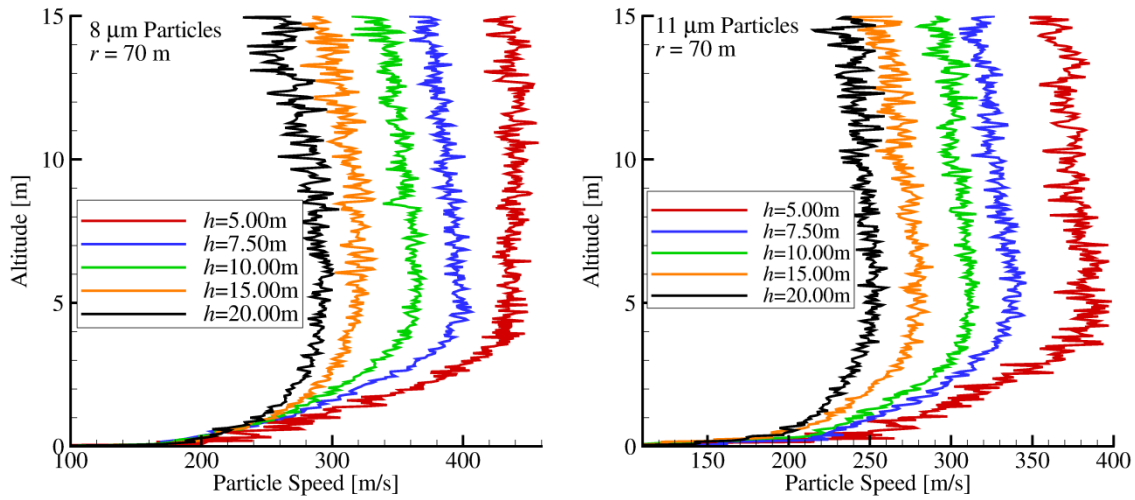


Figure 5.2.2. Speed profiles for 8 μm (left) and 11 μm (right) particles when the lander hovers at different altitudes. The profiles are taken 70 m from the jet axis.

The behavior for the smaller particles is different than that of the larger particles as shown in Figure 5.2.3.

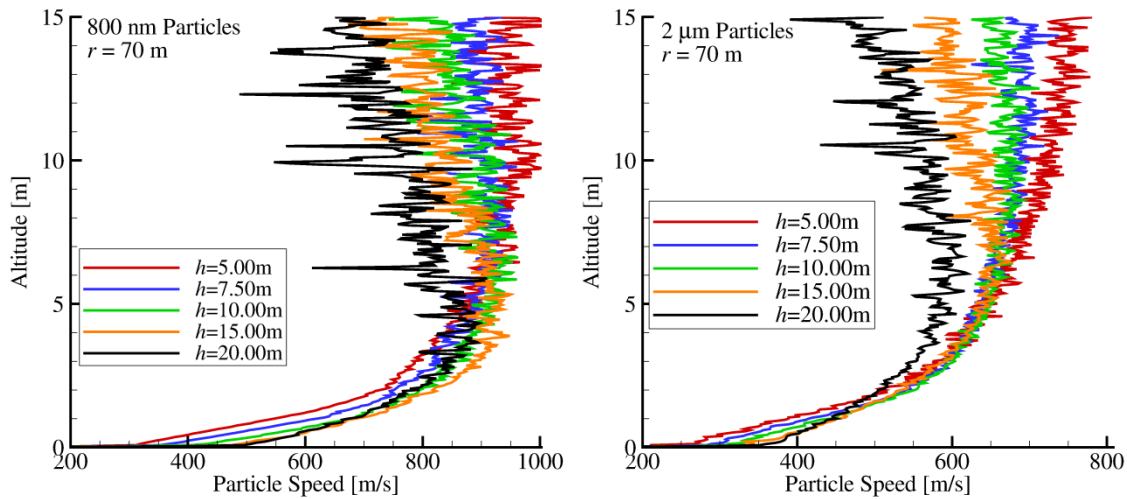


Figure 5.2.3. Speed profiles for 800 nm (left) and 2 μm (right) particles when the lander hovers at different altitudes. The profiles are taken 70 m from the jet axis.

Unlike the larger particles, the smaller particles tend to have speeds that are less dependent near the surface on the lander hovering altitude. In the upper portion of the dust layer, the particle speed profiles diverge in a manner similar to that of the larger particles with lower speeds for higher hovering altitudes.

Granular collisions provide a plausible explanation for why the small particles behave differently than large particles. Figure 5.2.4 shows that the collision rate for $2\text{ }\mu\text{m}$ particles is large near the surface for a rocket engine hovering at 3 m, but is relatively small at higher altitudes. When smaller particles collide with larger ones, the momentum of the small particles quickly accommodates to that of the more massive particles. When the collision rate is sufficiently high – lower hovering altitudes – the motion of the small particles is inhibited by the presence of the heavier particles. When the collision rate is low at higher hovering altitudes, the smaller particles can pass freely through the heavier ones. Despite the fact that gas drag forces (which *accelerate* the entrained particles) are reduced at higher hovering altitudes, the velocities of the smaller particles aren't significantly reduced because their motion is less restricted by the heavier particles.

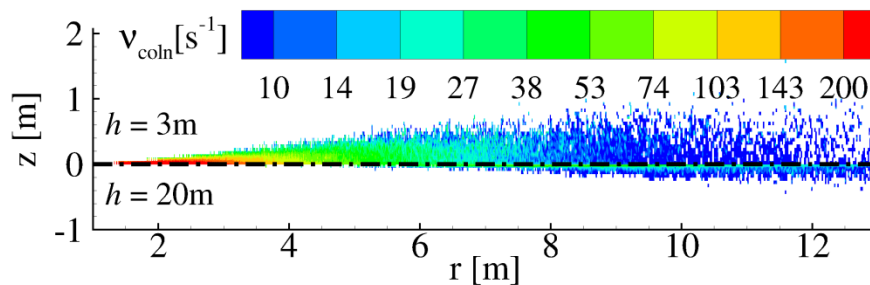


Figure 5.2.4. Collision rate for $2\text{ }\mu\text{m}$ particles when the rocket engine is hovering at 3 m (top) and 20 m (bottom).

A suitable scaling that collapses the speed profiles for all particle sizes was not found because of the complex interactions between the different physical processes.

Unfortunately, this is a typical problem for granular flows in general because they do not scale well (Goldhirsch, 2003). Trends can however be extracted for the heavier particles which are less affected by granular collisions. The maximum particle speed is plotted against hovering altitude for 5, 8, and 11 μm particles on Figure 5.2.5.

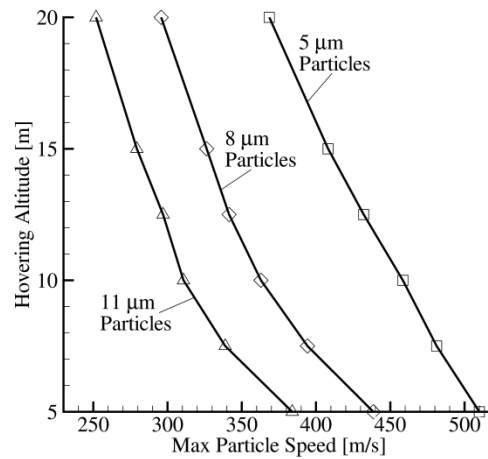


Figure 5.2.5. Maximum particle speed versus hovering altitude for 5, 8, and 11 μm size particles.

The maximum speed attained by the 5 μm particles decreases linearly with hovering altitude. The maximum speed for the larger 8 and 11 μm particles follows a linear trend from hovering altitudes of 20 m down to 10 m. Below 10 m, the gradient in maximum particle speed with respect to hovering altitude increases. This suggests that additional granular collisions at lower hovering altitudes assist in accelerating the heavier particles. These results are likely sensitive to the particle size distribution of aerosolized particles and this issue should be addressed in future work.

The particle mass flux is plotted at different radial positions for a rocket engine hovering 5 and 15 m above the surface on Figure 5.2.6. The dust particle stream lines are nearly linear once decoupled from the gas and before gravity becomes significant. The particle mass flux profiles collapse far from the jet axis for different radial positions

by plotting the elevation angle versus the particle mass flux scaled by a geometric factor. The elevation angle is simply $\tan^{-1}(z/r)$, where z is the height above the surface, and r is the radial distance along the surface from the plume centerline. The particle mass flux is scaled by the geometric factor r^{-2} .

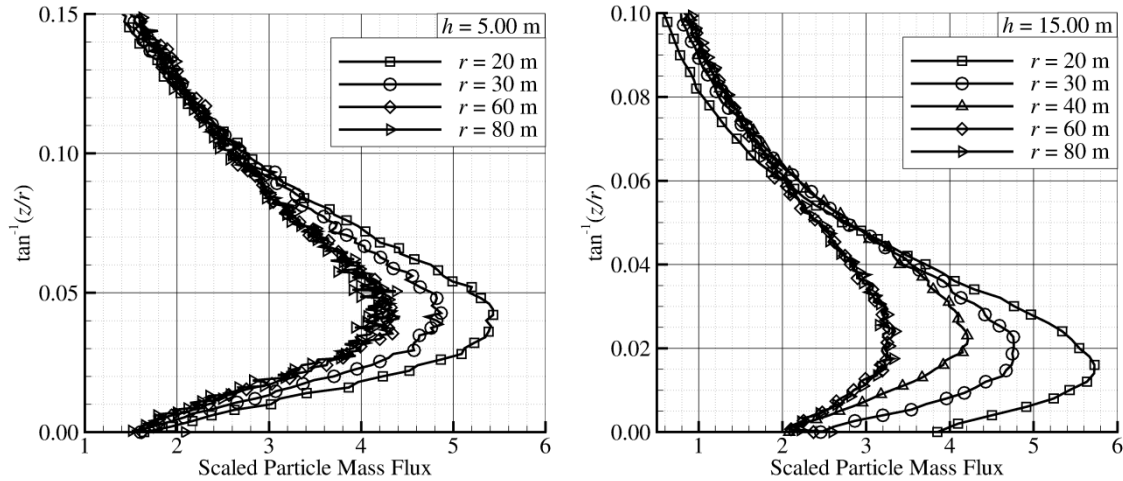


Figure 5.2.6. Scaled particle mass flux at different radial positions from the jet axis for a rocket engine hovering 5 m (left) and 15 m (right) above the surface. Note the differences in vertical scale between the two figures.

The above scaling is shown to collapse the particle mass flux profiles for radial distances greater than 60 m from the plume centerline. Even though the particle and gas motions decouple approximately 35 m from the jet axis, as shown on Figure 5.1.2, the mass flux profiles don't collapse until distances beyond 60 m from the axis. This occurs because the geometric scaling factor does not take into account that the location of peak erosion and origin of the dust spray occur at a distance offset from the plume centerline.

The particle mass and momentum flux profiles are shown for a set of different hovering altitudes in Figure 5.2.7. At lower altitudes, the angle of inclination of the dust sheet increases. This occurs because at lower altitudes, the dust layer is strongly sheared by the gas and increased granular collisions result in more diffusion of the dust

layer. A maximum particle mass flux occurs at hovering altitudes between 7.5 and 10 m. The maximum particle mass flux may be expected at lower hovering altitudes because of increased erosion. This is not true below a certain altitude because granular collisions diffuse the dust sheet and reduce the peak particle mass flux. This can also occur because the erosion region shifts towards the jet axis at lower altitudes. Consequently, the dust sheet has more distance to develop, resulting in a thicker dust sheet.

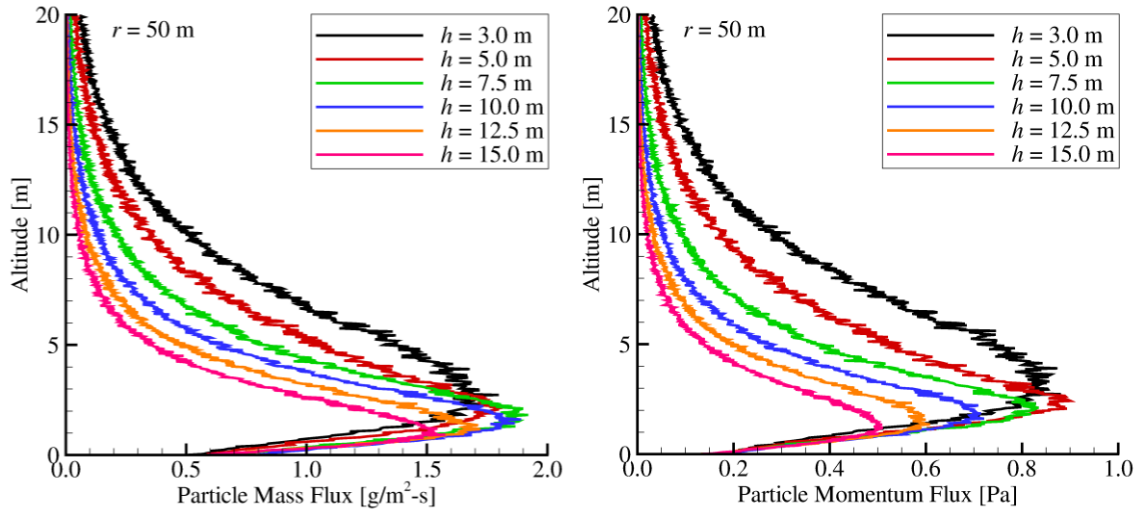


Figure 5.2.7. Particle mass flux (left) and momentum flux (right) profiles for a set of hovering altitudes ranging 15 to 3 m above the surface. The profiles were taken 50 m from the plume centerline.

The angle of inclination, α , measured at the location of peak particle mass flux is plotted for different hovering altitudes on Figure 5.2.8.

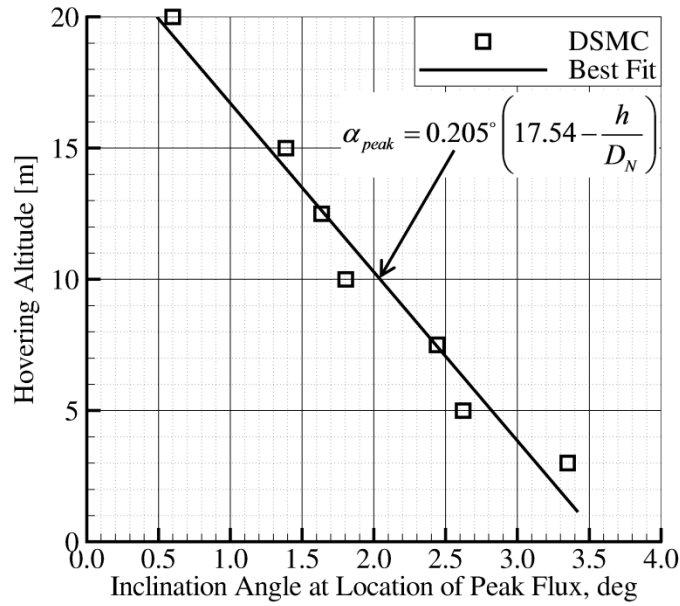


Figure 5.2.8. The angle of inclination measured at the location of peak particle mass flux for different hovering altitudes. The data are best fit by a linear function, the solid line.

The dust spray angle, α , is computed from the ratio of vertical to radial flow velocities. The angle of inclination of the dust spray reduces at higher hovering altitudes and follows a nearly linear trend. This angle can be misleading because the dust spray's angle of inclination is defined at the position of peak particle flux and does not take into account the thickness of the dust sheet. The dust sheets thicken at lower altitudes and consequently there are some particles that are deflected upwards at much higher angles.

Section 5.3. Variations in Dust Sprays with Thrust Levels

The effects that engine thrust have on the dust sprays are examined in this section. The thrust was throttled by adjusting the mass flow rate of the propellant while keeping the I_{sp} constant. Dust number density contours are plotted for thrusts 2.0 and 4.0 times

the nominal thrust cases previously discussed. Regions without any dust particles are blanked for clarity.

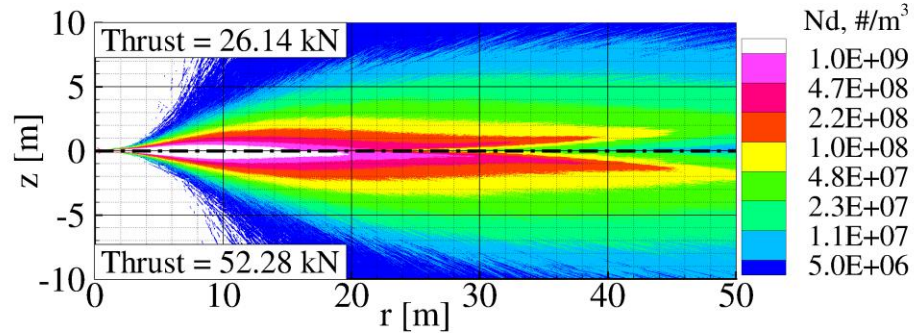


Figure 5.3.1. Number density contours for 2 μm particles for engines 2.0 (top) and 4.0 (bottom) the nominal thrust. The lander hovers 5 m above the lunar surface.

The particle number densities increase near the surface as the engine thrust increases. The erosion rate increases linearly proportional to the rocket thrust when the engine is throttled by changing the mass flow rate, see Section 4.4.3. The thickness of the dust sheet is not significantly altered by changes to the engine thrust. Figure 5.3.2 shows dust sprays produced at a lower thrust, half that of the nominal case, that are slightly different the higher thrust case.

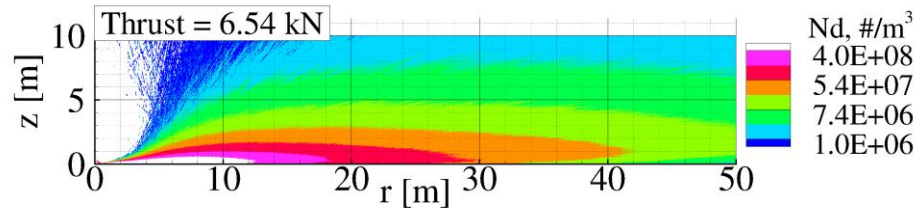


Figure 5.3.2. Number density contours for 2 μm particles for an engine with a thrust of 6.54 kN. The lander hovers 5 m above the lunar surface.

At a lower thrust, the gas is everywhere less dense and the drag forces on particles are smaller. Particles that are deflected upwards via granular collisions travel more vertically because they are not turned by the gas. This effect is also shown in Figure

5.3.1 where the scattered particles are turned radially outward more readily for higher thrust engines. The number of particles scattered nearly vertically upwards is still quite small compared to the rest of the dust spray and this phenomena is also very sensitive to inelasticity of granular collisions.

The particle number density flow fields are similar when the number density is scaled by the thrust of the engine. The scaled particle number density is plotted in Figure 5.3.3 for two different thrust engines. The scaled number density, \hat{n}_d is defined as

$$\hat{n}_d = n_d \frac{F_0}{F}, \quad 5.3-1$$

where F_0 is the thrust of the nominal engine, F is the actual thrust, and n_d is the dust particle number density.

The above scaling collapses the number density profiles reasonably well near the surface for two engines of different thrust. Both the dust erosion rate and particle number density are nearly proportional to the thrust of the engine near this surface. This suggests that the radial velocities near the surface are not sensitive to the engine thrust because of mass conservation arguments. Away from the surface, the scaled number density is slightly higher for the lower thrust simulation than it is for the higher thrust simulation.

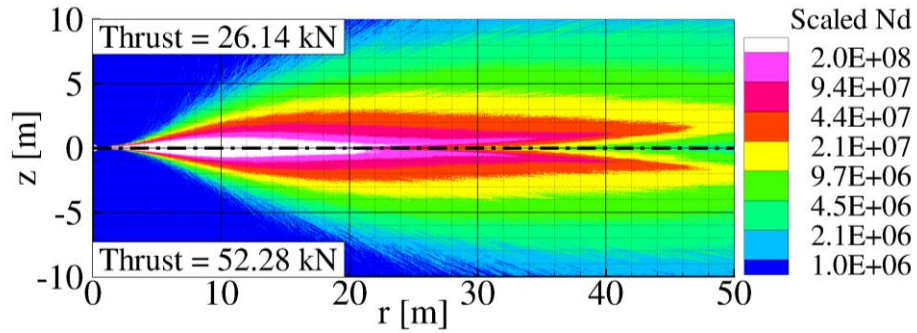


Figure 5.3.3. Scaled number density contours for 2 μm particles for a for different thrust landers hovering 5 m above the lunar surface.

The 2 μm particle velocity profiles are plotted for three different thrust engines at a distance 50 m from the jet axis on Figure 5.3.4.

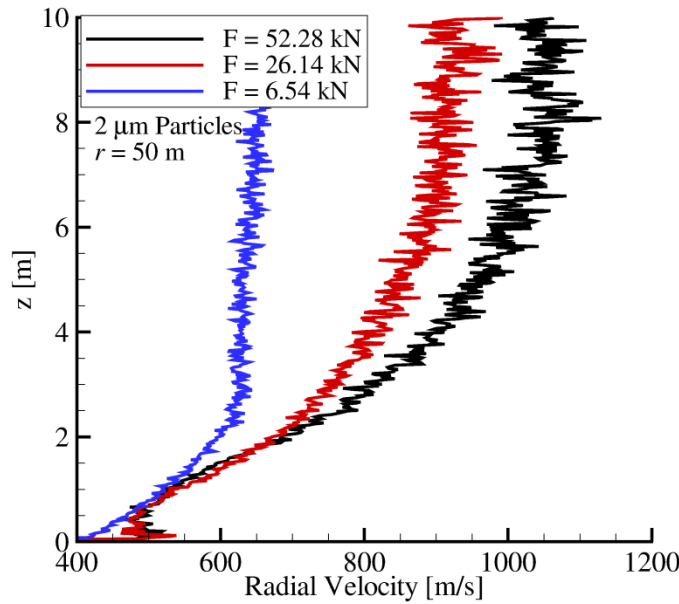


Figure 5.3.4. Velocity profiles for 2 μm particles taken at a distance 50 m from the jet axis. The lines correspond to engines operating at different thrust levels.

The radial velocity for the dust particles near the surface is the same for the 26.14 and 52.38 kN thrust engines. The particles that travel higher above the surface are accelerated to higher speeds for the engine operating at a higher thrust. This is expected because the gas dynamic pressure increases for higher thrust engines.

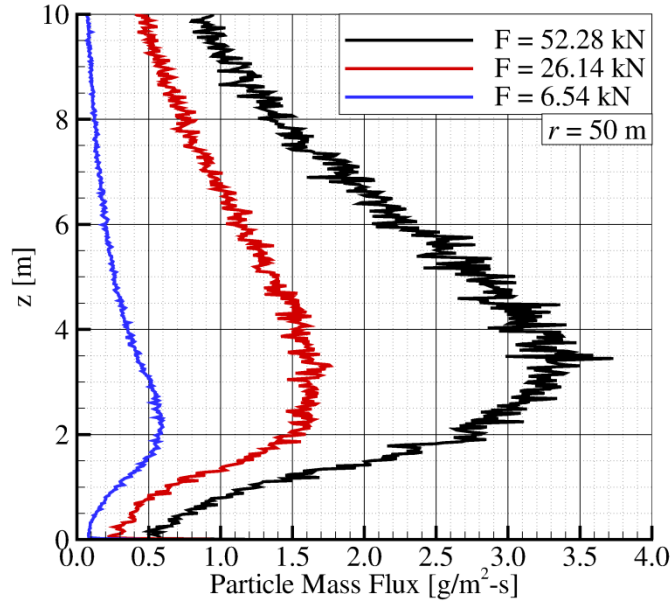


Figure 5.3.5. Particle mass flux profile taken 50 m from the jet axis for different thrust engines hovering 5 m above the lunar surface.

The particle mass flux is plotted in Figure 5.3.5 for different thrust engines. The angle of inclination measured at the location of maximum particle mass flux increases slightly at higher thrusts. The angle of inclination at the location of peak flux is 2.5° for the lowest thrust engine. This low thrust engine corresponds to half the thrust of the LMDE immediately before touchdown. For the higher 26.14 and 52.28 kN engines, the inclination angle does not change significantly and is approximately 3.9° . In (Immer, Lane, Metzger, & Clements, 2011), the authors observed that the dust ejection angle of regolith changes suddenly between frames, within 30 ms, when the Lunar Module was near the surface. They correlated the changes in ejection angle with a sudden change of engine thrust and argued that terrain modification would not be sufficient to cause the sudden change in ejection angle. Our simulations show that the engine thrust does not significantly affect the dust ejection angle either. Therefore, the sudden changes of dust ejection angle observed during the Apollo videos may have occurred because of terrain

modification. One possibility is that a large pebble was dislodged and able to roll along the surface. Surface obstructions such as rocks or pebbles would be more likely to cause an increase in dust ejection angle than engine thrust.

Section 5.4. Chapter Summary

Simulations of axisymmetric plume impingement and dust dispersal on a flat normal surface were discussed in this chapter. The sensitivity of the dust sprays to the different physical models is first discussed. Both the fully coupled gas-particle interaction model and inelastic granular collision model have significant effects on the dust sprays, but granular collisions were found to more strongly impact the dust sprays.

When the gas is coupled to the dust motion, momentum and energy are extracted from the gas and the dust particles tend to be accelerated to slower terminal speeds. In the regions of highest mass loaded, the mass of dust particles is approximately 25 times the mass of gas molecules. The gas coupling also tends to narrow the erosion profile, resulting in less dust entrainment. This results in lower granular number densities and granular collision rates when the gas is fully coupled. The presence of dust also acts to increase the displacement thickness of the gas boundary layer. The gas boundary layer thickens when the gas is fully coupled, but the dust layer has the opposite trend and becomes thinner. This occurs because of the complex coupling between the physical models. The erosion rate is decreased when the gas is coupled. Consequently, the granular collision rate decreases and fewer granular collisions result in a less diffuse dust spray.

As previously stated, granular collisions have the most significant impact on the dust sprays in this work. The inelasticity of the granular collisions is modeled by using an assumed constant coefficient of restitution and the flow fields were found to be very

sensitive to this parameter. The dust sheets are more diffuse for more elastic grain-grain collisions. Simulations with completely inelastic collisions look similar to simulations without any granular collisions. This occurs because perfectly inelastic collisions do not scatter particles upwards and consequently do not diffuse the dust sheet. In this work, the scattering is assumed to be isotropic because there is not enough information in the literature to provide a reasonable estimate for the friction coefficient and restitution coefficient between colliding grains. In future work, measurements made at the Colorado Center for Lunar Dust and Atmospheric Studies may help provide better estimates for restitution coefficients in high velocity impacts. In addition, the coefficient of restitution is in general a function of impact velocity and impact parameter. Further refinements of the granular collision model are likely to immediately improve the accuracy of these simulations.

The effects of hovering altitude on the dust sprays were also discussed in this chapter. At higher hovering altitudes, the dust erosion rate decreases and the particles are accelerated to slower terminal speeds. The terminal speeds for the larger particles tend to decrease nearly linearly as the hovering altitude increases. Smaller particles do not follow the same trend and their terminal speeds are less dependent on hovering altitude. This is thought to be related to granular collisions where at lower altitudes the particles experience a higher drag force but are also inhibited by collisions with larger grains. At higher altitudes, the drag forces are smaller but the particle motions are not inhibited by granular collisions. These effects partially cancel each other for the small particles, resulting in velocity profiles that depend weakly on hovering altitude and display a nearly linear trend. Although not tested in this dissertation, it is likely that these results depend on the particle size distribution of aerosolized particles. When first including granular collisions, a particle size distribution which best captures the mass

fraction of grains was included. This was done because polydispersity was thought to make a difference predominantly via coupling from the dust to the gas and the higher mass fraction grains influence the gas more. Granular collisions play a significant role, and a distribution of grain sizes that better resolves granular collisions may be important. This work will also be aided by improved erosion models that can predict the particle size distribution of aerosolized particles.

The effects of thrust were characterized by adjusting the propellant mass flow rate. The dust emission rate and particle number densities near the surface scale nearly linearly with increasing thrust. The velocity of dust particles near the surface does not change significantly as the engine thrust is increased. The particles traveling near the top edge of the dust sheet are accelerated to higher velocities for higher thrust engines. The inclination angle of the dust spray was not strongly affected by changes in lander thrust. These simulations suggest that observations of sudden changes in dust ejection angle when the lander was close to the surface may occur because of an alternative mechanism. Such a mechanism may be a large pebble or rock becoming dislodged, causing a localized highly deflected dust streak.

CHAPTER 6.

FAR FIELD SIMULATIONS

This chapter discusses the unsteady evolution of the particulate sprays as they travel into the far field. An approximate landing trajectory is simulated during the final 20 m of descent. Weak gravity and a negligible background atmosphere result in particulate sprays that can travel many kilometers from the landing site. This chapter will first discuss the numerical approach for simulating this unsteady problem where the time scales vary from the mean collision time, $\mathcal{O}(10^{-6} \text{ s})$ near the plume axis to mean ballistic times, $\mathcal{O}(10^2 \text{ s})$ in the far field. Simulation results are then presented for the gas and different dust particles as they progress into the far field.

Section 6.1. Method for Staged Simulations

The far field is simulated by using a set of staged calculations. This is done because the near field calculations require small cell sizes and time steps. These are impractically small in the far field where the flow length and time scales are significantly longer. As the solution progresses from the near to far field stages, the time step and cell size are increased. The gas and dust flow fields in the near vicinity of the lander can be treated as quasi-steady because the characteristic time for particles to convect across the computational domain is much shorter than the time associated with the descent velocity. In the far field, however, the descent time is comparable or small compared to the ballistic scale times and an unsteady solution is required. A landing trajectory is approximated by a set of discrete hovering altitudes and an assumed descent rate of approximately 0.5 m/s. The time spent at each altitude is summarized in Table 6.1.1.

There are two different types of staging: one where the boundary inflow is steady and one which is unsteady. The steady patch interface is discussed first. The slowest moving dust particles travel at approximately 300 m/s, see Figure 5.1.12, and the flow field is assumed quasi-steady at distances within 300 m of the lander. The near field is simulated using two computational domains for each hovering altitude that extend to 100 and 300 m respectively. The near field solutions are measured as steady when the particle mass flux at the boundary no longer changes. The gas flow tends to become steady much quicker than the dust particles and most of the simulation time is associated with the time for slow moving dust to convect across the domain. Once steady, the simulators that leave the innermost domain are stored to a patch file that is then used as an input for the next domain. In addition, the time, t_{patch} , over which molecules are stored and the cumulative number of simulators, N_{patch} , are recorded. Inside the next domain, molecules are randomly sampled with replacement from the patch file at each time step of new duration Δt . The number of created simulators is

$$N_{create} = N_{patch} \frac{\Delta t}{t_{patch}}. \quad 6.1-1$$

The weight, or number of real molecules represented by each simulator, also changes from the inner to outer domains. Since a spatially varying weighting function is used, not all patch simulators have the same weight. To ensure particle flux is conserved, created patch molecules are kept if $R_f < q_{old}/q_{new}$, where R_f is a uniformly distributed random number between 0 and 1 and q is the simulator's weight. The weight typically increases from the inner to outer domains and particle cloning never happens when staging.

At distances beyond 300 m from the jet axis, the convective time scales of the flow are no longer short compared to the lander descent rate and an unsteady patch

interface is used. The far field is simulated using two unsteady domains that extend to 5 and 500 km respectively. The first unsteady domain reads the molecules from all of the steady state patch files, starting at 20 m hovering altitude for 8 s and then progressing to lower altitudes. The molecules that exit the unsteady domain are stored along with the time at which they exited the domain. These molecules are then read by the second unsteady domain and created at the appropriate simulation time. The unsteady domains are then simulated until all of the dust particles leave the domain or impact the ground.

Table 6.1.1. Altitudes and durations simulated for an approximate landing trajectory.

Altitude	Duration
20.0 m	8 s
15.0 m	6 s
12.5 m	4 s
10.0 m	4 s
7.50 m	4 s
5.00 m	6 s
3.00 m	8 s

Section 6.2. Far Field Gas Flow

Within the first 300 m from the plume axis the gas flow can be regarded as steady. Contours of gas mean free path are plotted on Figure 6.2.1 for a rocket engine hovering at an altitude of 10 m for the two innermost computational domains. The lander hovering altitude does not significantly affect the gas flow field along the interface with the unsteady domain because the engine hovering altitude is small relative to the dimensions of the steady domain. The unsteady interface is constructed along a rectangle with a height and width of 200 m and 300 m, respectively. The gas mean free path along the unsteady interface is approximately 15 m.

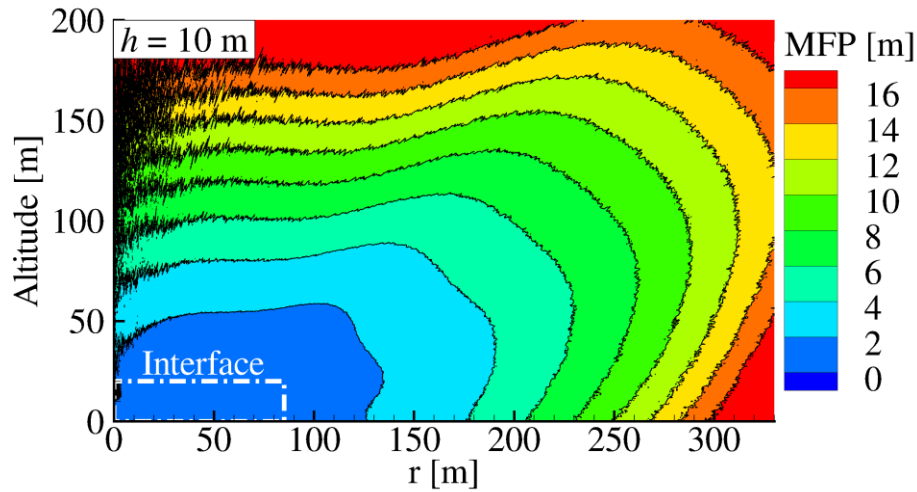


Figure 6.2.1. Contours of the gas mean free path within the two steady flow domains. The innermost domain interface is drawn via the white dash-dotted line. The rocket engine hovers at an altitude of 10 m.

The first unsteady domain extends 5 km high and 5 km from the axis. The radial cell spacing near the interface is 10 m and is progressively increased for processors further from the axis. The vertical cell spacing is a uniform 17 m for all processors. Near the axis, the flow is mean free path resolved in both radial and vertical directions. Far from the symmetry axis, the mean free path is over-resolved and the vertical cells are approximately 200 times smaller than the mean free path at a distance 5 km from the lander.

The second unsteady flow domain extends 175 km high and 500 km from the lander. The cell sizes in this domain are small compared to the mean free path and are 1 km tall and wide. The relatively small cell size is selected to resolve the ballistics of the flow. The time step resolves the mean convective time scale across cells and is 0.05 s in the outermost domain.

Contours of gas number density are shown in Figure 6.2.2 at instances 70 and 90 s after the lander first descends within 20 m of the lunar surface.

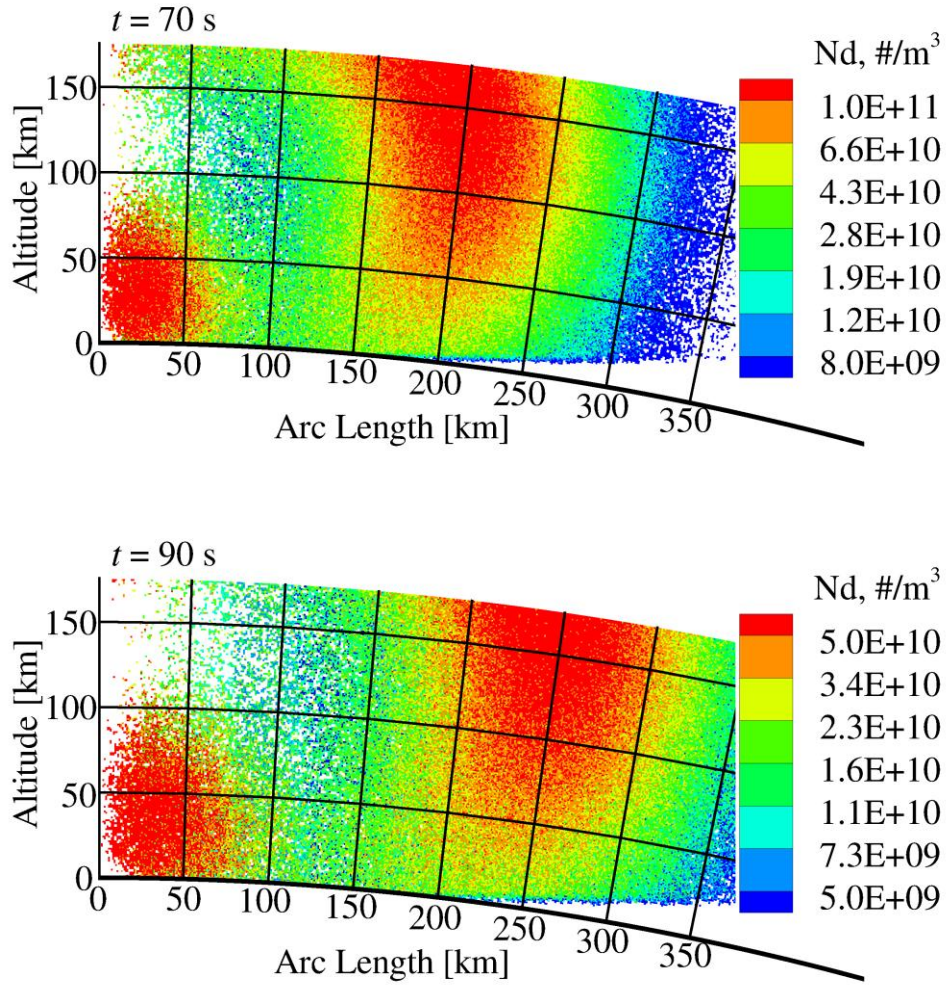


Figure 6.2.2. Gas number density contours 70 s (top) and 90 s (bottom) after the lander first entrains regolith at a hovering altitude of 20 m. Note the curvature of the planet limb.

There are two main features observed in the gas flow fields. First, the leading edge of the expansion is seen moving outwards at a speed of approximately 2700 m/s. Many of these molecules are expected to escape because lunar escape velocity is approximately 2370 m/s. These simulations neglect the exhaust gases emitted at altitudes higher than 20 m. Consequently, the leading front of the gas expansion is a thinner band than what would actually be observed if a full landing were simulated.

Behind the leading edge, there is a secondary puff of gas that slowly travels outwards. As will be discussed later, the secondary puff of gas corresponds with the location of the dust cloud. The secondary puff of gas results from molecules that are trapped within the dust spray.

There is also a region near the surface and leading edge of the gas expansion that is shielded from the gas. This occurs because the gas at the leading edge is hypersonic, approximately Mach 20, and unable to further expand and follow the curvature of the moon. The temperature and pressures are also extremely low. The translational gas temperature cools and is typically less than 50 K in the far field.

Section 6.3. Unsteady Dust Sprays and Deposition

An unsteady simulation has been performed to see where the scoured dust travels in the far field. At these distances from the lander, the gas flow is free molecular and the dust particles follow ballistic trajectories. In Figure 6.3.1, contours of dust number density are presented for 800 nm and 8 μm grains at different times after engine shutoff. The dust cloud diffuses as it travels outwards, but the different sized grains tend to separate. This separation occurs because the smaller particles are able to accelerate in the very near field to higher velocities, as discussed previously. The smaller 800 nm particles travel at approximately 1 km/s compared to 550 m/s for the 8 μm particles. These speeds are comparable to the near field speeds, see Figure 5.2.2 and Figure 5.2.3, indicating that the particles were not affected by the gas in the far field. The number densities of the various dust particles are very small because the dust spray is expanded over a very broad volume.

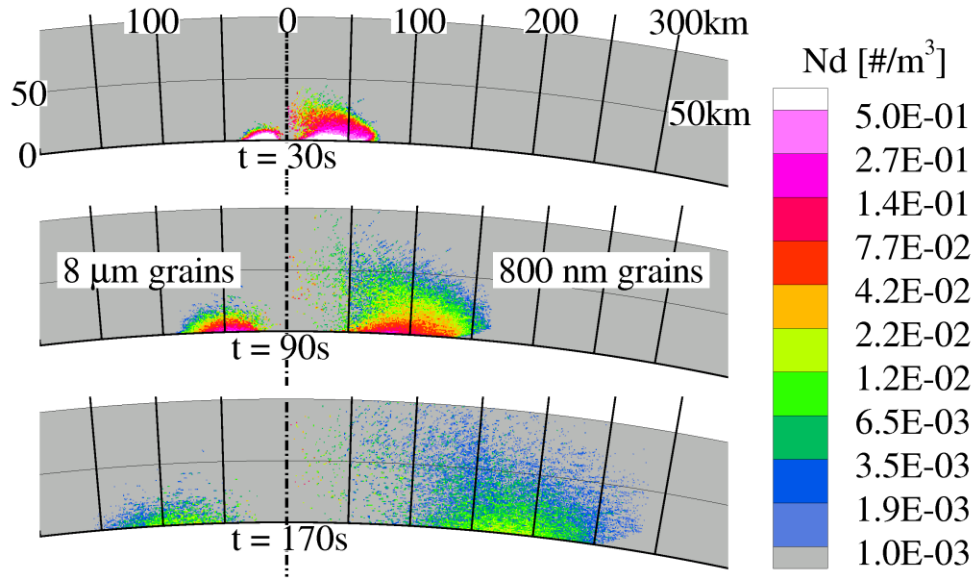


Figure 6.3.1. Snapshots of 800nm (right) and 8 μ m (left) particle number densities at times 30, 90, and 170s after engine shutdown. Note that the actual computational domain extends to much higher altitudes and distances from the lander.

The dust particles separate based on their size because smaller particles are accelerated to higher velocities.

The particles that strike the ground during an entire landing event are counted and the net deposited mass per unit area for different sized grains is shown in Figure 6.3.2. In an axisymmetric calculation, the mass deposition flux, Φ_d , can be time integrated to give the deposition areal density, D_d in equation 6.3-1

$$D_d(s) = \int_0^{\tau_{\text{landing}}} \Phi_d(s, t) dt \approx \sum_j \Phi_d(s; h_j), \quad 6.3-1$$

where s is the arc length along the surface measured from the lander and h_j are the set of discrete hovering altitudes. The particles that strike the ground during an entire landing event are counted and the net deposited areal density, D_d , is shown in Figure 6.3.2 for different sized grains. Within the first 100 km of the landing site, the 8 and 11 μ m grains comprise the bulk of the deposition. Deposition at greater distances from the

landing site is dominated by the smaller particles because only these particles are accelerated to high enough speeds to travel far from the landing site. The particle number densities and deposition rates are quite low and any appreciable accumulation of deposited particles is not expected at these distances. The discontinuities in the deposition distribution located approximately 40 km from the lander are thought to occur because the landing trajectory is modeled as a sequence of discrete hovering altitudes.

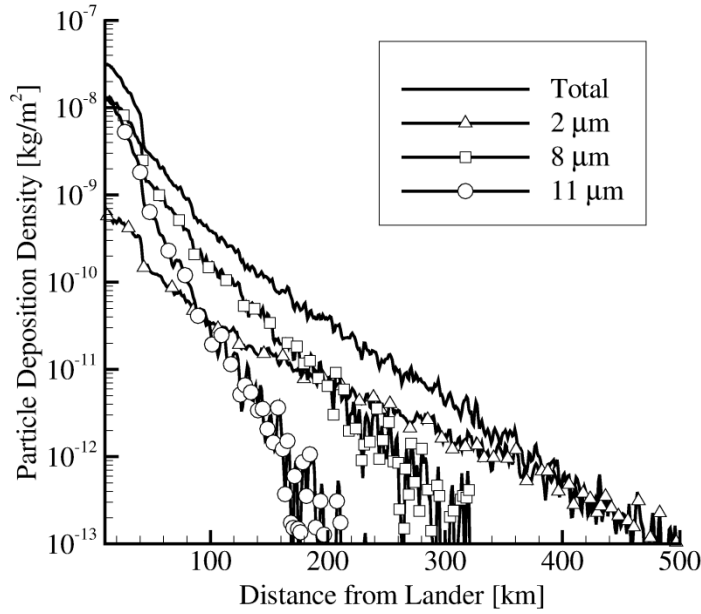


Figure 6.3.2. Distributions for 2, 8, and 11 μm particles as well as the total mass deposition density resulting from an approximate lunar landing. Note the logarithmic scale on the vertical axis.

The total mass deposited, M_d , can be computed by integrating the deposition areal density and is described by equation 6.3-2 for deposition on a spherical moon, where R_{Moon} is the radius of the Moon..

$$M_d = \int_0^{\pi R_{Moon}} 2\pi R_{Moon} \sin\left(\frac{s}{R_{Moon}}\right) D_d(s) ds, \quad 6.3-2$$

The integrand of equation 6.3-2 is the amount of mass that is deposited between an arc length s and $s + \Delta s$ of the landing site and is called the radial-weighted deposition density. This distribution is plotted versus the distance along the surface from the lander in Figure 6.3.3.

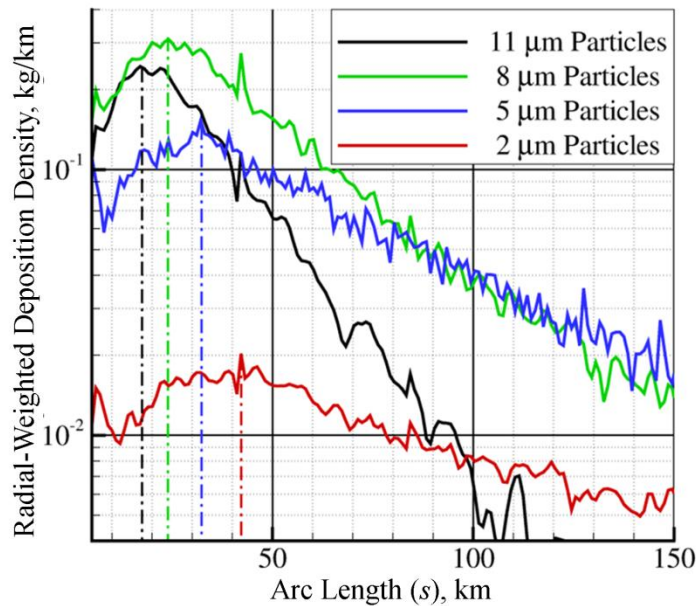


Figure 6.3.3. The total mass deposited with an arc length between s and $s + \Delta s$ of the lander. The different lines correspond to different size particles and the dash-dot lines indicate maxima. Note the log scale on the vertical axis.

This distribution is significant because it can be used to clearly show how far particles of different sizes travel during a typical lunar landing. As previously stated, the larger particles are typically deposited closer to the landing site. The distances at which the peak radial-weighted deposition density occurs is indicated by the color coded dash-dot lines. Although the gas is able to reach lunar escape velocity, 2300 m/s, none of the simulated grains obtain these speeds. In (Metzger, Lane, & Immer, 2008; Lane, Metzger, & Immer, 2008), some of the smaller particles approached escape velocity.

This was not observed in the present work, and may be due to mass-loading effects as well as granular collisions. These physical phenomena reduce the maximum speeds for smaller particles and are discussed in Section 5.1.

Particle separation is directly seen in Figure 6.3.4, where the distance from the lander at which peak radial-weighted deposition density occurs is evaluated for different sized grains.

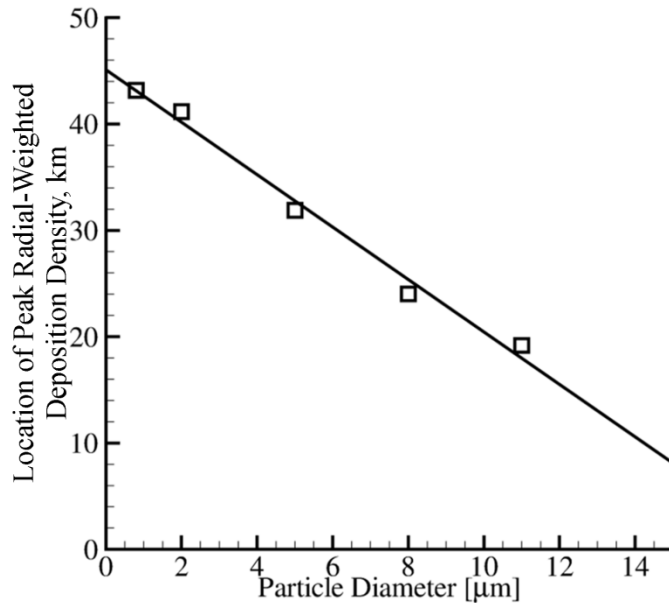


Figure 6.3.4. The distance from the lander at which peak radial-weighted deposition occurs (corresponding to data in Figure 6.3.3) for different sized particles and a linear best fit of the data.

Smaller grains are deposited further from the lander and the trend is approximately linear in particle diameter for values within the 800 nm to 11 μm range. Physical arguments suggest that the linear trend should not be extrapolated to particle sizes outside of the simulated range. Extremely small particles should closely track the gas velocity and would consequently reach escape velocity. If the linear fit were extrapolated to small particles, the location of peak deposition would incorrectly be predicted to not exceed 44.8 km from the landing site. If one were to extrapolate the

linear fit towards the largest grains, particles with diameters greater than $18.3\text{ }\mu\text{m}$ would not be entrained into the flow. From Apollo landing videos (Immer, Lane, Metzger, & Clements, 2011), large particles were observed to be blown or saltated by the rocket exhaust.

The simulated particle sizes in this work tend to be deposited at distances between 19 and 42 km from the lander, but the highest deposition areal density occurs closer to the lander. Images from the Lunar Reconnaissance Orbiter were analyzed and it was found that regions within 75 m of the Apollo landing sites were brightened compared to surrounding lunar regions (Clegg, Jolliff, & Metzger, 2012).

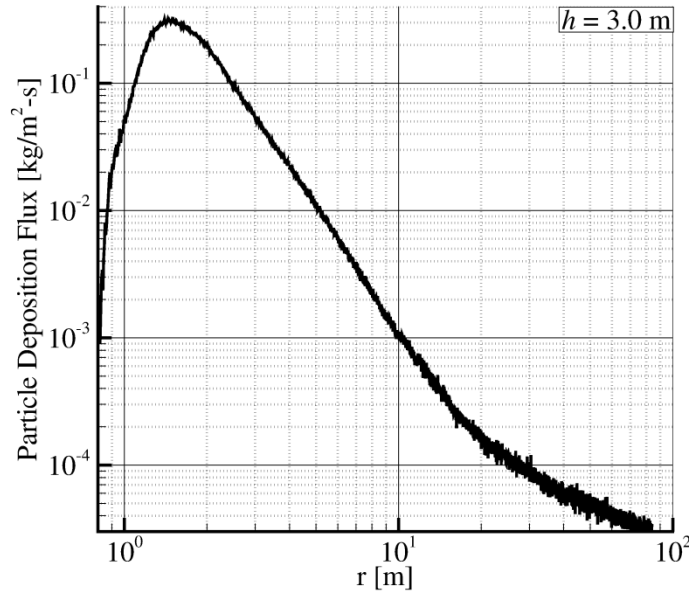


Figure 6.3.5. The total particle deposition flux in the near field of the lander when the rocket engine hovers 3.0 m above the surface. Note the log-log scale.

Although the distance of peak radial-weighted deposition density occurs many kilometers from the landing site, the non-weighted deposition density, we find, is extremely small because the deposition is spread over a large area. The particle deposition density is approximately $1.0 \times 10^{-8}\text{ kg/m}^2$ at a distance 20 km from the landing

site and is very small compared to the deposition density near the lander. The deposition flux within 100 m of the lander is shown in Figure 6.3.5 for an engine hovering 3 m above the surface. Time integration of the deposition flux in the near field shows that the deposition density in the near field is significantly larger than that in the far field that was previously shown in Figure 6.3.2.

Section 6.4. Chapter Summary

The transport of eroded dust during a typical lunar landing was simulated from the erosion regime to where particles were deposited many kilometers away. Within the near field, the flow fields are quasi-steady because the convective time scales are extremely short compared to the lander descent rate. In the far field, the ballistic time is long compared to the lander descent rate and an unsteady solution is necessary. The unsteady solution was obtained by using a set of steady state near field solutions as an inflow boundary condition for the outer domains. The computational time step and cell size were increased as computational domains progressed further from the landing site.

There were two distinct clouds of gas which progressed into the far field. The leading expansion of gas consisted of molecules which were unaffected by the presence of dust. A secondary cloud of gas lagged behind the leading edge of the expansion. The secondary cloud consisted of gas molecules trapped within the dust layer. The leading edge of the gas expansion traveled at high speeds, high enough that many molecules exceed lunar escape velocity. Although not examined in this work, it would be interesting to know how much gas remains trapped by lunar gravity. Over the course of many landings, the trapped gas may have an impact on the lunar atmosphere and environment.

Larger dust particles tend to decouple from the gas earlier and attain lower terminal velocities than the smaller particles. Consequently, as the dust cloud expands to the far field, particles of different sizes tend to separate. The largest particles are deposited closer to the lander than the smaller particles. For the particle sizes investigated the location of peak mass deposition within arc length s and $s + \Delta s$ is approximately inversely proportional to the particle diameter. The simulated particle sizes in this work tend to be deposited at distances between 19 and 42 km from the lander, but the highest deposition areal density occurs closer to the lander. Images from the Lunar Reconnaissance Orbiter indicate a brightened region within 75 m of the Apollo lander. The brightened regions are thought to occur (Clegg, Jolliff, & Metzger, 2012) because of either deposition of material or smoothing of the surface from erosion. Our findings suggest that the brightened regions could occur because of deposition on the surface as the regions with the highest deposition density occur near the landing point. The erosion region is also confined near the lander and would be unlikely to substantially smooth the surface to create such a large brightened region.

CHAPTER 7.

INTERACTION WITH A LUNAR FENCE

Without the construction of landing pads, it may be difficult to prevent the formation of high velocity dust sprays. These dust sprays can be hazardous to pre-existing structures on the Moon, such as a lunar outpost or scientific equipment. To protect such structures from the ejecta, different mitigation techniques such as a lunar fence or berm have been proposed. The interaction of the dust sprays with such a fence is examined in this chapter. The effects of fence placement, height, angle, and the sensitivity to the fence restitution coefficient are examined.

Section 7.1. Effects of Fence Placement

7.1.1. GAS INTERACTIONS

When gas molecules interact with the lunar fence, they undergo diffuse reflection with an assumed characteristic temperature of 350 K. When the fence is placed 15 m from the jet axis, an oblique shock forms upstream of the fence as the supersonic flow is deflected over the obstacle. These phenomena are shown by gas number density contours in Figure 7.1.1. This oblique shock impinges on the boundary layer, causing it to separate and a recirculation bubble forms in front of the fence. The boundary layer, without an obstacle, is approximately 2 m thick at a location 15 m from the jet axis (see Section 4.4.1 for boundary layer profiles). Outside of the boundary layer, the streamlines are deflected upwards as the gas is processed by the oblique shock. Downstream of the fence, the gas expands towards the surface and a new boundary layer develops.

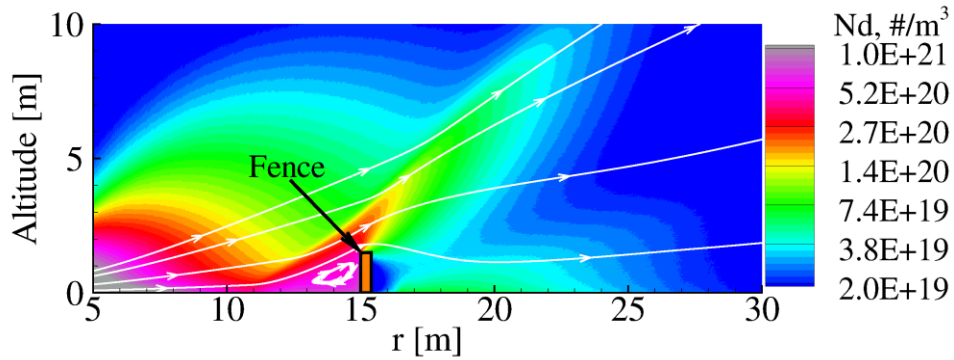


Figure 7.1.1. Gas number density contours and streamlines near a 1.5 m tall fence placed 15 m from the plume axis.

If the fence is placed further from the jet axis, shown in Figure 7.1.2, the boundary layer is very thick compared to the height of the fence and the flow structures change. The flow within the boundary layer is subsonic and an oblique shock does not form as the flow impinges on the obstacle. Consequently, the boundary layer is not separated and a separation bubble does not form upstream of the fence. Vortices downstream of the fence were neither evident in instantaneous nor time averaged samples.

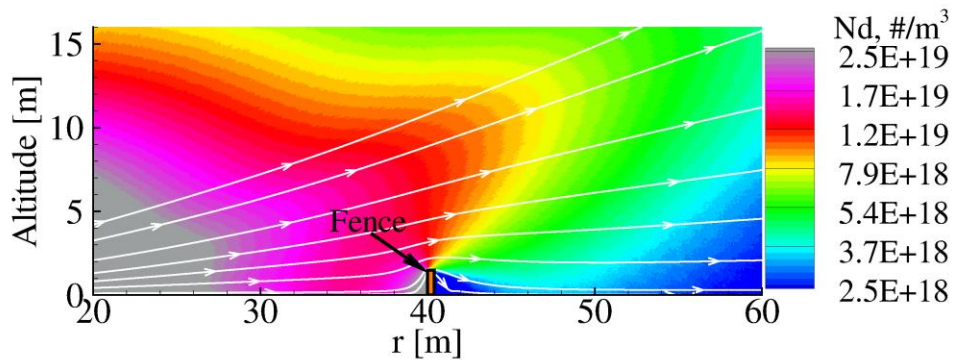


Figure 7.1.2. Gas number density contours near a 1.5 m tall fence placed 40 m from the plume axis.

Despite changes to the gas flow field, the dust trajectories are only significantly affected if the drag forces are large. The gas density upstream of the fence is

significantly less when the fence is placed at 40 m compared to a closer placement of 15 m. Consequently, the influence that the gas-fence interaction has on the dust is expected to diminish as the fence is placed further outboard.

7.1.2. DUST INTERACTIONS

In the following simulations, the fence normal and tangential coefficients of restitution for particle impacts are 0.1 and 0.5, respectively. The number density of 8 μm particles is contoured in Figure 7.1.3 when a 1.5 m tall fence is placed 15 m from the jet axis.

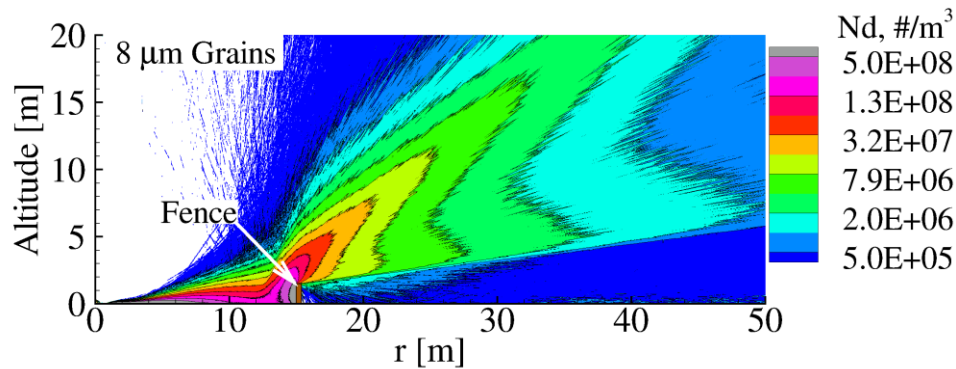


Figure 7.1.3. Number density contours for 8 μm particles impinging on a 1.5 m tall fence placed 15 m from the jet axis.

Downstream of the fence, there are two classes of particles: those that avoid the fence and continue streaming along at high velocities and those that bounce off the fence and are deflected upwards. Downstream of the fence, relatively few particles are deflected downward. At this location, the drag forces from the gas are insufficient to turn the high velocity dust particles. Some particles, however, are deflected downwards because of granular collisions. The heavier particles also behave differently than the lighter particles because the heavier ones have more inertia and are less influenced by the gas.

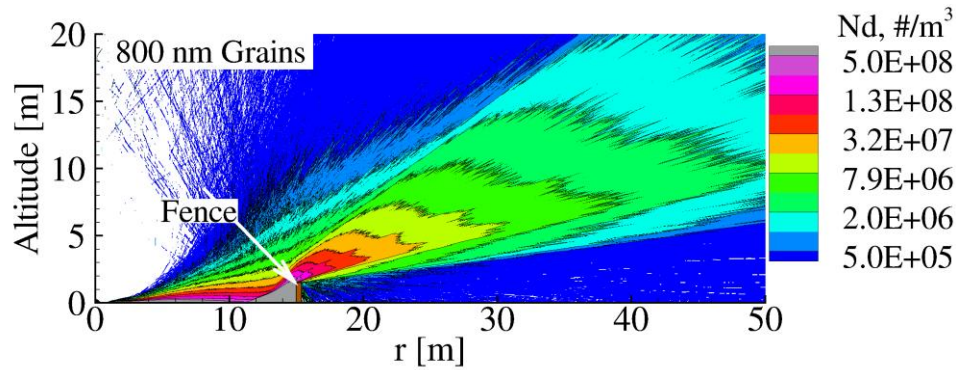


Figure 7.1.4. Number density contours for 800 nm particles impinging on a 1.5 m tall fence placed 15 m from the jet axis.

The number density for 800 nm particles is contoured in Figure 7.1.4. These particles are significantly lighter than the 8 μm particles and track the gas flow more closely. This is evident because some of the lighter particles are entrained into the separation bubble upstream of the fence, whereas the heavier particles are not. In addition, the lighter particles that reflect off the fence are not deflected at as high of an angle. This occurs because the lighter particles that are deflected upwards can more readily be turned outward by the gas. The 800 nm particles downstream of the fence can also be generally classified as either high speed particles that avoided the fence or slower particles that bounced off the fence.

The dust flow structures change as the fence is placed further from the jet axis. Dust number density profiles for a fences placed 30 and 40 m from the lander are shown in Figure 7.1.5. The dust grains tend to bounce further off fences further from the jet axis, and fewer dust particles are deflected vertically upward. The larger bounces occur because the gas is thinner and the particles can rebound a further distance before being turned back by the incident gas. When the fence is placed 15 m from the jet axis, the particles rebound approximately 2 m upstream of the fence while when the fence is at 30 and 40 m from the jet axis, the particles rebound 7 and 11 m, respectively. Fewer

particles are deflected vertically upward when the fence is placed 30 or 40 m from the axis, compared to 15 m. This occurs because the dust layer thickens as it expands outwards. Consequently, fewer particles strike the fence since the fence height is held constant. Despite relatively fewer particles being deflected upwards, the fence is still effective at shielding leeward structures that are shorter than the fence height.

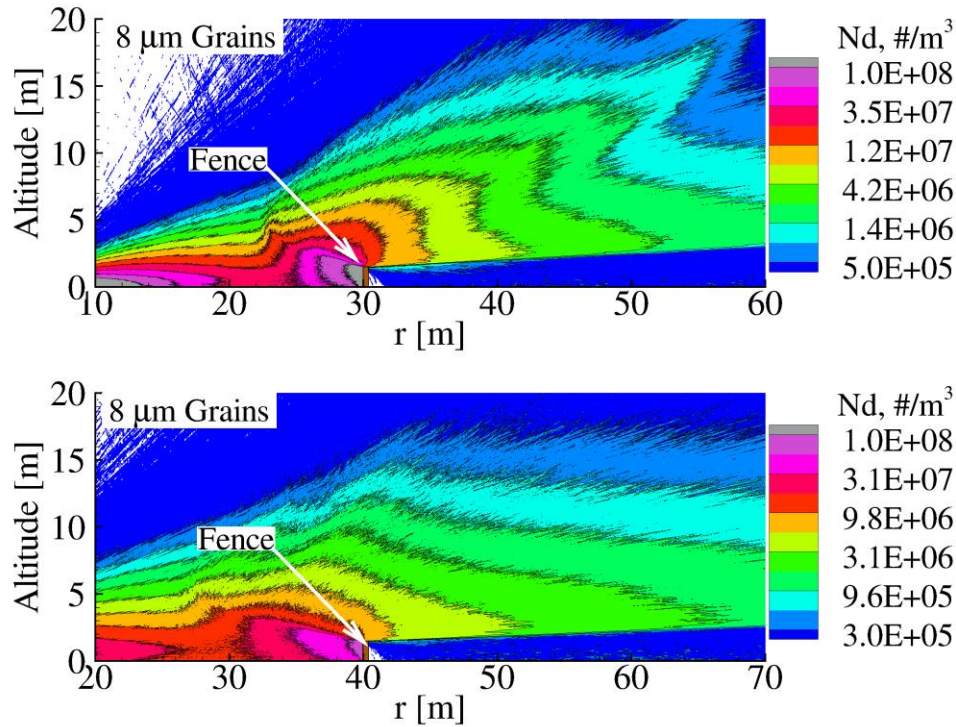


Figure 7.1.5. Number density for $8\ \mu\text{m}$ particles when a 1.5 m tall fence is placed 30 m (top) and 40 m (bottom) from the jet axis.

To assess the effectiveness of the fence, the particle mass flux downstream of the fence is compared for different fence placements and plotted in Figure 7.1.6. The effective shielding height decreases as the fence is placed further outboard. This occurs because the important parameter for fence design is the fence height to radial placement ratio. A fence placed inboard is able to block particles that travel with higher inclination angles compared to a fence of same size placed further from the landing site. The

particle mass flux is reduced as the fence is moved inwards because inboard fences are able to block more of the dust spray. The gas deflected by the shock and the back-scattered grains are together dense enough to deflect the oncoming stream. In regions not shielded by the fence, the particle mass flux profile is similar to the case without an obstacle.

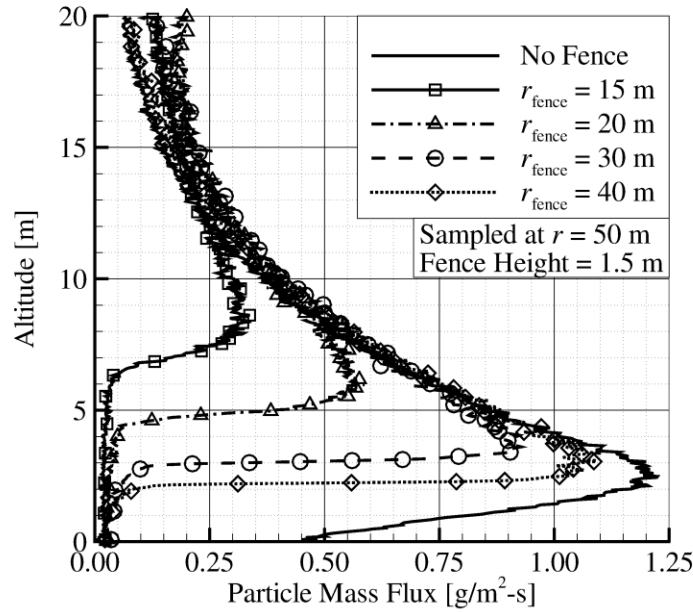


Figure 7.1.6. Particle mass flux sampled 50 m from the jet axis for lunar fences placed at 15, 20, 30, and 40 m. The particle mass flux is also plotted when a fence is not used.

The shielding angle, α_{shield} , shown schematically in Figure 7.1.7, is defined as the inclination angle of the top edge of the shielded region. As previously stated, the important parameter for fence design is the ratio of fence height to placement. Geometric arguments provide a reasonable prediction for how well a fence will shield the dust, where the shielding angle is approximately the arctangent of the ratio of fence height to placement. As the fence is placed further inboard, the measured shielding

angle exceeds the geometric approximation because the dust sprays originate from a virtual source that is offset from the jet axis.

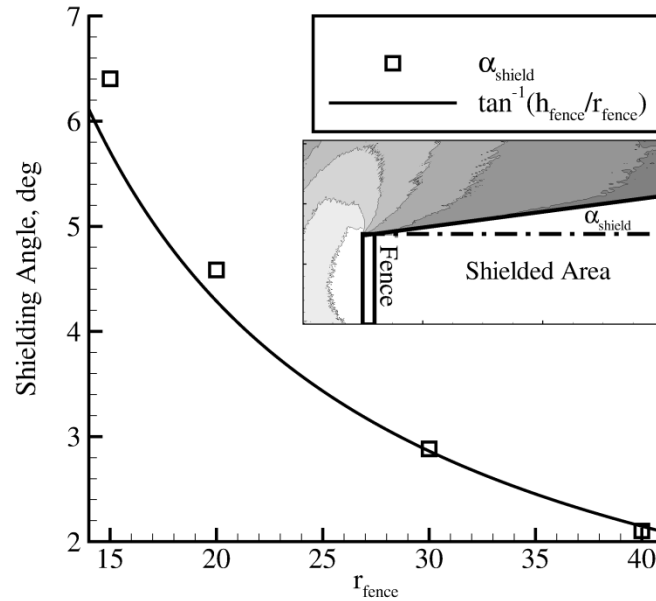


Figure 7.1.7. Shielding angle for 1.5 m tall fences placed at various locations.

Although not the focus of this dissertation, the particle impact energy downstream of the fence is important when predicting damage to nearby structures. The mean velocity of particles may be misleading because some particles travel at very high speeds where others that rebound off the fence travel much slower. An estimate for the maximum particle impact energy can be obtained by sampling velocities from a simulation without an obstacle at heights above the shielded area. This estimate is reasonably accurate because the particles that avoid the fence are not significantly affected by grain-grain collisions or the deflected gas.

These results suggest that a well designed lunar fence should be tall and relatively close to the landing site. The forces on the fence, however, increase as the fence is placed further inboard. The force exerted on the fence arises from gas pressure as well

as the impulse of particles striking the fence. The contributions from each of these components are plotted for fences placed 15 and 40 m from the jet axis on Figure 7.1.8.

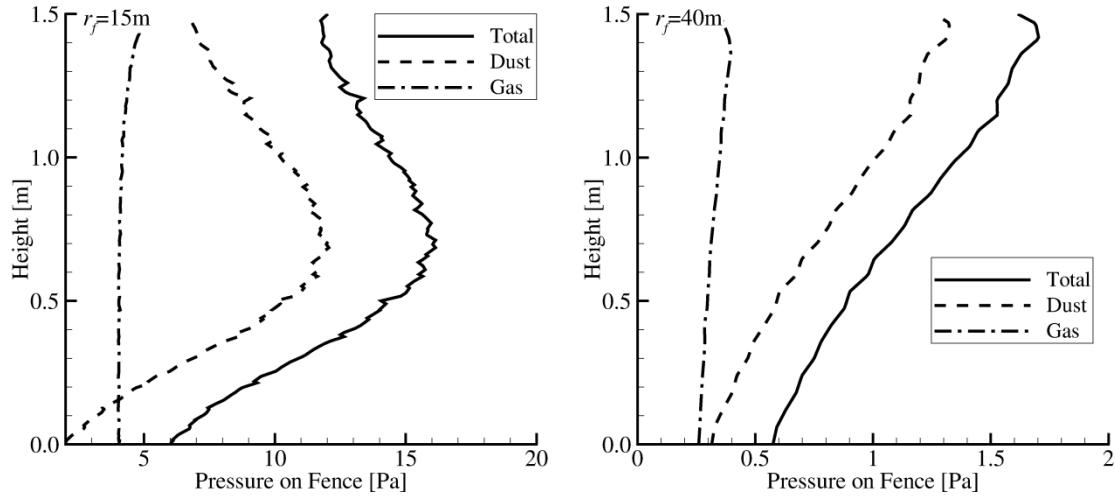


Figure 7.1.8. Pressure distribution on a 1.5 m tall fence placed 15 m (left) and 40 m (right) from the jet axis. The separate force contributions from the dust and gas are shown as well.

Dust particle impacts on the fence account for most of the force. The shape of the pressure profiles change as the fence is moved further away because the fence is exposed to different parts of the dust spray. When placed close to the lander, the fence blocks most of the dust spray and the maximum particle momentum flux occurs approximately midway up the fence. At further distances, the fence only shields the bottom regions of the dust layer where the particles are typically moving slower. The gas pressure is nearly constant along the height of the fence because upstream is a stagnation region. The stagnation pressure decreases at further distances because the boundary layer thickens and is quite large compared to the fence height at 40 m.

The average pressure exerted on a 1.5 m tall fence is plotted versus fence placement on Figure 7.1.9 (left). A best fit curve indicates that the force exerted on the

fence decreases approximately as $P_{avg} \propto r_f^{-2.463}$. Roberts theory predicts that the gas dynamic pressure decreases proportionally to r^{-2} , as shown on Figure 4.4.11. The fence pressure decays more rapidly because the boundary layer thickens and stagnation pressure in lower portions of the boundary layer decreases. The center of pressure increases as the fence placement increases from 15 to 30 m. This occurs because the dust layer thickens and the height of peak particle flux increases at greater distances. The location of peak pressure on the fence corresponds to the height of peak particle momentum flux. After 30 m, the center of pressure remains nearly constant because the fence is short compared to the dust layer thickness and the pressure profiles on the fence are nearly linear, illustrated on Figure 7.1.9 (right).

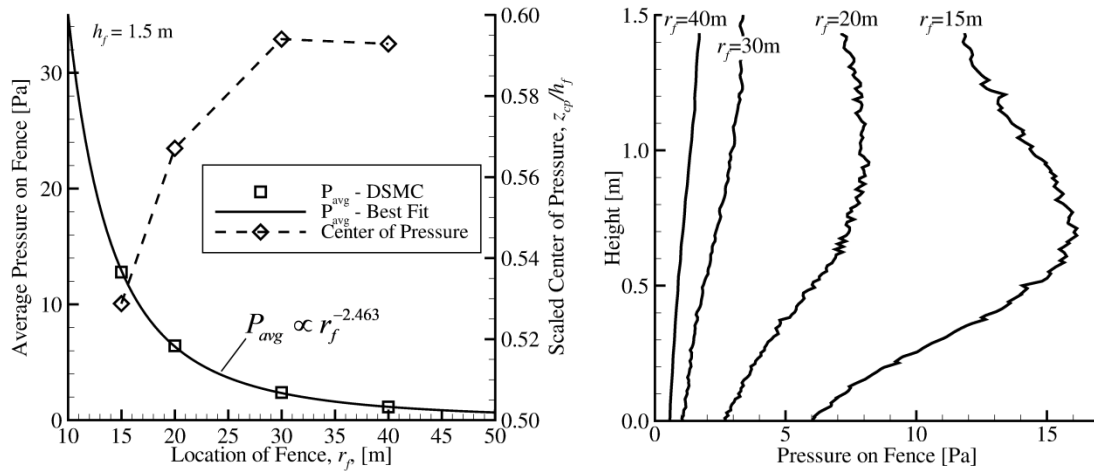


Figure 7.1.9. (left) Mean pressure exerted on fences placed at different locations from the lander. The center of pressure is plotted on the right axis. (right) Fence pressure distributions for different fence placements.

Section 7.2. Fence Height

The effects of fence height are examined for fences placed 15 m from the jet axis. The gas flow field changes for different heights, and is shown for 0.75 and 2.5 m tall fences in Figure 7.2.1. Without a fence, the maximum particle mass flux occurs at a

height of 0.7 m and the boundary layer thickness is approximately 2 m thick at a distance 15 m from the jet axis. A separation bubble upstream of the fence is present for both the small and tall fences. The size of the separation bubble extends to the top of the fence and is therefore significantly larger for the taller fence. The oblique shock is steeper for a taller fence because the streamlines are more substantially deflected upwards.

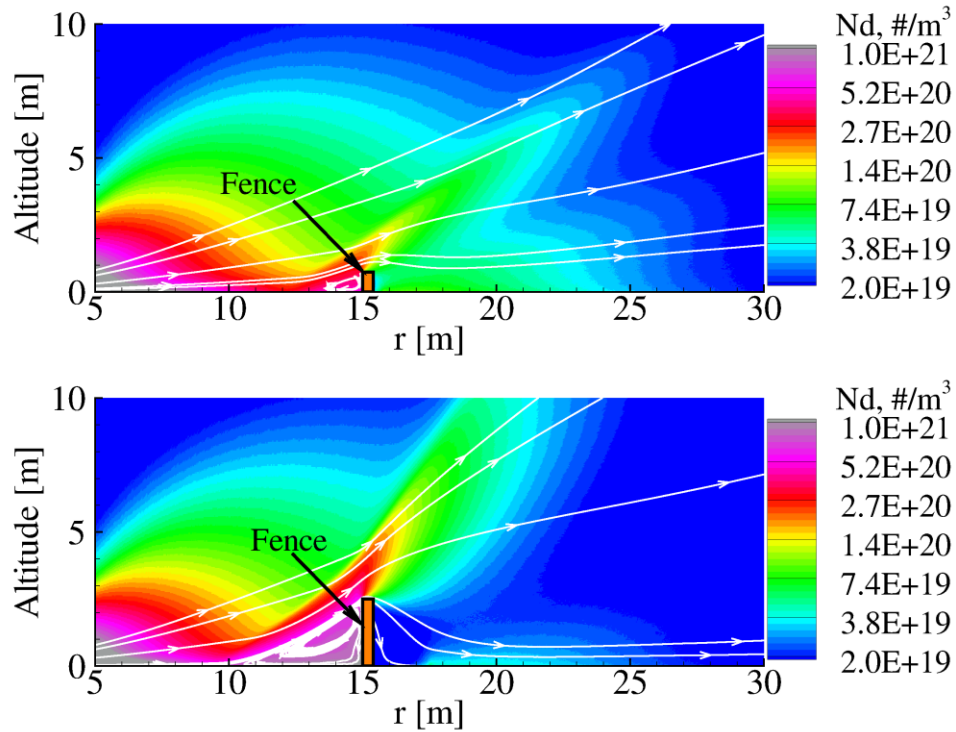


Figure 7.2.1. Contours of gas density for fences placed at 15 m that are 0.75 and 2.5 m tall respectively.

The gas expands over the fence and reattaches to the surface downstream of the fence. A new boundary layer develops as the flow downstream of the fence expands to vacuum. For the smaller fence, less of the gas flow is deflected upward and the downstream density near the surface is significantly higher compared to the taller fence.

The dust particles exhibit similar trends as the gas when interacting with different size fences. Dust number density contours are shown in Figure 7.2.2 for two different size fences.

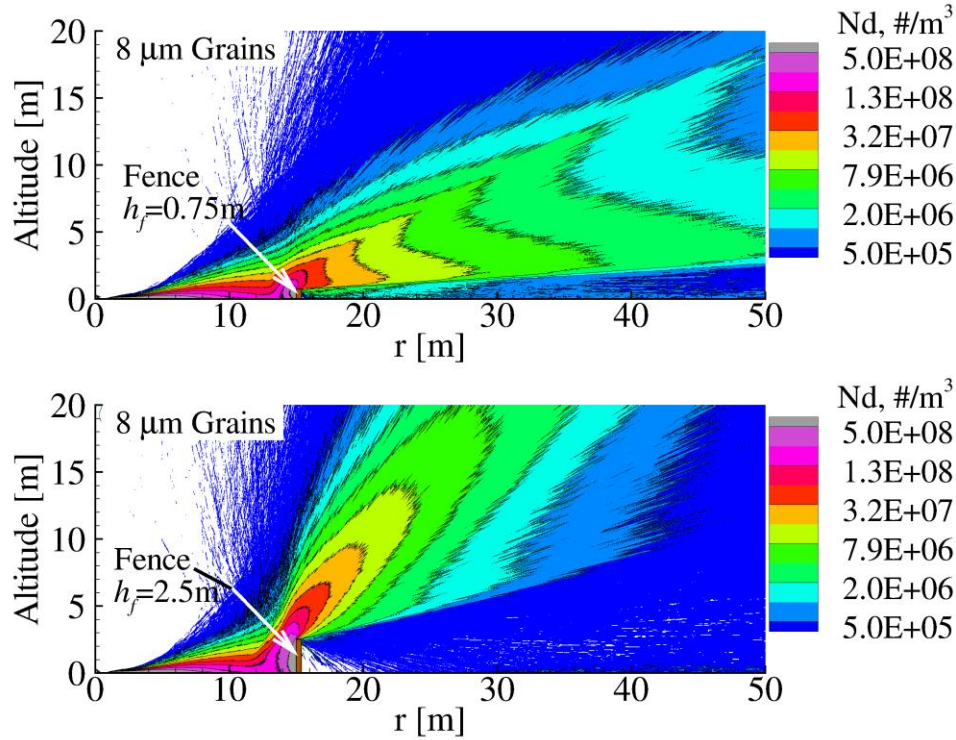


Figure 7.2.2. Number density profiles for 8 μm particles for a 0.75 m (top) and 2.5 m (bottom) tall fence placed 15 m from the jet axis.

The 2.5 m tall fence is large enough such that it blocks nearly all of the incident dust spray and deflects this dust upwards. Consequently, an arrowhead type structure does not form in the wake because relatively few particles pass by the fence without striking it or being strongly affected by the gas shock or grain-grain collisions. The shorter fence does not block the entire dust spray and consequently an arrowhead flow structure forms, where the lower portion of the dust wake consists of particles that avoided the fence.

The fence shielding angle is approximately 12.8° for the 2.5 m tall fence and only 3.0° for the shorter 0.75 m tall fence. The geometric fence angles, $\tan^{-1}(h_f/r_f)$, are 9.46° and 2.86° for the respective tall and short fences. The shielding angle is approximately 35% larger than the geometric angle for the tall fence and only 5% larger for the short fence. This enhanced shielding occurs because grains that reflect off the fence are deflected upwards at a high angle whereas grains that avoid the fence remain on a trajectory that is relatively unaffected.

One concern with a highly deflected dust spray is that the particles may rain down upon the structure to be protected. The heaviest particles travel the slowest and are most likely to be deposited closer to the landing site. A subset of the representative $11\text{ }\mu\text{m}$ particles, colored by their speeds, is overlaid upon line contours of particle number density in Figure 7.2.3. The highly deflected particles still travel at speeds in excess of 100 m/s. From ballistics arguments, these particles will not strike the lunar surface within many kilometers from the landing site and therefore do not pose a threat to nearer structures. There are several particles that are scattered towards the ground on the lee side of the fence. These particles are relatively infrequent but can still pose a potential threat to any structures close to the fence.

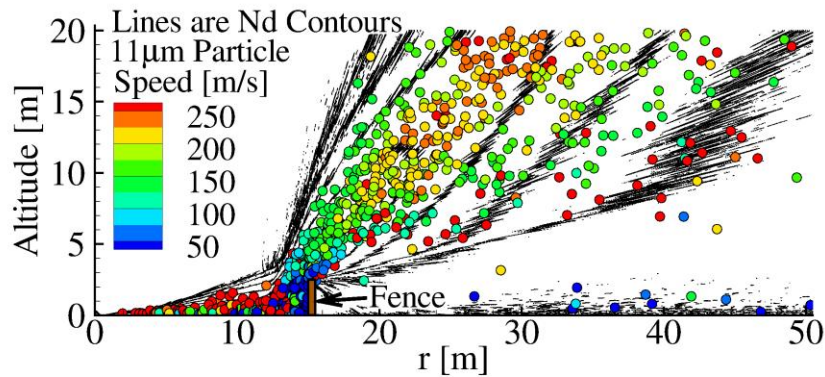


Figure 7.2.3. Simulators for 11 μm particles are colored by their speed and plotted on top of line contours of particle density.

Section 7.3. Fence Angle

A different mitigation technique is to use in situ resources to construct a berm out of lunar regolith. Such a berm would be constructed at the angle of repose of the soil. The angle of repose of lunar soil has a regional dependency and is estimated to be between 30° and 50° in Table 2.6.1. A berm can be modeled by tilting the fence and reflecting particles off it using tangential and normal coefficients of restitution. The coefficients of restitution in the normal and tangential direction were again assumed to be 0.1 and 0.5, respectively. The berm angles modeled are 30° and 45° and the hypotenuse of the berm is 2 m. The corresponding vertical heights of the berms are therefore 1.0 m and 1.4 m tall. The backside of the berm is neglected because hardly any particles impact the backside.

The number densities for 8 μm grains impacting the different berms are shown in Figure 7.3.1. The shielding is qualitatively similar to what was observed with a vertical lunar fence. The lower portion of the wake consists of particles that avoided the berm while the upward spray of deflected particles consists of those that impacted the berm or were scattered by grain-grain collisions.

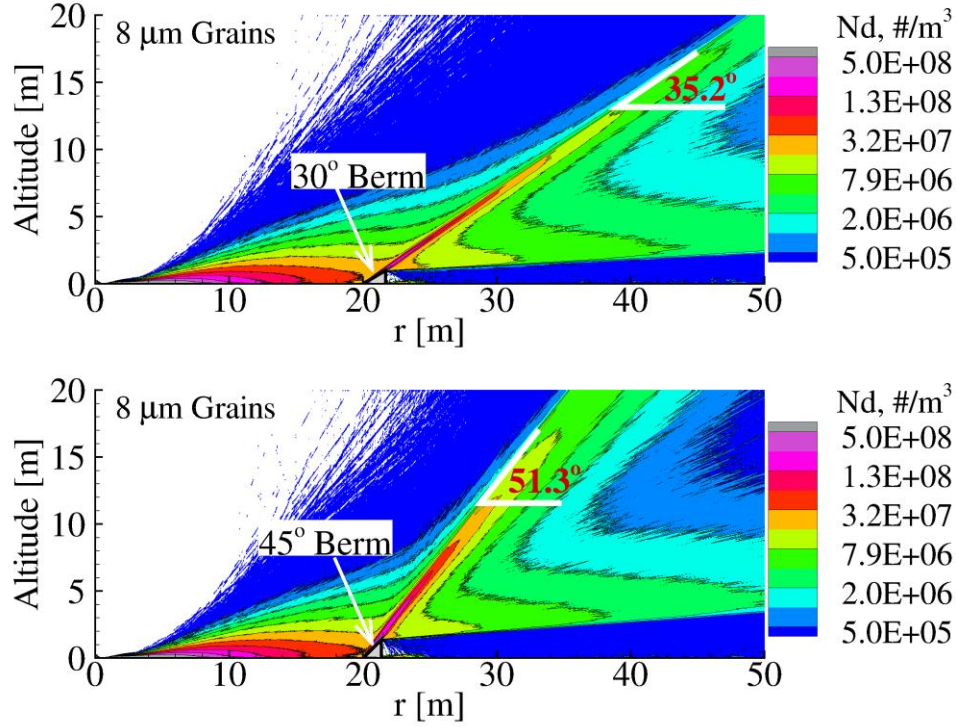


Figure 7.3.1. Number density contours for 8 μm particles impacting berms angled at 30° (top) and 45° (bottom).

The particles that impact the fence are deflected with inclination angles of 35.2° and 51.3° for the 30° and 45° berms. Although not shown, these angles are also the same for the other particle sizes that are larger than 2 μm . The smaller 200 and 800 nm particles are turned outward by the gas and have a relatively shallow inclination angle. The inclination angle of reflected particles depends on the geometry of the berm and the assumed tangential and normal components of restitution. If the grains were unaffected by the gas, the inclination angle of the deflected particles is deterministic and depends on the berm coefficients of restitution ε , berm angle θ_f , and the incident angle of inclination of the dust α_p . The inclination angle of deflected particles, α'_p , is approximately

$$\alpha'_p = \theta_f + \tan^{-1} \left(\frac{\varepsilon_{\perp}}{\varepsilon_{\parallel}} \tan(\theta_f - \alpha_p) \right). \quad 7.3-1$$

The minimum inclination angle of the deflected particles is the angle of the berm. For the cases simulated above, the predicted inclination angles from Equation 7.3-1 are 35.85° and 54.85° for the 35° and 45° berms. These predicted angles are only slightly larger than the measured inclination angles in the simulation. This suggests that the trajectories of particles that impact the fence are not significantly altered by the gas motion at these large radial distances and that the scattering largely depends on the grain-surface interaction model. The highly deflected particles are also unlikely to impact neighboring structures. The potentially hazardous particles are the ones that do not impact the berm. The trajectories of such particles are also not significantly influenced by the gas motion and can be predicted using simulations without a berm sampled at heights above the shielded region.

Section 7.4. Model Sensitivity

7.4.1. FENCE COEFFICIENT OF RESTITUTION

The dust motion has a strong dependence on the fence coefficient of restitution because the drag forces exerted on the dust are relatively weak near the fence. As the fence coefficient of restitution increases, the dust particles are able to rebound further upstream before being turned by the gas. When the fence restitution coefficient is 0.5, some particles that reflect off a vertical fence are able to travel back towards the landing site and potentially impact the spacecraft. Number densities for $8\text{ }\mu\text{m}$ and 800 nm particles are shown in Figure 7.4.1 for a fence with a restitution coefficient of 0.5. When a lesser restitution coefficient of 0.1 was used, see Figure 7.1.3, grains were turned outward by the gas before impacting the lander.

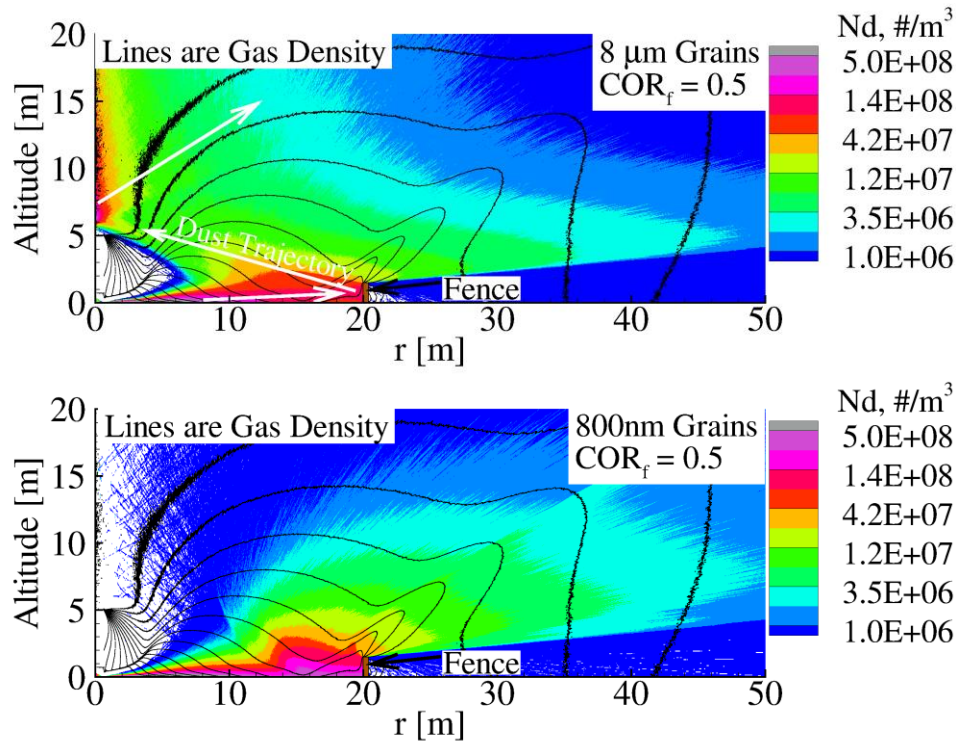


Figure 7.4.1. Color contours of 8 μm (top) and 800 nm (bottom) particle number densities for a 1.50 m tall fence with a normal restitution coefficient of 0.5. The black lines are gas density contours and the white arrows approximate dust path lines.

The smaller particles are more coupled to the gas motion and behave differently than the larger particles and tend to not bounce as far upstream off the fence. The 800 nm particles bounce approximately 10 m upstream of the fence before being turned outward again by the gas.

7.4.2. GRAIN-GRAIN COLLISIONS

Granular collisions were not included in our first attempts at simulating the interaction between the dust spray with a lunar fence. In these simulations, a 1 m tall fence was placed 15 m from the jet axis and only 1 μm particles were included. Despite the differences in simulated particle sizes, the total eroded mass is the same as the simulations discussed previously. Granular collisions enhance diffusion of the incident dust spray, resulting in a thicker and less dense particulate spray. Without granular

collisions, the incident spray impacts the fence at a very shallow inclination and then rebounds a short distance upstream before being turned by the gas, as shown in Figure 7.4.2.

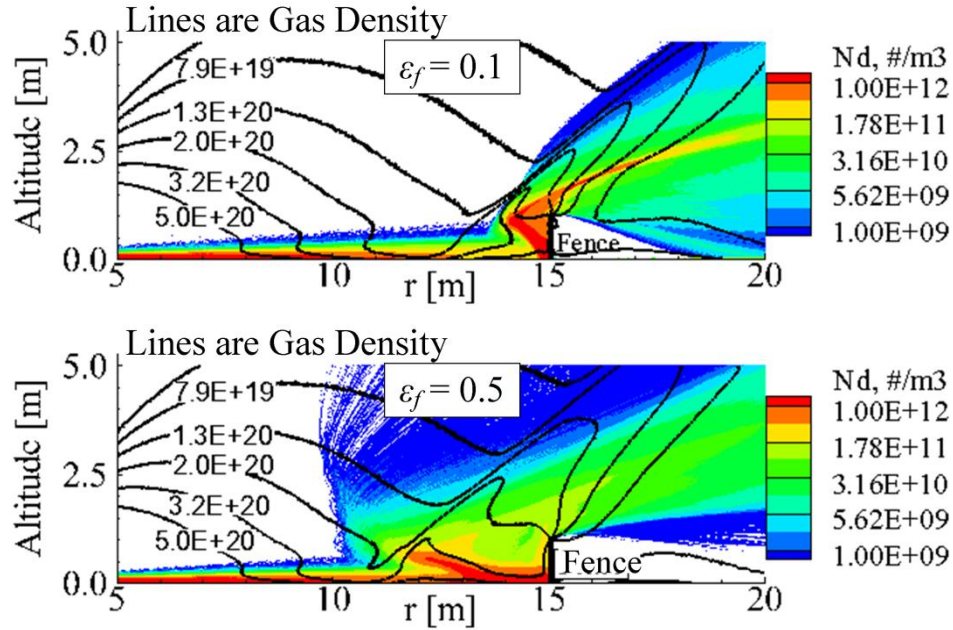


Figure 7.4.2. Number density contours for 1 μm particles impacting fences with restitution coefficients of 0.1 (top) and 0.5 (bottom). Granular collisions were not included and the line contours are gas density.

As the coefficient of restitution is decreased from 0.5 to 0.1, the grain rebound distance decreases from ~ 5 m to ~ 1 m. When the free stream gas flow impacts the reflected dust spray, the gas is compressed because of the relatively high particle number densities and large relative velocities between the incident gas and reflected dust. The gas response is illustrated in Figure 7.4.2 by the line contours and the foot of the oblique shock correlates well with the rebound distance, suggesting that the gas shock forms because of impingement on the rebounding dust instead of the fence. The oblique shock position, however, did not noticeably change when granular collisions and a polydisperse distribution of grain sizes were used. This occurs because granular collisions broaden

the incident dust sheet thus reducing the coupling from the particle to gas phase. A coupling parameter P_{2m} , defined by equation 7.4-1, which characterizes momentum coupling from the particles to the gas is derived in (Burt & Boyd, 2005). The parameter P_{2m} is proportional to the magnitude of the total drag force on the particle phase per unit volume, divided by the streamwise gas momentum flux and non-dimensionalized through multiplication by the length scale L .

$$P_{2m} = n_p D_p^2 L \frac{c_{r1} c_{r2}}{c_{g1}^2}. \quad 7.4-1$$

In the above equation, n_p is the particle number density, c_{r1} is the magnitude of the difference between the particle and gas bulk velocities, c_{r2} is the average gas molecule speed relative to the particle velocity, and c_{g1} is bulk speed of the gas. When granular collisions are included, the particle number density decreases because the incident dust spray broadens, resulting in less momentum coupling from the particles to the gas.

Section 7.5. Flow Unsteadiness

All of the simulations previously discussed were steady and the figures were generated from time averaged data. As the fence is moved to a close distance of 10 m from the lander, some simulations exhibited unsteadiness not observed at further fence placements. Such a fence placement may be impractically close to the lander, but an off-axis landing or unintended obstacles such as a large rock or crater rim may exhibit similar phenomena.

The dusty gas interactions with the fence generated unsteadiness, shown in Figure 7.5.1, when a 1 m tall fence was placed 10 m from the jet axis and granular collisions were neglected. Clusters of dust particles are shed off the top of the fence with a frequency of approximately 1000 s^{-1} . A series of convergence tests were performed to

ensure that the unsteadiness was not a numerical artifact. This solution is spatially resolved and the cell size is approximately 2.0 mean free paths across in the densest regions near the fence. The data were sorted onto a coarser output grid for visualization. The flow fields did not change significantly when the number of simulators was doubled, indicating convergence.

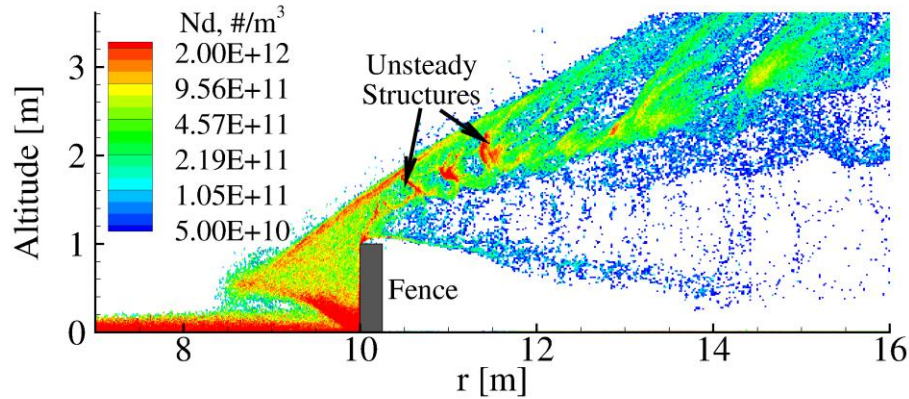


Figure 7.5.1. Number density contours for 1 μm grains exhibiting unsteadiness when interacting with a 1 m tall fence placed 10 m from the jet axis. Grain-grain collisions were neglected in this simulation.

To determine the cause of the unsteadiness various physical models were systematically tested. The erosion rate depends on the local gas properties near the surface. This however was not the source of unsteadiness because unsteady structures remain even when the erosion rate was forced to be temporally constant. The flow did however become steady when the gas motion was decoupled from the dust. This suggests that a feedback mechanism between the dust and gas motions could be the source of instability.

The instantaneous gas flow field is shown at two different times that are 0.02 s apart in Figure 7.5.2. The standoff distance and shape of the oblique shock as well as the structure of the stagnation region change at the different times. In the latter snap

shot, the oblique shock shifts noticeably upstream. Fluctuations in the gas flow field affect the dust trajectories which may give rise to the unsteady structures observed. The specific feedback mechanism is not fully understood, but it may relate to entrained particles in the recirculation bubble.

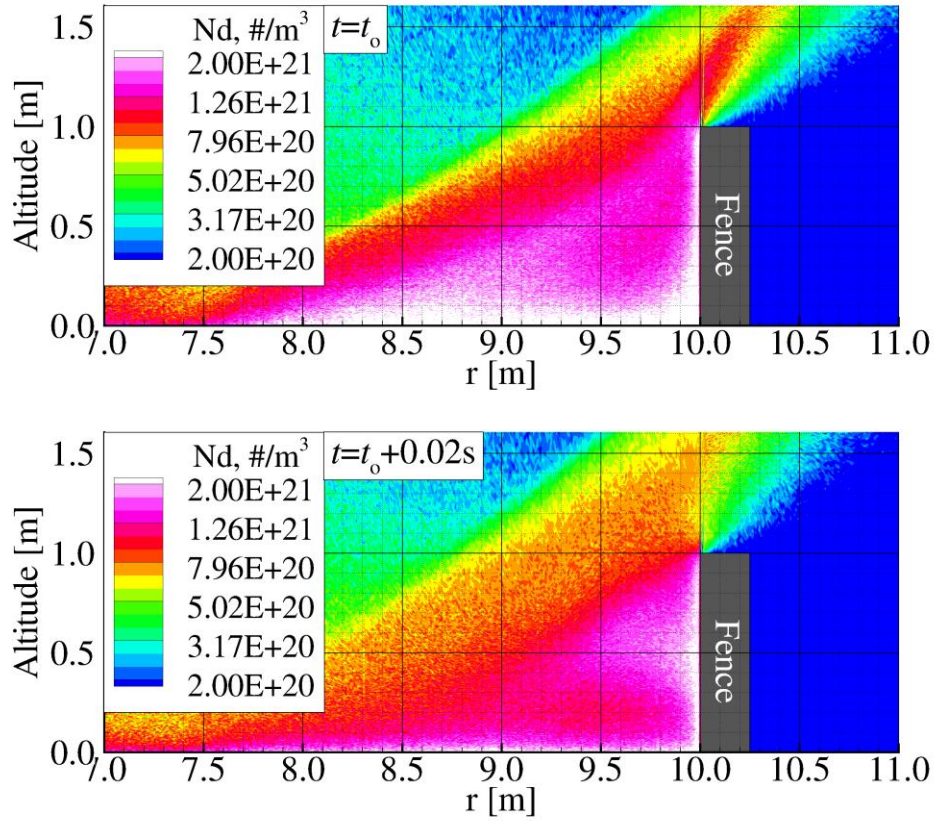


Figure 7.5.2. Two instantaneous snapshots of gas number density taken 0.02 s apart. These profiles are unsteady and occur when the gas impinges on a 1 m tall berm placed 10 m from the lander.

When granular collisions were included, the unsteadiness vanishes. Granular collisions were shown to reduce the interphase momentum coupling from the dust to gas. Consequently, granular collisions may stabilize the flow by reducing the coupling from the dust to the gas.

Section 7.6. Chapter Summary

The effectiveness of a lunar fence or berm have been simulated and studied in this chapter. Important engineering questions include: How tall should the fence be? Where should the fence be placed? Should the fence be angled? What forces are expected on the fence? The best answers to these questions depend on the object being protected and available resources, but several general recommendations are made.

For fences placed 15 m or further from the lander, the dust motion can be characterized as two classes of particles: those that impact the fence and are deflected upward and those that narrowly avoid the fence and remain on minimally altered trajectories. The latter class of particles is potentially dangerous because the associated particles travel outwards at shallow inclination angles and very high velocities. The trajectories of these particles are not significantly altered by the fence because the dust is sufficiently decoupled from the gas, even at distances 15 m from the lander. To shield such high speed particles, the fence height to placement ratio should be large relative to the inclination angle of the dust spray. The inclination angle of the dust spray depends on the assumed elasticity of granular collisions (discussed in Section 5.1.2) and is at most 3.12° in our simulations. The dust inclination angle tends to slightly decrease at higher hovering altitudes. Although not simulated, a fence designed to shield structures from dust at lower hovering altitudes should remain effective for higher hovering altitudes. This is expected because the incident scoured dust from a higher altitude lander travels closer to the lunar surface and the fence height remains tall compared to the thickness of the dust layer. To maximize the fence shielding, a larger fence should be placed as close to the lander as possible. A conservative estimate for the fence height to placement ratio that would deflect the bulk of the incident dust is around 1:10.

In some cases it may not be important to have a tall fence if the sensitive structure is relatively short. Our results show that structures downstream of the fence should be protected provided that they are shorter than the fence. The high velocity particles that avoided the fence would simply blow over the top of any sensitive hardware. The shielded area increases downstream of the fence. The shielded height increases with an inclination angle approximately equal to $\tan^{-1}(h_f/r_f)$. If it were necessary to protect a tall structure, a shorter fence could be placed close to the jet axis.

The normal stress on the fence increases as the fence is placed closer to the lander. A substantial amount of the force on the fence comes from particle bombardment. For a fence placed 10 m from the lander, the average pressure force on a 1.5 m tall fence is 34.3 Pa. This pressure decreases at further distances, approximately proportional to $r_f^{-2.463}$.

The rebounding dust spray is sensitive to the berm coefficient of restitution. At higher coefficients of restitution (probably unrealistically high), the dust particles are able to rebound further distances and can potentially strike the lander. The larger particles have more inertia and are able to bounce further upstream than the smaller particles. For a 1.5 m tall fence placed 20 m from the lander, particles larger than 2 μm that reflect off the vertical fence would strike the lander if the normal coefficient of restitution is greater than 0.5. A realistic fence would likely have a significantly lower restitution coefficient and possibly more diffuse scattering. Improved models for dust-fence interactions are necessary for more accurate simulations. Despite this model uncertainty, the particles that strike the fence tend to be deflected upward and are most likely to travel above any sensitive structure.

A berm constructed with lunar regolith has also been proposed as a mitigation technique. To model such a berm, the vertical fence was rotated to the angle of repose

of the soil. The restitution coefficient for lunar soil particles impacting a berm of compacted regolith is unknown. Normal and tangential coefficients of restitution were used as a simple model for what is a significantly more complex interaction. A coefficient of restitution model is not sufficient because particles that impact a bed of material could cause additional emission from saltation. Such particles may be able to be entrained in the flow depending on the proximity of the berm to the lander. These particles would behave differently than particles eroded near the lander because the gas dynamic pressure is significantly lower near the berm. Modeling this remains a task for future work. Nonetheless, the height of the berm should still be sized similarly to that of a fence placed at a similar location. Similar to the fence, the particles that are potentially hazardous to downstream structure are the ones that narrowly avoided the berm and travel at low inclination angles.

CHAPTER 8.

FOUR ENGINE CONFIGURATION

Future landers may use a multi-engine configuration and the effects that a 4-engine lander has on the dust motion are discussed in this chapter. Flows from multi-engine configurations are substantially more complicated than single engine landers because there are multiple plume-plume and plume-surface interactions. These phenomena are also computationally expensive to simulate because they are 3-dimensional. Each of the simulations discussed in this chapter used 360 processors for approximately 25,000 CPU-hours. In this chapter, the dust sprays and flow structures are only studied for a 4-engine configuration hovering at three different altitudes.

Section 8.1. Computational Domain

A four-engine configuration in which each engine is symmetrically offset about a central axis by one nozzle diameter is modeled. The computational domain is shown schematically in Figure 8.1.1.

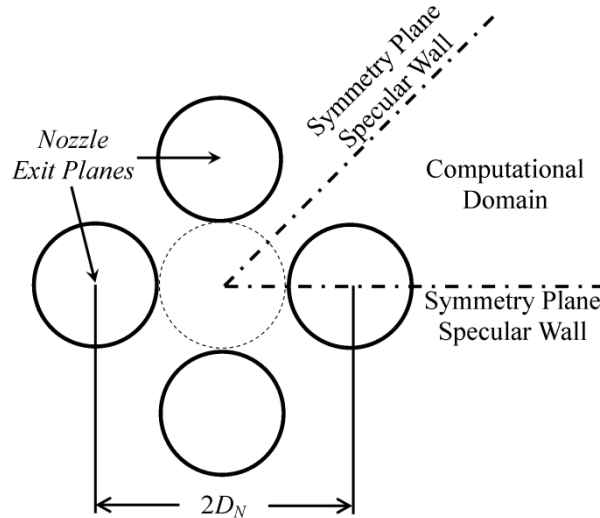


Figure 8.1.1. Schematic showing the computational domain and symmetry planes for the 4-engine nozzle configuration.

The thrust of each engine is reduced such that the four-engine configuration has the same net thrust as the single engine simulations discussed in previous chapters. There are two symmetry planes in this configuration; one which bisects each nozzle and the other between two adjacent nozzles. These symmetry planes are used to reduce the computational cost and simulators that strike these boundaries undergo specular reflection.

Section 8.2. Hovering Altitude Effects

8.2.1. GAS FLOW FIELD

The gas number density field for such a lander hovering 5 m above the surface is shown on a symmetry plane that bisects a nozzle in Figure 8.2.1.

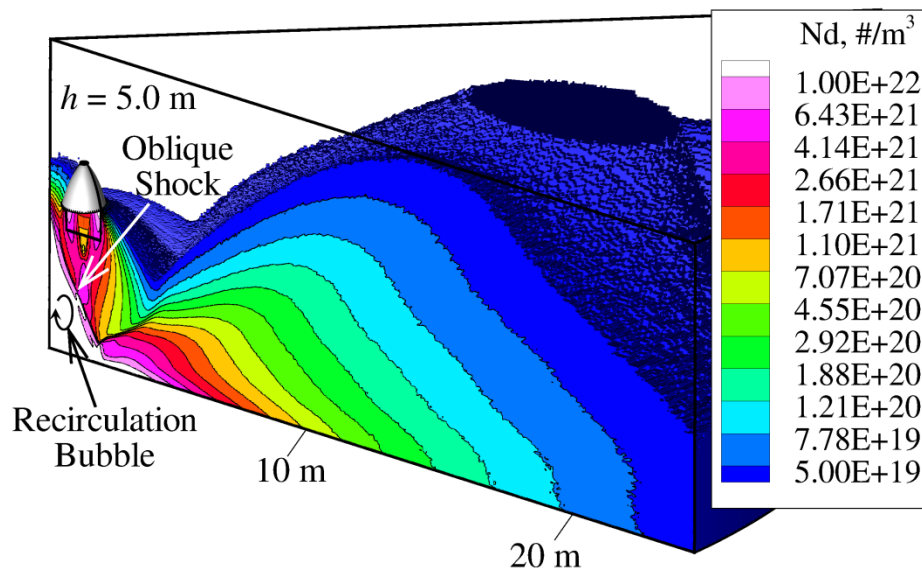


Figure 8.2.1. Gas number density profiles for a multi-engine lander hovering 5 m above the surface. This is a view of the plane that bisects an engine.

There are multiple plume-plume interactions, but only one is evident in this view. The rocket plumes interact in the region between the nozzles and form an oblique shock,

labeled in Figure 8.2.1, near the axis. This oblique shock impinges on the surface shock and forms a large recirculation bubble. The surface shock is qualitatively similar to that of single engine impingement outboard of the recirculation region.

Another plume-plume interaction occurs near the symmetry plane between adjacent nozzles. Such interactions are shown in Figure 8.2.2 along a curved cylindrical surface (shown schematically in the same figure) that cuts through the centers of adjacent nozzles.

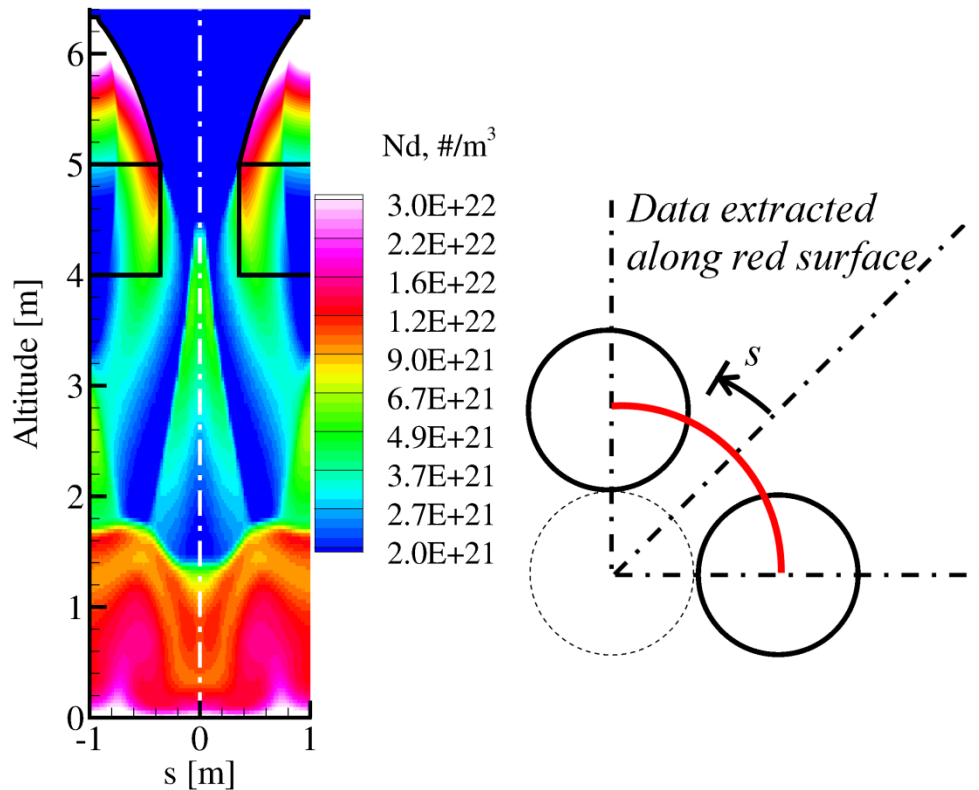


Figure 8.2.2. Gas number density on the surface formed by the section of a cylindrical shell that passes through the center of the rocket engines. The boxes immediately below the nozzle exit planes show the location of the hybrid interface.

An oblique shocks forms near the symmetry plane between adjacent nozzles. This oblique shock impinges on the surface shock and decreases the shock standoff

distance near the symmetry plane. This interaction with the surface shock is similar to a reflected nozzle compression wave interacting with the surface shock at low hovering altitudes (discussed in Section 4.3.2).

As the gas expands outward the flow becomes more axisymmetric. Contours of radial molecule mass flux are plotted on the surface of a cylindrical shell of radius 25 m that spans a quadrant of the flow. The symmetry plane between adjacent nozzles is indicated by the white dash-dot line at $s = 0$, where s is an arc length measured along the cylindrical surface. An oblique shock is not observed near the adjacent nozzle symmetry plane because at this distance most of the gas has already turned radially outward. These contours show that the gas flow field exhibits directional jetting. Most of the gas flow is focused near the symmetry plane between adjacent nozzles.

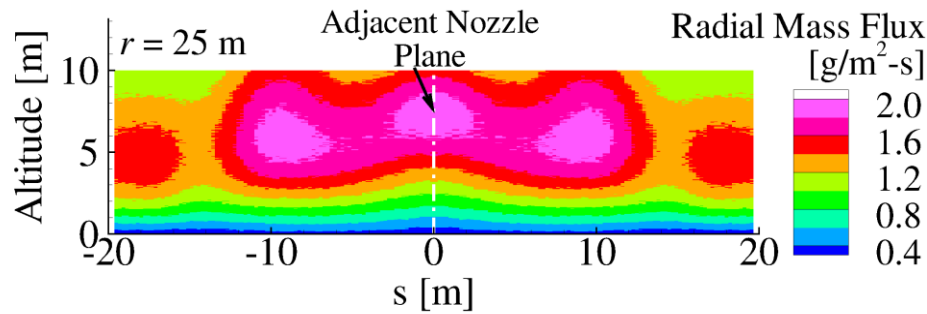


Figure 8.2.3. Radial mass flux contours for the gas along a constant radius cylindrical surface at 25 m. This surface spans a quadrant of the flow and the symmetry plane between adjacent nozzles is indicated by the white line at $s = 0$ m. The lander hovers 5 m above the surface.

The gas number density along the plane between adjacent nozzles is contoured in Figure 8.2.4. The recirculation bubble near the stagnation point is shaped as a cone and is also visible along the adjacent nozzle plane. There is a circular patch of high density on this 2-D surface centered at a radial distance of approximately one nozzle diameter

and altitude of about 3.75 m. This high density region is formed as the adjacent plumes impinge on each other and form an oblique shock. At radial distances beyond 5 m the gas density responds to the presence of dust. The gas is compressed as it penetrates through the dust layer, thus resulting in higher gas densities near the surface.

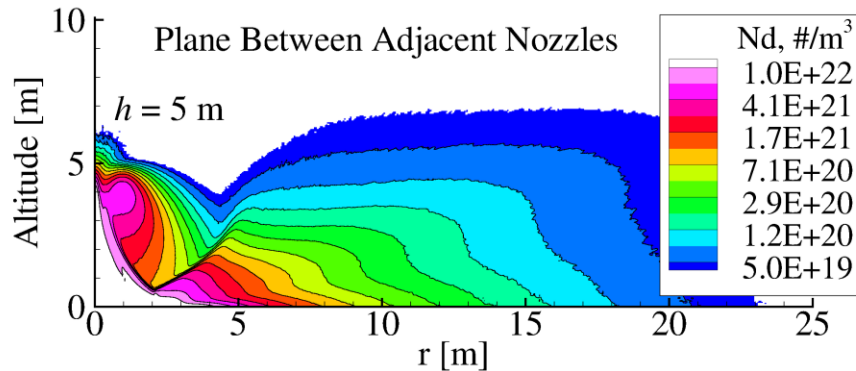


Figure 8.2.4. Gas number density contours on the symmetry plane between adjacent nozzles. The 4-engine lander hovers 5 m above the surface.

The interactions between the opposite and adjacent engine plumes with the surface depend on the hovering altitude. At a hovering altitude of 10 m, shown in Figure 8.2.5, the interactions along a nozzle symmetry plane are qualitatively different than the 5 m simulations. The surface shock is more normal near the symmetry axis and a significantly smaller recirculation bubble forms when the lander hovers at a higher altitude. At very high hovering altitudes, the rocket exhaust plumes will coalesce and the flow field is expected to appear like that from a single engine. At lower altitudes, 5 m and below, the surface shock structure transitions to an oblique shock and large recirculation bubble. This transition can be caused by a number of complex interactions between plume-plume oblique shocks, nozzle compression waves, and the lunar surface shock. The specific interaction which triggers this transition as well as the hovering height at which it occurs is unknown. Such details are likely dependent upon the details

of the nozzle shapes, cant angles, number of engines, and configuration. Therefore we simply highlight the phenomena of interest.

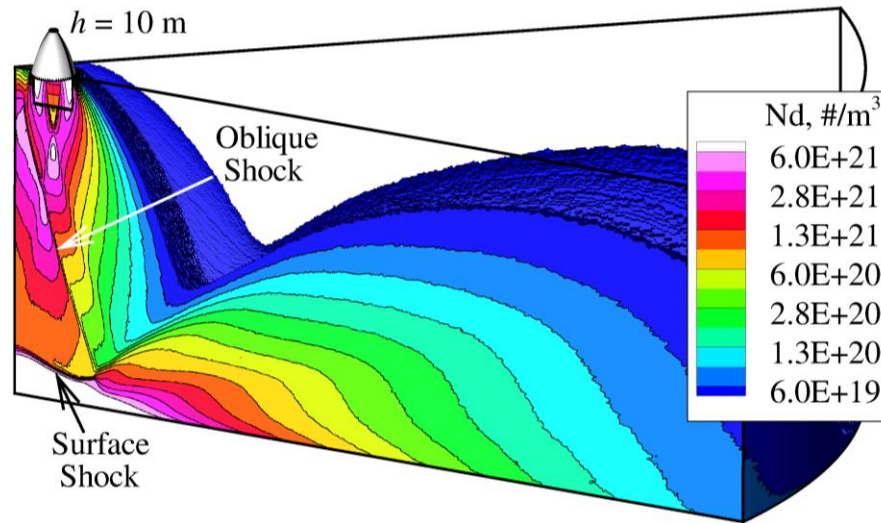


Figure 8.2.5. Gas number density profiles for a multi-engine lander hovering 10 m above the surface. This is a view of the plane that bisects an engine.

8.2.2. DUST MOTION

The dust sprays exhibit directional jetting when the lander hovers close to the ground. Number density contours for $8\text{ }\mu\text{m}$ sprays resulting from a lander hovering 3 m above the surface are shown in Figure 8.2.6. Particles are entrained into the recirculation bubble near the axis. Some of these particles then travel upward along the axis and can potentially impact bottom surfaces of the spacecraft. The particulate sprays are also focused along the two symmetry planes. At lower hovering altitudes, the gas is dense and the dust motion is tightly coupled to the gas. Consequently the dust follows the gas motion and is focused along the plane between adjacent nozzles. The peak $8\text{ }\mu\text{m}$ particle number densities are larger than 10^{10} m^{-3} .

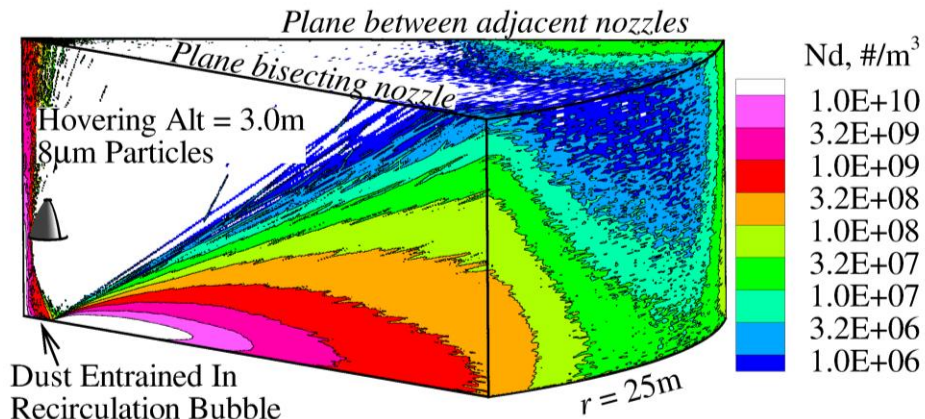


Figure 8.2.6. Number density contours from 8 μm particles scoured by a 4-engine lander hovering 3 m above the surface.

For a single engine lander with the same thrust, the peak number density for 8 μm particles was significantly less at approximately $4 \times 10^8 \text{ m}^{-3}$, as shown in Figure 5.2.1. The particles along the symmetry planes are also deflected upwards at high angles. This occurs for two reasons. The first reason is that the gas is deflected upward along these planes and the dust motion responds accordingly. In addition to being deflected upward by the gas, however, the particles are also scattered upwards by granular collisions. The sensitivity of the flow to the elasticity of granular collisions has not been thoroughly investigated for this configuration, but the “high risers” were also observed in early simulations where granular collisions were neglected.

The bulk speed for 8 μm particles is shown in Figure 8.2.7 for a lander hovering 3 m above the surface. The dust particles that travel upward along the axis move at relatively high speeds of approximately 250 m/s. The highest speed regions correspond to the top of the dust sheet where the particles are exposed to higher velocity fluid. The particles travel at slower speeds near the symmetry planes and near the surface. This occurs because the dust heavily mass loads the gas in these regions and reduces the gas

dynamic pressure. The maximum particle speeds are only slightly larger than what was observed with the single engine lander at the same altitude.

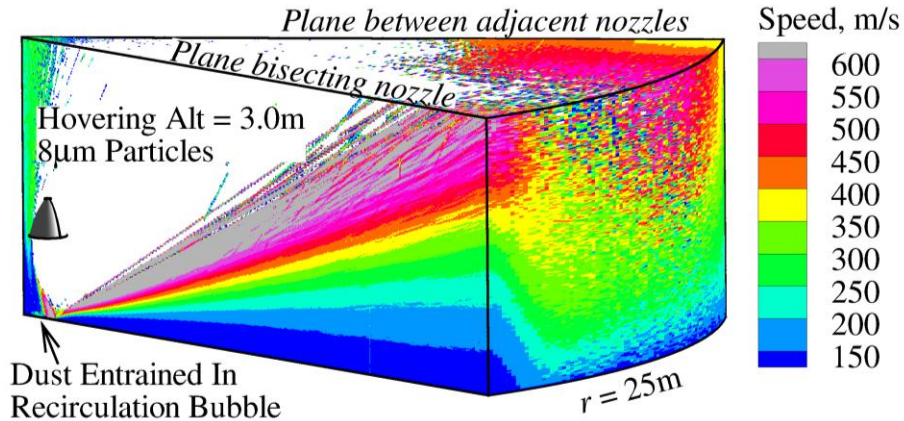


Figure 8.2.7. Bulk speed contours from 8 μm particles scoured by a 4-engine lander hovering 3 m above the surface.

The dust sprays show less directional jetting at higher hovering altitudes. The number density for 8 μm particles is shown in Figure 8.2.8 for a lander hovering 10 m above the surface. The recirculation bubble near the axis is smaller at a higher hovering altitude, but some dust particles are still entrained in it. Unlike the lower altitude simulation, these particles do not travel up the symmetry axis. The particle motion shows directional dependence, but generally much less than what was observed at lower hovering altitudes. In the high altitude simulation, the particle density tends to be higher along the symmetry planes. The inclination angle of the dust spray also tends to be much lower at higher hovering altitudes. This observation is consistent with what was seen for a single engine lander at different hovering altitudes. This occurred in the single engine simulations because there were fewer grain-grain collisions and consequent particle scattering for landers hovering at high altitudes. This argument also applies to the multi-engine lander. The dust also shows lower inclination angles at higher altitudes

because the gas flow exhibits less direction jetting as most of the plume-plume interactions occur well above the surface shock.

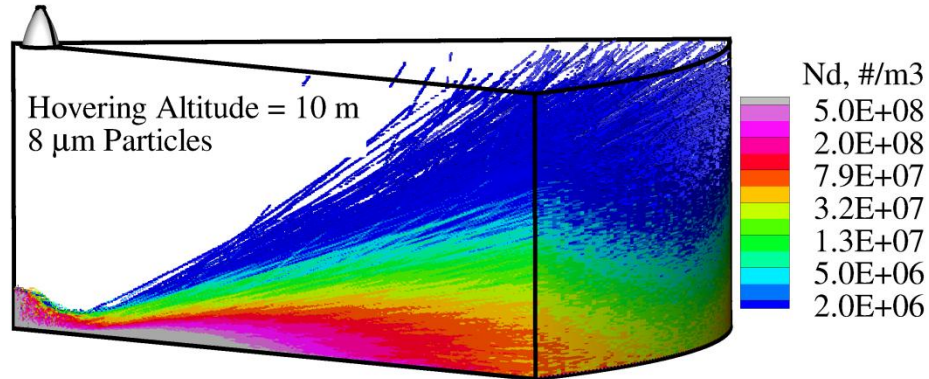


Figure 8.2.8. Number density contours for $8\ \mu\text{m}$ particles scoured by a 4-engine lander hovering 10 m above the surface.

The radial velocity of $8\ \mu\text{m}$ particles is shown in Figure 8.2.9 for a 4-engine lander hovering 10 m above the surface. Similar to the lower altitude lander, the particle velocities are highest near the two symmetry planes, but the focusing effect is less than that observed at lower hovering altitudes. The gas is also focused along these planes and consequently particles near the symmetry planes feel a stronger drag force. The maximum particle speed along these planes is approximately 450 m/s, which is significantly larger than the 365 m/s maximum velocity for the single engine case. The radial velocity does not increase significantly as the particles travel radially outward from 10 to 25 m as they are mostly decoupled from the flow.

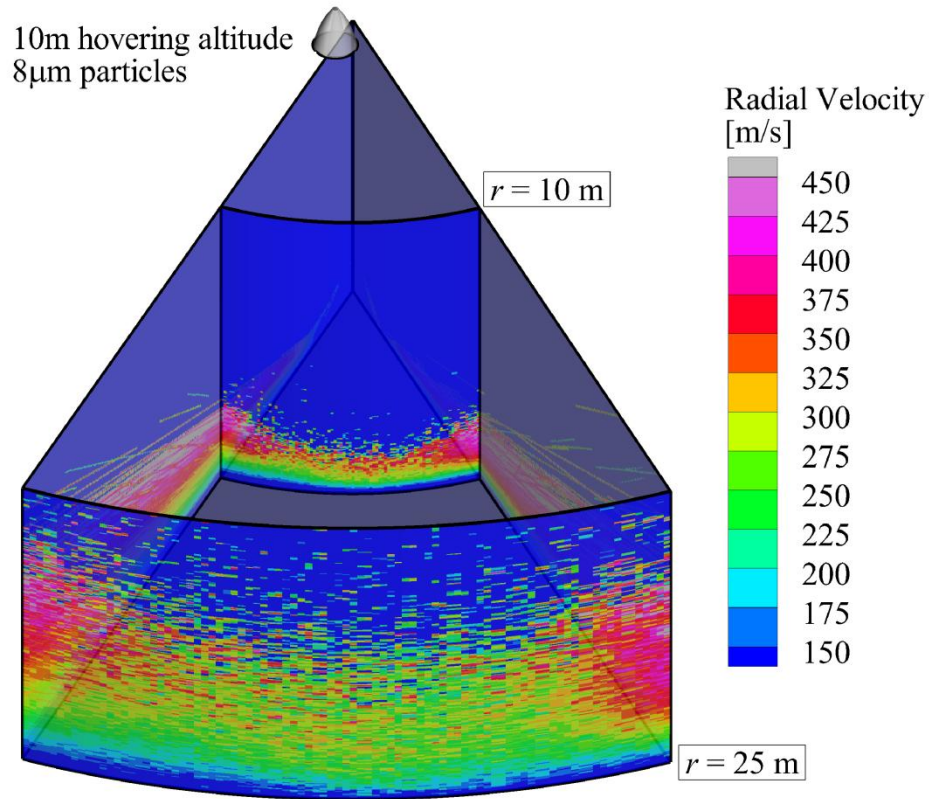


Figure 8.2.9. Contours of radial velocity for 8 μ m particles that are scoured by a lander hovering 10 m above the surface. Velocities slices are plotted at distance 10 and 25 m from the jet axis.

The dust motion exhibits changes in the 3-dimensional structure for different hovering altitudes. The particle mass flux is contoured in Figure 8.2.10 along a cylindrical surface of constant 25 m radius from the jet axis for landers hovering at different altitudes. The variable s on the x -axis is an arc length along the plane 25 m from the axis. A value $s = 0$ corresponds to the symmetry plane that bisects a nozzle and the value $s = 25 \times \pi/4$ corresponds to the symmetry plane between adjacent nozzles.

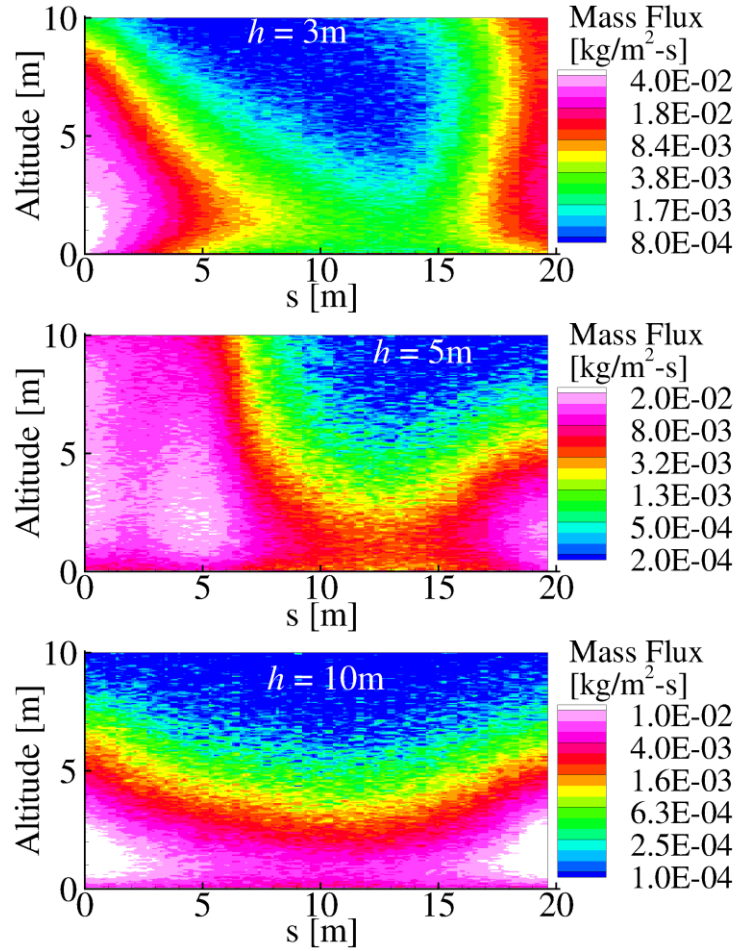


Figure 8.2.10. Particle mass flux along a plane of constant radius, $r = 25$ m, from the lander for hovering altitudes of 3, 5, and 10 m. Note the shift of color scale between panels.

The flow direction is radially outward and the 3-dimensional dust structures persist far from the plume axis even as the gas becomes more uniform. This occurs because the gas has a temperature and is able to diffuse whereas the dust decouples close to the lander and travels outward ballistically. At a hovering altitude of 3 m, the regions of highest dust particle mass flux are concentrated along the symmetry planes. At a higher hovering altitude of 10 m, the particle mass flux is more uniform than in the low

altitude case, but the regions of peak mass flux still tend to be focused along the two symmetry planes.

At an intermediate hovering altitude of 5 m, there are three maxima in the particle flux, one near each symmetry plane and a third approximately 4 m from the left symmetry plane. This third maximum is made up of particles that are eroded near the adjacent nozzle symmetry plane. The source of particles for this middle peak is shown in Figure 8.2.11. In this figure, particle streaks are obtained by outputting particle position over a short time interval – longer streaks correspond to faster moving particles. The particles are colored by speed and overlaid on grayscale contours of the flux of emitted particles. The particle flow is disorganized near the peak erosion region along the adjacent nozzle symmetry plane. In this region, there are large particle relative velocities and densities and consequently high grain-grain collision rates. The black arrow is drawn to clarify the motion of the particles, as they are entrained into a stream that represents the central peak in Figure 8.2.10. In addition, the particle emission flux is relatively small where the central jet of entrained particles travels outward. This suggests that the gas motion within the central dust jet is slowed by the dust motion. This central jet is not seen at a lower hovering of 3 m. Unfortunately, this shows that there is not a simple answer for predicting the directional jetting of particles by simply stating particles are always focused along symmetry planes.

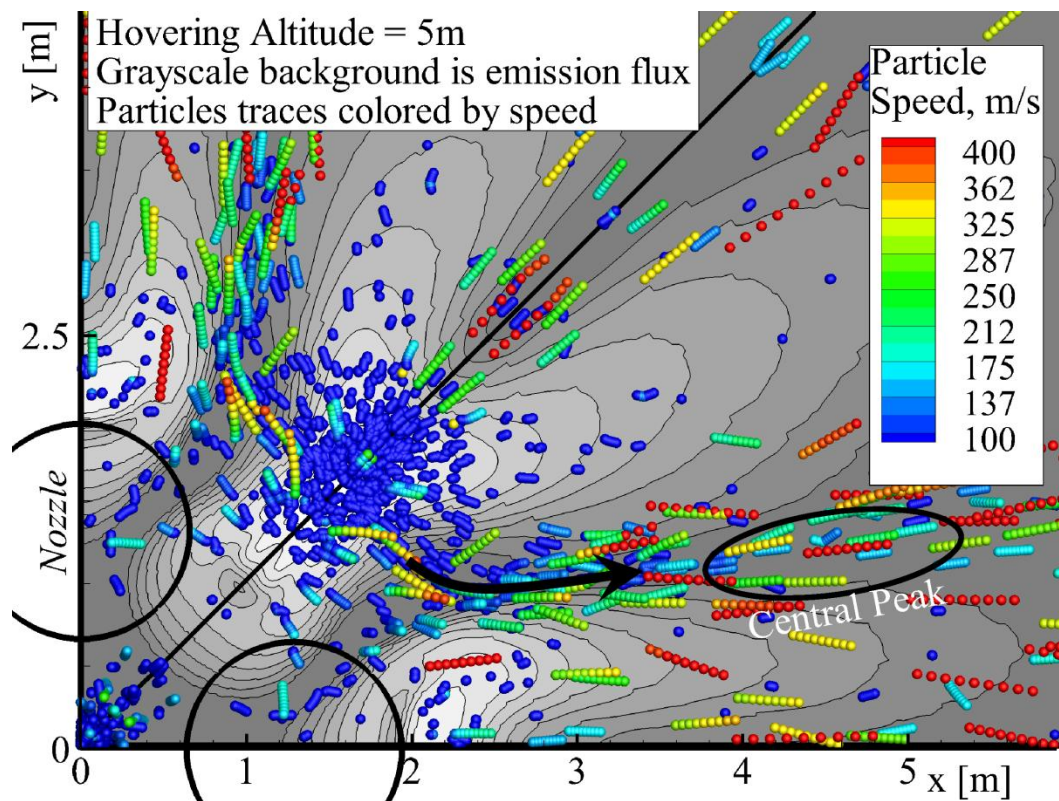


Figure 8.2.11. A top down view of particle streaks, colored by speed, overlaid on grayscale contours of particle emission flux. The lightly colored areas indicate high flux. Only particles larger than $1\text{ }\mu\text{m}$ are shown.

The particle mass flux across an octant of a cylindrical surface placed 25 m from the jet axis is shown in Figure 8.2.12 for particles of different sizes when a lander hovers 5 m above the surface. The symmetry plane that bisects the nozzle occurs at $s = 0$ and the symmetry plane between adjacent nozzles occurs near $s = 19.6$ m. The central peak particle mass flux shifts towards the left symmetry plane for larger particles. The central peak is comprised of particles originally eroded near the right symmetry plane that are then turned outward by the gas. The smaller particles are able to turn quicker because they have less inertia than the larger particles. The $2\text{ }\mu\text{m}$ particles also tend to travel at higher inclination angles than the $11\text{ }\mu\text{m}$ ones. This effect was also observed in

the single engine simulations because the smaller particles are more easily scattered upwards by granular collisions.

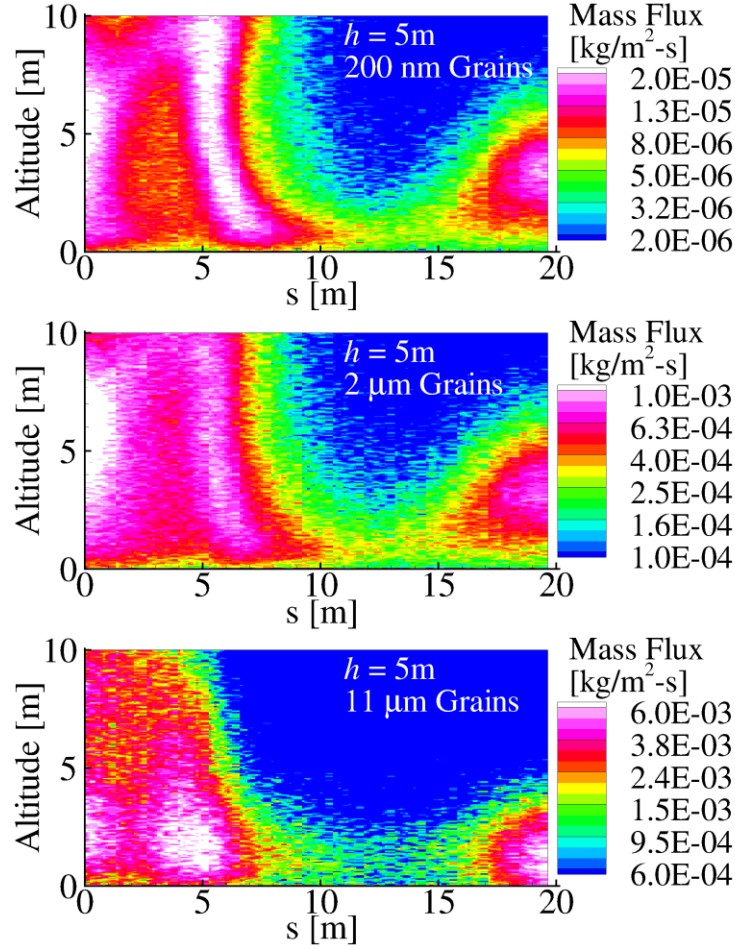


Figure 8.2.12. Mass flux for 200 nm, 2 μm , and 11 μm particles through an octant of a cylindrical surface 25 m from the jet axis. The hovering altitude of the lander is 5 m.

8.2.3. EROSION RATES AND TRENCHING BEHAVIOR

The particle emission flux also exhibit complex structure as a consequence of the 3-dimensional of the flow. The particle emission flux is are shown in Figure 8.2.13 for a lander hovering 3.0 m above the surface. The peak emission flux tends to occur nearly underneath each engine. The peak emission flux is approximately 2.0 kg/m²-s, which corresponds to a scouring rate of 1.3 mm/s for loosely packed lunar regolith. The final

approach for typical lunar landings is less than one minute and this scouring rate is not expected to excavate a large trench. More erosion tends to occur below each nozzle and at a distance slightly offset from the plane between adjacent nozzles. Away from the lander and along the adjacent nozzle symmetry plane, the erosion rate decreases. This occurs because many dust particles are also focused along this plane and consequently reduce the gas momentum. The same process happens on the symmetry plane bisecting each nozzle.

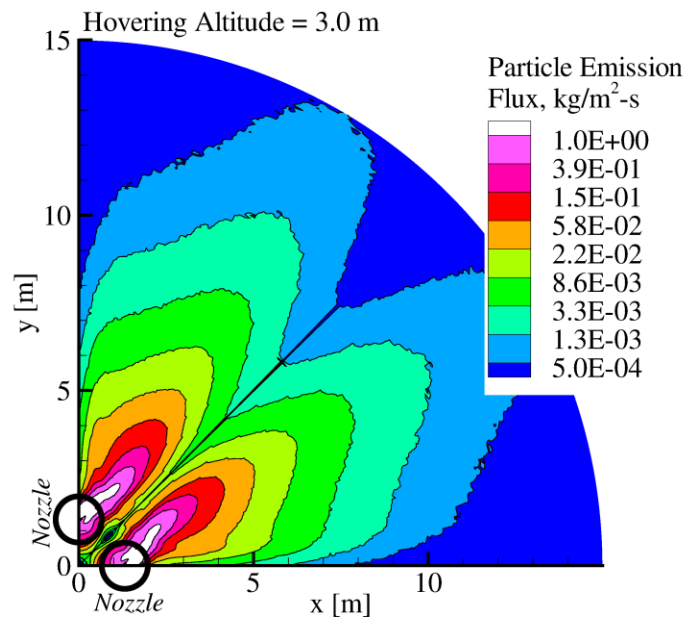


Figure 8.2.13. Particle emission flux for a 4-engine lander hovering 3.0 m above the surface.

The erosion profiles are different at higher hovering altitudes, as shown in Figure 8.2.14.

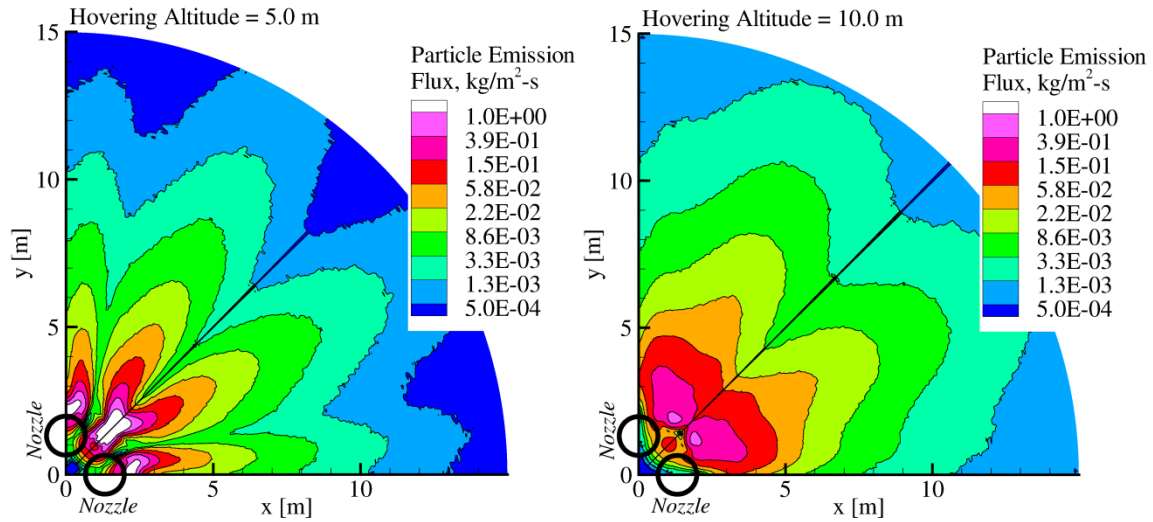


Figure 8.2.14. Particle emission flux for a 4-engine lander hovering 5.0 m (left) and 10 m (right) above the surface.

When hovering 5 m above the surface, the peak emission flux occurs along the two symmetry planes. Most of the particle emission, however, occurs near the symmetry plane between adjacent nozzles. Dust concentrates along the two symmetry planes and also at a central peak for a lander hovering 5 m above the surface, which was previously shown in Figure 8.2.11. The near-surface gas motion is again inhibited in regions where the dust concentrates resulting in lower particle emission. The peak emission flux is approximately twice as large as that for an equivalent net thrust single engine lander. The erosion profiles for the 10 m hovering altitude case are more axisymmetric than at the lower altitudes. The peak emission flux is significantly lower at this altitude, and has a maximum value of approximately $0.4 \text{ kg/m}^2\text{-s}$. This corresponds to a scouring rate of 0.27 mm/s .

Section 8.3. Chapter Summary

A 4-engine configuration with the same total thrust as the single engine case has been simulated and near field results are presented for different hovering altitudes. At lower altitudes the dust motion exhibits directional jetting. At higher altitudes, the dust sprays still exhibit some directionality but the flow is much more axisymmetric. Unlike for the gas, near field dust structure is preserved when particles travel into the far field because the dust decouples from the gas and travels ballistically without much lateral diffusion.

The dust sprays tend to focus along the two symmetry planes: one which bisects a nozzle and the other is the plane between adjacent nozzles. However, at certain altitudes the dust particles can be focused into a third jet between the two symmetry planes. In addition, the particles that are entrained along the two symmetry planes tend to be deflected at much higher inclination angles than observed for a single engine lander. This effect is much more apparent at lower altitudes. When hovering 3 m above the surface, many particles along the plane between adjacent nozzles are deflected upwards with an inclination of 30° . The peak outward particle mass flux is approximately 2.5 times greater than that for the single engine case. In void regions where the particles are not concentrated, the particle flux can be approximately an order of magnitude less than that of peak regions. The erosion profiles also depend on hovering altitude and engine configuration. Although the peak erosion rate can be twice the peak erosion for the single engine case, such an erosion rate is still not sufficient to scour a deep trench during nominal hovering periods.

Although not shown, the directionality of the jets is also likely to depend on the specific lander configuration. This chapter identifies different phenomena that can arise

when multiple engines are used, but the data cannot be extrapolated to other landing configurations. Future work could examine other configurations such as: three or two engine landers, engines tilted outward at different cant angles, and the effects of different spacing between rocket nozzles. Although the dust sprays tend to concentrate along symmetry planes, there are also regions void of dust. If one were able to use multiple engine interactions to control the void regions, the potential damage to nearby structures could be reduced. Before this can be done, additional work needs to be done on model sensitivity to dust-gas coupling as well as granular collisions. Granular collisions are very frequent when modeling this configuration and the collision elasticity is likely to affect the solution.

CHAPTER 9. CONCLUSIONS

Section 9.1. Summary

Rocket plume impingement and the resulting entrainment and transport of lunar dust have been simulated for different landing scenarios. The gas flow inside the rocket nozzle as well as the near field plume expansion were simulated with the continuum solver DPLR. The gas expansion to vacuum as well as the erosion, entrainment, and transport of dust were simulated using the direct simulation Monte Carlo method. The simulations in this work help characterize the dust sprays that result as a lander approaches from altitudes of 20 m to an altitude of 2 m above the surface. The effects of engine thrust were also studied to address how this work may translate to larger landers in the future. The sensitivity of the solutions to the various physical models such as two way dust-gas coupling and granular collisions was studied. The dust trajectories were also simulated from the erosion region to the final deposition many kilometers from the landing site. Such dust sprays may be unavoidable and pose a threat to any pre-existing structures on the moon. A fence or berm can be used to shield structures from the dust spray. Such mitigation techniques have been simulated and the effects of fence placement, height, angle, and fence coefficient of restitution are studied. A 4-engine lander configuration was simulated for a set of three different hovering altitudes and the resulting complex 3-dimensional dust sprays were analyzed.

Plume impingement simulations without dust were first discussed in Chapter 4. Simulation data were compared to the classical Roberts theory. Roberts theory was found to reasonably predict the impingement shear stresses at higher altitudes but had significant errors at lower altitudes. These deviations occur because Roberts theory did not account for nozzle geometry effects. A simple correction was introduced to Roberts

theory to more accurately predict the location of peak erosion for different hovering altitudes. The value of peak erosion was also found to decay quicker than Roberts theory predicted and a correction term was introduced to account for boundary layer growth. A sudden change in surface shock structure was discovered when the lander descended to only 2.0 m above the surface. At this hovering altitude, the changes in surface shock structure caused a large recirculation region to form near the jet axis. The recirculation region can enhance entrainment and produce a sudden onset of increased scouring. This transition occurred immediately before touchdown and may explain why astronauts observed a sudden expulsion of dust when the contact probe struck the lunar surface.

The dust motion was found to be very sensitive to granular collisions, particularly the assumed restitution coefficient of colliding grains. The simulations also suggested that the flow is heavily mass loaded near the surface and a fully coupled gas-dust model is important. A polydisperse distribution of discrete grain sizes ranging from 200 nm to 11 μm was simulated. The smallest particles were accelerated to maximum speeds above 1000 m/s while the larger 8 and 11 μm particles were accelerated to approximately 300 to 450 m/s. The particles were observed to quickly attain their maximum speeds within 30-40 m from the lander. At higher hovering altitudes, the dust erosion rate decreased and the particles were accelerated to slower terminal speeds. The terminal speeds for the larger particles tended to decrease nearly linearly as the hovering altitude increased. The dust emission rate and particle number densities near the surface scaled nearly linearly with increased thrust. The velocity of dust particles near the surface did not significantly change as the engine thrust was increased. The particles traveling near the top edge of the dust sheet, however, were accelerated to higher velocities for higher engine thrusts. The angle of inclination of the dust spray was not sensitive to the engine

thrust. This suggests that the sudden changes of particle inclination angles observed during the final moments before the Apollo Lunar Modules landed may occur because of terrain modification instead of thrust adjustments.

Gas flow fields and dust particle trajectories were simulated into the far field for an assumed landing trajectory. The leading edge of the gas expansion into the far field travels ahead of the dust cloud and can exceed lunar escape velocity. Some of the gas, however, remains trapped within the dust cloud and remains trapped on the Moon under lunar gravity. The dust particles also separate in the far field based on particle size. The larger particles travel slower and are deposited closer to the lander than the small particles.

The effectiveness that a lunar fence would have at shielding downstream structures from the dust spray was simulated and discussed in Chapter 7. Two classes of particles were observed for fences that were not tall compared to the dust layer thickness. One class consisted of particles that narrowly avoided the fence and were negligibly affected. The other class consisted of particles that struck the fence and were deflected upward. The trajectories of the particles that avoided the fence were hardly altered indicated that the gas and dust motions are loosely coupled near the fence. To maximize the shielding area, a taller fence should be placed inboard. However, a short fence placed further away from the lander can still be effective at shielding leeward structures that are short relative to the fence height. When the fence was set to an angle equal to the angle of repose of lunar soil, particles that struck the fence were deflected upwards at an angle that depends on the assumed particle-berm interaction model. The particles that pose a threat to downstream structures remain the ones that narrowly avoided the berm. Consequently, a well designed berm should still be tall relative to the structures it is intended to protect. The forces on the vertical fences were computed and it was found

that the pressure force is largest for inboard fences and decays rapidly as the fence is placed further out. The average pressure force for a fence placed 15 m from the jet axis was 13 Pa, a fairly small value suitably sustained by a cloth barrier.

A 4-engine nozzle configuration was also simulated for a set of different hovering altitudes. The dust sprays exhibit interesting 3-dimensional structure at lower altitudes. These structures form because of complex plume-plume and plume-surface interactions. Dust sprays tend to concentrate along the two symmetry planes: one between adjacent nozzles and one which bisects each nozzle. For certain hovering altitudes, however, some of the dust particles can also be focused at intermediate locations between the symmetry planes. The directionality likely depends on engine configuration and new simulations should be performed if a different engine configuration is used. The 4-engine configuration also results in concentrated erosion areas, but the peak erosion rates are unlikely to result in significant trenching.

Section 9.2. Future Work

There are many directions for future improvements to the work presented in this dissertation. Several possibilities for future work are outlined below. Improvements to the model are first discussed and are followed by recommendations for different scenarios to be simulated.

This work has shown that grain-grain collisions substantially affect the resulting dust flow fields. The solutions were also shown to be sensitive to the coefficient of restitution between colliding particles. The simplistic model in this work assumes that particles do not rotate and that the tangential and normal coefficients of restitution are equal. The model accuracy may be improved by using the discrete element method (DEM) to more realistically simulate grain-grain collisions. The discrete element

method is analogous to molecular dynamics, where the time-resolved collision dynamics are simulated. DEM simulations can model physical phenomena such as particle friction, electrostatic forces, particle shape, and grain rotation. Such simulations can be used to obtain cross sections as well as post-collision scattering distribution functions for grain-grain collisions. These cross sections and scattering functions can be tabulated for a set of different impact energies and directly used in the DSMC solver. The framework for such an approach already exists in our in-house DSMC solver, where MD-QCT (Molecular Dynamics Quasi Classical Trajectory) simulations are used to obtain impact energy dependent cross sections (for chemical reactions) for the DSMC solver (Moore, 2011).

Additional improvements can be obtained by using a more sophisticated erosion model. Erosion on the Moon occurs because of aerodynamic forces on the surface as well as bombardment from saltated particles and the disintegration of agglomerate particle clusters. These phenomena are not explicitly simulated and an empirical model is used in the current work. Other emission models exist that account for saltation bombardment and are described in detail in Hamilton and Shao (2008). Although these models may not be accurate under lunar conditions, they can be readily implemented and help answer questions about the sensitivity of the dust sprays to the assumed emission model. The Colorado Center for Lunar Dust and Atmospheric Studies (CCLDA) at the Laboratory for Atmospheric and Space Physics (LASP) studies high velocity impacts of lunar dust particles. The particles are accelerated in a vacuum chamber by using electric fields and impacts speeds between 1 and 100 km/s are obtained. This work may eventually provide data that can be used for better models of erosion via saltation bombardment under lunar conditions. These experiments can also be used to help

improve models for the interactions of dust with a berm by constraining the grain-berm interaction model.

The model accuracy can also be improved by simulating the multi-species chemical composition of the exhaust gases more accurately. The exhaust species for the LMDE and exit plane properties for Aerozine-50 fuel can be predicted by using a rocket nozzle solver such as JANAAF. Simmons (2000) argues that the molecular mass of the exhaust products and the ratio of specific heats of the mixture can affect the structure of the exhaust plume. Changes in the plume structure may affect the impinging flow field and can thus affect the entrainment and transport of dust.

The methodology developed in this work can also be used to simulate other scenarios and to improve understanding of the model sensitivity. The sensitivity of the model to the assumed particle size distribution (PSD) of aerosolized particles has not yet been studied. The PSD may also change as the lander approaches the surface; smaller particles may be eroded at higher altitudes and leave behind only large particles near the ground. One approach to do this would be to use particle size distributions measured either at different Apollo sites or depths beneath the surface and to characterize the impact that it has on the grain motion.

Lunar soil consists of particles that range from the 100 nm to 1 mm in diameter, but only particles sizes less than 11 μm were simulated in this work. Larger particles are difficult to simulate because they tend to move slower and take a long time to traverse the computational domain. Consequently, simulations become expensive for the large particle motion to become steady. Further, the gas mean free path may be small compared to the particle diameter and free molecular assumptions in the gas-dust interaction model break down. An overlay method can be used to rapidly simulate the motion of the larger dust particles. The average gas properties can be used as an input

for Loth's equations (see Section 2.5.4) for computing the momentum transfer to larger particles. For larger particles, gravity will eventually dominate and the aerodynamic forces will be insufficient to entrain the particles. These simulations would help constrain the maximum size particles that can be entrained by the gas.

Additional simulations should include the effects of near field surface topography on the erosion and transport of dust. Streaks of dust were observed during the Apollo landing videos. These streaks may occur because of local surface features such as a craters or small rocks. Additional code development to account for surface geometry must be done, but some of the framework currently exists in the routines for modeling an angled berm. Craters located in the near field result in 3-dimensional flow and can affect the ejection angle of particles entrained in the flow. Simulations of a vertical fence placed very close to the lander (see Section 7.5) suggest that unsteadiness may occur if a large obstacle exists close to the lander. Such unsteadiness could result in clusters of granular material that are then launched into the far field.

Simulations for multi-engine landers were only executed for one specific 4-engine configuration. In addition to simulating additional hovering altitudes, different engine configurations can also be analyzed. Several possibilities include: simulating 2- or 3-engine configurations, tilting the rocket engines outward at a small angle, and changing the offset distance between nozzles. Different configurations will likely affect the directionality as well as ejection angles of the dust.

Landings on an inclined surface have not been studied in this work and would be expected to result in directional jetting of dust. There are two ways to simulate such landings in the current model. The first would be writing a routine to rotate the creation cells at the hybrid interface, thus rotating the engine, and to readjust the direction of the gravity vector. Another option would be to use software already written for angled

berm simulations, and represent the lunar surface by a very large berm inclined at a shallow angle. These simulations could help predict the directionality of dust sprays and may help in deciding the best location for a lunar outpost or the approach trajectory of a lander.

APPENDIX A. MOMENTUM AND ENERGY CONSERVATION FOR THE GAS- PARTICLE INTERACTION MODEL

A proof for conservation of momentum and energy within the particle-gas interaction model is presented in this appendix. To do this, the momentum and energy transfer to the gas phase is computed and then compared to the momentum and energy transfer to the particle phase. Please refer to Section 3.3.3 for the dust-gas interaction model analyzed in this appendix.

Consider gas molecules of the same velocity class colliding with a single particle in the particle fixed reference frame. The momentum of a single gas molecule, P_g , in the direction of the pre-collision relative velocity vector and pre-collision energy, E_g , are

$$P_{g,rel} = m_g c_r, \quad \text{A-1}$$

$$E_g = \frac{1}{2} m_g c_r^2 + e_{rot}. \quad \text{A-2}$$

The molecular mass of the gas is m_g , the pre-collision relative speed is c_r , and the rotational energy of the gas molecule before the collision is e_{rot} . Vibrational energy is assumed to be unaltered by the gas-particle collision and is therefore neglected in the energy equation. Momenta in other directions are neglected because, on average, only momentum in the direction of the relative velocity vector is transferred via dust-gas interactions. The post-collision momentum and energy, P'_g and E'_g , are

$$P'_{g,rel} = -m_g c'_r \cos \delta, \quad \text{A-3}$$

$$E'_{g,rel} = \frac{1}{2} m_g c'^2_r + e'_{rot}, \quad \text{A-4}$$

where δ is the scattering angle between the post- and negative pre-collision relative velocity vectors (shown schematically in Figure 3.3.6). The expectation values

(indicated by angle brackets) for the post-collision momentum and energy is obtained by integrating over the post-collision distribution functions for \underline{c}_r' and δ ,

$$\langle P'_{g,rel} \rangle = - \int_0^\infty m_g c_r' f(c_r') dc_r' \int_0^\pi (\cos \delta) f(\delta) d\delta, \quad A-5$$

$$\langle E'_{g,rel} \rangle = \int_0^\infty \frac{1}{2} m_g c_r'^2 f(c_r') dc_r' + \langle e'_{rot} \rangle. \quad A-6$$

The case of specular reflection is first considered. The relative speed remains unchanged after a specular collision and the scattering distribution is $f(\delta) = 1/2 \sin \delta$, derived in Burt (2004). These distributions are substituted into equations A-5 and A-6 to determine the expectation post-collision momentum and energy for specular reflections. The post-collision momentum in the direction of the relative velocity vector is zero and the energy remains unchanged. The post-collision momentum, measured from the dust particle reference frame, is zero because the gas scattering is isotropic; forward and back scatter are equally likely. The total force and heat transfer are obtained by multiplying the change in momentum and energy by the collision rate. The collision rate between gas molecules represented by one simulator with a dust particle is $\pi R_p^2 N_p c_r / V_c$, where N_p is the number of actual gas molecules represented by each simulator, V_c is the volume of a DSMC collision cell, and R_p is the radius of a dust particle. The expectation value for the force is in the direction of the relative velocity vector and is found for specular reflections to be

$$\langle \mathbf{F} \rangle = \frac{\pi R_p^2 N_p \mathbf{u}_r}{V_c} (m_g c_r - 0). \quad A-7$$

The energy remains unchanged for specular reflections, resulting in no heat transfer to the particle. The expectation values of drag force and heat transfer are equivalent to the expressions in equations 3.3-6 and 3.3-7 for the drag and heat transfer to

a particle for specular collisions, i.e. when τ_p is 0. This proves that the expectation values for momentum and energy transfer to the gas exactly balance the momentum and energy to the dust for specular reflections.

A similar analysis is performed for the case of diffuse reflection. For diffuse reflections, the scattering function is discussed in Section 3.3.3 and is

$$f(\delta)d\delta = \frac{1}{2\pi} \sin(2\theta) \sin(2\varphi) d\varphi d\theta d\varepsilon. \quad \text{A-8}$$

The cosine of the scattering angle (refer to Section 3.3.3) can be expressed in terms of angles θ, φ , and ε and is

$$\cos \delta = (\cos \theta - \sin \theta \tan \varphi \cos \varepsilon) \cos \varphi. \quad \text{A-9}$$

The post-collision relative speed distribution for diffuse reflections off a particle of thermal temperature T_p is the speed distribution of an equilibrium gas fluxing across a plane and is

$$f(c'_r) = 2 \left(\frac{m_g}{2k_b T_p} \right)^2 c'^3_r \exp \left(-\frac{m_g}{2k_b T_p} c'^2_r \right). \quad \text{A-10}$$

The post-collision distribution of rotational energies is Boltzmann distributed based on the temperature of the particle. The expectation value for the cosine of the scattering angle, δ , is

$$\langle \cos \delta \rangle = \int_0^{2\pi} \int_0^{\frac{\pi}{2}} \int_0^{\frac{\pi}{2}} \frac{\cos \delta \sin(2\theta) \sin(2\varphi)}{2\pi} d\theta d\varphi d\varepsilon = \frac{4}{9}. \quad \text{A-11}$$

The expectation value for the post-collision gas momentum for diffuse reflection is obtained by substituting equations A-10 and A-11 into A-5, and is

$$\langle P'_{g,rel} \rangle = -\frac{1}{3} m_g \sqrt{\pi \frac{2k_b T_p}{m_g}}. \quad \text{A-12}$$

Similarly, the expectation value for the post-collision energy of the gas molecule is

$$\langle E'_{g,rel} \rangle = 2k_b T_p + \frac{\Lambda}{2} k_b T_p. \quad \text{A-13}$$

The expectation values for the drag force and energy transfer to the particle for diffuse reflection are:

$$\langle \mathbf{F} \rangle = \frac{\pi R_p^2 N_g \mathbf{u}_r}{V_c} \left(m_g c_r + \frac{1}{3} \sqrt{2\pi m_g k_b T_p} \right), \quad \text{A-14}$$

$$\langle Q \rangle = \frac{\pi R_p^2 N_g c_r}{V_c} \left(\frac{1}{2} m_g c_r^2 + e_{rot} - \left(2 - \frac{\Lambda}{2} \right) k_b T_p \right). \quad \text{A-15}$$

The above expectation values are equivalent to the force and energy transfer to the particle phase for diffuse reflections, shown by equations 3.3-6 and 3.3-7 when $\tau_p = 1$. Diffuse reflections result in additional momentum transfer from the gas to the particle phase because gas molecules that undergo diffuse reflection preferentially backscatter off the dust particle.

These derivations show that the expectation values for momentum and energy transfer from the particle to gas phase are equivalent to the momentum and energy transferred from the gas to the dust particles. Although the gas-particle interaction model does not instantaneously conserve momentum and energy, the analyses in this appendix prove that momentum and energy are conserved on average after many collisions.

BIBLIOGRAPHY

- Alfaro, S. C., Gaudichet, A., Gomes, L., & Maille, M. (1997). Modeling the Size Distribution of a Soil Aerosol Produced by Sandblasting. *Journal of Geophysical Research*, 102, 239-250.
- Anderson, J. D. (2003). *Modern Compressible Flow: With Historical Perspective* (3rd ed.). New York: McGraw-Hill.
- Bagnold, R. A. (1941). *The Physics of Blown Sand and Desert Dunes*. London: Methuen.
- Bennett, F. V. (1972). *Apollo Experience Report - Mission Planning for Lunar Module Descent and Ascent*. Washington, D. C.: NASA.
- Bird, G. A. (1981). Breakdown of Continuum Flow in Freejets and Rocket Plumes. *Proceedings of the 12th International Symposium on Rarefied Gas Dynamics*, (pp. 681-694). Charlottesville, VA.
- Bird, G. A. (1994). *Molecular Gas Dynamics and the Direct Simulation of Gas Flows*. Oxford: Oxford University Press.
- Bizon, C., Shattuck, M. D., Swift, J. B., McCormick, W. D., & Swinney, H. L. (1998). Patterns in 3D Vertically Oscillated Granular Layers: Simulation and Experiment. *Phys. Review Letters*, 80, 57-60.
- Borée, J., Ishima, T., & Flour, I. (2001). The Effect of Mass Loading and Inter-Particle Collisions on the Development of the Polydispersed Two-Phase Flow Downstream of a Confined Bluff Body. *Journal of Fluid Mechanics*, 443, 129-165.
- Boyd, I. D., & Stark, J. P. (1990). Modeling of a Small Hydrazine Thrust Plume in the Transition Flow Regime. *Journal of Propulsion and Power*, 6(2), 121-126.
- Boyd, I. D., Beattie, D. R., & Cappelli, M. A. (1994). Numerical and Experimental Investigations of Low-Density Supersonic Jets of Hydrogen. *Journal of Fluid Mechanics*, 280, 41-67.
- Boyd, I. D., Chen, G., & Candler, G. V. (1995). Predicting Failure of the Continuum Fluid Equations in Transitional Hypersonic Flows. *Physics of Fluids*, 7(1).
- Boyd, I. D., Penko, P. F., Meissner, D. L., & Dewitt, K. J. (1992). Experimental and Numerical Investigations of Low-Density Nozzle and Plume Flows of Nitrogen. *AIAA Journal*, 30(10), 2453-2461.
- Brilliantov, N. V., & Pöschel, T. (2004). *Kinetic Theory of Granular Gases*. New York: Oxford University Press.
- Burt, J. M., & Boyd, I. D. (2005). Monte Carlo Simulation of a Rarefied Multiphase Plume Flow. *43rd AIAA Aerospace Sciences Meeting and Exhibit*. Reno, NV.
- Burt, J., & Boyd, I. (2004). Development of a Two-Way Coupled Model for Two Phase Rarefied Flows. *42nd AIAA Aerospace Sciences Meeting and Exhibit*. Reno, NV.
- Campbell, C. S. (1990). Rapid Granular Flows. *Annual Review of Fluid Mechanics*, 57-92.
- Castellanos, A., Valverde, J. M., Perez, A. T., Ramos, A., & Watson, P. K. (1999). Flow Regimes in Fine Cohesive Powders. *Physical Review Letters*, 82(6), 1156-1159.

- Cherne, J. M. (1967). *Mechanical Design of the Lunar Module Descent Engine*. Redondo Beach, CA: TRW Systems.
- Choate, R., Batterson, S., Christensen, E., Hutton, R., Jaffe, L., Jones, R., & Sperling, F. (1969). Lunar Surface Mechanical Properties. *Journal of Geophysical Research*, 74(25), 6149-6174.
- Clegg, R. N., Jolliff, B. L., & Metzger, P. T. (2012). Photometric Analysis of the Apollo Landing Sites. *Proceedings of Earth and Space 2012: Engineering, Science, Construction, and Operations in Challenging Environments* (pp. 218-227). Pasadena, CA: ASCE.
- Clift, R., Grace, J. R., & Weber, M. E. (1978). *Bubbles, Drops, and particles*. New York: Academic Press.
- Dettleff, G. (1991). Plume Flow and Plume Impingement in Space Technology. *Progress in Aerospace Sciences*, 28(1), 1-71.
- Draper, J., & Hill, J. (1966). Analytical Approximation for the Flow From a Nozzle Into a Vacuum. *Journal of Spacecraft and Rockets*, 3, 1552-1554.
- Gaier, J. R. (2005). *The Effects of Lunar Dust on EVA Systems During the Apollo Missions*. Cleveland, OH: NASA.
- Gallis, M. A., Torczynski, J. R., & Rader, D. J. (2001). An Approach for Simulating the Transport of Spherical Particles in a Rarefied Gas Flow Via the Direct Simulation Monte Carlo Method. *Physics of Fluids*, 13(11), 3482-3492.
- Garcia, A., & Alder, W. (1998). Generation of the Chapman-Enskog Distribution. *Journal of Computational Physics*, 140(66).
- Gillette, D. A., & Passi, R. (1988). Modelling Dust Emission Caused by Wind Erosion. *Journal of Geophysical Research*, 93, 233-247.
- Goldhirsch, I. (2003). Rapid Granular Flows. *Annual Review of Fluid Mechanics*, 267-293.
- Greeley, R., & Iversen, J. D. (1985). *Wind as a Geological Process: On Earth, Mars, Venus, and Titan*. New York: Cambridge University Press.
- Greenberg, P., Chen, D.-R., & Smith, S. (2007). *Aerosol Measurements of the Fine and Ultrafine Particle Content of Lunar Regolith*. Cleveland: NASA Glenn Research Center.
- Hamilton, K., & Shao, Y. (2008). *Physics and Modelling of Wind Erosion*. Springer.
- Heiken, G., Vaniman, D., & French, B. (1991). *Lunar Sourcebook: A User's Guide to the Moon*. Cambridge: Cambridge University Press.
- Humphries, C., Hammock, W., Currie, E. C., Taylor, R. E., & Fisher, A. E. (1973). *Apollo Experience Report: Descent Propulsion System*. NASA.
- Hutton, R. E. (1971). *Lunar Surface Erosion During Apollo 11, 12, 14, and 15 Landings*. Redondo Beach, CA: TRW Systems.
- Hyakutake, T., & Nishida, M. (2000). Numerical Simulations of Rarefied Plume Impingements. *Proceedings of the 22nd International Symposium on Rarefied Gas Dynamics*, (pp. 806-811). Sydney, Australia.
- Immer, C., Lane, J., Metzger, P., & Clements, S. (2011). Apollo Video Photogrammetry Estimation of Plume Impingement Effects. *Icarus*, 214(1), 46-52.

- Immer, C., Metzger, P., Hintz, P. E., Nick, A., & Horan, R. (2011). Apollo 12 Lunar Module Exhaust Plume Impingement on Lunar Surveyor III. *Icarus*, 211(2), 1089-1102.
- Ivanov, S. M., Markelov, N. G., Kashkovsky, V. A., & Giordano, D. (1997). Numerical Analysis of Thruster Plume Interaction Problems. In M. Perry (Ed.), *Proceedings of the Second European Spacecraft Propulsion Conference, 1997 in Noordwijk, the Netherlands*. Edited by Michael Perry (pp. 603-610). Noordwijk, Netherlands: European Space Agency.
- Kannenbergh, K. C., & Boyd, I. D. (1999). Three-Dimensional Monte Carlo Simulations of Plume Impingement. *Journal of Thermophysics and Heat Transfer*, 13(2), 226-235.
- Koppenwallner, G. (1983). *Rarefied plume interference and scaling laws*. Göttingen, Germany: DFVLR Internal Report IB.
- Lane, J., Metzger, P., & Immer, C. (2008). Lagrangian Trajectory Modeling of Lunar Dust Particles. *Earth and Space 2008: Conference on Engineering, Construction, and Operations in Hazardous Environments*. Long Beach, CA: ASCE.
- Legge, H. (1990). Plume Impingement Forces on Inclined Flat Plates. *Proceedings of the 17th International Symposium on Rarefied Gas Dynamics*, (pp. 955-962). Aachen, Germany.
- Legge, H., & Boettcher, R. (1985). Modeling Control Thruster Plume Flow and Impingement. *Proceedings of the 13th International Symposium on Rarefied Gas Dynamics* (pp. 983-992). Novosibirsk: Plenum Press.
- Loosmore, G. A., & Hunt, J. R. (2000). Below-threshold, Non-abraded Dust Resuspension. *Journal of Geophysical Research*, 105, 663-683.
- Loth, E. (2008). Compressibility and Rarefaction Effects on Drag of a Spherical Particle. *AIAA Journal*, 46(9), 2219-2228.
- Luding, S., Müller, M., & McNamara, S. (1998). The Validity of "Molecular Chaos" in Granular Flows. *World Congress on particle Technology*.
- Lumpkin, F. E., Stuart, P. C., & LeBeau, G. J. (1996). Enhanced analyses of plume impingement during Shuttle-Mir docking using a combined CFD and DSMC methodology. *31st AIAA Thermophysics Conference*. New Orleans.
- Marichalar, J., Prisbell, A., Lumpkin, F., & LeBeau, G. (2011). Study of Plume Impingement Effects in the Lunar Lander Environment. *Proceedings of the 27th International Symposium on Rarefied Gas Dynamics*, 1333, pp. 589-594. Pacific Grove, CA.
- McDoniel, W., Buchta, D., Goldstein, D., Kieffer, S., Varghese, P., Trafton, L., & Freund, J. (2011). Simulating Irregular Source Geometries for Ionian Plumes. In D. Levin, I. Wysong, & A. Garcia (Ed.), *Rarefied Gas Dynamics*, 27th International Symposium on Rarefied Gas Dynamics, 1333. Pacific Grove, CA.
- McNamara, S., & Young, W. (1992). Inelastic Collapse and Clumping in a One-Dimensional Granular Medium. *Physics of Fluids A*, 4(3), 496.
- Mehta, M., Sengupta, A., Pokora, M., Hall, L., & Renno, N. (2010). Mars Landing Engine Plume Impingement Ground Interaction. *Earth and Space 2010*:

- Engineering, Science, Construction, and Operations in Challenging Environments*. Honolulu, HI: ASCE.
- Metzger, P. T., Immer, C. D., Donahue, C. M., Vu, B. M., Latta III, R. C., & Deyo-Svendsen, M. (2009). Jet-Induced Cratering of a Granular Surface with Application to Lunar Spaceports. *Journal of Aerospace Engineering*, 21(1), 24-32.
- Metzger, P. T., Lane, J. E., Immer, C. D., Gamsky, J., Hauslein, W., Li, X., . . . Donahue, C. M. (2010). Scaling of Erosion Rate in Subsonic Jet Experiments and Apollo Lunar Module Landings. *Earth and Space 2010: Engineering, Science, Construction, and Operations in Challenging Environments*. Honolulu, HI: ASCE.
- Metzger, P. T., Latta III, R. C., Schuler, J. M., & Immer, C. D. (2009). Craters Formed in Granular Beds by Impinging Jets of Gas. *Powders and Grains 2009: Proceedings of the 6th International Conference on Micromechanics of Granular Media*. 1145, pp. 767-770. AIP Conference Proceedings.
- Metzger, P. T., Smith, J., & Lane, J. (2011). Phenomenology of soil erosion due to rocket exhaust on the Moon and the Mauna Kea lunar test site. *Journal of Geophysical Research*, 116.
- Metzger, P., Lane, J., & Immer, C. (2008). Modification of Roberts' Theory for Rocket Exhaust Plumes Eroding Lunar Soil. *Earth and Space 2008* (pp. 1-8). Honolulu, HI: ASCE.
- Moon, S. J., Swift, J. B., & Swinney, H. L. (2004). Role of Friction in Pattern Formation in Oscillated Granular Layers. *Physical Review E*, 69, 031301.
- Moore, C. (2011). *Monte Carlo Simulation of the Jovian Plasma Torus Interaction with Io's Atmosphere and the Resultant Aurora During Eclipse*. PhD Dissertation, The University of Texas at Austin.
- Morris, A. B. (2010). Plume Impingement on a Dusty Surface. *Proc. of the 27th Intl. Symposium on Rarefied Gas Dynamics*, 1333, 1187-1192.
- Müller, M., Luding, S., & Herrmann, H. J. (1997). Simulations of Vibrated Granular Media in 2D and 3D. (D. E. Wolf, & P. Grassberger, Eds.) *Friction, Arching, and Contact Dynamics*.
- Nickerson, C. R., Dang, L., & Coats, D. E. (1985). *TDK Two-dimensional Kinetic Reference Computer Program*. Ultrasystems, Inc. Marshall Space Flight Center.
- Park, J., Liu, Y., Kihm, K., & Taylor, L. (2008). Characterization of Lunar Dust for Toxicological Studies. I: Particle Size Distribution. *Journal of Aerospace Engineering*, 21(4), 266-271.
- Rao, G. V. (1958). Exhaust Nozzle Contour For Optimum Thrust. *Jet Propulsion*, 28, 377.
- Roberts, L. (1963). The Action of a Hypersonic Jet on a Dusty Surface. *Institute of the Aerospace Sciences*. IAS Paper 63-50.
- Roberts, L. (1966). The Interaction of a Rocket Exhaust With the Lunar Surface. *The Fluid Dynamic Aspects of Space Flight*, 2, pp. 269-290.

- Roberts, L., & South Jr., J. (1964). Comments on Exhaust Flow Field and Surface Impingement. *AIAA Journal*, 2(5), 971-974.
- Romine, G. L., Reisert, T. D., & Gliozzi, J. (1973). *Site Alteration Effects from Rocket Exhaust Impingement During a Simulated Viking Mars Landing Part 1*. NASA.
- Schäfer, J., Dippel, S., & Wolf, D. E. (1996). Force Schemes in Simulations of Granular Materials. *Journal de Physique I*, 6, 5-20.
- Schmidt, D. P., & Rutland, C. J. (2000). A New Droplet Collision Algorithm. *Journal of Computational Physics*, 164, 62-80.
- Schwager, T., Becker, V., & Pöschel, T. (2008). Coefficient of Tangential Restitution for Viscoelastic Spheres. *The European Physical Journal E*, 27, 107-114.
- Sengupta, A., Kulleck, J., Sell, S., Norman, J. V., Mehta, M., & Pokora, M. (2009). Mars Lander Engine Plume Impingement Environment of. *IEEE Aerospace Conference*, (pp. 1-10). Big Sky, MT.
- Shattuck, M. D., Bizon, C., Swift, J. B., & Swinney, H. L. (1999). Computational Test of Kinetic Theory of Granular Media. *Physica A*, 274, 158-170.
- Sibulkin, M., & Gallaher, W. (1969). Far-field Approximation for a Nozzle Exhaust Into a Vacuum. *AIAA Journal*, 1(6), 1452-1453.
- Simmons, F. S. (2000). *Rocket Exhaust Plume Phenomenology*. El Segundo, CA: The Aerospace Press.
- Simoneit, B. F., Burlingame, A. L., Flory, D. A., & Smith, I. (1969). Apollo Lunar Module Engine Exhaust Products. *Science*, 166(3906), 733-738.
- Simons, G. A. (1972). Effect of Nozzle Boundary Layers on Rocket Exhaust Plumes. *AIAA Journals*, 10, 1534-1535.
- Spahn, F., Schmidt, J., Petzschmann, O., & Salo, H. (2000). Stability Analysis of a Keplerian Disk of granular Grains: Influence of Thermal Diffusion. *Icarus*, 145, 657-60.
- Steltzner, A. D., Burkhard, P. D., Chen, A., Comeaux, K., Guernsey, C., Kipp, D., . . . Way, D. W. (2006). Mars Science Laboratory Entry, Descent, and Landing System Overview. *Proc IEEE Aerospace Conference*. Big Sky, MT.
- Stephani, K. A., Goldstein, D. B., & Varghese, P. L. (2012). Generation of a Hybrid DSMC/Navier-Stokes Solution Via a Non-equilibrium Surface Reservoir Approach. *Journal of Computational Physics*.
- Stewart, B. D., Pierazzo, E., Goldstein, D. B., Varghese, P., & Trafton, L. (2011). Simulations of a Comet Impact on the Moon and Associated Ice Deposition In Polar Cold Traps. *Icarus*, 215(1), 1-16.
- Stewart, B., Pierazzo, E., Goldstein, D., Varghese, P., & Trafton, L. (2009). Parallel 3D Hybrid Continuum/DSMC Method for Unsteady Expansions into a Vacuum. *AIAA ASM Meeting*. Orlando: AIAA.
- Strutzenberg, L. L., Dougherty, N. S., Liever, P. A., West, J. S., & Smith, S. D. (2007). *Space Shuttle Propulsion Systems Plume Modeling and Simulation for the Lift-Off Computational Fluid Dynamics Model*. Huntsville, AL: Marshall Space Flight Center.

- Sutton, G. P. (1992). *Rocket Propulsion Elements, 6th ed.* New York: John Wiley and Sons, Inc.
- Tosh, A., Liever, P. A., Arslanbekov, R. R., & Habchi, S. D. (2011). Numerical Analysis of Spacecraft Rocket Plume Impingement Under Lunar Environment. *Journal of Spacecraft and Rockets*, 48(1), 93-102.
- Umbanhowar, P. B. (1996). *Wave Patterns in Vibrated Granular Layers*. The University of Texas at Austin.
- Vick, A. R., & Andrews, E. H. (1966). *An Investigation of Highly Underexpanded Exhaust Plumes Impinging Upon a Perpendicular Flat Surface*. Langley Research Center. Hampton, VA: NASA.
- Wagner, S. A. (2006). *The Apollo Experience Lessons Learned for Constellation Lunar Dust Management*. Johnson Space Center. Houston, TX: NASA.
- Walton, O. (1993). Numerical Simulation of Inelastic, Frictional Particle-Particle Interactions. (M. C. Roco, Ed.) *Particulate Two-Phase Flow*, 884-911.
- Wright, M. J., Candler, G. V., & Bose, D. (1998). Data-Parallel Line Relaxations Method for the Navier-Stokes Equation. *AIAA Journal*, 36(9), 1603-1609.
- Zhang, J., Goldstein, D. B., Varghese, P., Trafton, L., Moore, C., & Miki, K. (2004). Numerical Modeling of Ionian Volcanic Plumes with Entrained Particulates. *Icarus*, 172, 479-502.
- Zheng, X. (2009). *Mechanics of Wind-blown Sand Movements*. Berlin: Springer.

VITA.

Aaron Morris received his Bachelors of Science in Mechanical Engineering degree in May of 2006. He then interned at the Jet Propulsion Laboratory during the summer of 2006 and began his graduate studies at The University of Texas at Austin in the fall of 2006. After being a teaching assistant for the first semester, he began researching novel methods for solving the Boltzmann equation via a discrete velocity model. In January of 2009 he finished his thesis on this research and received his Master's degree in Aerospace Engineering under the supervision of Profs. David Goldstein and Philip Varghese. He then began work on his doctorate degree with Profs. Goldstein and Varghese on plume impingement and dust dispersal on the Moon.

Permanent Address: 300 Osborne Rd
 Loudonville, NY 12211

This dissertation was typed by the author.